

Abstract Volume



LPI Contribution No. 1097

WORKSHOP ON MERCURY: SPACE ENVIRONMENT, SURFACE, AND INTERIOR

**The Field Museum
Chicago, Illinois
October 4–5, 2001**

Conveners

Mark Robinson, Northwestern University
G. Jeffrey Taylor, University of Hawai'i

Sponsored by

Lunar and Planetary Institute
The Field Museum
National Aeronautics and Space Administration

Lunar and Planetary Institute 3600 Bay Area Boulevard Houston TX 77058-1113

LPI Contribution No. 1097

Compiled in 2001 by
LUNAR AND PLANETARY INSTITUTE

The Institute is operated by the Universities Space Research Association under Contract No. NASW-4574 with the National Aeronautics and Space Administration.

Material in this volume may be copied without restraint for library, abstract service, education, or personal research purposes; however, republication of any paper or portion thereof requires the written permission of the authors as well as the appropriate acknowledgment of this publication.

This volume may be cited as

Author A. B. (2001) Title of abstract. In *Workshop on Mercury: Space Environment, Surface, and Interior*, p. xx. LPI Contribution No. 1097, Lunar and Planetary Institute, Houston.

This report is distributed by

ORDER DEPARTMENT
Lunar and Planetary Institute
3600 Bay Area Boulevard
Houston TX 77058-1113, USA
Phone: 281-486-2172
Fax: 281-486-2186
E-mail: order@lpi.usra.edu

Please contact the Order Department for ordering information.

Preface

This volume contains abstracts that have been accepted for presentation at the Workshop on Mercury: Space Environment, Surface, and Interior, October 4–5, 2001. The Scientific Organizing Committee consisted of Mark Robinson (*Northwestern University*), Marty Slade (*Jet Propulsion Laboratory*), Jim Slavin (*NASA Goddard Space Flight Center*), Sean Solomon (*Carnegie Institution*), Ann Sprague (*University of Arizona*), Paul Spudis (*Lunar and Planetary Institute*), G. Jeffrey Taylor (*University of Hawai'i*), Faith Vilas (*NASA Johnson Space Center*), Meenakshi Wadhwa (*The Field Museum*), and Thomas Watters (*National Air and Space Museum*).

Logistics, administrative, and publications support were provided by the Publications and Program Services Departments of the Lunar and Planetary Institute.

Contents

Mercury's Global Topography from Radar Ranging Data <i>J. D. Anderson, G. Schubert, S. W. Asmar, R. F. Jurgens, E. L. Lau, W. B. Moore, M. A. Slade III, and E. M. Standish Jr.</i>	1
Applying Numerical Dynamo Models to Mercury <i>J. M. Aurnou and F. M. Al-Shamali</i>	2
Reflectance Spectra of Lunar Pure Anorthosites and of Mercury <i>D. T. Blewett, B. R. Hawke, and P. G. Lucey</i>	4
ENA Imaging at Mercury? Lessons from IMAGE/HENA <i>P. C. Brandt, D. G. Mitchell, and S. Barabash</i>	6
Reflectance Spectra of Aubrites, Sulfides, and E Asteroids: Possible Implications for Mercury <i>T. H. Burbine, T. J. McCoy, and E. A. Cloutis</i>	7
The Nature of the Mercury Polar Radar Features <i>B. J. Butler, M. A. Slade, and D. O. Muhleman</i>	9
The MESSENGER Science Planning Tool <i>T. H. Choo, S. L. Murchie, and J. S. Jen</i>	11
A Multi-Colour Imaging System for the Bepi Colombo Mercury Lander <i>L. Colangeli, P. Palumbo, C. Barbieri, G. Bellucci, A. Bini, A. Blanco, G. Cremonese, V. Della Corte, S. Fonti, E. Mazzotta Epifani, G. Preti, H. Yano, and S. Vergara</i>	13
Digital Elevation Model Mosaic of Mercury <i>A. C. Cook, T. R. Watters, and M. S. Robinson</i>	14
Mid-Infrared Spectra of Mercury <i>B. Cooper, A. E. Potter, R. M. Killen, and T. H. Morgan</i>	16
A Wide Angle Camera for Bepi Colombo <i>G. Cremonese, V. Achilli, C. Barbieri, A. Caporali, M. T. Capria, L. Colangeli, G. Forlani, S. Fornasier, M. Lazzarin, F. Marzari, L. Marinangeli, G. Naletto, P. Palumbo, R. Ragazzoni, G. Salemi and S. Verani</i>	18
X-Ray Science on ESA's BepiColombo Mission to Mercury <i>S. K. Dunkin, M. Grande, and B. J. Kellett</i>	19

Measuring the Chemical Composition of the Surface of Mercury Using Orbital Gamma-Ray and Neutron Spectroscopy <i>C. d'Uston, J. Brückner, W. C. Feldman, O. Gasnault, N. Hasebe, D. J. Lawrence, S. Maurice, and T. H. Prettyman</i>	21
IMS: The Infrared Mapping Spectrometer of the BepiColombo Mission <i>S. Erard</i>	23
The Electron Environment at Mercury <i>R. A. Frahm, R. Link, J. D. Winningham, A. J. Coates, and O. Norberg</i>	25
Using Remotely Sensed Observations of Ancient Mare Deposits on the Moon as Possible Analogs to the Intercrater Plains on Mercury <i>J. J. Gillis and M. S. Robinson</i>	26
Magnetosphere-Regolith/Exosphere Coupling: Differences and Similarities to the Earth Magnetosphere-Ionosphere Coupling <i>J. W. Gjerleov and J. A. Slavin</i>	28
The MESSENGER Scientific Payload <i>R. E. Gold, R. L. McNutt Jr., A. G. Santo, S. C. Solomon, and the MESSENGER Team</i>	29
CIXS — An X-Ray Spectrometer for ESA's BepiColombo Mission to Mercury <i>M. Grande, S. K. Dunkin, and B. J. Kellett</i>	31
The Charged Particle Environment of Mercury and Related Electric Phenomena <i>R. Grard and H. Laakso</i>	33
BepiCOLOMBO, an Interdisciplinary Mission to the Planet Mercury <i>R. Grard and T. Mukai</i>	34
Space Weathering and the Composition of the Crust of Mercury <i>B. Hapke</i>	35
Radar Imaging of Mercury's North and South Poles at 3.5 cm Wavelength <i>L. J. Harcke, H. A. Zebker, R. F. Jurgens, and M. A. Slade</i>	36
Mercury Radar Imaging at Arecibo <i>J. K. Harmon</i>	38
Mercury's Thermal, Tectonic, and Magmatic Evolution <i>S. A. Hauck II, A. J. Dombard, R. J. Phillips, and S. C. Solomon</i>	40

Overview of the MESSENGER Mercury Dual Imaging System <i>S. E. Hawkins III, J. D. Boldt, E. H. Darlington, M. P. Grey, C. J. Kardian Jr., S. L. Murchie, K. Peacock, E. D. Schaefer, and B. D. Williams</i>	42
Theoretical Aspects of Magma Generation, Ascent and Eruption on Mercury and Comparison with Composition and Morphology of Surface Features <i>J. W. Head and L. Wilson</i>	44
Estimation of Mercury's Obliquity and Physical Librations by Earth-based Radar Speckle Displacement Interferometry <i>I. V. Holin</i>	46
Neutral Atom Imaging Near Mercury <i>M. Holmström, S. Barabash, and A. Lukyanov</i>	47
Diurnal Variation of Na and K at Mercury <i>D. M. Hunten and A. L. Sprague</i>	48
On the Modeling of the Mercury-Solar Wind Interaction by a Quasineutral Hybrid Model <i>E. Kallio and P. Janhunen</i>	50
In Search of Lunar Like Rilles on Mercury <i>A. Kereszturi</i>	51
Ar Atmosphere: Implications for Structure and Composition of Mercury's Crust <i>R. M. Killen and T. H. Morgan</i>	53
Measuring the Plasma Environment at Mercury: The Fast Imaging Plasma Spectrometer <i>P. L. Koehn, T. H. Zurbuchen, L. A. Fisk, and G. Gloeckler</i>	54
Resolved Ground Based Observation of Mercury <i>L. V. Ksanfomality</i>	55
Properties of the Hermean Surface <i>L. Ksanfomality, A. Sprague, C. Cremonese, L. Jorda, N. Thomas, and J. Warell</i>	56
Electric Field Double Probe Antenna for the BepiColombo/MMO Satellite <i>H. Laakso, R. Grard, B. Johlander, D. Klinge, and J.-P. Lebreton</i>	57

An Artificial Seismic Impact Experiment on BepiColombo <i>P. Lognonné, D. Giardini, Y. Langevin, and H. Mizutani</i>	58
Specific Character of the Formation of Mercury as the Densest Planet <i>A. A. Marakushev, O. V. Chaplygin, and A. V. Bobrov</i>	59
Radar Techniques for the Measurement of Mercury's Obliquity and Librations <i>J. L. Margot, S. J. Peale, and M. A. Slade</i>	60
The Mercury Atmospheric and Surface Composition Spectrometer (MASCS) for the Mercury: Surface, Space Environment, Geochemistry, Ranging (MESSENGER) Mission <i>W. E. McClintock and G. M. Holsclaw</i>	62
Identification of Mercurian Volcanism: Resolution Effects and Implications for MESSENGER <i>S. M. Milkovich and J. W. Head</i>	63
Crater Production Function and Cratering Chronology for Mercury <i>G. Neukum, B. A. Ivanov, and R. Wagner</i>	65
Constraining the Mean Crustal Thickness on Mercury <i>F. Nimmo</i>	67
Space Weathering in the Mercurian Environment <i>S. K. Noble and C. M. Pieters</i>	68
A Combined Stereo Camera/Laser Altimeter Experiment Package for the BepiColombo Polar Orbiter <i>J. Oberst, R. Wagner, H. Hoffmann, R. Jaumann, and G. Neukum</i>	70
Scientific Merits and Technical Aspects of a Thermal/Energetic Neutral Particle Detector On Board the ESA BepiColombo Mission <i>S. Orsini, E. De Angelis, A. M. Di Lellis, S. Barabash, I. A. Daglis, D. Delcourt, E. Kallio, R. Killen, S. Livi, A. Milillo, A. Mura, P. Wurz, and V. Zanza</i>	72
A Procedure for Determining the Nature of Mercury's Core <i>S. J. Peale, R. J. Phillips, S. C. Solomon, D. E. Smith, and M. T. Zuber</i>	73
Ratio of Sodium to Potassium in the Mercurian Exosphere <i>A. E. Potter, C. M. Anderson, R. M. Killen, and T. H. Morgan</i>	75
The Distant Sodium Tail of Mercury <i>A. E. Potter, R. M. Killen, and T. H. Morgan</i>	77

Rheological Inferences on the Mercurian Crust from Crater Morphometric Analyses of the Moon, Mars, and Mercury <i>L. V. Potts, R. R. von Frese, and C. K. Shum</i>	79
Gas Ring Condensation Model for the Origin and Bulk Chemical Composition of Mercury <i>A. J. R. Prentice</i>	81
Low Albedo, Blue, and Opaque Rich Spectral Anomalies in the Mercurian Crust <i>M. S. Robinson and B. R. Hawke</i>	83
Complexity of the Mercurian Crust <i>M. S. Robinson, G. J. Taylor, P. G. Lucey, and B. R. Hawke</i>	85
The Magnetic Field and Magnetosphere of Mercury <i>C. T. Russell</i>	87
Repeat-Orbit Interferometric Precision Measurement of Mercury Obliquity <i>M. A. Slade, R. F. Jurgens, J.-L. Margot, and E. M. Standish</i>	88
Estimating the Libration of Mercury by Remote Sensing of Gravity and Altimetry <i>D. E. Smith, M. T. Zuber, S. J. Peale, R. J. Phillips, and S. C. Solomon</i>	90
Mantle Convection and Thermal Evolution of Mercury Revisited <i>V. S. Solomatov and C. C. Reese</i>	92
The MESSENGER Mission to Mercury <i>S. C. Solomon, R. L. McNutt Jr., R. E. Gold, A. G. Santo, and the MESSENGER Team</i>	94
Mercury's Atmospheric Species <i>A. L. Sprague</i>	96
Mid-Infrared Spectroscopy of Mercury's Surface with BASS <i>A. L. Sprague, R. W. Russell, D. K. Lynch, A. L. Mazuk, and K. L. Donaldson</i>	98
The Geological History of Mercury <i>P. D. Spudis</i>	100
The X-Ray Spectrometer for Mercury Messenger <i>R. D. Starr, G. C. Ho, C. Schlemm, R. E. Gold, J. O. Goldsten, W. V. Boynton, and J. I. Trombka</i>	102

Mercury: An End-Member Planet or a Cosmic Accident? <i>G. J. Taylor and E. R. D. Scott</i>	104
Application of an Updated Impact Cratering Chronology Model to Mercury's Time-Stratigraphic System <i>R. J. Wagner, U. Wolf, B. A. Ivanov, and G. Neukum</i>	106
Disk-resolved Multicolor Photometry and Spectroscopy of Mercury <i>J. Warell</i>	108
A Study of Mercury-like Orbits <i>J. Warell, O. Karlsson, and E. Skoglöv</i>	109
Mechanical Modeling of the Discovery Rupes Thrust Fault: Implications for the Thickness of the Elastic Lithosphere of Mercury <i>T. R. Watters, R. A. Schultz, M. S. Robinson, and A. C. Cook</i>	111
Quality Assessment of Mariner 10 Digital Elevation Models <i>S. L. Wilkison, M. S. Robinson, T. R. Watters, and A. C. Cook</i>	113
High Definition Imaging of Mercury's Surface and Atmosphere <i>J. K. Wilson, M. Mendillo, and J. Baumgardner</i>	115
Photon- and Electron-stimulated Desorption of Alkalis from Model Mineral Surfaces: Relation to Planetary Atmospheres <i>B. V. Yakshinskiy and T. E. Madey</i>	116
The Mercury Plasma Environment: MHD Predictions and Mercury Pickup Ions <i>T. H. Zurbuchen, P. L. Koehn, L. A. Fisk, G. Gloeckler, and K. Kabin</i>	117

MERCURY'S GLOBAL TOPOGRAPHY FROM RADAR RANGING DATA. J. D. Anderson¹, G. Schubert², S. W. Asmar¹, R. F. Jurgens¹, E. L. Lau¹, W. B. Moore², M. A. Slade III¹, and E. M. Standish Jr.¹, ¹Jet Propulsion Laboratory, California Institute of Technology, Pasadena, California 91109 E-mail: john.d.anderson@jpl.nasa.gov, ²Department of Earth and Space Sciences, Institute of Geophysics and Planetary Physics, University of California, Los Angeles, California 90095-1567 E-mail: schubert@ucla.edu.

Introduction: When Mercury's radius is expanded in Legendre functions to the second degree and order, the systematic error in radar ranging data is reduced substantially [1]. Previously, data spanning an observing interval from 1966 to 1990 were used to infer an equatorial ellipticity $(a - b)/a = (540 \pm 54) \times 10^{-6}$ and a center-of-figure minus center-of-mass offset of (640 ± 78) m. The magnitude of this equatorial center of figure offset implies an excess crustal thickness of 12 km or less, comparable to the Moon's excess. By comparing the equatorial ellipticity with the Mariner 10 gravity field [2], and assuming Airy isostatic compensation, bounds on crustal thickness can be derived. Mercury's crustal thickness is in the range from 100 to 300 km.

New Results: The Mercury radar ranging observing interval has been extended from 1966 to the present. In addition, improvements in data reduction techniques have resulted in a set of Mercury ranging data less affected by systematic error, in particular the biases introduced by local topographic variations. We use this new set of reduced ranging data to improve Mercury's global topography and center-of-figure minus center-of-mass offset. New results on crustal thickness are derived, and prospects for further improvement with Mercury Orbiter data are discussed.

References: [1] Anderson, J. D. et al. (1996) *Icarus*, 124, 690-697. [2] Anderson, J. D. et al. (1987) *Icarus*, 71, 337-349.

APPLYING NUMERICAL DYNAMO MODELS TO MERCURY. J. M. Aurnou, *Department of Terrestrial Magnetism, Carnegie Institution of Washington, Washington DC 20015, USA, (jona@dm.ciw.edu)*, F. M. Al-Shamali, *Department of Physics, University of Alberta, Edmonton AB, CANADA T6G 2J1.*

Introduction

Measurements made during the Mariner 10 fly-bys detected that Mercury has an intrinsic magnetic field. It was inferred that the field is dominantly dipolar with an average equatorial field intensity of 0.003 gauss. This corresponds to a dipole moment of $5 \times 10^{12} \text{ T m}^3$ [1], roughly 0.07% that of the Earth. In dynamo theory [2], the magnetic field intensity is often non-dimensionalized by the Elsasser number, $\Lambda = \sigma B^2 / 2\rho\Omega$, where σ is the electrical conductivity, B is the magnetic induction, ρ is the density and Ω is the angular velocity of planetary rotation. The Elsasser number represents the ratio of the Lorentz forces produced by the magnetic field and the Coriolis forces due to planetary rotation. Estimates of Λ for most of the known planetary dynamos in our solar system are of order unity. For Mercury, we estimate that $\Lambda \sim 5 \times 10^{-4}$ using core parameter values [3] of $\sigma \sim 10^6 \text{ mho m}^{-1}$, $B \sim 0.03 \text{ gauss}$, $\rho \sim 7 \times 10^3 \text{ kg/m}^3$ and $\Omega = 2\pi/58.6 \text{ days}$. Clearly, this Λ estimate is far less than unity. This indicates that the Hermean field is weak, not only in absolute magnitude, but also dynamically, in that the Lorentz forces are far smaller than the Coriolis forces generated by planetary rotation.

Two main explanations have been put forward to explain the weak magnetic field of Mercury. The first argues that the magnetic field measured by Mariner 10 is produced by global-scale remanent magnetization of Mercury's crust [4]. In this theory, the presently observed field has been frozen into magnetic minerals contained in the crust. The remanent magnetization was acquired when the crust cooled in the presence of an early dynamo field. This scenario is similar to those proposed to explain the strong magnetic anomalies detected in the southern hemisphere of Mars [5]. If this theory is correct, then Mercury's magnetic field should remain fixed in time, with no detectable secular variation occurring over any timescale of measurement. In addition, strong short-wavelength crustal signals may also be detected, similar to the magnetic anomalies on Mars.

The second possibility is that Mercury's magnetic field is internally-generated by an active fluid dynamo within the planet's large, iron-rich core [3,6,7]. The necessary (but not sufficient) conditions for the possible existence of a planetary dynamo require 1) a sufficiently large region of electrically-conducting fluid present within the planet, 2) an energy source to drive motions of the conducting fluid and 3) a planetary rotation rate that is strong enough to appropriately organize the net fluid motions. Thermal evolution models of Mercury show that the core can remain partially liquid depending on the amount of sulfur present [6, 8]. For non-zero values of the core sulfur content, the melting point of the core material will be strongly depressed such that a spherical shell of liquid core material may exist. Assuming that such a liquid layer exists, and is not exceedingly thin, thermochemical convection

is likely to occur [3]. Experiments in liquid metals show that for even very weakly supercritical thermal convection, the fluid motions tend to be turbulent [9]. Thus, if there is sufficient energy such that convective motions exist in the core fluid layer, then those motions may be able to sustain dynamo action [10]. In addition, the rotation rate of Mercury is sufficiently rapid to organize the turbulent flow in all but the thinnest fluid layers. This claim is based on the findings of the present generation of geodynamo simulations [11] which are all run at numerical rotation rates far slower than that of Mercury. In these simulations, the flow field remains strongly controlled by rotation even for $\Lambda \approx 10$ [12].

Numerical Simulations

In this study, we are carrying out a series of numerical simulations of thermal convection in a rotating, 3D spherical shell of electrically-conducting, Boussinesq fluid. The region interior to the shell, i.e., the solid inner core, is given the same electrical conductivity as that of the shell fluid, while the region exterior to the shell is electrically insulating. The goal of these calculations is to ascertain the likelihood of dynamo processes occurring within Mercury's metallic core. Specifically, we focus on how dynamo generation is affected by varying the fluid layer aspect ratio η , which is the ratio of the inner radius and outer radius of the fluid layer. We assume that core solidification in Mercury has proceeded from the center outwards as on Earth. Therefore, the aspect ratio denotes the ratio of the inner core boundary and core-mantle boundary, $\eta = r_i/r_o$. In the simulations, the spherical boundaries are isothermal and co-rotate at angular velocity Ω . The mechanical boundary conditions are non-slip. Gravity increases linearly with increasing shell radius.

The following equations are solved, subject to the conditions listed above,

$$\begin{aligned} Ek(Du/Dt - \nabla^2 u) + 2\hat{z} \times u + \nabla p &= RaEk/Pr g/g_o T + 1/Pr \nabla \times B \times B \\ \partial B/\partial t &= \nabla \times u \times B + 1/Pr \nabla^2 B \\ DT/Dt &= 1/Pr \nabla^2 T \\ \nabla \cdot (u, B) &= 0 \end{aligned} \quad (2) \quad (3) \quad (4)$$

where u is the velocity vector, \hat{z} is a unit vector parallel to the rotation axis, p is the pressure perturbation, g is the gravity vector and g_o is the value of gravity at r_o , T is the temperature perturbation and B is the magnetic field vector. The non-dimensional parameters are the Ekman number $Ek = \nu/\Omega D^2$, the Rayleigh number $Ra = \alpha g_o \Delta T D^3 / \kappa \nu$, the Prandtl number $Pr = \nu/\kappa$ and the magnetic Prandtl number $Pm = \nu/\eta$. Here α is the thermal expansion coefficient, ν is the kinematic viscosity, κ is the thermal diffusivity, $D = r_o - r_i$ is the shell thickness, and ΔT is the temperature difference across the shell. The Ekman number is the ratio of viscous to Coriolis forces. The Rayleigh number is the ratio of buoy-

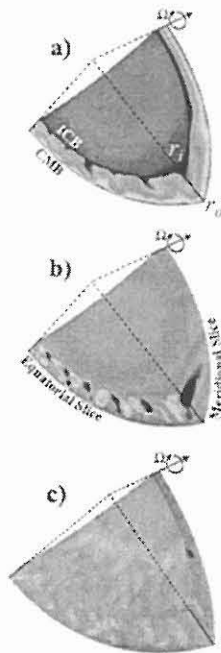


Figure 1: Volumetric cutaway of the illustrative, $\eta = 0.75$ spherical shell test case. The inner core is not depicted in the images. The center of the shell is marked by the intersection of the three dashed lines and the rotation axis is denoted by the Ω vector. The shell is sliced along three orthogonal planes: along 0° and 90° longitude as well as through the equatorial plane. a) Temperature contours. b) Contours of radial velocity. c) Contours of the radial magnetic field. The color scale is such that maximum values are blue and minimum values are red.

ancy versus viscous forces. Convection occurs for Ra -values greater than the critical value $Ra_C = Ra_C(Ek, \eta)$. The two Prandtl numbers define the physical properties of the fluid. Note that the Elsasser number, Λ , is not listed here. Instead Λ is determined from the solution in the dynamo regime.

The numerical technique is described in [13] under method CWG and in [11]. Within the fluid spherical shell region, Chebyshev polynomials are used in the radial direction and spherical harmonics are used in colatitude and longitude. Within

the inner core, the relevant equations are solved on a second similar grid.

Preliminary Results

Figure 1 shows color contours of temperature, radial velocity and radial magnetic field from an qualitative and illustrative test case that is presently being run. In this case, the grid contains 33 radial nodes in the fluid shell and 17 radial nodes in the inner core. There are 96 and 192 nodes in colatitude and longitude, respectively, which allows the solution to be expanded in spherical harmonics up to degree and order 64. Four-fold longitudinal symmetry is imposed on the solution for increased computational efficiency. The parameter values are $Ra = 1.5 \times 10^5$, $Ek = 10^{-3}$, $Pr = 1$, $Pm = 5$ and $\eta = 0.75$. This test case has been produced by restarting the simulation from the results of a case with all the same parameter values except the aspect ratio, which was 0.35, corresponding to the geometry of the Earth's outer core. For $\eta = 0.35$, the magnetic field is well-organized and drifts steadily westward in time. For the $\eta = 0.75$ test case shown, the temperature contours in Figure 1a show that the convection has an azimuthal wavenumber near to 24 and that most of the heat transfer is occurring within $\pm 30^\circ$ of the equatorial plane. The radial velocity contours in Figure 1b show that the flow is columnar. The convection columns surround the inner core boundary and tend to be parallel to the rotation axis. The magnetic field in Figure 1c is made up of small-scale structures that are not well-organized. The field intensity is much smaller than in the corresponding $\eta = 0.35$ case. The $\eta = 0.75$ test case is not yet equilibrated but appears to no longer be in the dynamo regime. These preliminary results suggest that the critical Rayleigh number for dynamo action strongly increases with fluid layer aspect ratio.

References

- [1] N. F. Ness et al. (1975), *J. Geophys. Res.* **80**, 2708.
- [2] D. Gubbins & P. Roberts (1987), in *Geomagnetism*, Vol. 2, (ed. J.A. Jacobs), Academic Press, Orlando.
- [3] D. Gubbins (1977), *Icarus* **30**, 186.
- [4] A. Stephenson (1976), *Earth Planet. Sci. Lett.* **28**, 454.
- [5] M. Acuna et al. (1999), *Science* **284**, 790.
- [6] J. Schubert et al. (1988), in *Mercury*, (eds. F. Vilas, C. R. Chapman & M. S. Matthews), University of Arizona Press, Tucson.
- [7] D. J. Stevenson (1987), *Earth Planet. Sci. Lett.* **82**, 114.
- [8] H. Harder & J. Schubert (2001), *Icarus* **151**, 118.
- [9] J. Aurnou & P. Olson (2001), *J. Fluid Mech.* **430**, 283.
- [10] D. J. Stevenson (1983), *Rep. Prog. Phys.* **46**, 555.
- [11] U. Christensen et al. (1999), *Geophys. J. Intl* **138**, 393.
- [12] P. Olson & G. A. Glatzmaier (1995), *Phys. Earth Planet. Inter.* **92**, 109.
- [13] U. Christensen et al. (2001), *Phys. Earth Planet. Inter.*, in press.

REFLECTANCE SPECTRA of LUNAR PURE ANORTHOSITES and of MERCURY. D. T. Blewett¹, B. R. Hawke², and P. G. Lucey², ¹NovaSol (Innovative Technical Solutions, Inc.), 2800 Woodlawn Dr. #192/120, Honolulu, HI 96822 USA; dave@nova-sol.com, ²Planetary Geosciences/Hawaii Institute of Geophysics & Planetology, University of Hawaii, 2525 Correa Road, Honolulu, HI 96822 USA.

Introduction: Remote sensing measurements at a variety of wavelengths indicate that the surface of Mercury must be low in iron and titanium, with FeO + TiO₂ <~6 wt.% [e.g., 1, 2, 3]. Earth-based reflectance spectrometry has discovered portions of the lunar surface that are extremely low in FeO, <2-3 wt.%, and are believed to be composed of pure anorthosite (>90% plagioclase) [4]. Global imaging from the Clementine mission, along with a method for the determination of FeO abundance from multispectral measurements [5] has led to the identification of large regions of the lunar farside that are low in FeO content. The present work extends a previous study [6] comparing spectra of Mercury to those of lunar anorthosites. The newly-identified mature areas of very low iron content on the Moon may be analogs for much of Mercury.

Lunar Anorthosites: The lunar pure anorthosites discovered with Earth-based telescopes (which are limited to examining the nearside) are optically immature areas such as massifs, small craters, and crater central peaks. Such bright features contribute greater amounts of flux to the spectrometer, and yield information on the properties of the material least affected by space weathering. Pure anorthosites are often found in association with basin rings, and give important clues to lunar stratigraphy and crustal origin [7]. Figure 1 shows two of the highest quality near-infrared (NIR) reflectance spectra of pure anorthosites. They show an increase in reflectance with increasing wavelength (red spectral slope), with no absorption features. Specifically lacking is an absorption near 1 μ m caused by ferrous iron in mafic minerals or glasses. Lack of this absorption band indicates that iron-bearing pyroxenes or olivines must be present at levels below ~5%, and hence the locations for which the spectra were obtained are classified as pure anorthosite. Figure 1 also shows Clementine UVVIS spectra for approximately the same locations as the telescopic NIR spectra.

No Earth-based telescopic spectra of mature pure anorthosites exist. Disc-integrated spectra of Mercury are expected to be dominated by mature material because fresh crater deposits make up only a small proportion of the surface area. In addition, the space environment at Mercury may be such as to promote greater rates and states of optical maturity [8]. Thus a better spectral analog for Mercury could be obtained if mature lunar anorthosites can be identified.

Searching for Mature Lunar Anorthosites. In order to locate areas of mature lunar anorthosite, we conducted a search using FeO and optical maturity (OMAT) maps constructed from 1-km/pixel Clementine mosaics [9]. By simultaneously displaying the FeO and OMAT images, we sought areas with very low values in both images (low OMAT value=high degree of maturity), avoiding slopes that might produce erroneous values. Four candidate regions were located, each containing from ~1600 to 3800 pixels. The average FeO of these areas, all of which are on the farside, ranged from 2.8 to 3.1 wt.%. Figure 2 shows the average UVVIS spectra of the areas, along with the two fresh anorthosites from Figure 1 for comparison. The mature anorthosite regions are darker and have steeper NIR slopes than the fresh anorthosites.

Mercury: Figure 3 presents two of the best Earth-based reflectance spectra of Mercury, a two-beam spectrum from October 1974 and an IRCVF spectrum from April 21, 1976, plotted along with the four mature lunar anorthosite UVVIS spectra. The mercurian and lunar spectra appear to be alike, with about the same spectral slope in the UV-VIS (~0.4-0.75 μ m) and NIR (~0.75-1.0 μ m) regions. This strengthens the case that the lunar mature anorthosites are a good spectral analog for Mercury.

Additional Study: We plan to perform more quantitative comparisons of the UV/VIS ratios and NIR spectral slopes of the mercurian and lunar spectra. Additional work with Clementine full spatial resolution (~100 m/pixel) FeO and OMAT maps may lead us to smaller deposits of material with even lower FeO than the average values in the four regions described above. Hapke [10] suggested that at least 3% FeO is required for optical maturation to occur, so it will be interesting to examine any regions with very low iron contents for information they can provide to aid our understanding of the space weathering process [11].

Acknowledgement: Thanks to F. Vilas and R. Clark for digital versions of the Mercury spectra.

References: [1] F. Vilas (1988) *Mercury*, pp. 59-76, U. Arizona Press, and references therein. [2] A. Sprague et al. (1994) *Icarus* **109**, 156-167. [3] R. Jeanloz et al. (1995) *Science* **268**, 1455-1457. [4] P. Spudis et al. (1984) *Proc. LPSC 15th*, C197-C210; P. Spudis et al. (1989) *Proc. LPSC 19th*, 51-59; C. Pieters (1986) *Rev. Geophys.* **24**, 557-578; B. Hawke et al. (1991) *Geophys. Res. Lett.* **18**, 2141-2144; B. Hawke

PURE ANORTHSITE SPECTRA: D. T. Blewett et al.

et al. (1993) *Geophys. Res. Lett.* **20**, 419-422. [5] P. Lucey et al. (1995) *Science* **268**, 1150-1153. [6] D. Blewett et al. (1997) *Icarus* **129**, 217-231. [7] B. Hawke et al. (1993) *Meteoritics* **28**, 361; C. Peterson et al. (2001) *Lunar Planet. Sci. XXXII*, abstr. #1592. [8] M. Cintala (1992) *J. Geophys. Res.* **97**, 947-973. [9] P. Lucey et al. (2000) *J. Geophys. Res.* **105**, 20,297-20,306. [10] B. Hapke (1977) *Phys. Earth Planet. Inter.* **15**, 264-274. [11] B. Hapke (2001) *J. Geophys. Res.* **106**, 10,039.

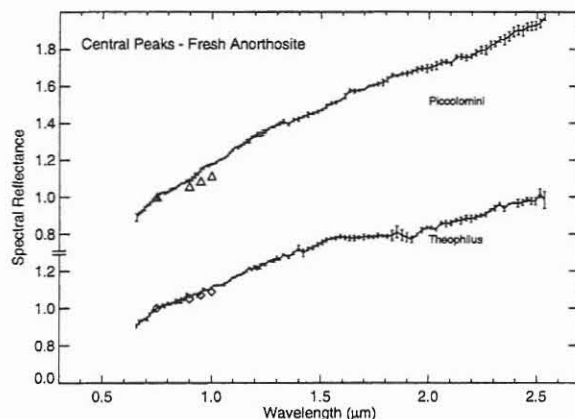


Fig. 1 (above). NIR reflectance spectra of pure anorthositic central peaks, with Clementine UVVIS spectra (triangles, diamonds) of approximately the same area. All spectra have been scaled to 1.0 at 0.75 μm .

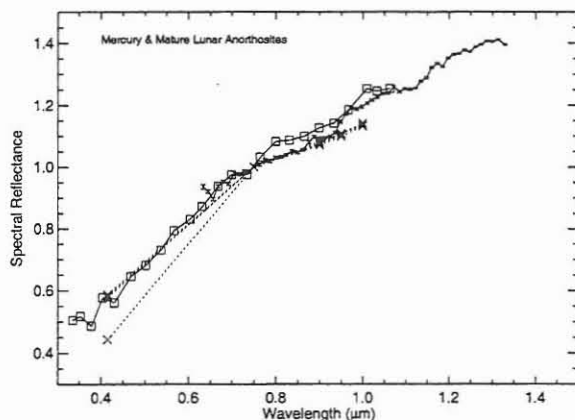


Fig. 3 (above). Spectra scaled to 1.0 at 0.75 μm . Solid line with error bars: Mercury IRCVF, 21 Apr 1976. Squares: Mercury filter photometer Oct 1974. \times : lunar mature anorthosite Clementine UVVIS.

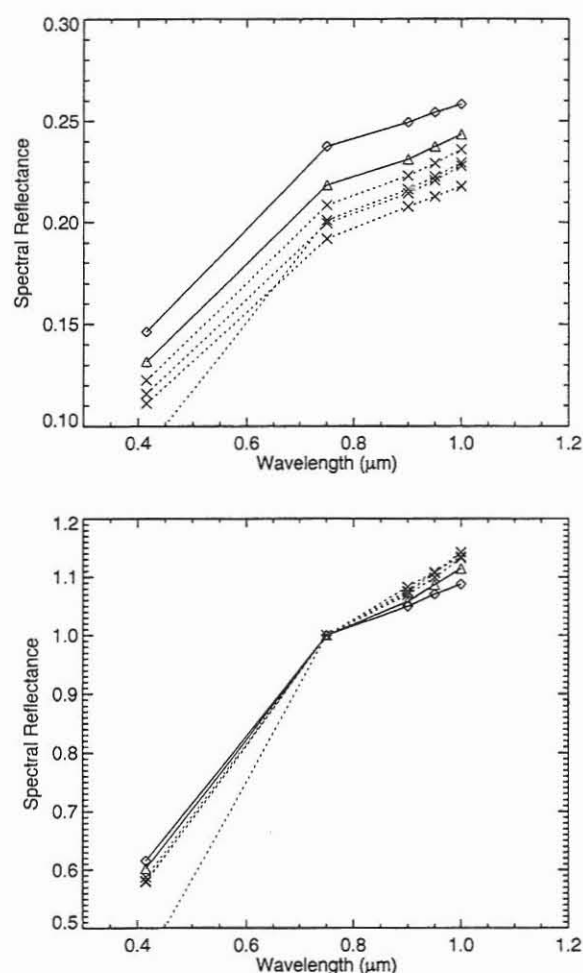


Fig. 2 (above). Clementine UVVIS spectra of pure anorthositic central peaks (triangles and diamonds, see Fig.1) and for four areas of lunar mature anorthosite (\times). Top: absolute reflectance spectra. Bottom: spectra scaled to 1.0 at 0.75 μm to emphasize slope differences.

ENA imaging at Mercury? Lessons from IMAGE/HENA.

P. C:son Brandt, D. G. Mitchell

Applied Physics Laboratory, Johns Hopkins University, Laurel, MD, USA

S. Barabash

Swedish Institute of Space Physics, Kiruna, Sweden

Abstract. Due to the extremely dynamic nature of the Hermean magnetosphere there is a demand for global imaging techniques in a future mission to Mercury. Energetic neutral atom (ENA) imaging is a new technique that allows space plasma to be imaged. A few mission has utilized this technique at Earth and it has proven to be a powerful tool for space plasma diagnostics. There are plans to apply ENA imaging to investigate the Hermean magnetosphere. Questions have been raised what ENA imaging really can measure at Mercury and simulations have been trying to partly answer those questions. In this presentation we will present ENA images from the Terrestrial magnetosphere and explore what lessons can be given when applied to the Hermean magnetosphere.

REFLECTANCE SPECTRA OF AUBRITES, SULFIDES, AND E ASTEROIDS: POSSIBLE IMPLICATIONS FOR MERCURY. T. H. Burbine¹, T. J. McCoy¹, and E. A. Cloutis², ¹Department of Mineral Sciences, National Museum of Natural History, Smithsonian Institution, Washington, DC 20560-0119, USA (burbine.tom@nmnh.si.edu), ²Department of Geography, University of Winnipeg, 515 Portage Avenue, Winnipeg, MB, Canada R3B 2E9.

Introduction: One of the science objectives of the proposed missions to Mercury is to determine its surface composition. Telescopic observations of Mercury from Earth are extremely difficult due to Mercury's proximity to the Sun. Previous spectral measurements (Figure 1) [1,2,3] show a weak feature centered at $\sim 0.9 \mu\text{m}$; however, it is not entirely certain [3] if this feature is due to Fe^{2+} in the silicates or due to the incomplete removal of an atmospheric water feature in the spectra. Many researchers [1,2,3] have noted the spectral similarity in shape and slope of Mercury to the lunar highlands. Analyses of the "best" telescopic spectra have led to estimates [2,4] of FeO contents of Mercury's surface to be between 3-6 wt.%, assuming Mercury has a surface composition similar to lunar anorthosites.

However, it has also been postulated that Mercury's crust contains lower amounts of FeO [5,6]. One possibility is that it has a surface composed predominately of enstatite (a Mg-rich pyroxene) [5]. Enstatite found in meteorites has a featureless spectrum due to the almost complete absence of iron in the silicates. Mercury's location at 0.4 AU may be consistent with its formation out of highly reduced material, possibly similar to the enstatite chondrites, which then experienced significant degrees of melting. These meteorites contain minerals (primarily enstatite) that condense out of the solar nebula at relatively high temperatures. Sulfur, volatilized from sulfides in Mercury's crust, has been proposed [7] as a possible alternative to water ice as the cause of Mercury's bright radar spots at its poles [8].

Our closest analog to Mercury's composition could be the differentiated enstatite-rich meteorites called the aubrites and their proposed asteroidal parent bodies, the E asteroids. Aubrites are composed [9] of essentially iron-free enstatite plus minor accessory phases such as metallic iron and sulfides. Sulfides found in aubrites include troilite (FeS), oldhamite (CaS), ferromagnesian alabandite ($(\text{Mn,Fe})\text{S}$), and daubréelite (FeCr_2S_4).

These questions on Mercury's surface compositions should be answered by the *MESSENGER* and *Bepi-Colombo* missions. Both spacecrafts will obtain visible and near-infrared reflectance spectra and elemental ratios from X-ray and gamma-ray measurements of Mercury. Elemental ratios such as Al/Si, Ca/Si, Fe/Si, and Mg/Si can easily distinguish between a surface

composition similar to the lunar highlands and one similar to the aubrites.

If Mercury has an enstatite-rich surface, what would be its spectral properties? To investigate the spectral properties of an enstatite-rich surface, we have done a spectral survey of aubrites and their constituent minerals. We will focus on sulfur and sulfides, which have distinctive spectral characteristics.

Spectra of Aubrites: The aubrites measured spectrally represent a wide variety of lithologies. Khor Temiki is a whitish-grayish rock containing fine-grained (1-3 mm) enstatite. Peña Blanca Spring is primarily a whitish, fine-grained rock containing a large ($\sim 10 \text{ cm}$) clast with $\sim 1 \text{ cm}$ grayish enstatite. Mayo Belwa is very shock-darkened and contains enstatite clasts in a dark matrix.

Spectra (particle sizes less than $125 \mu\text{m}$) of Khor Temiki, Mayo Belwa, and Peña Blanca Spring are all relatively featureless with slight UV features. Both Khor Temiki and Peña Blanca Spring have slight features at $\sim 1.9 \mu\text{m}$ indicative of terrestrial weathering. Their visual albedos (reflectances at $0.55 \mu\text{m}$) vary from 0.41 to 0.53.

Spectra of Sulfur: Elemental sulfur [10] (Figure 1) is known to have a strong absorption feature in the visible wavelength region. The visual albedo of this sulfur spectrum is 0.78. For sulfur and sulfides, this absorption edge is due to transitions between a low-energy valence band and a high-energy conduction band [11]. This absorption feature would make sulfur deposits on Mercury very spectrally distinctive.

Spectra of Sulfides: Troilite is the most abundant sulfide found in aubrites; however, it composes only $\sim 1 \text{ vol.}\%$ of most aubrites [9]. Samples of a synthetic troilite [12,13] have been found to have a feature centered at $\sim 0.5 \mu\text{m}$; however, meteoritic troilite does not always have a sharp absorption feature.

We have measured the spectra of sulfides found in two aubrites (Norton County and Peña Blanca Spring) and one LL5 chondrite (Paragould). Norton County oldhamite (CaS) (Figure 1) has a deep absorption band centered at $\sim 0.49 \mu\text{m}$ plus a weaker feature centered at $\sim 0.95 \mu\text{m}$. The band depth of this feature is $\sim 40\%$. In the visible, the oldhamite spectrum (normalized to unity at $0.55 \mu\text{m}$) is extremely red and reaches a value of ~ 2 at $\sim 0.9 \mu\text{m}$. Its visual albedo is 0.17. A spectrum of mixed sulfides from Peña Blanca Spring shows

SPECTRA OF AUBRITES: POSSIBLE IMPLICATIONS FOR MERCURY: T. H. Burbine, T. J. McCoy, and E. A. Cloutis

a sharp absorption edge shortwards of $\sim 0.7 \mu\text{m}$ that is centered at $\sim 0.4 \mu\text{m}$. Its visual albedo is 0.11. Troilite extracted from Paragould has an absorption feature shortwards of $\sim 0.8 \mu\text{m}$ that is centered at $\sim 0.4 \mu\text{m}$. Its visual albedo is 0.05.

E asteroids: One possible analog to Mercury's surface may be the E asteroids. E asteroids have relatively featureless reflectance spectra and high visual albedos [$>30\%$]. These spectral characteristics have been interpreted as indicating surfaces dominated by an essentially iron-free silicate. One possible meteoritic analog is the aubrites. The only known near-Earth E-asteroid (3103 Eger) has been postulated [14] as the source body for at least some of the aubrites.

Recently, a feature centered at $\sim 0.5 \mu\text{m}$ with a strength that reaches $\sim 8\%$ has been identified in the CCD (charge-coupled device) spectra (Figure 1) of a number of E asteroids [15,16]. One suggestion for the origin of this feature is a sulfide. The synthetic troilite and oldhamite have absorption features that match the position of the feature in the E asteroid spectra.

Real and theoretical mixtures of enstatite and oldhamite were made in an attempt to duplicate the strength of this absorption feature in an enstatite-rich assemblage. However, a mixture (particle sizes less than $125 \mu\text{m}$) of 95 wt.% enstatite from Peña Blanca Spring and 5% oldhamite only produced a $\sim 0.5 \mu\text{m}$ feature with a strength of ~ 1 percent. Modeling (assuming a checkerboard structure of enstatite and oldhamite) produces a feature with a strength of $\sim 8\%$ using $\sim 40\%$ oldhamite. These oldhamite abundances are much higher than those found in aubrites where oldhamite constitutes much less than 1 vol.% [9]. Further work needs to be done in modeling the effects of very fine-grained sulfides with enstatite, which would produce the $\sim 0.5 \mu\text{m}$ feature with lower abundances than those found in the checkerboard model.

The $\sim 0.5 \mu\text{m}$ feature appears consistent with a sulfide; however, the required abundances needed to produce this feature are much higher than those found in aubrites. Further work needs to be done to understand the required abundances to produce this feature in the regolith of a planetary body.

Conclusions: Sulfur and sulfides have distinctive absorption features in the visible wavelength region, while enstatite is virtually featureless. If Mercury has a highly reduced surface composition, these absorption bands due to sulfur and sulfides may be present in the spectral measurements obtained by MESSENGER and Bepi-Colombo

References: [1] McCord T. B. and Adams J. B. (1972) *Science*, 178, 745-747. [2] McCord T. B. and Clark R. N. (1979) *JGR*, 84, 7664-7668. [3] Vilas F. (1988) in *Mercury*, 59-76. [4] Blewett D. T. et al.

(1997) *Icarus*, 129, 217-231. [5] Lucey P. G. and Bell J. F. (1989) *Lunar Planet. Sci.*, XX, 592-593. [6] Jeanloz R. et al. (1995) *Science*, 268, 1455-1457. [7] Sprague A. L. et al. (1995) *Icarus*, 118, 211-215. [8] Butler B. J. et al. (1993) *JGR*, 15003-15023. [9] Waters T. R. and Prinz M. (1979) *Proc. 10th Lunar Planet. Sci. Conf.*, 1073-1093. [10] Clark R. N. et al. (1993) *U.S. Geological Survey Open File Report*. [11] Fritsch E. and Rossman G. R. (1988) *Gems & Gemology*, 24, 81-102. [12] Cloutis E. A. and Gaffey M. J. (1993) *Earth, Moon, and Planets*, 63, 227-243. [13] Burbine T. H. et al. (1998) *Bull. Am. Astron. Soc.*, 30, 1025-1026. [14] Gaffey M. J. et al. (1992) *Icarus*, 100, 95-109. [15] Bus S. J. (1999) Ph.D. Thesis, MIT. [16] Fornasier S. and Lazzarin M. (2001) *Icarus* 152, 127-133.

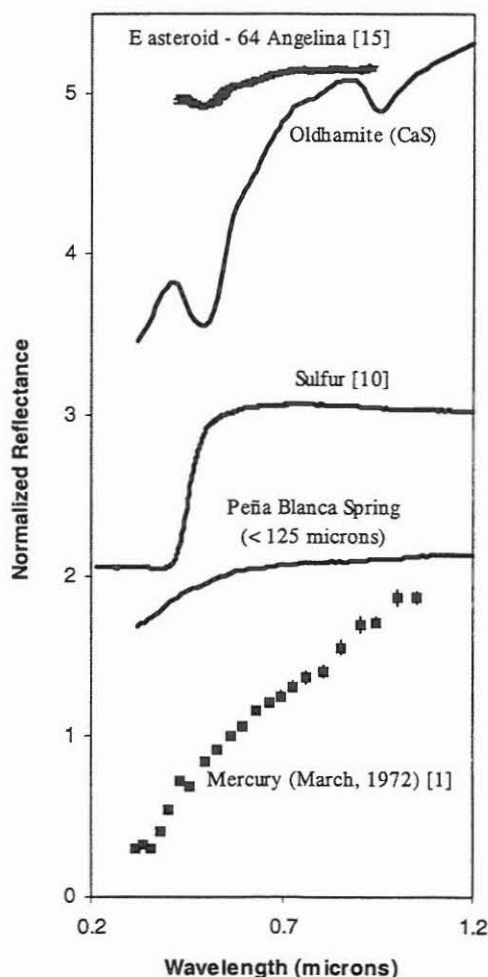


Figure 1. All spectra are normalized to unity at $\sim 0.55 \mu\text{m}$ and offset by 1.0 in reflectance from each other.

THE NATURE OF THE MERCURY POLAR RADAR FEATURES. B.J. Butler, *NRAO* (bbutler@nrao.edu), M.A. Slade, *JPL*, D.O. Muhleman, *Caltech*.

In 1991, two new radar techniques were used for the first time to probe the surface of Mercury, by two different groups [1-4]. The results were quite unexpected, and puzzling. In both experiments, the regions of the surface which had the highest radar albedo (were the best radar reflectors) were very near the north and south poles (see figures 1 and 2). These polar features also had the very unusual characteristic that more signal was received in the same circular polarization sense as had been transmitted, rather than the opposite sense. This is an unexpected occurrence (radar astronomers call it a "polarization inversion"), since single reflections of the radar will result in a polarization reversal, and so more signal is generally received in the opposite sense than that transmitted. This peculiar radar signature is generally only observed in regions on solar system bodies which are known to have some kind of ice present, like the large moons of Jupiter [5], the polar caps of Mars [6], and portions of glaciers and ice and snow fields in Greenland [7] and the Himalayas and Andes [8] on Earth.

From the initial Arecibo observations, it was clear that the feature near the south pole was related to the large (150 km diameter) crater Chao Meng-Fu. The feature near the north pole seemed to be composed of several smaller features, and was somewhat more confusing and harder to interpret with the initial data. Further experiments from Arecibo (after the power upgrade) produced extremely good, high resolution (1.5-3 km) images of the north polar region [9]. Unfortunately, the south polar region has not been accessible to Arecibo since the upgrade, and so the images of that region are not quite so good (resolution only about 15 km), but are still quite spectacular. Where these radar images could be compared to the photographs from Mariner 10, it was immediately apparent (even from the lower resolution images) that the high albedo, polarization inversion regions were all located within the boundaries of craters.

The currently favored explanation for these features is that they are caused by volatile deposits which collect in the permanently shaded portions of polar craters. Note that "volatile" here has a very broad definition (many exotic volatiles may exist at the high temperatures in the mercurian equatorial regions!). How much volatile material would be needed to form the deposits? From the best Arecibo radar imagery, the total areal coverage of the deposits is ~ 30 -50 thousand km^2 (roughly the size of the Netherlands). This is less than 0.07% of the total surface area of Mercury. The depth is somewhat harder to estimate, since it is linked to the detailed physics of the radar wave scattering in the deposits, but the best estimates are that it is between 5 and 10 m. This means that a total volume of volatile material of order a few hundred km^3 is needed to create the deposits (somewhat less than the volume of Lake Erie).

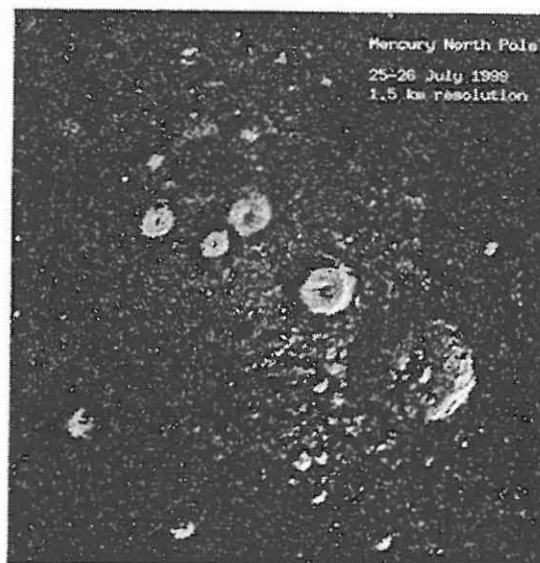


Figure 1. Polar stereographic projection of radar reflectivity near the north pole of Mercury from Arecibo experiments (from Harmon *et al.* 2000). Brighter regions are more reflective, and are generally contained within craters.

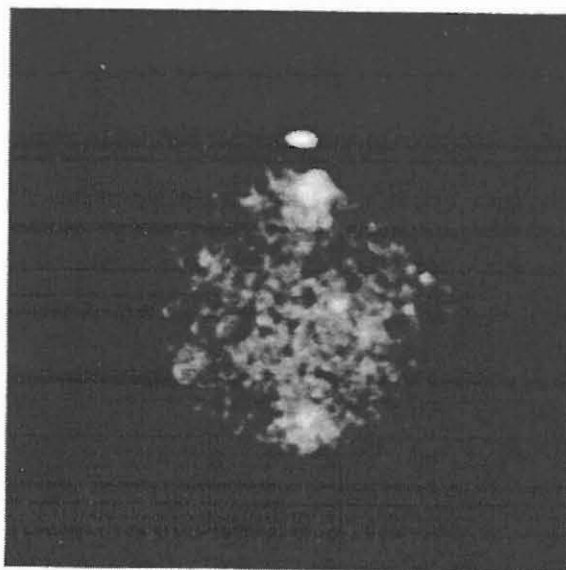


Figure 2. Goldstone/VLA radar image of the full facing hemisphere of Mercury (after Butler *et al.* 1993). Brighter regions are more reflective - the bright north pole reflection is apparent at the top of the image.

MERCURY POLAR DEPOSITS: B.J. Butler *et al.*

There must be 3 conditions which are met in order for volatile deposits to collect in the polar regions of Mercury: 1 - there must be *delivery* of a sufficient quantity of the volatile material to the surface, 2 - that volatile material must be able to *migrate* to regions where it is stable (the polar craters) and a sufficient quantity of the volatile must survive that migration, and 3 - the environment in these locally stable locations must allow the condensed volatiles to remain *stable* for long periods of time (otherwise we must presume that we are looking at Mercury at a special time). It seems clear that the delivery and migration are not particular problems (at least for more common solar system volatiles) [10,11], but what about the stability? The survivability of volatile deposits is determined mostly by their temperature, since the dominant loss mechanism is through thermal evaporation (sublimation).

How cold is it in the craters near the poles of Mercury? The temperature of interest is the maximum temperature throughout the extent of the entire mercurian day (176 Earth days). Accurate thermal models indicate that non-shaded polar regions reach temperatures near 175 K during the warmest part of the mercurian day [3]. However, in the permanently shaded portions of the floors of craters in the polar regions, temperatures can be much colder. The exact maximum temperature is determined by the precise shape of each crater as well as its latitude, but typical maximum temperatures in the permanently shaded parts of the larger polar craters are less than 100 K, and they can be as cold as 60 K [13].

With combined information on supply, migration, and stability of a number of volatiles, as well as information on the observed deposits and estimated temperatures, it is possible to narrow down the possibilities of what the actual volatile material could be. The first consideration is that the observed deposits are only in the floors of craters, not in true polar "caps". This means that volatiles which evaporate very slowly at temperatures above about 200 K are unlikely to be the major constituent of the deposits. For example, it would take a 1 meter deposit of sulfur about a billion years to evaporate at a temperature of 225 K. This means that if the observed deposits were made up primarily of sulfur, then polar "caps" should also be observed, which is not the case. The other "warm" volatiles are similar, i.e., they are just too stable to be the main ingredient of the deposits. On the other hand, volatiles which are not stable enough to last for long periods of time at temperatures above about 100 K are also unlikely to be the major constituent of the deposits. For example, a carbon dioxide ice deposit would have to be colder than about 60 K to last for a billion years. Other ices like ammonia and sulfur dioxide are

similarly unstable. There are some regions in some mercurian craters for which the maximum temperature is this low, but the total areal size of these regions is very small. This means that there could be very small amounts of these more unstable ices in isolated regions, but they do not explain the majority of the observed radar features. Some ices have the right temperature characteristics to make them likely candidates for the majority of the deposits (i.e., they would not form "caps" at temperatures around 200 K, but are stable for long periods at temperatures around 100 K), but their supply is too small. Examples of such ices are HCOOH (formic acid) and CH₃OH (methanol).

Water ice, however, has the right temperature characteristics to make it a likely candidate for the majority of the deposits, and is abundant enough that the required amount of material could be supplied. At a temperature of 150 K, it takes only about a thousand years to evaporate a 1 meter thick deposit of water ice. So, true polar "caps" would not last for very long, explaining their absence in the radar images. Lower the temperature to just 110 K, however, and that same 1 meter thick deposit of water ice will last for almost a billion years. Detailed analysis has shown that about 10% of water molecules migrating around the surface will make it to the polar cold traps. Further analysis has shown that impacts of short period Mercury-crossing comets (either extinct or active) or larger meteorites could supply the required amount of water to the planet.

Though this interpretation is compelling, it is certainly not conclusive. This is because there is currently no single piece of evidence which can be used to determine exactly what it is in the polar craters which causes the observed signal. There are, however, several measurements which could be made which would either determine directly what was the cause of the features, or at least provide valuable information which would help in that determination. Future spacecraft missions hold the most promise for delivering this information. Unfortunately, the two currently planned missions to Mercury (MESSENGER and BepiColombo) are not equipped with instruments which will answer this question unambiguously.

References

- [1] Harmon & Slade, *Science*, 258, p.640, 1992; [2] Slade *et al.*, *Science*, 258, p.635, 1992; [3] Butler *et al.*, *JGR*, 98, p.15003, 1993; [4] Harmon *et al.*, *Nature*, 369, p.213, 1994; [5] Ostro *et al.*, *JGR*, 97, p.18227, 1992; [6] Muhleman *et al.*, *Science*, 253, p.1508, 1991; [7] Rignot *et al.*, *Science*, 261, p.1710, 1993; [8] Haldemann & Muhleman, *JGR*, 104, p.24075, 1999; [9] Harmon *et al.*, *Icarus*, 149, p.1, 2001; [10] Moses *et al.*, *Icarus*, 137, p.197, 1999; [11] Butler, *JGR*, 102, p.19283, 1997; [12] Vasavada *et al.*, *Icarus*, 141, p.179, 1999.

The MESSENGER Science Planning Tool. Teck H. Choo¹, Scott L. Murchie¹ and Julia S. Jen¹, ¹The Johns Hopkins University/Applied Physics Laboratory, 11100 Johns Hopkins Road, Laurel, MD 20723-6099.

The MErcury Surface, Space ENvironment, GEochemistry, and Ranging (MESSENGER) mission [1] will substantially improve the knowledge of the planet Mercury. Its seven science payload elements [2] include scannable, dual wide- and narrow-angle cameras (WAC and NAC) for color and stereo imaging; a gamma-ray and neutron spectrometer; an X-ray spectrometer; a magnetometer; a laser altimeter; a combined UV and visible-NIR spectrometer; an energetic particle and plasma spectrometer; and a radio science investigation.

Key constraints on the acquisition of science data are: limitations on off-sun pointing of the spacecraft, required to keep it shielded from solar illumination by a sunshade; the volumes of data that can be stored on either of the 8-Gb solid-state recorders and that can be downlinked daily; and the viewing and illumination conditions resulting from MESSENGER's elliptical orbit. The goal of planning science data acquisition is to maximize the MESSENGER instruments' coverage of the planet under favorable illumination conditions and at high spatial resolution, while keeping within spacecraft pointing limits and not exceeding available data storage and downlink resources. The MESSENGER Science Planning Tool (SPT) has been developed to find the optimal solution to this problem in an automated fashion, to minimize the cost and time required for observation planning and to respond efficiently to changes in the spacecraft's predicted trajectory on-orbit.

The Science Planning Tool consists of two major components, the Science Opportunities Visualizer (SOV) and Science Sequence Optimizer (SSO). The Visualizer provides graphical representations of flight geometry and viewing conditions. The Optimizer uses as its starting point the prioritized science objectives (expressed as rules for instrument pointing and operation at different ranges to the surface and illumination conditions) and the spacecraft constraints (expressed as rules governing pointing, stored data volume, and requirements for downlink). Based on these rules and an input trajectory, the optimizer generates a hypermap of all possible observation times and conditions, and selects those with optimal values of user-definable data attributes (e.g., spatial resolution, illumination geometry, etc.). An example is the goal of acquiring a global low emission-angle image mosaic at an average spatial resolution of 250 m/pixel or better. The ideal case would be to use NAC to obtain the highest possible resolution. However this is not practical because the resolutions attained would be as high as 20 m/pixel over much of the planet, and there is insufficient storage and bandwidth available for the resulting data volume. Instead, the Optimizer chooses either WAC or

NAC for any particular opportunity, to maximize resolution while obeying resource constraints. The optimizer's outputs include both a time-series of instrument operations and pointing, and a description of the acquired data. For the example of the global map, the preliminary timeline of images over the first Mercurian solar day (352 orbits) is shown in Figure 1. For these observations (shown in map format in Figure 2), average spatial resolution exceeds the 250 m/pixel target yet the time-series of images fits within downlink and data storage resources.

The SOV (Figure 3) has a graphical user interface and can be used to find out the position and orientation of MESSENGER at any given time during the orbit phase and flybys. The SOV has two panels that provide 3-D perspective of the spacecraft position and orientation with respect to the Sun, Mercury, and Earth. In addition, it can be used to obtain MESSENGER's ground track and instrument fields-of-view and footprints and the time profile of operational modes and pointing. All plots can be saved as Postscript output, and various information on MESSENGER's trajectory and pointing can be saved as ASCII tables. Currently, the MESSENGER SOV is used primarily to facilitate visualization of observation opportunities. However, it can be used by anyone to quickly learn about MESSENGER's trajectory, observing modes, and pointing profile. In addition, it can also be used in the future to aid the analysis of returned data.

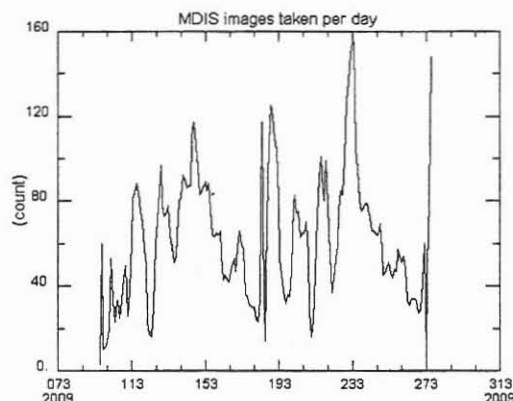


Figure 1. Preliminary timeline of imaging required to obtain a global mosaic at an average resolution 250 m/pixel or better during the first Mercurian solar day of the orbital mission (the first 352 orbits).

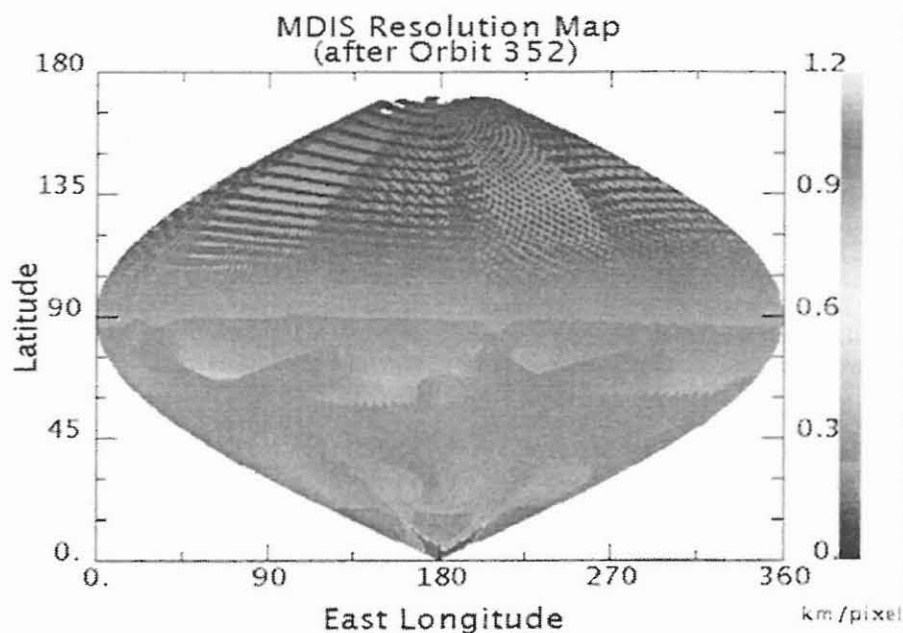


Figure 2. Geographic coverage and spatial resolution of the imaging shown in Figure 1. The gap at the north pole is filled with separately targeted observations.

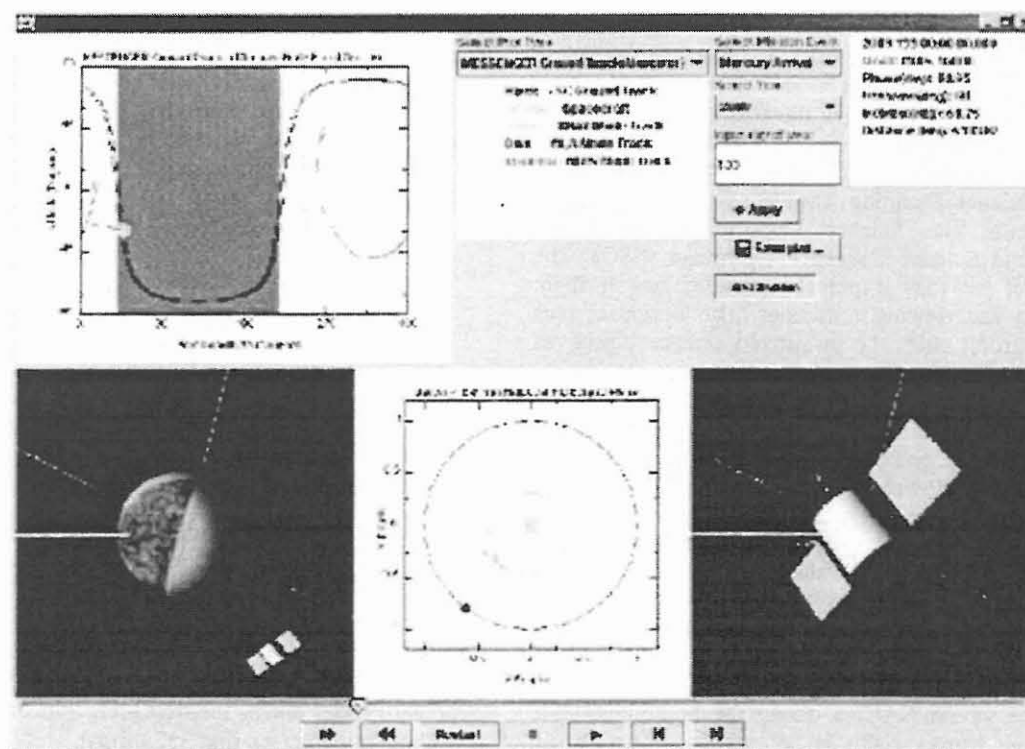


Figure 3. MESSENGER Science Opportunities Visualizer.

References: [1] Solomon, S. C. et al. (2001) The MESSENGER mission to Mercury: Scientific objectives and implementation, *Planet. Space Sci.* Special Issue. [2] Gold, R. E. et al (2001) The MESSENGER mission to Mercury: Science payload, *Planet. Space Sci.* Special Issue.

A MULTI-COLOUR IMAGING SYSTEM FOR THE BEPI COLOMBO MERCURY LANDER.

L. Colangeli¹, P. Palumbo², C. Barbieri³, G. Bellucci⁴, A. Bini⁵, A. Blanco⁶, G. Cremonese³, V. Della Corte¹, S. Fonti⁶, E. Mazzotta Epifani¹, G. Preti⁵, H. Yano⁷, S. Vergara¹, ¹Osservatorio Astronomico di Capodimonte, Via Moiarriello 16, 80131 Napoli – Italy, e-mail: colangeli@na.astro.it, ²Università "Parthenope", Napoli – Italy, ³Osservatorio Astronomico di Padova, Padova - Italy, ⁴IFSI - CNR, Rome, Italy, ⁵Alenia Difesa - Officine Galileo, Campi Bisenzio - Italy, ⁶University of Lecce, Lecce - Italy, ⁷Planetary Science Division, ISAS, Kanagawa, - JAPAN

The ESA "Bepi Colombo" space mission to Mercury includes a lander system for the study of planet surface characteristics. Surface-based geology and mineralogy measurements are needed to expand and complement remote sensing observations. In the complement of the lander payload, cameras are required to provide (multi-colour) images of the landing site during and after descent.

The study of Mercury surface morphology and composition is particularly relevant in the context of the Solar System exploration due to the heavy evolution/processing of this planet. However, available information is rather poor and in situ multi-spectral imaging investigation of the local environment will provide essential clues to the understanding of Mercury present state and past evolution.

In this work we present a preliminary study of a multi-spectral imaging system, potentially candidate for the lander camera. Technical details must be defined considering the stringent requirements imposed by the mission profile, harsh environment and foreseen limited resources. Therefore, selected technologies are aimed at a miniaturised system.

DIGITAL ELEVATION MODEL MOSAIC OF MERCURY. A. C. Cook¹, T. R. Watters¹ and M. S. Robinson²,
¹Center for Earth and Planetary Studies (CEPS), National Air and Space Museum, Washington D.C. 20560-0315
 (Email: tcook@nasm.si.edu), ²Northwestern University, 1847 Sheridan Road, Locy Hall 309, Evanston, IL 60208
 (Email: robinson@eros.earth.northwestern.edu).

Introduction: At CEPS work has been underway since 2000 to semi-automatically stereo match all Mariner 10 [1,2] stereo pairs [3,4]. The resulting matched image coordinates are converted into longitude, latitude, and height points and then combined to form a map projected Digital Elevation Model (DEM) mosaic of the planet's surface. Stereo images from Mariner 10 cover one quarter [5] of the planet's surface, mostly in the southern hemisphere.

Method: The refined camera positions and orientations [6] of images from an improved image mosaic of Mercury were used initially to determine a revised list of stereo pairs according to a set of stereo criteria [5].

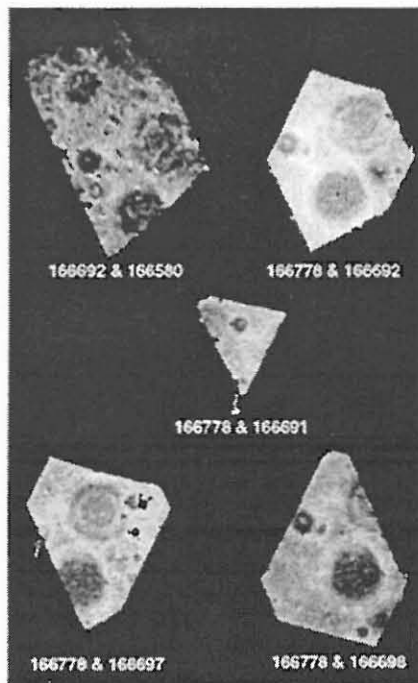


Figure 1 Gray-scale DEMs from five overlapping stereo pairs, varying in quality.

To stereo match an image pair, 3-20 seed points have to be located manually between left and right images. This sets up an affine transform between the image pair for stereo matching. The matcher software, "Gotcha" [7] uses a patch-based correlation algorithm to find corresponding points between left and right images to sub-pixel accuracy. We match image pairs 12 times using correlation patch radii of between 1 and 12 pixels. Small patch sizes yield DEMs with high spatial resolution, but suffer increased topographic noise, especially in low textured areas (poor correlation).

Large patch sizes suffer less from noise, but tend to blur spatial resolution. We are experimenting with different methods to combine different patch size results together to achieve best spatial resolution, and least topographic noise.

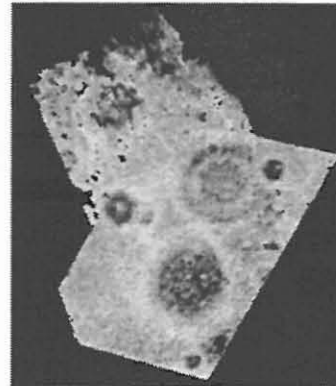


Figure 2 Mosaic of Fig 1 DEMs (94-81W, 21-5S, black= -3.2km, white=+3.2km. The lower large crater is Sullivan (diameter 135 km) and above it lies a double ring crater.

To convert stereo matcher pixel coordinates into longitude, latitude, and height (a Digital Terrain Model or DTM), the coordinates are passed through a stereo intersection camera model using previously determined camera positions and orientations, based upon a photogrammetric adjustment [6] of Mariner 10 images. The DTMs generated (Fig 1) must then be combined together to generate a map projected DEM mosaic (Fig 2). The DTMs have different height accuracies, and can contain localized topographic errors from badly detected image reseaux or stereo matcher errors due to image noise. Furthermore, errors in camera positions and orientations may introduce slight vertical offsets and horizontal first order tilts. An iterative process is being used currently whereby a weighted average DEM (Fig 2) is generated from all DTMs, then each DTM tile is fitted to this to compensate for offset and first order tilt, then the process repeats a specified number of times. The weighting scheme we use depends upon the average topographic noise present in the tile, and the photogrammetric error (skew) for each matched point.

Results: Out of 2326 predicted stereo pairs [5], ~1800 have proved suitable for stereo matching. A total of 493 images form these stereo pairs. Unsuitable stereo pairs include those with image data gaps and where the overlap is too small. As of 6/28/2001, 200 stereo pairs remain to be matched. An preliminary large area DEM mosaic was generated in February 2000 and is shown in Fig 3.

DEM MOSAIC OF MERCURY: A. C. Cook, T. R. Watters and M. S. Robinson

Discussion: A unique set of DTM tiles has been produced, each revealing the relative topography of different sections of one quarter of Mercury's surface. No other large area topographic dataset of Mercury is likely other than increased Earth-based radar altimetry around the equator [8], future radar interferometry [9], or until spacecraft revisit Mercury at the end of this decade [10,11]. Experiments are underway to refine our existing DEM mosaicking technique (Fig 3) so as to preserve both good quality height accuracy and spatial resolution DEMs, whilst using lower quality DEMs to fill in gaps. This dataset when completely mosaicked and analyzed will be released to the planetary science community. Additional information can be found on: <http://www.nasm.edu/ceps/research/cook/topomerc.html>

References: [1] Murray B. and Burgess E. (1977) *Flight to Mercury*, 162pp. [2] Dunne J. A. and Burgess E. (1978)

The Voyage of Mariner 10, NASA SP-424, 221 pp. [3] Davies M. E. et al. (1978) *Atlas of Mercury*, NASA SP-423, 127pp. [4] JPL (1976) *MVM '73 stereo data package user guide*. [5] Cook A. C. and Robinson M. S. (2000) *JGR*, 105, 9429-9443. [6] Robinson, M.S. et al. (1999) *JGR*, 104, 30,847-30,852. [7] Day T. et al. (1992) *Int. Arch. Photogramm. Rem. Sens.*, 29(B4), 801-808. [8] Harmon et al. (1986) *JGR*, 91, 385-401. [9] Slade et al. (2000) *Spring AGU*. [10] Solomon S. C. (2001) *Planet. Space. Sci.* (in press). [11] ESA (1999) *Colombo - the ESA Cornerstone*, SCI(92)2.

Acknowledgment: to University College London / Laser-scan for the loan of the Gotcha stereo matcher by Tim Day, and to Geoff Franz for recent help in stereo matching the remaining Mariner 10 images. This research was funded by NASA PG&G grants NAG5-9076 and NAG5-10291

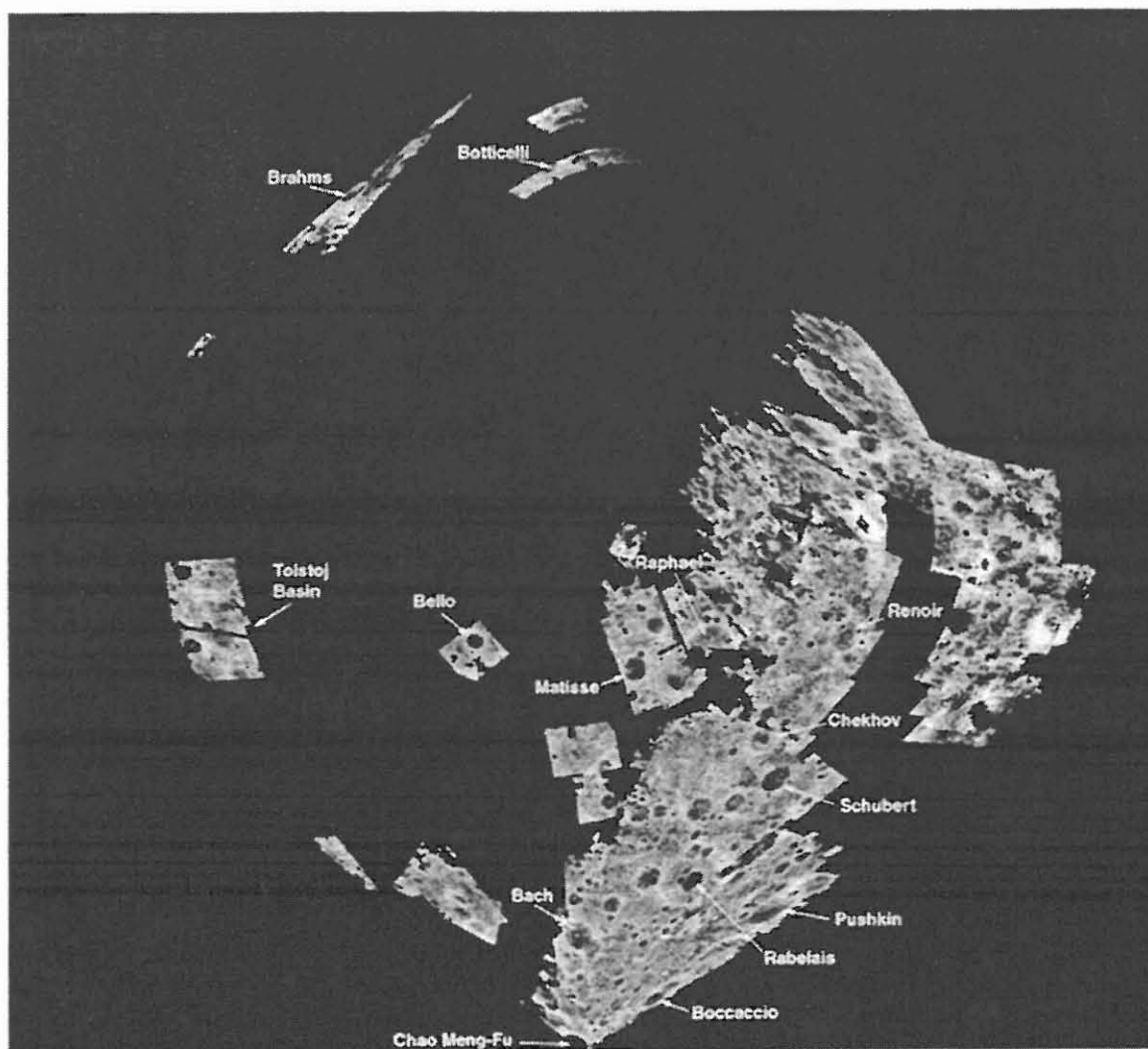


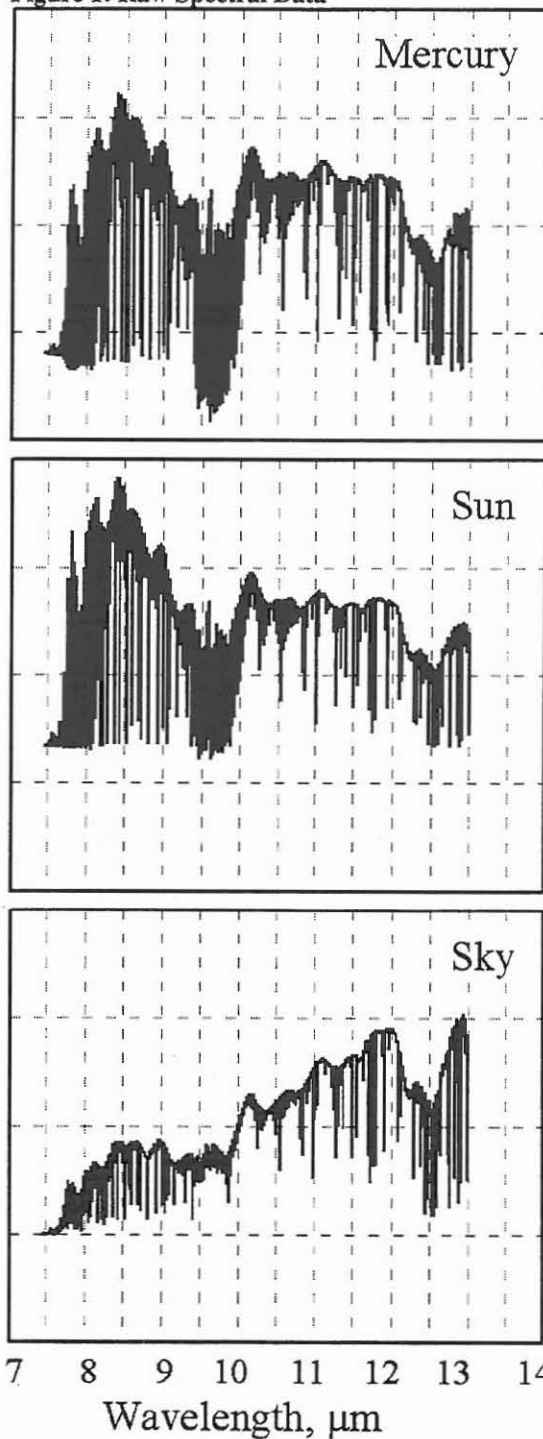
Figure 3 DEM mosaic generated in Feb 2001 from ~700 stereo pairs (sinusoidal equal-area projection, 200W-0W, 90N-90S, black= -3.2km, white =+3.2km). The region on the extreme right suffers from poor quality stereo. When complete most of the left quadrant and equatorial region will be filled in.

MID-INFRARED SPECTRA OF MERCURY. B. Cooper¹, A. E. Potter², R.M. Killen³, and T.H. Morgan⁴,
¹Oceanering Space Systems, 16665 Space Center Blvd, Houston, TX 77058-2268, ²National Solar Observatory,
 P.O. Box 26732, 950 N. Cherry Avenue, Tucson, AZ 85726-6732, apotter@noao.edu, ³Southwest Research Institute,
 P.O. Drawer 28510, 6220 Culebra Road, San Antonio, TX 78228-0510, ⁴NASA HQ, 300 E Street SW, Wash-
 ington, DC 20546-0001.

Introduction: Mid-infrared (8-13 μm) spectra of radiation emitted from the surface of solar system objects can be interpreted in terms of surface composition [1]. However, the spectral features are weak, and require exceptionally high signal-to-noise ratio spectra to detect them. Ground-based observations of spectra in this region are plagued by strong atmospheric absorptions from water and ozone. High-altitude balloon measurements that avoid atmospheric absorptions can be affected by contamination of the optics by dust. We have developed a technique to obtain mid-infrared spectra of Mercury that minimizes these problems [2]. The resulting spectra show evidence of transparency features that can be used to qualitatively characterize the surface composition.

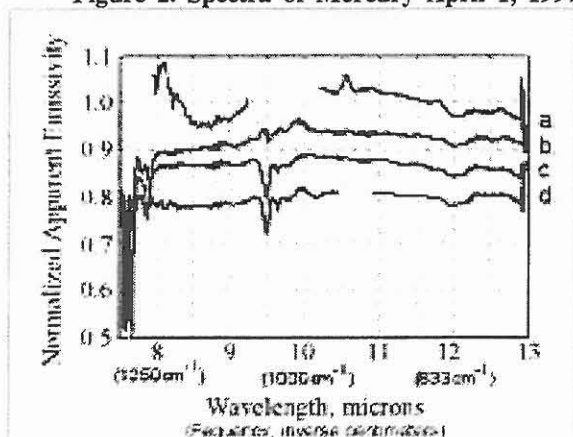
Observations and Data Analysis: We obtained 8-13 μm spectra of the whole planet Mercury during daylight with the Fourier Transform spectrometer (FTS) on the main mirror of the McMath-Pierce Solar Telescope at the National Solar Observatory on Kitt Peak during six observing runs performed from 1987 to 1998. The spectral resolution was 0.05 cm^{-1} and spectral dispersion was 0.03 cm^{-1} for most of the measurements. Our objective in working at as high a resolution as possible was to be able to see between the atmospheric absorption lines. We made the measurements in sets of three—Sun, Mercury and sky. We subtracted the sky spectrum from the Sun and Mercury spectra, and then divided the sky-subtracted Mercury spectrum by the sky-subtracted Sun spectrum to obtain a ratio spectrum that, in principle, had divided out all the atmospheric absorptions and the instrument response. In practice, we found that water absorptions shortward of $8\text{ }\mu\text{m}$ and ozone absorptions in the range 9.6 to $10.2\text{ }\mu\text{m}$ could not be satisfactorily corrected, and our data in those regions were not useful. The Mercury-Sun ratio spectra were corrected for the spectral dependence of the solar brightness temperature and for the spectral dependence of the Mercury surface temperature. The latter was calculated using a theoretical thermal model that treated the surface of Mercury as a sphere illuminated by sunlight. Examples of the raw Mercury, Sun and sky spectra are shown in Figure 1. These spectra show both atmospheric absorption features and the instrumental response function.

Figure 1: Raw Spectral Data



Results: Figure 2 shows a fairly typical set of processed spectra from one day's observation. These are spectra of Mercury from April 1, 1997, offset vertically in increments of 0.1. Curves (a), (b), (c), and (d) represent consecutive observations on this date, processed with a Mercury continuum removal based on our own smooth-surface model. The regions below about 7.5 μm and between 9.6 and 10.2 μm are too noisy to be of use, because of atmospheric absorptions by water and ozone.

Figure 2. Spectra of Mercury April 1, 1997



We looked for three kinds of spectral features in the spectra: Christiansen peaks, reststrahlen bands, and transparency features.

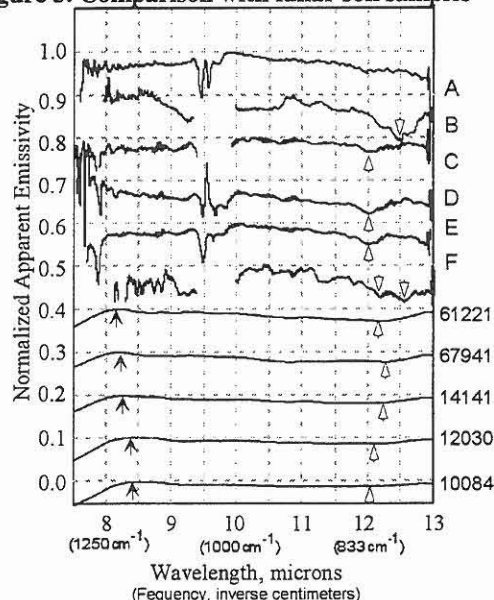
Christiansen features. Our spectra in the Christiansen feature region (below 8 microns) do not provide any useful information because of water vapor absorptions..

Reststrahlen bands. Reststrahlen features are expressed as peaks in reflectance spectra, and we would only expect to see troughs corresponding to them in our emission spectra if the signal were produced by crystalline rock rather than fine powder, in which case they would most likely in the 8-9.5 μm region for silicates. But there were no reproducible features found in this region in any of the spectra.

Transparency features. Transparency features appear in the spectra of powdered samples as shallow troughs in the region between reststrahlen bands, where the material is transparent enough to see radiation from deeper, cooler layers below the sunlit surface. Figure 2 displays a reproducible shallow trough at around 12 μm . It appears to be a transparency feature. This feature represents a 1.3% to 1.8% reduction in emissivity in all the curves. We found similar reproducible features in most of the spectra, at wavelengths ranging from 12 μm to 12.5 μm .

Comparison with lunar samples. Figure 3 shows a summary comparison of spectra from all the Mercury observations with laboratory emission spectra of lunar soils measured by Salisbury, *et al.* [3]. Solid arrows mark the Christiansen features in the lunar soils. There are no corresponding features clearly seen in the Mercury spectra. The transparency features in the lunar soils are marked by open arrows, as are also the putative transparency features in the Mercury spectra.

Figure 3. Comparison with lunar soil samples



The legends A through F refer to different dates of observation, and the numbers refer to the lunar soil samples.

Summary and Conclusions: We see strong indications of transparency features in the Mercury spectra. A shallow trough occurs at 12 microns in spectra centered at 80°, 256°, and 266° longitudes. A minimum occurs at 12.5 microns in the spectra centered at 15°, and a doublet minimum with a trough at 12.2 microns and a second at 12.4 to 12.6 microns at longitude 229°. These features indicate the presence of a fine powder on the Mercurian surface, and their low spectral contrast suggests a significant percentage of glass or agglutinitic material. Based on the positions of the transparency features, we conclude that our spectra are indicative of intermediate, mafic and ultramafic rock types. Further specificity is not warranted by the data.

References: [1] Salisbury, J. W., Hapke, B., and Eastes, J. W., (1987) *J. Geophys. Res.* 92, 702-710. [2] Cooper, B., Potter, A. E., Killen, R. M., and Morgan, T. H. (2001) *J. Geophys. Res.* to be published. [3] Salisbury, J.W., Basu, A. and Fischer, E. M., (1997), *Icarus*, 130, 125-139.

A WIDE ANGLE CAMERA FOR BEPI COLOMBO. G.Cremonese, V.Achilli, C.Barbieri, A.Caporali, M.T.Capria, L.Colangeli, G.Forlani, S.Fornasier, M.Lazzarin, F.Marzari, L.Marinangeli, G.Naletto, P.Palumbo, R.Ragazzoni, G.Salemi, S.Verani

In the frame of the ESA Cornerstone Mission BepiColombo to planet Mercury, we are working on the concept for a Wide Angle Camera aiming to fulfill the main scientific goals set forth in the ESA document (ESA-SCI[2000]1) about surface morphology, mineralogy and exosphere.

A primary requirement is the complete coverage of the surface with a resolution of about 50 m in all three coordinates.

Relying on previous experience in advanced imaging systems, both in our Institutes and in consulting industries, novel technological solutions are investigated for optics, detectors and data acquisition and analysis.

A conceptual design of the WAC will be presented.

X-RAY SCIENCE ON ESA'S BEPICOLOMBO MISSION TO MERCURY

S. K. Dunkin^{1,2}, M. Grande¹, and B.J. Kellert¹

¹Space Science and Technology Department, Rutherford Appleton Laboratory, Chilton Didcot, OX11 0QX, UK

²Department of Geological Sciences, University College London, London WC1E 6BT, UK (s.k.dunkin@rl.ac.uk)

Introduction: Mercury has been visited only once by a spacecraft, with Mariner 10 completing 3 flybys in 1974/5. Its closeness to the Sun makes ground-based observations very difficult, and hence our knowledge of Mercury is extremely limited. This paper outlines the science drivers of an X-ray instrument (i.e. CIXS, [1]) to fly on a spacecraft such as ESA's Bepi-Colombo mission.

The Surface of Mercury: Only 45% of the surface of Mercury was imaged by Mariner 10, at only 2 wavelengths, and only ~1% with a resolution of better than 0.5km. Our knowledge of the surface of Mercury is therefore very limited, but what we do know tells us that any resemblance to the Moon is superficial. Mercury has a systematically higher albedo at visible wavelengths than comparable terrains on the Moon, but at UV wavelengths has a very much lower albedo, indicating that the surface composition is very different.

Mercury can be split into a number of terrains. The *cratered areas* are analogous to the lunar highlands and represent the oldest terrain on Mercury. Impact craters are a probe into the crust, and hence studying their features and ejecta may provide insight into different compositional layers beneath the surface. The highest albedo areas on Mercury are all associated with crater rays (fresh material ejected from impact craters) supporting the idea of different compositions and/or maturities being related to impact ejecta.

There is controversy over the origin of the plains units on Mercury, which could either be of impact origin or of a volcanic nature. The *intercrater plains* are older than smooth plains, since they have a greater crater density, and cover the largest area of all the terrains imaged. They show evidence of all the phases of Mercury's geological history except the very earliest, and hence are believed to be around 4 billion years of age [2]. They therefore represent one of the oldest materials still visible on the surface, and it is of great importance to determine their true nature. An X-ray spectrometer will be able to distinguish between a volcanic and impact origin as it is expected that abundances of Al and Mg in particular would differ between the two (Al would be richer in the impact ejecta, Mg richer in the volcanic rocks). Their wide extent over the whole of the imaged side of Mercury means that only a global survey of the planet can obtain a complete picture of the nature of these deposits. The *smooth plains* are much younger and appear to be related to impact basins in the most part. Smooth plains are analogous to

the lunar maria (dark lava plains) although with very important differences. They have a much higher visible albedo than the lunar maria and no areas of low albedo blue-colour material representative of the high-titanium mare basalts found on the Moon. However, the smooth plains appear to fill in craters, suggesting a flowing nature (i.e. volcanic deposition). This, along with their comparative youth relative to the basins they occupy, and some irregular depressions which suggest volcanic origin, all imply that volcanism has played an important part in Mercury's past. There are suggestions that a highly differentiated magma may have produced more alkaline basalts (i.e. those rich in Na and K, [3]) an X-ray spectrometer such as CIXS is ideal to detect such elements.

Spectra of Mercury have average spectral characteristics midway between Na-rich plagioclase ($\text{NaAlSi}_3\text{O}_8$), and Ca-rich plagioclase ($\text{CaAl}_2\text{Si}_2\text{O}_8$) implying that Mercury may be more Na-rich than the lunar surface (which is mainly of the Ca-rich variety). An X-ray spectrometer with sufficiently high spectral resolution will be able to resolve the Na line from the neighbouring Mg line. In addition, by observing the X-ray albedo of the regolith at different phase angles, we will be able to probe the fine structure of the soil. This new technique [4] is being prototyped on DCIXS, an X-ray spectrometer due to fly on the SMART-1 mission to the Moon [5].

The Origin and Evolution of Mercury:

There are a number of theories relating to the origin and evolution of Mercury, relating specifically to its high uncompressed density compared to the other terrestrial planets. Each theory predicts different compositions of the present day planet.

1. Selective accretion: This theory predicts that Fe is enriched due to dynamical and mechanical accretion processes in the innermost part of the Solar System. In this model, the silicate portion of Mercury should contain around 3.6-4.5% alumina, 1% alkali oxides (Na_2O and K_2O) and between 0.5 and 6% FeO [6]. MgO is expected to vary between 32 and 38wt% [7].
2. Post accretion vaporisation: proposes that the solar wind in the early phases of the Sun's evolution vaporised most of the silicate portion of Mercury. In this scenario, there should be almost no alkali oxides present at all, with very little FeO and a high enrichment of refractory elements (CaO and Al_2O_3) to the level of over 30wt%. MgO would

also be enriched, with an abundance of 30-40wt% [8].

3. Giant impact: a large, planet sized body impacted into Mercury, stripping it of most of its outer silicate crust and mantle. In this case the FeO content will be much the same as for the selective accretion scenario, but with a depletion in both alkali and refractory elements (0.01-0.1% and 0.1-1% respectively) (see [3]).

An important point to note is that these abundances are bulk crust/mantle abundances and therefore only a global elemental dataset can fully address the question of which theory most accurately represents the present day composition of Mercury. Clearly, many of the important differences are to be seen in elements such as Al, Na, Ca, Fe, and also Mg and K, all of which can be observed with an X-ray spectrometer that covers the energy range 0.5-10keV and which has sufficiently high resolution to resolved such lines (~150ev).

Magnetospheric science: Mariner 10 revealed the presence of a highly active magnetosphere around Mercury. The field observed is compatible with a strong dipole, although higher order terms and anomalies may be more important than for the Earth. Explaining the presence of this field is a highly complex question, which could hinge on establishing the concentrations of trace elements such as sulphur. While the overall picture of the magnetosphere may resemble that of the Earth, the end result of space weather effects on Mercury must be very different. Recently [10] has presented a model in which the magnetosphere is almost entirely driven, with reconnection on a global scale occurring during periods when the interplanetary magnetic field is southward. [11] show images of Na emission in the exosphere, which are highly variable, and may be the footprints of such activity.

Mariner 10 found clear signatures of behaviour very reminiscent of terrestrial substorms. Bursts of electrons were observed with energies of several hundred keV [12]. The precipitating auroral electrons could result [13] in a total energy deposit, during an inferred duration of order ten seconds, of between 10^{11} J and 10^{14} J. Such precipitation would be a copious source of X-rays [14,15]. At the Earth, the PIXIE X-ray imager recently launched on POLAR has produced [eg 16] the first global X-ray images of the aurora. In general, the bremsstrahlung spectrum has roughly the same spectrum as the incident electrons. An estimate for Mercury is an overall efficiency of 10^{-4} [14], implying a peak average emission which is comparable to the coherent scatter of reflected solar X-rays. These two components will make up the main continuum in

spectra observed at Mercury, on which will be superimposed the fluorescent lines which we observe. Localised peak emission could be significantly brighter, since our calculation for Mercury is based on average fluxes. Moreover, since all these estimates are based on a simple scaling of the terrestrial magnetosphere, the real situation may be very different.

The interaction of electrons with the surface will also produce some line emission. The majority of the energy of a 100 keV electron striking the surface goes into ionisation, and of order 2% ends up as fluorescence. In the case of the Moon there have also been observations of X-rays produced by the high energy tail of the solar wind electron striking the surface [17], and energy stored in high charge states of minor ions will also be released. It is anticipated that in the case of the magnetopause being driven down to the surface of Mercury [9], these mechanisms would provide strong emission from the dayside, enabling CIXS to remote sense the global magnetospheric connectivity.

Thus, in addition to quantitative surface analysis and mapping using the X-ray fluorescence technique, we will also be able to provide valuable insights into the magnetospheric precipitation. These comments of course directly imply that very efficient monitoring of the input solar spectrum is required in order to deconvolve the different effects.

Summary: ESA's BepiColombo mission and NASA's Mercury Messenger mission will start to unravel many of the mysteries of Mercury. An X-ray spectrometer will provide a vital addition to the instrument complement of both missions, addressing many of the most important issues remaining about this planet.

References: [1] Grande M., Dunkin S.K., Kellett B.J., this volume [2] Strom R.G., Neukum G. (1988), in *Mercury*, University of Arizona Press [3] Strom R.G., (1997) *Adv. Space Res.*, **19**, 1471 [4] Muinonen K., et al. (2001) *Planetary and Space Science*, in press [5] Grande M. et al. (2001) *Planetary and Space Science*, in press [6] Lewis J.S. (1988) in *Mercury*, University of Arizona Press [7] Goettel K.A., (1988) in *Mercury*, University of Arizona Press [8] Cameron et al. (1988) in *Mercury*, University of Arizona Press [9] Slavin J. A., Holzer R. E., (1979) *JGR*, **84**, 2076 [10] Luhman, J. G.; et al. *JGR*, **103**, 9113 [11] Potter A, E, Killen, R, M and Morgan T, H (1999), *Planet. Space Sci.*, **47**, 1441-1448 [12] Russell C. T., D. N. Baker and J. A. Slavin, (1988) in *Mercury* University of Arizona Press [13] Baker D. N. et al. (1987), *JGR*, **92**, 4707 [14] Grande, M (1997) *Adv. Space Res.* **19**, 1609-1614 [15] Grande M., Dunkin S.K., Kellett B.J., (2001) *Planetary and Space Science*, in press [16] Anderson P. D. et al. (1998), *Geophys. Res. Lett.* **25**, 4105 [17] Schmitt J. H. M. M. et al. (1991) *Nature* **349**, 583.

Measuring the Chemical Composition of the Surface of Mercury using Orbital Gamma-ray and Neutron Spectroscopy. C. d'Uston¹, J. Brückner², W. C. Feldman³, O. Gasnault³, N. Hasebe⁴, D. J. Lawrence³, S. Maurice⁵, and T. H. Prettyman³; ¹Centre d'Etude Spatiale des Rayonnements, 9, Avenue du Colonel Roche, Toulouse, France, (Lionel.Duston@cesr.fr); ²Max-Planck-Institut f. Chemie, Mainz, Germany; ³Los Alamos National Laboratory, Los Alamos, NM, USA; ⁴Waseda University, Tokyo, Japan; ⁵Observatoire Midi-Pyrénées, Toulouse, France.

Introduction: Many of the fundamental questions regarding the formation and evolution of Mercury can be addressed by measuring the global chemical composition of its surface. For example, the FeO composition of the Mercury surface can reveal information about the condensation temperature of Mercury during its accretion along with information about its volcanic history after formation [1]. Knowledge of the iron abundance will in turn enable discrimination between different models that explain the formation and evolution of Mercury (see e.g., [1]). Abundance measurements of refractory elements such as Ca, Mg, Al, Ti and radioactive elements such as K, Th, and U can also help to discriminate between various models of formation and enable us to better understand the environment in which Mercury formed. In addition to measuring the global abundance of these elements, it is also important to derive abundance maps to be able to characterize the degree of composition inhomogeneity that exists on the surface of Mercury.

Abundance measurements of volatile elements, such as hydrogen, are important to understand the origin and nature of the radar-bright spots located in the permanently shaded regions of the north and south poles [2]. In particular, hydrogen abundance measurements may help to determine if these regions are populated by large amounts of water ice [2].

One of the best ways to carry out all these measurement objectives is to use orbital gamma-ray and neutron spectroscopy to make measurements of absolute elemental abundances on the surface of Mercury.

Orbital Gamma-ray and Neutron Spectroscopy: Galactic cosmic rays (GCR) constantly impinge all planetary bodies and produce characteristic gamma-ray lines and leakage neutrons as reaction products. Together with gamma-ray lines produced by radioactive decay, these nuclear emissions provide a powerful technique for remotely measuring the chemical composition of airless planetary surfaces. The ability of planetary gamma-ray spectroscopy to remotely measure planetary surface compositions was first demonstrated with the Apollo Gamma-Ray (AGR) measurements of the lunar surface [3]. The full value of combined gamma-ray and neutron spectroscopy has been shown with the Lunar Prospector Gamma-Ray (LP-GRS) and Neutron Spectrometer (LP-NS) measurements of the lunar surface [4]. With the inclusion of gamma-ray instruments on the NEAR mission to Eros

[5] and the SELENE mission to the Moon [6], and gamma-ray and neutron instruments on missions to Mars [7] and Mercury [8, 9], it is clear that gamma-ray and neutron spectroscopy is becoming a standard technique for remotely measuring planetary compositions.

While some studies have used lunar sample ground truth data to derive absolute abundances [e.g., 3, 10, 11], it has been shown with the LP data that it is possible to make detailed maps (with a surface resolution of $\sim [50\text{km}]^2$) of absolute abundances without relying upon ground truth calibrations [12, 13]. In the context of Mercury – a planet from which we have no returned samples – it is essential to have this ability to make absolute abundance measurements that are independent of ground truth.

In addition to specific elemental abundances, LP neutron data has been used to determine more general composition parameters such as the average atomic soil mass [14] and the iron-rich mafic content of lunar soil [15]. Table 1 shows the variety of composition information that has been measured to date using LP gamma-ray, thermal, epithermal and fast neutron data. Table 2 summarizes the additional abundance measurements that are expected but not yet reported from existing experiments.

Table 1: Measured Composition Information

Measured quantity (abundances)	Technique	Instrument	References
K, Th, Fe, and Ti	gamma-rays	LP-GRS	11, 12, 13, 16
Enhanced polar H	epi. neutrons	LP-NS	17
Global H	epi. neutrons	LP-NS	18, 19
Gd and Sm	therm and epi. neutrons	LP-NS	20, 21
Mafic content	therm, epi. neutrons; gamma-rays	LP-NS/LP-GRS	15, 22
Average soil mass	fast neutrons	LP-GRS	14

Table 2: Expected Composition Information from Existing Experiments

Measured quantity (abundances)	Technique	Instrument
Mg, U, K, Al, Ca, Si	gamma-rays	LP-GRS, Mars Odyssey GRS
C	therm and epi. neutrons	Mars Odyssey NS

Considerations of Gamma-ray and Neutron Spectroscopy as related to Mercury: Combined gamma-ray and neutron spectroscopy is an ideal technique to use for measuring the most important chemical composition parameters of the Mercury surface. Because iron plays a central role in our understanding of the formation and evolution of Mercury, it is essential to accurately measure its abundance on the surface of Mercury. The standard technique for measuring iron abundances is to measure the flux variations of the 7.6 MeV line produced by neutron capture [10, 11]. However, as explained by [11], the neutron capture reaction rate (and hence the gamma-ray flux) is highly dependent on the local neutron number density. The neutron number density (which is directly related to the measured thermal neutron flux) in turn can vary greatly depending on the relative amounts of neutron absorbing elements such as Fe, Ti, Gd, Sm, and others [20]. In regards to lunar data, it is shown by [11] that if corrections for neutron number density variations (as independently measured by neutron spectrometer data) are not carried out, then it is possible to have relative errors of up to 300% in the determination of lunar iron abundances. Similar corrections will need to be applied to all the gamma-ray lines produced by neutron capture. In addition to Fe, the elements Ti, Ca, Al, U, Th, and K are all important for better understanding the origin and evolution of Mercury and can be measured using gamma-ray spectroscopy.

Finally, if there do exist excess abundances of hydrogen at the Mercury poles, these abundances may be detected using the measured fluxes of epithermal neutrons. This is the same technique that was used to measure excess hydrogen abundances at the poles of the Moon [17].

Current Missions to Mercury: Both of the current missions to Mercury (MESSENGER and Bepi-Colombo) are planning to carry gamma-ray and neutron experiments [7, 8]. One of the key aspects to ensure a successful experiment is to maximize the measured gamma-ray and neutron counting rate from the planet and minimize their spacecraft background. In particular, since the measured counting rate is proportional to the solid angle subtended by the planet as viewed by the detectors, the counting rate is highly dependent on the distance from the planet to the spacecraft. In this respect, the two missions are complementary in how the gamma-ray/neutron experiments will be carried out. The MESSENGER spacecraft will be in a highly elliptical orbit with a periapsis of 200 km near 60°N [23]. This will allow high counting rates with relatively good spatial resolution to be achieved during the closest approach portion of the orbit. The

MESSENGER apoapsis, however, will be quite large (~15,000 km). Therefore, during the farthest portion of the orbit, there will be a very small gamma-ray and neutron counting rate from the planet. In contrast, the orbit of the BepiColombo Mercury Planetary Orbiter (MPO) will be less elliptical with a periapsis of 400 km near the equator and an apoapsis of 1500 km [8]. While the MPO periapsis is larger than that of MESSENGER, a larger proportion of the orbit will be spent close to the planet, thereby increasing the measured gamma-ray and neutron fluence during the mission. This in turn enables a broader spatial coverage of statistically significant counting rates to be measured. In particular, it should be possible to derive global composition maps using gamma-ray/neutron data from the MPO spacecraft. Work is in progress to define the gamma-ray and neutron sensors, which in turn will allow a detailed estimate of expected counting rates, coverage, and spatial resolution for the BepiColombo gamma-ray/neutron experiment.

References: [1] Brückner J., and Masarik J., (1997) *Planet. Space Sci.*, 45(#1), 39; [2] Harmon J. K., et al., (2001) *Icarus*, 149, 1; [3] Metzger, (1993) *Remote Geochem. Analysis: Elemental and Min. Compos.*, Pieters and Englert Eds., pg. 341; [4] Feldman et al. (1999) *Nuc. Inst. and Meth. A*, 422, 562; [5] Trombka et al. (1999) *Nuc. Inst. and Meth. A*, 422, 572; [6] Kobayashi M., et al., (2000) *4th Int. Conf. on Explor. and Util. of the Moon*; [7] Boynton et al. (1992) *J. Geophys. Res.*, 97(#E5), 7681; [8] Solomon S. C., (2001) *32nd Lunar Planet. Sci. Conf.*, Abstract #1345; [9] Grard R. et al., (2000) *ESA Bulletin*, 103. [10] Davis P. A., (1980) *J. Geophys. Res.*, 85(#B6), 3209; [11] Lawrence et al., (2001) *32nd Lunar Planet. Sci. Conf.*, Abstract #1830; Lawrence et al., (2001, submitted) *J. Geophys. Res.*; [12] Lawrence et al., (1999) *Geophys. Res. Lett.*, 26, 17, 2681; Lawrence et al., *J. Geophys. Res.*, 105(#E8), 20307; [13] Prettyman et al., *32nd Lunar Planet. Sci. Conf.*, Abstract #2122; [14] Gasnault et al., (2001) *32nd Lunar Planet. Sci. Conf.*, Abstract #1963; Gasnault et al., (2001, submitted) *Geophys. Res. Lett.*; [15] Feldman W. C., et al., (2000) *J. Geophys. Res.*, 105(#E8), 20347; [16] Lawrence et al., (1998) *Science*, 284, 1484; [17] Feldman et al. (1998) *Science*, 281, 1496; Feldman et al., (2000) *J. Geophys. Res.*, 105(#E2), 4175; [18] Maurice et al. (2001) *32nd Lunar Planet. Sci. #2033*; [19] Johnson et al. (2001) *32nd Lunar Planet. Sci.*; [20] Elphic et al. (2000) *J. Geophys. Res.*, 105(#E8), 20333; [21] Maurice et al. (2000) *31st Lunar Planet. Sci. #1433*; [22] Feldman et al. (1998) *Science*, 281, 1489; [23] <http://sd-www.jhuapl.edu/MESSENGER/>; The MESSENGER Mission.

IMS: THE INFRARED MAPPING SPECTROMETER OF THE BEPICOLOMBO MISSION. S. Erard,
Institut d'Astrophysique Spatiale, bât. 121, Université Paris-Sud, 91405Orsay, France. Erard@ias.fr

Introduction: The IR Spectrometer on board BepiColombo's MPO (Mercury Planetary Orbiter) aims at investigating the 0.8-2.8 μm range, where the absorption bands of major rock-forming minerals are found. Spatial resolution values on the order of 100 m are needed for regolith mixing studies ($\sim 200 - 300$ m mixing scale), while moderate spectral resolution only is required (~ 20 -40 nm spectral sampling).

Configuration and Performance Features: The IMS experiment currently consists of two physical units, namely the detector and the electronics. The former contains the optics, the focal plane array and the readout system. The electronics unit includes the data compression electronics, the data buffers for data coming from the camera and waiting to be processed and for processed data waiting to be shifted out to the MPO OBDH unit, and the MPO I/F circuitry for power, commands and data.

The optical system has a FOV of 256 mrad, and a focal length of 32 mm. The optics feeds the incoming radiation onto a grating and from there onto a 512x512 array. Line binning can be performed by 4 in the spectral dimension to obtain 128 channels. The resulting IFOV is 0.5 mrad.

The instrument works in pushbroom mode, with spectral dispersion along the lines of the matrix, and spatial information along the other direction. The above figures translate into the swath width and resolution features as described in Table 1.

Exposure times are no less than 5 ms in order to minimize frame transfer effects. The upper bound is dictated by thermal problems (focal plane heating), and can be assumed to be close to the lowest value. Requirement for signal to noise ratio is ≥ 100 in the whole spectral range.

However, the above spectral range does not allow to determine the surface temperature in every day-time situation (see estimates of the signal in Fig. 1). The addition of 2 or 3 photodiodes measuring the emitted flux at longer wavelength, up to $\sim 5 \mu\text{m}$, would provide such information and would allow to compute thermal inertia of surface materials. Such information has been used to estimate grain size and rock fraction on the Moon. The use of more recent models is expected to allow the estimate of sub-surface thermal gradients from such measurements, provided that enough measurements are performed of similar areas.

Orbit, Operations and Pointing Requirements: A polar orbit is required to allow global mapping of Mercury's surface; a 20% swath overlap is required for

global mapping at lower resolution. With an elliptical orbit, periapsis precession is required to cover all latitudes at minimum altitude, and the maximum altitude ought to allow for subsequent swaths to at least marginally overlap.

Low-resolution observations taken at apoapsis will allow global mapping, and identification of areas of interest. Observations at periapsis will be reserved for the highest resolution studies of selected areas. Operational altitudes fall in the 300 – 2500 km range.

Interface and Physical Resource Requirements:

Two thermal I/F are required, such that temperatures are kept in the working range of the experiment.

A cryo-interface has to be provided to cool down the detector in the $-153 \pm 73^\circ\text{C}$ range. Alternatively, IMS could include some suitable cooling device. A Peltier-like cooling system may be taken as a baseline (2-stage device at least).

It is also noted that the IR input may at times exceed that from the unit itself, unless proper radiation re-routing or rejection is possible.

The data volume generated per orbit is highly variable, depending on the spectrum collection repeat rate.

For the given 256 mrad ($\sim 14.67^\circ$) FOV, IMS swath width at pericenter is about 102 km crosstrack by 200 m downtrack footprint, and it is ~ 386 km by 750 m at apocenter. To get complete coverage and avoid equatorial belt coverage gaps, a 25% duty cycle is envisaged.

Assuming a pixel of 750 m (low resolution), an overlap factor of 25%, a resolution of 12 bits, a complete coverage represents 260 Gbits uncompressed. With compression rates of 3 (lossless) and 8 (lossy), this leads to 85 Gb and 30 Gb respectively. This coverage is performed in 6 months, which requires a continuous transfer rate of 5.5 kb/s (lossless compression) or 1.9 kb/s (compression rate of 8).

A similar data rate should be reserved for high resolution observations, so that the overall continuous transfer rate ranges from 4 to 12 kb/s. At maximum repeat rate and high resolution (512 pixels, 128 channels/pixels) values around 1.6 Gbit/orbit are reached even after 3:1 compression, to get continuous coverage. Data rates up to several Mbps can be transferred to the MPO data handling. Binning, timelining and moderately lossy compression may be applied to reduce the data volume.

Open issues: The main critical issues have to do with thermal control and marginally with data rates. In order to solve the problem of high thermal input on the

sensor, a possible approach is to set a cut-off at $\lambda > 2.8 \mu\text{m}$ in the wavelength detection. This approach may reduce the thermal load down to $\sim 0.29 \text{ W}$ (external heat load on aperture). Filtering the visible range could

also help reduce the thermal load on the detector by another factor of 2.

Parameter	Value/Description
Type of optics	telescope + grating
Type of detectors	2D Infrared array + photodiodes
OPTICS	
Aperture	$> 8 \text{ mm}$
Focal length	$> 32 \text{ mm}$
Focal number	4
Field of View	0.256 rad
Pixel IFOV	0.5 mrad
Spectral Range	0.8 - 2.8 μm + discrete measurements at longer wavelengths
Spectral Channels	128
FOCAL PLANE ARRAY	
Pixel lines in array	512
Pixels per array line	512
Exposure time	$> 5 \text{ msec}$
Repeat time	$\sim 250 - 450 \text{ msec}$
Operating temperature	$-153 \div -73 \text{ }^{\circ}\text{C}$
A/D conversion	12 bit/pixel
SIZE and RESOLUTION	
Swath width	102.98 km @ 400 km 386 km @ 1500 km
Swath length	$> 200 \text{ m}$ @ 400 km $> 750 \text{ m}$ @ 1500 km
Spectral sampling	15.6 nm
Angular resolution	0.5 mrad
Spatial resolution	200 m @ 400 km, 750 m @ 1500 km

Parameter	Value/Description
PHYSICAL	
Mass, total	6 kg
Dimensions (total)	300 x 150 x 150 mm
POWER	
Average power	10 W
Peak power	20 W
DATA RATE/VOLUME	
Data volume/Image cube	403 Mbit (raw), 34 Mbit (bing/4 + compr./3)
Compression factor	3:1 - 8:1
Own buffer memory	560 Mbit
Data volume per orbit	$< 1.6 \text{ Gbit}$
POINTING / ALIGNMENT	
Pointing	Nadir
Pointing stability	1 $^{\circ}/\text{s}$
Pointing knowledge accuracy	0.2 arcmin
Alignment knowledge	0.2 arcmin
Alignment stability	0.2 arcmin
THERMAL	
Focal plane	$-153 \div -73 \text{ }^{\circ}\text{C}$
Detector unit operating temperature range	$\leq -27 \text{ }^{\circ}\text{C}$
Electronics	$< +30 \text{ }^{\circ}\text{C}$

Table 1: Infrared Mapping Spectrometer data sheet

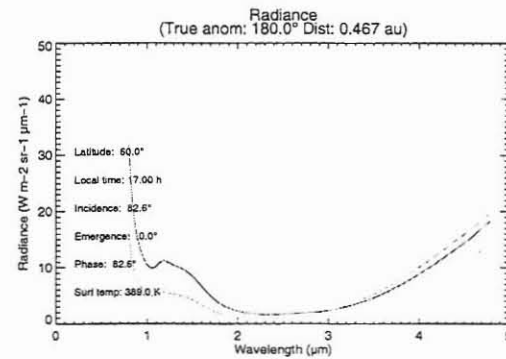
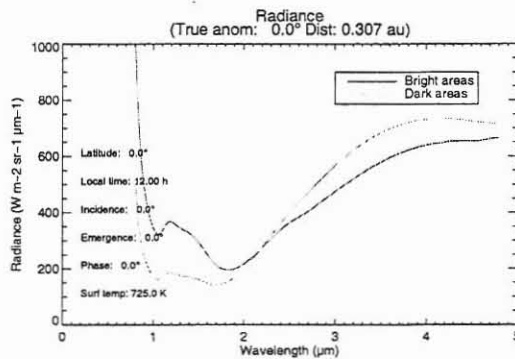


Fig. 1: Simulations of Mercury flux in the NIR range a) warmest possible situation (perihelion, sub-solar pointing); b) cold situation (aphelion near sunset).

The Electron Environment at Mercury. R. A. Frahm,¹ R. Link,¹ J. D. Winningham,¹ A. J. Coates,² O. Norberg³ and, ¹ Southwest Research Institute, San Antonio, TX 78238, USA, rudym@espsun.space.swri.edu, rlink@swri.edu, david@cluster.space.swri.edu, ² Mullard Space Science Laboratory, University College London, Dorking, Surrey, RH5 6NT, England, ajc@mssl.ucl.ac.uk, ³ Esrange, SSC, Box 802, 98128, Kiruna, Sweden, Olle.Norberg@esrange.ssc.se.

Introduction: The Electron environment at Mercury is unique. The planet has a magnetic field, which is similar to that of Earth, but Mercury's magnetic field is significantly smaller than that of Earth, so the planetary body dominates a larger area of Mercury's field compared to the Earth system. The solar wind interacts with the magnetic field of Mercury and an Earth-like plasma interaction with the solar wind is expected to occur. However, Mercury has no substantial ionosphere, so that the mechanism by which the magnetospheric currents are closed remains a matter of debate.

Environment Characteristics: Studying the electron environment can help describe the processes active at Mercury. Electrons are often more mobile than ions, and thus, can provide a quicker indication of process occurrence. In addition, fluxes of electrons are expected to be slightly greater than fluxes of ions at Mercury as they are at all solar system bodies. The difference between Mercury's and Earth's magnetic field systems relative to the planet body should emphasize the differences in reactions between a planet with radiation belts. Radiation belts are a loss mechanism for magnetospheric plasma and a way to transport away energy from the magnetic field system as it reacts with the IMF which are not expected at Mercury. Thus, the loss mechanism should be absent at Mercury.

Mercury has no appreciable atmosphere, and thus, no ionosphere to interact with solar plasma entering the magnetosphere. The combination of no planetary ionosphere and a more rapid magnetic field change for Mercury should allow separation of the effect of a planetary ionosphere when compared to that of the Earth. The lack of an ionosphere reduces the current flows in the magnetosphere of Mercury.

The absence of a tangible ionosphere also means that plasma processes may take place directly on the surface of Mercury. Solar X-ray and extreme ultraviolet photons, as well as solar flare electrons and protons, interact directly with the planet surface on the daylight hemisphere, ionizing the surface and ejecting secondary electrons. X-ray flares are of particular interest because they result in production of Auger electrons which may be detected in the magnetosphere during the flare. Since Auger electrons are ejected at energies characteristic of each element, they serve as a

tracer of surface ion production and magnetospheric ion composition. Photon and particle interactions could provide a localized surface charge which could generate a current path for magnetospheric plasma flow. Thus, electron current flow could be detected during solar flares.

Earth-like magnetospheric interactions are expected to occur at Mercury, but on a shorter time scale. Changes in the Interplanetary Magnetic Field (IMF) occur on a shorter time scale because of Mercury's proximity to the sun. It is anticipated that electron measurements could be used to track interactions of the IMF and Mercury's magnetic field.

Measurements: A 270° electron top hat instrument for detecting electrons within a high solar ultraviolet and X-ray flux environment has been developed under the Planetary Instrument Design and Development Program. An example of the electron spectra seen at Mercury is compared with a detected spectra to determine what is retrieved by the ideal instrument. Characteristics of the 270° detector are employed to determine the expected measurements.

USING REMOTELY SENSED OBSERVATIONS OF ANCIENT MARE DEPOSITS ON THE MOON AS POSSIBLE ANALOGS TO THE INTERCRATER PLAINS ON MERCURY. J. J. Gillis¹, M. S. Robinson².

¹Washington University, Department of Earth and Planetary Sciences, Saint Louis, MO, 63130. ²Northwestern University, 1847 Sheridan Rd., Evanston, IL, 60208. Gillis@levee.wustl.edu

Introduction: Two commonly held models for the formation of the mercurian intercrater plains are: a global volcanic resurfacing event [1] or basin-ejecta material [2,3]. Although Mariner 10 images have provided morphologic and limited compositional information [4] of the intercrater plains, the origin of these materials remains ambiguous. We examine whether Mariner 10 image at 355 (UV) and 575 nm (orange) can be used to distinguish between these models. Here we use Clementine image data (415 and 750 nm) for ancient lunar mare deposits to evaluate this suggestion.

The inventorying of "hidden" volcanic deposits is important to mercurian studies because they provide evidence of ancient volcanism, which yields clues to the thermal evolution of the planet. The greater abundance of intercrater plains on Mercury, relative to the intercrater plains observed within the lunar highlands, suggests that the resurfacing was comparably more intense. Mercury may represent an intermediate member of planet resurfacing; with the extremes being the Moon (~17% resurfacing) and Venus (global resurfacing).

Geology: The timing of the resurfacing event on Mercury is constrained by the morphology of the terrain. Intercrater plains material is described as level to hilly relatively smooth terrain, and lying between and around the heavily cratered terrain [5]. Superposed on the intercrater plains is a high density of craters in the size range 5-10 km. Many of these craters are morphologically and distributionally analogous to secondary impact craters. They range from elongate and shallow to open on one side, and they occur in clusters and crater chains. The only likely sources for these craters appears to be the large craters and basins of the heavily cratered terrain, and therefore the majority of the intercrater plains predate the heavily cratered terrain [5]. The heavily cratered terrain contains closely packed overlapping craters like those of the lunar highlands. Thus, the lack of heavily cratered regions on Mercury, in contrast to the lunar highlands, suggests that a nearly planet wide resurfacing event wiped out or buried most of the early heavily cratered terrain.

Impact-related origins have been proposed for the mercurian plains because they do not show high-contrast albedo [5] or color boundaries [4] with the surrounding highlands. Moreover, the intimate association of lineated terrain [6] (similar to the Imbrium sculptured terrain) with intercrater plains suggests that intercrater plains may be a facies of basin ejecta analogous to impact-related lunar light plains deposits such as the Cayley Formation.

Distinguish between Smooth plain and intercrater plains

Perhaps the occurrence of the intercrater plains early in the geologic evolution of Mercury is analogous to the lunar ancient mare deposits. Some smooth lunar highland light plains have been shown to represent ancient basaltic units covered by ejecta debris from the last major basin-forming impacts [7]. Overlying, high-albedo feldspathic lunar basin ejecta obscure the typical, low albedo signature of the mare basalt deposits. Similarly, basin deposits on Mercury may have obfuscated surface landforms and compositions indicative of early volcanism. Identifying whether the intercrater plains had a volcanic heritage or not is important because it contains information about the early thermal history of Mercury.

Approach: We use the Clementine UVVIS images of the Schickard crater to investigate whether the presence of volcanic landforms could be observed or whether compositional differences between the light plains covered cryptomare and surrounding highlands could be detected using only two bands (415, 750 nm) of remotely sensed data. The Schickard area was chosen for study because it contains two mare basalt units, an ancient mare deposit (designated light plains in Fig. 1), and secondary craters from Orientale (Fig. 1).

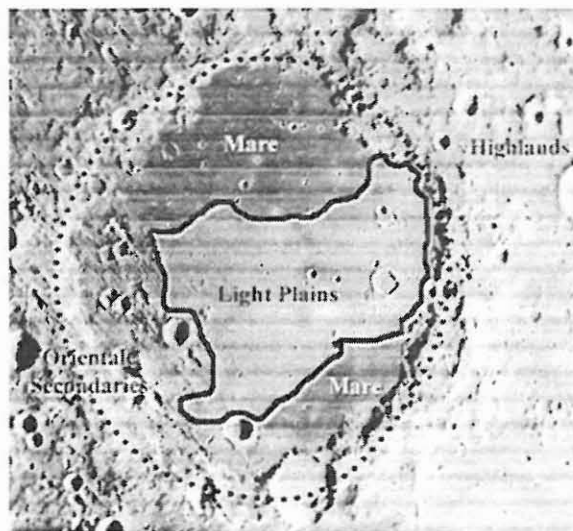


Fig. 1. Lunar Orbiter image (IV-160-H2) of Schickard crater (44°S, 55°W; 227 km diameter).

The Mariner 10 image data consist of only two wavelengths, 355 nm (UV) and 575 nm (orange). Two parameters (UV/orange ratio versus orange albedo)

CRYPTOMARE DEPOSITS AND INTERCRATER PLAINS: J. J. Gillis and M. S. Robinson

were used satisfactorily to decouple the spectral effects of ferrous iron content plus soil maturity from spectrally neutral opaque minerals into two perpendicular trends [4]. Separating spectral effects of ferrous iron content from maturity caused by space weathering is problematic using only these two particular wavelengths [4]. Most color variation in the iron-maturity image was from surface maturity and not from composition [4], on the basis that most color variation is associated with crater rays and ejecta.

To examine whether the intercrater plains should possess a unique compositional signature as buried ancient basalt flows covered by highlands, we use the Clementine UVVIS data processed using the latest calibration parameters by the USGS, Flagstaff [8]. We reproduce the relative color versus albedo technique of [4] at Clementine wavelengths, 415/750 versus 750 nm reflectance, to look for color differences caused by iron and maturity or opaque mineral content in the surface soils among mare, light plains and typical highlands soils in the Schickard area.

Discussion: Examination of Clementine and Lunar Orbiter images of the ancient mare unit within Schickard yields no obvious evidence for volcanic constructs (e.g., cones, domes, rilles, pyroclastic deposits). Either they never existed (e.g. the fluid lunar lava flows buried their source vents) or they were obliterated by the ejecta superposed on them. We favor the former interpretation on the basis that we do not find volcanic landforms within the mare basalt deposits, either.

Examination of the color composite image (Fig. 2) shows that there is little brightness difference between the ancient mare unit and the surrounding highlands, with the exception of a dark halo crater (dhc Fig. 2). This indicates that the detection of ancient mare deposits using only two bands in the ultraviolet and visible wavelengths is difficult, even for mixtures with compositional differences as great as that between lunar highlands and basalt (4-5 wt.% FeO for feldspathic highlands and 18-20 wt.% FeO for mare basalt).

Implications: The absence of color difference between lunar light plains, which are known to overly ancient mare basalt [7], and the surrounding highlands demonstrates that an absence of similar color differences between intercrater plains and surrounding material does not indicate conclusively whether or not the intercrater plains possess a volcanic lineage. The lack of distinct color or albedo boundaries between the intercrater plains and typical highly cratered plains [4,5,9] is likely the result of mixing two geologic units of similar FeO composition. Examination of mercurian plains interpreted morphologically to be volcanic in origin reveals relatively low contrast boundaries in the maturity-plus-iron image, indicating that these units have very similar FeO contents [4,10], making distinct color differences for these units less likely than for the lunar

case. A more powerful method for Mercury is obviously needed.

Increased spatial and spectral resolution obtained MESSENGER and BepiColombo will undoubtedly aid in determining whether the intercrater plains are analogous to lunar ancient mare deposits by identifying dark halo craters with mafic signatures. In addition, the MESSENGER's laser altimeter will show whether volcanic flows on Mercury (if any) and the intercrater plains exhibit similar elevations; an indication of similar elevation distributions suggests a similar origin. For example, the Cayley light plains exhibit elevations from 6 km to 8 km above the mean lunar datum, the highest ponded lunar basalts are approximately 5 km [7].

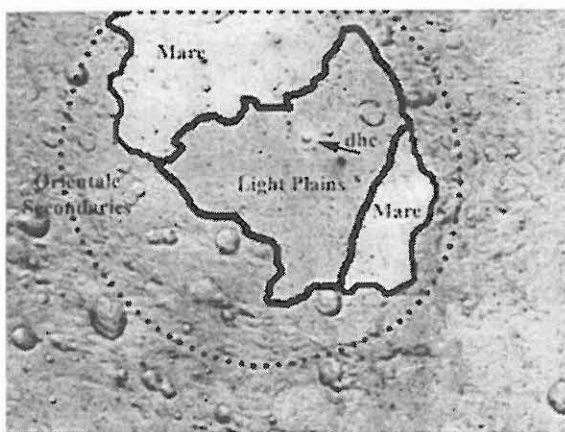


Fig 2. Color composite image of Schickard Crater. The red channel is (750/415), green is 750 nm or the iron-maturity parameter of [1], and blue is 415/750. Areas of increasing iron and maturity appear bright green. The intensity of the iron maturity parameter for the light plains unit is comparable to the surrounding highlands. The dark halo crater (dhc) is the only hint that ancient mare basalt exists below the light plains unit.

Acknowledgments: This research was supported in part by NAG5-8905.

References: [1] Murray et al., *JGR*, **80**, 2508-2514, 1975; [2] Wilhelms, *Icarus*, **28**, 551-558, 1976; [3] Oberbeck et al., *JGR*, **82**, 1681-1698, 1977; [4] Robinson and Lucey, *Science*, **275**, 125-272, 1997; [5] Hapke et al., *JGR*, **80**, 2431-2443, 1975 [6] Trask and Guest, *JGR*, **80**, 2462-2477, 1975; [7] Schultz & Spudis, *PLPSC 10th*, 2899-2918, 1979; [8] Eliason et al., *The Clementine UVVIS Global Images*, 1999; [9] Robinson and G. J. Taylor, *MAPS*, **36**, 841-847.

MAGNETOSPHERE-REGOLITH/EXOSPHERE COUPLING: DIFFERENCES AND SIMILARITIES TO THE EARTH MAGNETOSPHERE-IONOSPHERE COUPLING. J. W. Gjerleov and J. A. Slavin.

Of the three Mercury passes made by Mariner 10 the first and third went through the Mercury magnetosphere. The third encounter which occurred during northward IMF showed quiet time magnetic fields. In contrast the third encounter observed clear substorm signatures including dipolarization, field-aligned currents (FACs) and injection of energetic electrons at geosynchronous orbit. However, the determined cross-tail potential drop and the assumed height integrated conductance indicate that the FAC should be 2-50 times weaker than observed. We address this inconsistency and the fundamental problem of FAC closure whether this takes place in the regolith or in the exosphere. The current state of knowledge of the magnetosphere-exosphere/regolith coupling is addressed and similarities and differences to the Earth magnetosphere-ionosphere coupling are discussed.

THE MESSENGER SCIENTIFIC PAYLOAD. Robert E. Gold¹, Ralph L. McNutt, Jr.¹, Andrew G. Santo¹, Sean C. Solomon², and the MESSENGER Team. ¹The Johns Hopkins University Applied Physics Laboratory, 11100 Johns Hopkins Road, Laurel, MD 20723, robert.gold@jhuapl.edu; ²Department of Terrestrial Magnetism, Carnegie Institution of Washington, 5241 Broad Branch Road, N.W., Washington, DC 20015.

Introduction: The MErcury, Surface, Space ENvironment, GEOchemistry, and Ranging (MESSENGER) spacecraft will be the first to orbit the planet Mercury and the first spacecraft to visit Mercury in more than 30 years. MESSENGER will launch in March 2004 with a miniaturized set of seven instruments. Along with the spacecraft telecommunications system, these instruments will provide a comprehensive view of the structure and composition of the planet. MESSENGER will orbit Mercury for one Earth year following two flybys of Venus and two of Mercury.

Mercury, the least studied of the terrestrial planets, holds the prospect for unraveling important aspects of the origin and early history of the solar system [1]. Mercury is a challenging body to orbit, however, because of high propulsive-energy requirements and the severe thermal environment [2]. To date, Mercury has been visited by spacecraft only during three flybys by Mariner 10 in 1974 and 1975.

The MESSENGER mission has been designed on the basis of a detailed progression from the science questions to be answered, through mission design and implementation [1], to the instrument suite needed to obtain the necessary data. By adhering strictly to the science requirements while also pursuing aggressively miniaturization and packaging optimization so as to minimize payload mass, the instrument suite meets all mission constraints while enabling the measurements required for addressing fully the science questions that define the mission.

Instrument Suite: MESSENGER carries seven scientific instruments plus radio science. The instrument suite includes the Mercury Dual Imaging System (MDIS), a Gamma-Ray and Neutron Spectrometer (GRNS), an X-ray Spectrometer (XRS), a Magnetometer (MAG), the Mercury Laser Altimeter (MLA), the Mercury Atmospheric and Surface Composition Spectrometer (MASCS), an Energetic Particle and Plasma Spectrometer (EPPS), and Radio Science (RS). MDIS has both a wide-angle (WA) and a narrow-angle (NA) imager. MASCS includes an Ultraviolet-Visible Spectrometer (UVVS) and a Visible-Infrared Spectrograph (VIRS). EPPS includes an Energetic Particle Spectrometer (EPS) sensor and a Fast Imaging Plasma Spectrometer (FIPS). The MESSENGER instruments capitalize on emerging technologies developed over several years. The selected instruments accomplish the required observations at low cost with the low masses

essential for implementing this difficult mission. Mass restrictions on a Mercury mission are severe. The total mass available for the payload, including all electronics, thermal accommodations, booms, brackets, and cables, is about 47 kg.

All instruments except MAG are fixed and body mounted for high reliability and low cost. The directional instruments are all co-aligned and located on the bottom deck of the spacecraft. Despite the extreme thermal inputs from the Sun and Mercury, the MESSENGER spacecraft design provides a benign thermal environment for the payload.

A compact, shared data-processing unit (DPU) supports all of the instruments. In addition, most instruments have a miniature data processing unit to perform their real-time, event-by-event processing. Because of the limited downlink bandwidth available, several lossless and lossy data compression techniques are provided to the instruments as required.

Mercury Dual Imaging System: MDIS combines a 12-filter WA imager (10.5° field of view), with a high-resolution, NA imager (1.5° FOV) on a small pivot platform. Both imagers have 1024x1024 pixels and 12-bit quantization. The pivot platform provides for full coverage of the planet during orbital operations and during the two Mercury flybys. Each imager has manual and automatic exposure control over a range of 1 ms to 10 s with electronic shuttering. A subframing capability allows the selection of a chosen rectangular segment of the image to be saved and downlinked. Several image-compression techniques are available and may be used individually or in combination.

Gamma-Ray and Neutron Spectrometer: GRNS has an active-shielded γ -ray scintillator that measures a range of elemental abundances (O, Si, Fe, H, K) and a neutron spectrometer to provide high sensitivity to possible H₂O ice at Mercury's poles. The γ -ray spectrometer (GRS) scintillator is mounted in a cup-shaped active shield of bismuth germanate (BGO) 1.25 cm thick. The shield defines a $\sim 45^\circ$ FOV, provides an anticoincidence veto for cosmic rays, protects the central scintillator from locally generated backgrounds, reduces the Compton continuum, and captures escaping γ -rays generated by pair-production in the central scintillator. The primary GRS detector is a 50 x 50 mm cesium iodide (CsI) scintillator. Energy resolution better than 8.0% has been demonstrated. CsI works near room temperature, so cryogenic cooling is

not required, and it is nearly immune to radiation damage, important for this long-duration mission. The neutron spectrometer uses two lithium glass scintillators separated by a block of borated-polymer scintillator to measure thermal, epithermal and fast neutrons.

X-ray Spectrometer: XRS is an improved version of the NEAR Shoemaker X-ray spectrometer design [3]. Three gas proportional counters view the planet, and a state-of-the-art Si-PIN detector views the sun. Thin absorption filters on two of the planet-facing detectors differentially separate the lower energy X-ray lines (Al, Mg, and Si) [4]. A Be-Cu honeycomb collimator provides a 12° FOV. Energy spectra are accumulated from 1 to 10 keV, which covers the K-fluorescence emission lines of the elements Mg, Al, Si, S, Ca, Ti, and Fe.

Magnetometer: MAG is a miniature three-axis, ring-core fluxgate magnetometer mounted on a 3.6-m boom in the anti-sunward direction. The principal range is ± 2048 nT with 16-bit quantization. There are selectable averaging intervals from 0.04 s to 1 s. An extensive program is in place to minimize stray spacecraft magnetic fields. Potential magnetic field sources are identified early in the design process, and mitigation techniques are selected for their minimum impact on the design.

Mercury Laser Altimeter: MLA will determine the topography of Mercury in the northern hemisphere where the MESSENGER orbit is less than 1000 km above the surface. A Q-switched, diode-pumped Cr:Nd:YAG laser transmitter operates at 1064 nm. When the laser fires, a small fraction of the laser beam is sampled by an optical fiber and relayed onto the start detector, which initiates the timing process. A 4-lens refractive receiver telescope, collects the back-scattered laser echo pulses which are detected with a hybrid avalanche photodiode assembly. Receiver electronics record the arrival time of individually reflected photons with 75-cm (5-ns) resolution.

Mercury Atmospheric and Surface Composition Spectrometer: MASCS is derived from the Galileo Ultraviolet Spectrometer (UVS) [5]. UVVS is optimized for measuring the composition and structure of the atmosphere and surface reflectance. VIRS is optimized for measuring visible (VIS) and near-infrared (IR) surface reflectance (0.3-1.45 μm). VIRS is mounted on top of the UVVS and is coupled to the telescope focal plane with a short optical fiber. UVVS has 25 km resolution at the limb; VIRS has 100-m to 7.5-km resolution on the surface of Mercury, depending on altitude.

A Cassegrain telescope feeds an 1800-groove/mm Ebert-Fastie diffraction grating spectrometer in the UVVS. The spectrum is scanned by rotating the grat-

ing in 0.25 nm steps, providing a factor of 4 oversampling. Three small photomultiplier tubes, behind separate slits, are used in pulse-counting mode for the atmospheric observations.

The VIRS concave holographic diffraction grating images onto two semiconductor detectors. The visible detector (300-1025 nm) is a 512-element silicon line array. The IR detector (0.95-1.45 μm) is a 256-element InGaAs array. Both detectors are digitized to 12 bits.

Energetic Particle and Plasma Spectrometer: EPPS measures ions from thermal plasmas through ~ 5 MeV and electrons from ~ 20 keV to 400 keV. EPPS combines a Fast Imaging Plasma Spectrometer (FIPS) head and an Energetic Particle Spectrometer (EPS) head for energetic ions and electrons. EPPS is mounted near the top deck of the spacecraft where it can observe low-energy ions coming up from the surface of Mercury, pickup ions, ions and electrons accelerated in the magnetosphere, and the solar wind when the spacecraft is turned near its maximum allowed off-Sun pointing angle. EPS is a hockey-puck-sized, time-of-flight (TOF) spectrometer that measures the energy spectra, atomic composition, and pitch-angle distributions of energetic ions and electrons. The FOV is 160° by 12° with six active segments of 25° each; the geometric factor is $\sim 0.1 \text{ cm}^2\text{sr}$.

FIPS measures low-energy plasmas with a nearly full hemispherical coverage. Particles pass through an innovative electrostatic deflection system into a position-sensing TOF telescope. The mass per charge of a given ion follows from E/q and the TOF, allowing reconstruction of distribution functions for different mass/charge species.

Radio Science: RS observations are required for measurements of Mercury's gravity field and in support of the laser altimetry investigation. Accurate knowledge of spacecraft location is required to recover the magnitude of the physical libration of the planet, a key mission objective [1]. Tracking will determine the spacecraft velocity to 0.1 mm/s root-mean-square error.

References: [1] Solomon, S. C., et al., The MESSENGER mission to Mercury: Scientific objectives and implementation. (2001, in press) *Planet. Space Sci.* [2] Santo, A. G., et al., The MESSENGER mission to Mercury: Spacecraft and mission design (2001, in press) *Planet. Space Sci.* [3] Trombka, J. I., et al. (1997) *JGR*, 102, 23,729-23,750. [4] Trombka, J. I., et al. (2000) *Science*, 289, 2101-2105. [5] Hord, C. W., et al. (1992) *Space Sci. Rev.* 60, 503-530.

CIXS – AN X-RAY SPECTROMETER FOR ESA’S BEPICOLOMBO MISSION TO MERCURY

M. Grande¹, S. K. Dunkin^{1,2} and B.J. Kellett¹

¹ Space Science and Technology Department, Rutherford Appleton Laboratory, Chilton Didcot, OX11 0QX, UK

² Department of Geological Sciences, University College London, London WC1E 6BT, UK (m.grande@rl.ac.uk)

Introduction: Mercury can be considered as an “end-member” of the terrestrial planets in our Solar System – it is the closest planet to the Sun, it is the smallest and has the highest uncompressed density. It remains mostly unexplored apart from three flybys by Mariner 10 in 1974 and 1975. Understanding the composition of Mercury is a key to our understanding of the process of the formation and evolution of the Solar System

BepiColombo, ESA’s Cornerstone mission to Mercury, will conduct an extensive investigation of the planet using two orbiters and a lander. This paper outlines a possible X-ray spectrometer that would be ideally suited to the BepiColombo mission, and highlights some of the outstanding science that can be achieved with such an instrument.

Science Drivers: The technique of X-ray spectrometric analysis is well known for remote sensing the atomic composition of planets, having been used at the Moon [1,2], and Eros [3]. [4] have described a possible instrument for investigating the composition of Mercury, based on the experiments flown on Apollo. A very similar instrument is currently under construction for the NASA Mercury Messenger mission. Recently DCIXS (Demonstration of a Compact X-ray Spectrometer), an instrument based on much newer technology [5] has been developed for lunar use on the SMART-1 mission. CIXS, the next generation of such technology, builds upon the experience gained in developing the DCIXS instrument. The primary science goals of the CIXS instrument are based around the following fundamental questions:

- *What is the surface composition?* CIXS provide multi-species global elemental maps to address this question
- *How did Mercury form?* CIXS will measure the critical minor elemental species that can distinguish between the currently competing theories.
- *How has Mercury evolved?* The evolution of the surface will leave its own signature in the surface composition that CIXS can measure.
- *What is the source of the highly variable exosphere?* CIXS will be able to study the X-rays produced by precipitating magnetospheric particles.

These questions place strict requirements on any X-ray instrument to fly on BepiColombo or Messenger:

- *The bandwidth must cover the energy range of the key elemental lines, Na, Mg, Al, Si, K, Ca, Ti and Fe . (i.e. 0.5 to 6.5 keV)*
- *The bandwidth must match the most efficient generation of X-ray fluorescence by the incident solar spectrum. (i.e. 0.5 to 5 keV)*
- *The instrument must be able to separate the fluorescence lines of these key elements. This requires an energy resolution ~150 eV.*
- *Global coverage of the surface is required.*
- *The instrument must have high time resolution, and hence high throughput, both to resolve magnetospheric effects, and because of the high spacecraft ground speed.*
- *We must include a solar monitor, to calibrate the incident flux, and hence provide absolute elemental abundances.*
- *Solar and particle effects must be separated. This can be done with a separate fluorescence monitor.*

The CIXS instrument has been designed specifically with these requirements in mind.

The Instrument: The instrument, shown in Figure 1, centres around a new CMOS detector, mounted behind low profile gold collimators and aluminium thin-film filters. The new detector, designed specifically for the instrument and mission, will enable low noise, photon-counting readout of X-ray generated charge signals while avoiding the charge transfer process of CCD’s. One of the major technical advances of DCIXS has been the development of microstructure collimators, based on new micro-manufacturing technologies developed for solid state and microwave technology. Essentially, this makes it possible to produce the large effective area, essential for detecting the weak planetary fluorescence signal, in a low profile instrument that can be built within a resource envelope far smaller than previously possible. Preliminary calculations suggest that for the BepiColombo baseline orbit, which has a 400×1500 km altitude, an appropriate configuration might consist of a mix of 3°, 4° and 6° collimator facets.

Energy Resolution: CIXS will have a geometric area of 100 cm² leading to an effective area of 58cm² at 1keV with a multi-faceted field of view. CIXS would operate in the energy range of 0.5-10 keV, allowing for the observation of Na, Mg, Al, Si, K, Ca, Ti and Fe, as well as a range of others during a solar flare. An energy resolution of ~150eV would be re-

quired to resolve the lines, and this will easily be achieved. A degradation of the spectral resolution to 250eV makes it impossible to resolve the Na, Al or minor lines in the cases we have modelled, and this has been a strong driver in our choice of detector.

Spatial Resolution: The maximum spatial resolution available to the instrument is defined by the collimator, and this is the resolution available during very bright illumination conditions (i.e. exceptional flares). However, in general, when mapping planetary fluorescence in average illumination conditions, the mapping resolution is limited by the need to have a statistically significant number of photons in the pixel [7]. Even allowing for the fact that the BepiColombo nominal mission occurs at close to the maximum X-ray emissivity of the Sun, the average X-ray emission during the mission will only allow us to produce maps with a 30km pixel, even with our large 58cm² effective area at 1keV. 28% of the time during the mission we can expect C1 or larger flares to be occurring. While these only increase the total X-ray counts by ~50%, they do produce a significant hardening of the spectrum. From the statistics of flare occurrence around solar maximum, we estimate that the limiting spatial resolution (10 km) will be achieved much less than 1% of the time.

An important goal of this instrument is to provide global coverage of the surface in X-rays. The footprint over the surface moves by 52km each orbit at the equator. Therefore a surface footprint of that order is required to ensure full global surface coverage, and this will be achieved by having a 5 faceted view. The central facet will have the smallest field of view to maximise the science return during flare events, when

higher spatial resolution measurements are possible. We will ensure that we can make the most of such opportunities while still providing a global dataset.

Solar and Fluorescence Monitors: One prerequisite for achieving absolute elemental abundances is the full characterisation of the incident flux. The fluorescence produced is a strong function of the slope of the solar continuum in the range 0.5 to 20 keV, and this, as well as the absolute intensity, is highly variable. Thus during strong flares, which produce a hard spectrum, a great deal of extra information may be derived about less abundant species. The solar monitor will be based on the X-ray Solar Monitor (XSM) flown on DCIXS, provided by the University of Helsinki.

One major difference between the Moon and Mercury is the presence of a magnetosphere. The X-ray emission from precipitating particles forms a significant contribution. In order to resolve this, in addition to a conventional solar monitor, we will include a fluorescence monitor. This exposes to the Sun a simulated piece of the surface of Mercury created in the laboratory, and directly monitors the fluorescence produced. Such an instrument has been developed for the Japanese SELENE lunar mission, and will be provided by our Japanese colleagues.

References: [1] Mandelshtam S.L., I.P. Tindo, V.I. Karev, (1966) *Kosmich. Issled.*, 4, 827 [2] Adler I, et al. (1972) *Proc Lunar Sci Conf*, 3, 2157 [3] Squyres S.W., et al., 2000, *DPS*, 32, 2.04 [4] Clark P.E and Trombka J.I. (1997) *Plan Space Sci* 45, 57 [5] Grande et al. (2001) *Plan. Space Sci.* in press [6] Dunkin et al. This volume [7] Grande M., Dunkin S.K., Kellett B.J. (2001) *Plan. Space Sci.* in press.

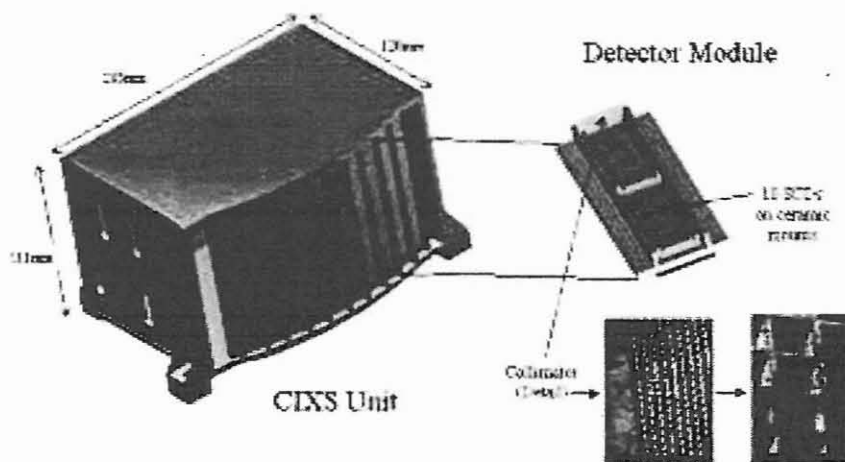


Figure 1: The CIXS instrument, with its 5 faceted field of view. The outer two facets have a 6° FOV, the central facet a 3° FOV and the other two a 4° field of view. This configuration maximises the number of photons arriving for a given integration period, while maintaining a high spatial resolution. Importantly, each of the detectors can be read out separately, and either combined during normal solar conditions, or kept as a single

facet to maximise the spatial resolution during scientifically valuable flare conditions. CIXS will utilise the expertise gained from the DCIXS experiment, using SCD's and micro-collimators, allowing us to fit within the mass budget of 4.5kg. The solar and fluorescence monitors, which would be mounted on the opposite side of the spacecraft, are not shown.

The Charged Particle Environment of Mercury and Related Electric Phenomena. R.Grard¹
and H. Laakso^{2, 1&2}ESA/ESTEC, Space Science Department, Postbus 299, Keplerlaan 1 - NL
2200 AG Noordwijk – Netherlands. Rejean.Grard@esa.int, Harri.Laakso@esa.int

Like the Moon, Mercury has a vestigial atmosphere and no ionosphere, but it possesses a small intrinsic magnetic field. Due to the weakness of this field, of the order of few 100 nT at the equator, and the relatively high solar wind pressure which prevails at the orbit of Mercury, the size of the magnetospheric cavity is much smaller than that of the Earth. The solar wind may even reach the surface of Mercury when its pressure is sufficiently large. The formation of radiation belts is probably impeded for lack of a sufficiently strong magnetic

confinement. The environment is permeated by a current system which is basically unknown and the plasma is extremely rarefied, like in the lobes of the Earth magnetosphere. The absence of an atmosphere permits the circulation of electric currents directly between the solid planet and its space environment. Due to the proximity of the Sun, the emission rate of photoelectrons is up to 10 times larger than at the Earth orbit and leads to unique electrostatic phenomena on orbiting spacecraft and at the planetary surface.

BepiCOLOMBO, an Interdisciplinary Mission to the planet Mercury. R. Grard¹ and T. Mukai², ¹ESA/ESTEC, Space Science Department, Postbus 299, Keplerlaan 1 NL 2200 AG, Noordwijk, Netherlands. Rejean.Grard@esa.int, ²Institute of Space and Astronautical Science, 3-1-1 Yoshinodai, Sagami-hara, Kanagawa 229-8510, Japan. mukai@stp.isas.ac.jp

The questions about Mercury as a planet that form the central rationale of the BepiColombo mission include:

- What will be found on the uninspected hemisphere of Mercury?
- How did the planet evolve geologically?
- Why is Mercury's density so high?
- What is its internal structure and is there a liquid outer core?
- What is the origin of Mercury's magnetic field?
- What is the chemical composition of the surface?
- Is there any water ice in the polar regions?
- Which volatile materials compose the vestigial atmosphere (exosphere)?
- How does the planet's magnetic field interact with the solar wind?

BepiColombo's other objectives go beyond the exploration of the planet and its environment, to take advantage of Mercury's close proximity to the Sun:

- Fundamental science: is Einstein's theory of gravity correct?
- Impact threat: what asteroids lurk on the sunward side of the Earth?

A system and technology study has revealed that the best way to fulfil the scientific goals is to send two orbiters and one lander to Mercury.

- The Planetary Orbiter is dedicated to remote sensing, radio science and asteroid observations.

- The Magnetospheric Orbiter accommodates mostly the field, wave and particle instruments.
- The Surface Element, a lander module, makes in situ observations that serve as ground-truth references.

The method for transporting the spacecraft elements to their destinations emerges from a trade-off between mission cost and launch flexibility. It combines ion propulsion, chemical propulsion and gravity assists. BepiColombo will be launched in 2009. ESA is discussing a cooperation with the Japanese Institute of Space and Astronomical Science (ISAS) which has expressed a keen interest to provide the Magnetospheric Orbiter.

SPACE WEATHERING AND THE COMPOSITION OF THE CRUST OF MERCURY. B. Hapke, Dept. of Geology and Planetary Science, University of Pittsburgh, Pittsburgh, PA 15260, hapke@pitt.edu.

Introduction: The vapor deposition model of space weathering [1, 2] is now widely accepted [3]. The changes in the optical properties of pulverized crustal material of a planet, including spectral darkening, reddening and obscuration of absorption bands, are caused by vapor deposits containing submicroscopic metallic iron (SMFe) particles; the vapor is generated by both solar wind sputtering and micrometeorite vaporization. Mercury's magnetic field stands off the solar wind most of the time. However, Cintala [4] estimates that micrometeorite vapor generation is 20 times greater on Mercury than on the moon, which implies that vapor deposits probably make up more than half of the Mercurian regolith. This paper discusses the implications of these deposits on the interpretation of observations that bear on the composition of the regolith.

Observations Bearing on Composition: The composition of the crust is poorly determined. The photometric and polarimetric properties are similar to the moon's [5], implying a lunar like regolith. However, because of the higher rate and velocities of impacts, the Mercurian regolith should be more mature. Hapke et al [6] were the first to point out that the crust of Mercury must be low in Fe and Ti, based on the albedo and color relationships in the Mariner 10 images. McCord and Adams [7] found that the visual albedo and reflectance spectrum are similar to the moon's, but Vilas [8] has been unable to reliably detect a 1 mm ferrous band. Adams and McCord [9] estimate that the 1 mm band would be difficult to observe if the FeO abundance is less than about 6%. Hapke [5] pointed out that there is no sign of a visible band near 0.5 mm that would be consistent with perovskite, which argues against a crust of highly refractory minerals. Jeanloz et al [10] found that the loss tangent in the Mercurian regolith is similar to low-Fe lunar anorthosites. Sprague [11] reports the detection of an IR Christiansen feature near 8 mm that is consistent with an intermediate to mafic feldspathic crust.

Models: Thus, it may be asked whether there is any Fe present at all on the surface of Mercury. This paper addresses that question. Blewett and Lucey [12] applied their algorithm for the removal of space weathering effects and estimated that the FeO abundance is about 4%. However, their method is critically dependent on data set calibration, and it is not clear how reliable this is in the case of Mercury. Assuming that the crust is siliceous, there are several possible compositional models, each of which will now be evaluated.

High-Fe Models:

MODEL H-1: there is abundant Fe, but it is present only in the form of FeO, as in for instance, enstatite chondrites. In that case the 1 mm band would be absent. However, experiments have shown [13, 2] that adding as little as 5% metallic Fe to silicate powder causes the vapor deposits to contain so much SMFe that the albedo would be too low and the spectrum too flat to match Mercury.

MODEL H-2: there is abundant Fe, and much of it is in the form of high-Fe+2 minerals, as in lunar maria basalts. On the moon this amount of Fe results in a regolith containing about 0.5% SMFe. However, because of the expected much higher abundance of vapor deposits the Mercurian regolith would contain several percent SMFe. This much SMFe would result in an albedo that is too low and a spectrum that is too flat, although the 1 mm band would be totally obscured [2].

Low-Fe Models:

MODEL L-1: the crust completely is iron-free. If this were the case space weathering would be unable to generate SMFe. Experiments show that vapor deposits made from such material absorb strongly only in the UV [5]. The 1mm band would be absent, but the visible/near-IR albedo would be too high and spectrum too flat.

MODEL L-2: Mercury has a low-Fe crust, but Fe is not completely absent. Experiments show that unless the parent material contains more than about 1% FeO the vapor deposits will not have enough SMFe to be absorbing in the visible/near-IR [5].

Conclusions: Mercury has a regolith that is more mature than the moon's and consists of more than 50% impact generated vapor deposits. The crust of Mercury is feldspathic with about 2-6% FeO.

References: [1] Hapke B. et al. (1965) Moon, 13, 339-354. [2] Hapke B. (2001) JGR 106, 10,039-10,063. [3] Pieters C. et al. (2000) Meteorit. Planet. Sci. 35, 1101-1106. [4] Cintala M. (1992) JGR 96, 946-964. [5] Hapke B. (1966) Phys. Earth Planet. Interiors 15, 264-264. [6] Hapke B. et al. (1965), JGR 80, 2431-2443. [7] McCord T. and Adams J. (1962) Science 136, 645-646. [8] Vilas F. (1988) in Mercury (ed. by Vilas F. et al) Univ. of Ariz. Press, p.59-66. [9] Adams J. and McCord T. (1966), paper presented at AAS Div. Planet. Sci annual meeting (abstract). [10] Jeanloz R. et al. (1995) Science 268, 1455-1456. [11] Sprague A. et al. (1994) Icarus 109, 156-166. [12] Blewett D. et al. (1996) Icarus 129, 216-231. [13] Hapke B. (1968) Science 159, 66-69.

RADAR IMAGING OF MERCURY'S NORTH AND SOUTH POLES AT 3.5 CM WAVELENGTH. L.J. Harcke, H.A. Zebker, *Dept. of Electrical Engineering, Stanford University, Stanford, CA 94305-9515 (lharcke@stanford.edu)*, R.F. Jurgens, M.A. Slade, *Jet Propulsion Laboratory, California Inst. of Technology, Pasadena, CA 91109-8099.*

The Goldstone Solar System Radar has been used to image the north and south poles of Mercury during the inferior conjunctions of February 2001 and June 2001. The sub-Earth latitude was -10.7° in February during observations of the southern hemisphere, and $+8.4^\circ$ in June during observations of the northern hemisphere. These excellent viewing angles provided an opportunity to resolve the radar bright material in polar craters at 6 km range resolution. Fine-scale (1.5 km) resolution images of the northern craters have previously been obtained at 13 cm wavelengths during the July 1999 inferior conjunction (Harmon et al., 2001). However, due to geometric constraints, the Arecibo radar cannot observe the southern polar region of Mercury until 2004. Our new Goldstone 6 km data are a factor of two higher resolution than Arecibo data collected in March 1992 at 15 km range resolution (Harmon et al. 1994), and will remain the most highly resolved images of the south polar region for the next few years.

The long-code method of delay-Doppler mapping (Harmon et al., 1992) was used to prevent aliasing of the radar return, as Mercury is nearly 5 times overspread at 3.5 cm. The radar transmitted RC polarization and received both RC and LC polarizations. Several transmit-receive cycles were averaged in delay-Doppler space to obtain the images in Figures 1 (4 cycles averaged) and 2 (10 cycles averaged). In these delay-

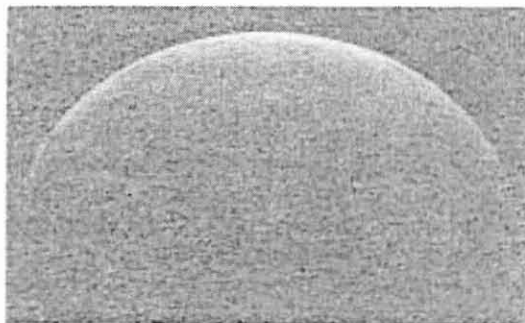


Figure 1: Mercury north hemisphere 2001 June 13

Doppler space images, the pole appears near the center of the image, as the projection into radar coordinates approximates a polar stereographic projection. The hemisphere opposite the sub-Earth point lies in radar shadow, and does not appear in the picture. The standard north-south ambiguity of delay-Doppler mapping does not affect observations of the polar region at these viewing geometries, as the corresponding points at the opposite pole lie in radar shadow. Only data from the same circular (SC) polarization as transmitted are shown, as the strong specular reflection in the OC data from the sub-radar point lowers the overall contrast of the image and masks the polar return.

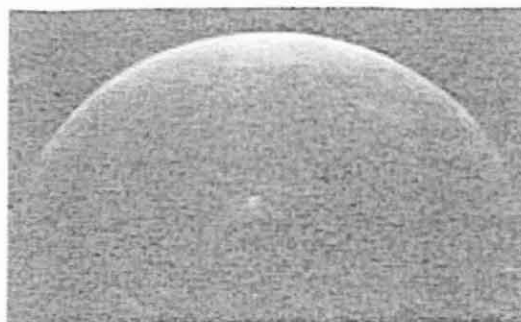


Figure 2: Mercury south hemisphere 2001 Feb. 20

The north polar craters (Figure 3) exhibit brightest reflections from material at their southern rims as noted previously (Harmon et al., 2001; Slade et. al, 2000), which are the areas that are permanently in shadow from the Sun. The south

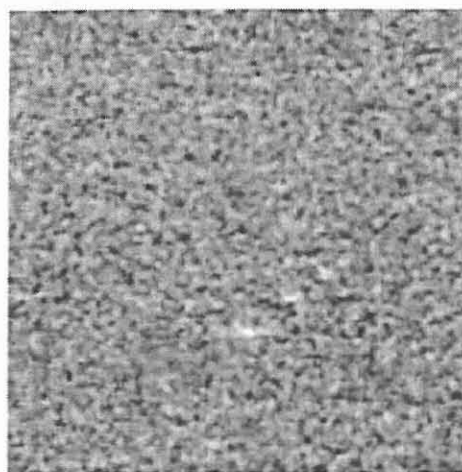


Figure 3: Mercury north pole 2001 June 13

polar scene (Figure 4) is dominated by the reflection from the Chao Meng-Fu crater, though bright reflection from numerous smaller craters can be seen. The brightness of these features is consistent with volume scattering from cold-trapped volatiles. Similar radar bright echo and polarization inversion (SC stronger than OC) has been noted for the Galilean satellites since the mid 1970's (Campbell et al., 1978), and is usually explained using models of coherent backscatter from icy media (Hapke, 1990). Comparison of the radar albedo at the Arecibo

RADAR IMAGING: L.J. Harkke et al.

and Goldstone wavelengths has the potential to constrain scattering mechanisms, and lead to a better understanding of the environment in and around the crater which allows the volatiles to become trapped.

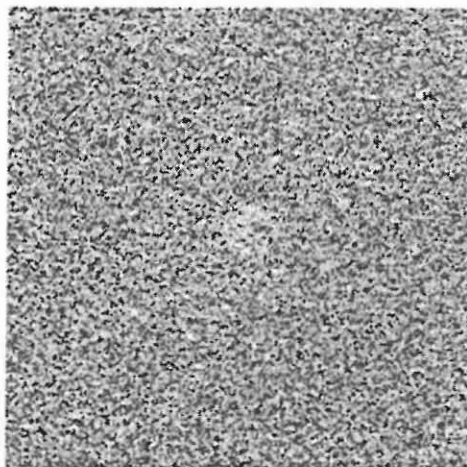


Figure 4: Mercury south pole 2001 Feb. 20

- Campbell, D.B. et al. (1978). *Icarus*, **34**, 254.
Harmon, J.K. et al. (1992). *Icarus*, **95**, 153.
Harmon, J.K. et al. (1994). *Nature*, **369**, 213.
Harmon, J.K. et al. (2001). *Icarus*, **149**, 1.
Hapke, B. (1990). *Icarus*, **88**, 407.
Slade, M.A. et al. (2000). *31st LPSC*, abstract 1305.

MERCURY RADAR IMAGING AT ARECIBO. J. K. Harmon, *National Astronomy and Ionosphere Center, Arecibo Observatory, Arecibo PR 00612, USA, (harmon@naic.edu).*

Introduction. Until ten years ago, Mercury radar studies consisted primarily of CW and delay-Doppler observations of the polarized echo for altimetry, scattering analysis, and imaging of the equatorial region near the subradar track. The last decade has seen a shift in emphasis to full-disk imaging of both the polarized and depolarized echoes. Several advances have made this more practicable. One of these was the advent of bistatic radar synthesis imaging with Goldstone/VLA [1], which circumvented the north-south ambiguity and overspread aliasing problems inherent in delay-Doppler radar. Another advance was the development of the long-code method [2], which mitigates echo overspreading in delay-Doppler. Both of these methods were developed for observing Mars, but were immediately adaptable to Mercury. Finally, there has been the recent upgrading of the Arecibo telescope. This upgrade has given a more than 5-fold improvement in the sensitivity of the Arecibo S-band radar, enabling delay-Doppler imaging with better quality and resolution.

In this talk I review recent Arecibo delay-Doppler radar imaging results for Mercury, concentrating mainly on data obtained with the newly upgraded system. I will begin with a discussion of the putative "ice" features that have been seen at the poles, and then go on to a discussion of the major non-polar radar features seen in the Mariner-unimaged hemisphere. Some of the results discussed in this abstract are based on preliminary analysis of new data. The final images resulting from more complete analysis will be presented at the meeting.

Polar Features. A major surprise from the Goldstone/VLA observations was the discovery in 1991 of an anomalously bright radar feature at the north pole [3]. Long-code Arecibo observations made that same year also showed this feature, and revealed the existence of a bright spot at the south pole as well [4]. Subsequent reanalysis and averaging of Arecibo data from 1991-1992 produced images with 15-km resolution that showed the anomalies at both poles are concentrated in crater-size spots, many of which could be identified with known polar craters [5]. These radar results, with support from thermal studies (e.g., [6]), suggest the presence of thick deposits of cold-trapped volatiles (probably water ice) in the permanently shaded floors of polar craters.

When the upgraded radar came on line in the spring of 1998, we immediately trained it on Mercury to obtain improved images of the north pole. Data obtained in the summers of 1998 and 1999 produced high-quality delay-Doppler images of that pole with resolutions of 3 and 1.5 km, respectively [7]. Although these were conventional repeating-code observations (the long-code system was unavailable at that time), the Doppler aliasing had a negligible effect at the pole. One of the 1999 images is shown in Fig. 1. The order of magnitude resolution improvement revealed fine structure in the north polar features for the first time. This structure includes highlighting and shadowing from central peaks, rim

walls, and rim terraces. The circular features near the center of Fig. 1 indicate near-complete "ice" filling in the floors of these four craters, while the large crescent feature in the lower right (feature K) indicates partial ice filling confined to the sun-shaded area under the south rim of this large (90 km diam.) crater. The sizes and locations of these and many other features are consistent with recent thermal models of insulated (buried) water ice in permanently shaded zones [8]. However, some of the smallest features seen in Fig. 1 and elsewhere fall in craters less than 10 km in diameter, which the same models suggest should not be capable of supporting even insulated ice. Another challenge to these thermal models is the discovery in the 1998-1999 images of several "ice" features at low latitudes between 71-75°N; while it is plausible these features are permanently shaded, the floor temperatures are still sufficiently high to require very rapid burial by a protective mantle. It is quite possible that the new radar results are merely pointing to limitations in our current understanding of ice maintenance in the Mercury environment and do not pose true problems for the water ice hypothesis. There still seems to be room for better understanding of sublimation at low temperatures, the diffusion barrier effects of thin mantles, the role of photodissociation and ionization in net ice loss, etc.

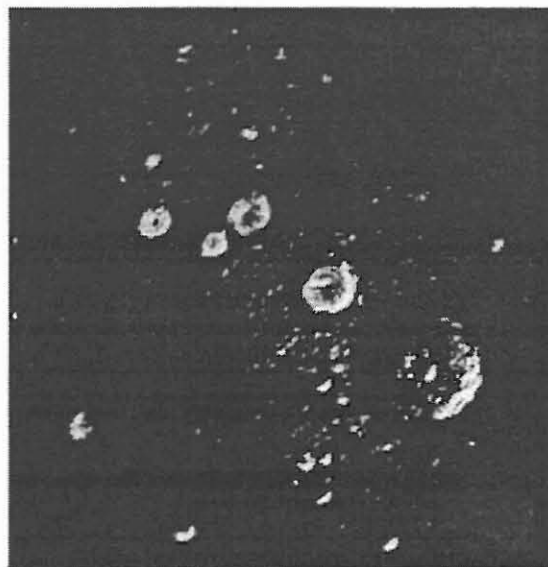


Fig. 1

Additional Arecibo observations have been and will continue to be made of Mercury's poles. Imaging observations at 600-m resolution were made in 2000 and 1.5-3 km long-code observations were made in 2000 and 2001 from different sub-Earth aspects. Results of these observations will be presented. We also plan future observations of the south pole as the observing aspect from Arecibo becomes more favorable.

MERCURY RADAR IMAGING: J. K. Harmon

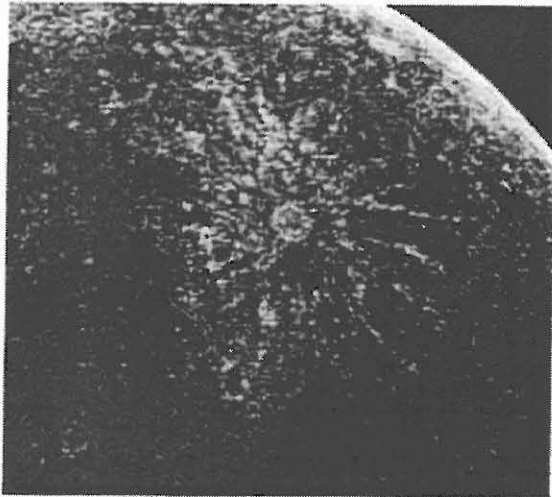


Fig. 2

Non-polar Features. The polar features were originally just a serendipitous discovery made in the course of Goldstone/VLA and Arecibo efforts to make full disk images of the planet, and especially of the hemisphere that was not "photographed" by the Mariner-10 spacecraft. The 1991-1992 results from these radars [3,4] revealed three major bright features in the unphotographed hemisphere, including two midlatitude features in the north and south near 345°W longitude, and a large equatorial feature centered near 240°W longitude. The south midlatitude, north midlatitude, and equatorial features have since been dubbed features A, B, and C, respectively [9]. Features A and B were insufficiently resolved by the Goldstone/VLA images to determine their nature, although Butler *et al.* [10] referred to them provisionally as "impact basins" because of their rough circularity. Since then, improved Arecibo images based on the 1991-1992 data have revealed structure in these two features [9]. In these images feature A showed up unambiguously as a fresh, Tycho-class impact crater with a prominent ejecta blanket and ray system. Feature B had an entirely different appearance, showing a dark central "hole" surrounded by a brighter ring and a large amorphous halo. The combination of a small, dark center with a large, featureless halo is unusual for

an impact feature (based on lunar radar comparisons), which raised the possibility that B is a large volcano [9]. However, bright crater rings with dark floors, albeit without the halo, are seen on Mercury as well as the Moon, so it is perhaps more likely that B is just an unusual impact feature. The large equatorial feature C shows some structure in both the Arecibo [9] and Goldstone/VLA images [10], but in neither case were there any diagnostic features suggesting an origin. Unlike A and B, there is no evidence of a central feature from C, nor are there any rays like those coming from A.

An effort is currently being made to make improved images of these features and other regions of Mercury using the upgraded radar. Long-code observations in the summer of 2000 produced good images at the feature A/B longitudes with 20- μ s delay resolution (a factor of five improvement over the 1991-1992 images). An example of an image from these data is shown in Fig. 2. This shows the raw delay-Doppler image averaged over one of the four observing days from that epoch. Feature A and its prominent rays can be clearly seen. Feature B can be seen just below and slightly left of A, although it is fainter and partially overlapped by foldover from A. The final image in planetary coordinates based on a full 4-day average will be shown at the meeting. I will also show the results of 10- μ s long-code imaging of this same region from recently completed observations in June 2001. Long-code observations are also planned for July 2001 which will cover the longitudes of feature C and Caloris, and any results from those will also be presented.

References

- [1] Muhleman, D. O. (1991). *Science*, 253, 1508.
- [2] Harmon, J. K. et al. (1992). *Icarus*, 95, 153.
- [3] Slade, M. A., B. J. Butler, and D. O. Muhleman (1992). *Science*, 258, 635.
- [4] Harmon, J. K., and M. A. Slade (1992). *Science*, 258, 640.
- [5] Harmon, J. K., et al. (1994). *Nature*, 369, 213.
- [6] Paige, D. A., S. E. Wood, and A. R. Vasavada (1992). *Science*, 258, 643.
- [7] Harmon, J. K., P. J. Perillat, and M. A. Slade (2001). *Icarus*, 149, 1.
- [8] Vasavada, A. R., D. A. Paige, and S. E. Wood (1999). *Icarus*, 141, 179.
- [9] Harmon, J. K. (1997). *Adv. Space Res.*, 19(10), 1487.
- [10] Butler, B. J., D. O. Muhleman, and M. A. Slade (1993). *J. Geophys. Res.*, 98, 15,003.

MERCURY'S THERMAL, TECTONIC, AND MAGMATIC EVOLUTION. Steven A. Hauck, II¹ [now at²] (hauck@wurtzite.wustl.edu), Andrew J. Dombard², Roger J. Phillips¹, and Sean C. Solomon², ¹McDonnell Center for the Space Sciences, Dept. of Earth and Planetary Sciences, CB1169, Washington Univ., One Brookings Drive, St. Louis, MO 63130, ²Dept. of Terrestrial Magnetism, Carnegie Institution of Washington, 5241 Broad Branch Rd., NW, Washington, DC 20015.

INTRODUCTION: An important problem in the understanding of Mercury's history is the reconciliation of thermal evolution models with interpretations of its surface geology. This is true on two specific fronts regarding: (1) the surface contractional history (especially as recorded in lobate scarps such as Discovery Rupes) [e.g., 1-3], and (2) the origin and significance of plains materials [e.g., 4-7].

Estimates of contractional strain recorded in the lobate scarps range between ~0.04 and 0.10% [2], the most recent analysis favoring values near the lower end of this range [3]. Such strain suggests ~1-2 km of planetary radial contraction, yet thermal models [e.g., 8] predict at least 2-6 times as much contraction.

The origin of widespread intercrater plains and younger smooth plains and the nature of volcanism on Mercury are points of some debate [2, 5-7]. On the basis of surface reflectance at visible, infrared and microwave wavelengths, Mercury's surface is inferred to be generally low in Fe²⁺ [e.g., 5, 6 and references therein]. Some workers [5] have interpreted this result to mean that high-albedo regions (at visible wavelengths) have a surface composition that is devoid of basaltic material. If this inference were true, despite the presence of Fe-poor lavas (e.g., some komatiites) on Earth, it would have profound consequences for the thermal evolution of Mercury. However, re-analysis of Mariner 10 color images illustrates that some plains units are spectrally distinguishable on the basis of their opaque mineral content and that these units are stratigraphically and morphologically consistent with volcanic emplacement [6]. This result is contrary to some thermal models that suggest that volcanism is not an important part of Mercury's energy budget [4].

APPROACH: Until new data are returned from the pending MESSENGER [9] and BepiColombo missions to Mercury, we can attempt to address this conundrum by bringing to bear recent understanding of how planetary mantles convect [e.g., 10]. In particular, we apply a model of coupled mantle convection and melt production [11] to Mercury.

We model planetary thermal evolution via a parameterized convection scheme, including core cooling and inner core formation [e.g., 12]. The thermal evolution is coupled to a model of partial melting [13]. Furthermore, we calculate the thermoelastic stresses in a spherical shell with an inner radius evolving as a func-

tion of elastic blocking temperature and a thermally and magmatically evolving interior volume. This integrated thermal, magmatic, and tectonic model allows comparison of evolutionary models and surface geology.

Our thermal history calculations exploit a 1-D (radial) model of convection in a spherical shell overlaying a spherical core. Mantle convection is parameterized with a relationship between the Rayleigh number and the Nusselt number [e.g., 14]. We include the latent heat energy of melting in the mantle energy balance equation. Assuming complete extraction of melt, the latent heat is an energy sink for the mantle and an energy source in the crust. Additionally, we use recent scaling relationships for fluids with highly temperature-dependent viscosity. These relationships, in a regime known as stagnant lid convection, are likely appropriate for one-plate planets with an immobile lithosphere over a convecting mantle [e.g., 10]. Instead of assuming a linear temperature profile through the lithosphere, we use a 1-D, adaptive remeshing, finite element scheme to solve the advection-diffusion equation. This scheme allows us to track the thermal thickening (or thinning) of the lid as well as introduce depth and temperature dependence for material properties such as heat production and thermal conductivity.

Model surface strains are estimated by solving the equations of equilibrium for a sphere undergoing a temperature change. The outer, thick, elastic shell [15, cf. 16] is defined by the depth to an elastic blocking temperature (~950 K), which overlies an interior incapable of supporting shear stresses over geologic time. Internal (and shell) volume changes drive the generation of surface strains. Such volumetric changes may be caused by purely thermal effects due to the thermal expansivity of mantle materials as well as phase changes, such as precipitation of an inner core and mantle melting. We sum the predicted strain rates from these sources and integrate in time to obtain cumulative surface strains during Mercury's evolution.

We use a simple, well-known model for the generation of partial melt due to adiabatic decompression [13], using the phase relations for KLB-1 [17]. These results, especially at high pressures, are noticeably different from previous parameterizations [e.g., 13], partially due to composition, but also to experimental technique [17]. While the composition of Mercury's

mantle is poorly constrained [18], our approach provides a starting point for studying the planet's magmatic history. However, differences between the KLB-1 and Mercurian mantle iron content should not seriously affect the results. Recent reviews of peridotite melting [19, 20] suggest that Mg content has a minor influence on the location of the peridotite solidus. Thus if the Mercurian mantle is dominated by peridotite, then terrestrial analogs may be applicable, despite the potential difference in mantle iron content between Mercury and Earth.

PRELIMINARY RESULTS: Simple, back-of-the-envelope calculations illustrate the extraordinary limits that surface strain estimates may place on the internal evolution of Mercury. If all the observed strain in the lobate scarps [3] is due to simple thermal contraction of the interior due to cooling, then the interior cannot have cooled more than ~ 60 K since the end of heavy bombardment (assuming a volume coefficient of thermal expansion of $3 \times 10^{-5} \text{ K}^{-1}$). Alternatively, we can bound the maximum size of the inner core that satisfies surface contractional strain assuming no thermal changes and that inner core precipitation initiated after the end of the heavy bombardment. With a volumetric difference between liquid and solid iron of 5% [1], the maximum inner core radius must be less than ~ 800 km. A combination of cooling and inner core formation requires both the temperature change and inner core size to be smaller than these upper bounds.

Using nominal rheological parameters for dry olivine in the Newtonian creep regime [21], internal heat generation provided by 26 ppb U and 120 ppb Th (we neglect K because of Mercury's presumed refractory nature) [22, and references therein], a time-dependent convective regime [10], and an inner core with an initial mass fraction of sulfur of 0.05 [1], we predict accumulated contractional surface strains of ~ 0.2 - 0.25% since 4 Ga. One possible mechanism for slowing interior cooling, and hence the accumulation of surface strains, is to increase the strength of the mantle. An increase in the activation energy for creep of 10-15% brings predictions for accumulated strain in line with observations of ~ 0.05 - 0.10% . However, such models include a period of global expansion extending up to 3.5 Ga, evidence for which is not apparent in the geological record.

Preliminary models that include the generation of and extraction of melt from a peridotite-dominated mantle suggest that pervasive melting may have continued up to 2.5 Ga and provided several tens of kilometers of crustal material. However, the bulk (75% or more) of the basaltic magma generation is limited to the period of heavy bombardment.

DISCUSSION, AND THE FUTURE: While the results are preliminary, certain aspects are robust. If the strain

recorded in the lobate scarps records the majority of strain due to planetary cooling and contraction since the end of heavy bombardment, that cooling must have been limited and at a low rate, especially if inner core growth proceeded during that time. Nominal thermal history models suggest at least 2-5 times more surface contractional strain than is recorded in the lobate scarps imaged by Mariner 10. While it is conceivable that either our reference time for the end of the heavy bombardment is significantly in error or the unimaged side hosts proportionally more strain, recent work has shown that there is a possibility that long-wavelength folding of Mercury's lithosphere [23] accommodated more strain than is presently estimated. Such long-wavelength folds could be of sufficiently low amplitude that they would be extremely difficult to discern in Mariner 10 images. However, such surface undulations should be observable in data to be returned from the laser altimeter on the MESSENGER spacecraft. In addition, if Mercury mantle is peridotitic as we have assumed, basaltic volcanism is to be expected. Late-stage volcanism may be relatively small in volume, however, and could be affected by global contraction of the lithosphere sealing off pathways to the surface.

New data to be acquired by the MESSENGER and BepiColombo missions will provide important information relevant to these problems. The topographic, gravity, imagery, and compositional data to be returned all bear on our understanding of the history of the planet closest to the Sun.

REFERENCES: [1] Solomon, S. C. (1976) *Icarus*, 28, 509-521. [2] Strom, R. G. et al. (1975) *JGR*, 80, 2468-2507. [3] Watters, T. R. et al. (1998) *Geology*, 26, 991-994. [4] Spohn, T. (1991) *Icarus*, 90, 222-236. [5] Jeanloz, R. et al. (1995) *Science*, 268, 1455-1457. [6] Robinson, M. S. and Lucey, P. G. (1997) *Science*, 275, 197-200. [7] Wilhelms, D. E. (1976) *Icarus*, 28, 551-558. [8] Hauck, S. A., II, et al. (2000) *Eos. Trans. AGU*, 81, S296. [9] Solomon, S. C. et al. (2001) *Planet. Space Sci.*, in press. [10] Solomatov, V. S. and Moresi L.-N. (2000) *JGR*, 105, 21795-21817. [11] Hauck, S. A., II, and Phillips, R. J. (2001) *JGR*, submitted. [12] Stevenson, D. J. et al. (1983) *Icarus*, 54, 466-489. [13] McKenzie, D. P. and Bickle, M. J. (1989) *J. Petrology*, 29, 625-679. [14] Turcotte, D. L., and Schubert, G. (1982) *Geodynamics*, Wiley. [15] Timoshenko, S. P. and Goodier, J. N. (1982) *Theory of Elasticity*, McGraw-Hill. [16] Turcotte, D. L. (1983) *J. Geophys. Res.*, 88, A585-A587. [17] Zhang, C. and Herzberg, C. (1994) *J. Geophys. Res.*, 99, 17729-17742. [18] Goettel, K. A. (1988) in *Mercury*, U. Arizona Press, 613-621. [19] Herzberg, C. et al. (2000) *Geochem. Geophys. Geosyst.*, 1. [20] Hirschmann, M. M. (2000) *Geochem. Geophys. Geosyst.*, 1. [21] Karato, S.-I. and Wu, P. (1993) *Science*, 260, 771-778. [22] Lodders, K. and Fegley, B. (1998) *The Planetary Scientist's Companion*, Oxford Univ. Press. [23] Dombard, A. J. et al. (2001) *LPSC*, 2035.pdf.

OVERVIEW OF THE MESSENGER MERCURY DUAL IMAGING SYSTEM. S. E. Hawkins, III, J. D. Boldt, E. H. Darlington, M. P. Grey, C. J. Kardian, Jr., S. L. Murchie, K. Peacock, E. D. Schaefer, B. D. Williams, *The Johns Hopkins University Applied Physics Laboratory, Laurel MD 20723-6099, USA, (ed.hawkins@jhuapl.edu).*

The Mercury Dual Imaging System (MDIS) is part of the science payload to be flown on the NASA Discovery mission MESSENGER [1]. MDIS is comprised of wide- and narrow-angle cameras sensitive to visible wavelengths. The MErcury Surface, Space ENvironment, GEOchemistry, and Ranging (MESSENGER) spacecraft will be launched in the spring of 2004 aboard a Delta 2925H-9.5 rocket. MESSENGER will arrive at Mercury in the spring of 2009 to begin its year-long mission to study the planet. Prior to Mercury orbit insertion, the two Mercury flybys will provide imaging opportunities in addition to those during the mission orbital phase. Mission goals are to produce a global monochrome map at 250-m average resolution or better and a color map at 2-km average resolution or better. The success of MESSENGER is strongly tied to developing a capable and robust spacecraft and science payload with minimal mass [2].

Mercury's eccentric orbit poses a challenge to the design of the spacecraft, with the intensity of the solar radiation varying from about 4.6–10.6 times the total irradiance falling on the Earth. Because of this severe thermal environment, a sunshade protects the spacecraft from direct solar illumination, but strongly constrains its range of pointing. To compensate for this limited pointing capability, the dual cameras of MDIS are mounted on either side of a rotating platform, pivoted about a common axis as shown in Fig. 1. The two cameras will be

features with minimal impact on spacecraft pointing. The nominal scan range of the platform is -40° in the sunward direction to $+50^\circ$ planetward.

The wide-angle camera (WAC) has a 10.5° field-of-view (FOV) and consists of a refractive telescope using a dogmar-like design having a collecting area of 48 mm^2 . A 12-position multispectral filter wheel provides color imaging over the spectral response of the CCD detector (395–1040 nm). Ten spectral filters are defined to cover wavelengths diagnostic of different surface compositions and have bandwidths from 10–40 nm. A medium-band filter provides fast exposures for high resolution imaging, and the last filter is panchromatic for OpNavs. In order to achieve diffraction limited image quality, residual chromatic aberration is removed by varying the optical thickness of each filter, optimized for the center wavelength of the filter's passband, as was done for the the Multi-Spectral Imager on the NEAR Shoemaker spacecraft [3]. The narrow-angle camera (NAC) has a 1.5° FOV and uses a reflective design with a single medium-band filter with a passband identical to the one used in the WAC (650–850 nm). Both cameras have identical detector electronics contained in a modular focal plane unit (FPU). Due to thermal constraints, only one camera will operate at a time.

Protective covers for optical components are very desirable during ground-based testing, launch, and trajectory maneuvers requiring large thruster burns. However, due to the severe mass limitations on MESSENGER, a conventional protective cover for MDIS was not practical. Instead, the critical first optic of each telescope can be protected by rotating the platform 180° from nadir, such that both cameras look downward into the deck. This innovative approach ensures a circuitous path for any particulate or molecular contamination. Small incandescent bulbs are mounted in the base of the bracket to facilitate testing of the instrument in its stowed configuration.

The base of the pivot assembly is made of an advanced composite material (graphite/cyanate ester fabric pre-preg). This was chosen to match the material of the instrument deck, thus eliminating mechanical stresses due to differences in differential coefficients of expansion. The composite bracket assembly is thermally isolated from the spacecraft and the pivot platform. A rotary actuator is located on one side of the bracket, containing a stepper motor, resolver, and harmonic drive assembly. The stepper motor contains redundant windings so that the two fully redundant data processing units (DPUs) can independently control the motion of the pivot, enhancing the overall reliability of the pivot mechanism.

The MDIS harmonic drive has a 100:1 gear-reduction resulting in an output step resolution of 0.075° . Harmonic drive gear reducers provide very precise pointing and high torque ratios at lower mass than comparable conventional gear systems. These devices use a radial motion to engage the teeth of a flexspline and a circular toothed spline, rather than the

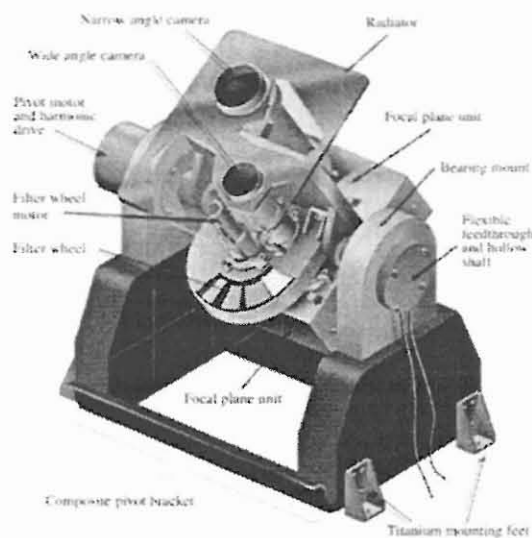


Figure 1: Artistic rendering of MDIS.

co-aligned to within the pointing accuracy of the spacecraft of 0.1° . The pivot platform design enables the instrument to acquire optical navigation (OpNav) images and star field calibrations, and greatly increases opportunities to image key

OVERVIEW of the MESSENGER MDIS: Hawkins et al.

rotating motion of other gear systems. This motion allows for very high gear ratios and near zero-backlash performance. The baseline plan to move the pivot mechanism is to count pulses sent to the stepper motor. A low resolution resolver ensures no steps are missed during motion. Calibration of each output step of the pivot mechanism prior to launch, will provide absolute pointing knowledge of the pivot position to $\lesssim 100 \mu\text{rad}$, essential for elevation determination from stereo imaging.

The bracket opposite the pivot actuator supports a bearing mount and a flexible diaphragm. A rotary feedthrough passes through a hollow shaft and provides all power, clocking control, and data to the two FPUs, the filter wheel and its position sensor, and the heaters and temperature sensors on the pivot platform. Connections to the platform from the two redundant DPUs pass through an interface adapter box, mounted to the bracket and just below the rotary feedthrough. The adapter box switches between the DPUs in a master/slave configuration and converts the low-voltage differential signals from the DPU to single-ended signals. This approach limits the number of circuits needed to pass through the rotary interface. The $<1 \text{ W}$ dissipated in the adapter box gets conducted into the spacecraft deck through a thermal strap.

The two FPUs with their CCD detectors are passively cooled. Because the instrument payload is protected from direct solar illumination by the spacecraft sunshade, the thermal environment of the instruments is largely benign with the exception of short intervals during the 12-hour orbital period. The thermal design takes advantage of the eccentric orbit of MESSENGER around Mercury by radiatively cooling the pivot platform during most of an orbital period using a 0.022 m^2 radiator. Near periaapsis, the thermal flux radiated from the planet will be absorbed by this radiator and the instrument is designed such that the latent heat of the pivot platform does not allow the temperature of the cameras to rise above the maximum operating temperature of -10°C . During the remainder of the orbit, the radiator cools the pivot platform and thermostatically controlled heaters limit the minimum operating temperature to -40°C . There are two redundant survival heaters coupled to the pivot platform, with the setpoint for one configured to switch-on at the MDIS low operating temperature, effectively making it an operational heater. Each image will include four columns of dark reference elements in order to correct for variations in operating temperature.

In order to minimize mass, defocusing, and misalignment effects resulting from operating over a wide range of temperatures, the pivot platform and most of the components are made of magnesium. The two shafts supporting the rotating platform are made of titanium, selected for its relatively poor thermal conductivity. The instrument deck and the bracket will remain near room temperature. The entire instrument and bracket assembly are covered with multilayer insulating blankets.

The design of the detector electronics is based on the CONTOUR/CRISP instrument, and is identical for both the wide- and narrow-angle cameras. Because of the mass constraint on MESSENGER, the FPU electronics have been further miniaturized. The highly capacitive CCD is driven by custom designed hybrid circuits which significantly increase the component density in the FPU. A field-programmable gate array in

each FPU provides the necessary clocking and control for each camera. The detector is an Atmel TH7888A CCD array with 1024×1024 pixels with built-in antiblooming control. The fill factor for the $14 \times 14 \mu\text{m}$ pixels is 71%. The maximum frame rate is 1 Hz with a frame transfer time of 3 ms.

Optical navigation using MDIS is critical to the success of the MESSENGER mission. To increase the low-light sensitivity, the maximum exposure is approximately 9.9 s with a readout time of $\lesssim 1 \text{ s}$. Typical exposures will be $\sim 100 \text{ ms}$. An autoexposure algorithm similar to that used on NEAR [3] will also be used regularly.

Although the peak of the quantum efficiency of the CCD is only about 18%, the expected signals at Mercury are large. We have assumed a reflectance spectrum for Mercury to be the same as a laboratory spectrum of the Apollo 16 lunar sample 62231 [4]. Telemetry limitations constrain MDIS rather than signal strength. The FPU electronics perform a correlated double sample of each pixel then digitize it to 12-bits resulting in a 12 Mb full image. At the expected acquisition rates of ~ 100 images/day, the two 8 Gb solid-state recorders (SSR) on board would be filled in less than two weeks. MESSENGER is not equipped with a high gain antenna, and so downlink opportunities are less frequent. To reduce the image downlink, yet minimize the effect on the science return, a number of imaging and compression modes are utilized.

On-chip pixel binning of 2×2 and 4×4 are available within the FPU. To simplify the interface between the FPU and the DPU, the binned and non-binned images appear identical in size by padding invalid pixels in the binned images with dummy values. A valid pixel gate is passed to the DPU to indicate when a pixel should be saved from within the serial data stream. Once the data are transferred to the DPU, they can be streamed directly to the SSR, or compressed in hardware using a variety of 12-to-8 bit lookup tables, differencing of adjacent pixels, and/or the FAST algorithm. These data are then sent to the SSR over a high speed link. The spacecraft's main processor (MP) can read both the hardware-compressed images as well as the raw images from the SSR. The MP can then perform additional binning, extract image subframes, and use much more sophisticated compression algorithms to substantially reduce the total downlink.

References

- [1] S. C. Solomon et al. The MESSENGER mission to Mercury: Scientific objectives and implementation. *Planet. Space Sci.*, in press.
- [2] A. G. Santo et al. The MESSENGER mission to Mercury: Spacecraft and mission design. *Planet. Space Sci.*, in press.
- [3] S. E. Hawkins, III et al. Multi-Spectral Imager on the Near Earth Asteroid Rendezvous Mission. *Space Sci. Rev.*, 82(1-2):3-29, 1997.
- [4] F. Vilas. Surface composition of Mercury from reflectance spectrophotometry. In *MERCURY*, pages 59-76. University of Arizona Press, Tucson, 1988.

THEORETICAL ASPECTS OF MAGMA GENERATION, ASCENT AND ERUPTION ON MERCURY AND COMPARISON WITH COMPOSITION AND MORPHOLOGY OF SURFACE FEATURES.

James W. Head¹ and Lionel Wilson², ¹Department of Geological Sciences, Brown University, Providence RI 02912 USA, ²Department of Environmental Science, Lancaster University, Lancaster LA1 4YQ, UK.

Introduction: Despite exploration of Mercury by Mariner 10, some fundamental questions remain about the basic surface processes on the planet. Did Mercury, like the Moon [1], experience crustal intrusion and surface extrusion, resulting in the formation of volcanic deposits and landforms during its early thermal evolution? Did secondary crustal formation occupy a significant part of the resurfacing history of Mercury as it did for the Moon? How did the environmental parameters associated with Mercury modify and change the geologic record and eruptions styles there, relative to the Moon? And how can the better-known lunar record be used to address these issues?

Fundamental questions remain as to whether there are any unambiguous signs of volcanism visible on Mercury's surface. This debate stems from the initial analyses of Mariner 10 monochrome images (~1 km / pixel over about half the planet). Workers identified the existence of widespread plains deposits, occurring as relatively smooth surfaces between craters and as apparently ponded material, somewhat analogous to lunar mare units. It was proposed that at least some of these units were volcanic in origin [2-5]. Others argued that the plains deposits must be considered to be basin ejecta, similar to those found at the lunar Apollo 16 landing site [6, 7], raising the possibility that there are no identifiable volcanic units on Mercury (for a summary of the controversy see [8]).

Recalibrated Mariner 10 mosaics made by combining images taken through various filters and having significantly increased signal-to-noise ratio have been interpreted to indicate that indeed color units correspond to mapped plains units on Mercury, and further that some color units are the result of compositional heterogeneities in the mercurian crust [9, 10]. From these new data, color units can be identified that correspond with previously mapped smooth plains deposits. The dark blue material associated with the crater Homer exhibits diffuse boundaries consistent with fragmental material emplaced ballistically, and a pyroclastic origin is favored. A similar deposit is seen northwest of the crater Lermontov; examination of the iron-maturity parameter and opaque index images reveal that the darkest and bluest material in this deposit is not associated with an ejecta pattern. The relatively blue color, high opaque index, and low albedo of these materials (for both areas) is consistent with a more mafic material, possibly analogous to a basaltic or gabbroic composition. A tentative identification of basalt-like material in this hemisphere [11] was made with Earth-based thermal IR measurements, whereas later microwave measurements were interpreted to indicate a total lack of areally significant basaltic materials on Mercury [12]. From the data currently available it is not possible to make an unambiguous identification of basaltic material or indeed of any rock type; however the spectral parameters, stratigraphic relations and morphology of various units are consistent with volcanically emplaced materials. Regardless of the mode of emplacement,

the presence of the materials found around the craters Homer and Lermontov, and of the plains units identified above [9, 10], argues that significantly different compositional units occur within the mercurian crust and that at least some of them were emplaced during volcanic eruptions.

Key questions are: Did Mercury, like the Moon, form a primary crust which served as a barrier to, and filter for, magma ascent? Did secondary crustal formation (e.g., analogous to that of the lunar maria) occupy a significant part of the resurfacing history of Mercury? Did basaltic volcanism contribute to the resurfacing history of Mercury or did the formation of the iron core so alter the mantle geochemistry that other rock types dominate any eruptives? Does the tectonic history of Mercury (which exhibits significant global compressional deformation) mean that extrusive volcanism was inhibited or precluded by the state of stress in the lithosphere in its early to intermediate history? Will high resolution and global image data reveal presently lacking evidence for vents and landforms associated with extrusive volcanism? We address these questions through an assessment of the ascent and eruption of magma under mercurian conditions under a variety of settings.

Theoretical considerations: It is commonly assumed that the large iron/silicate ratio of Mercury is the result of its early modification by a giant impact [e.g., 13-15]. The extent of Mercury's differentiation prior to this event is moot as regards surface features and surface chemistry if most of the original crust and much of the original mantle were stripped away and lost into the Sun [13], and much of the remaining crust and mantle were left as a molten magma ocean [13-15]. However, the extent of any early differentiation and the details of the impact event are significant for the size of the iron core and for the bulk compositions of the residual unmelted mantle and the postulated overlying magma ocean. In particular, it is not automatically safe to assume that the mantle which is related to the present crust was very close to chondritic in composition.

Whatever the composition of the mantle after the giant impact, there is uncertainty about the extent to which solid state convection could have proceeded in that mantle [13, 16, 17]. The vigor of any convection that was occurring would have varied with time as a function of the ever-decreasing amounts of long-lived radioactive heat sources and the ever-increasing temperature difference across the mantle as a result of the cooling of the overlying magma ocean.

If convection in the mantle did take place, then partial melting should have occurred and buoyancy forces should have been able to extract melts; these would have been of basaltic composition if the mantle were chondritic but clearly other compositions are possible [12]. Bodies of buoyant melt would have risen, probably diapirically, until they encountered one or other of two kinds of trap [18]. The first option is a density trap, i.e. a level at which melts be-

ASCENT AND ERUPTION OF MAGMA: J. W. Head and L. Wilson

came neutrally buoyant on encountering less dense overlying rocks: the base of the crust is an obvious possibility for this. The second option is a rheological trap, i.e. a level at which the surrounding rocks are no longer able to deform in a plastic fashion fast enough to relax the stresses caused by the buoyancy forces.

Magma present in a rheological trap will still in general be buoyant and may be able to rise further by opening a brittle crack in the overlying rocks, i.e. by propagating a dike. However, any dike which forms will have a limited vertical extent [18] and will pinch off from the main magma body when its length reaches a critical value determined by the density contrast and the ambient stress distribution in the host rocks [19]. Multiple such dikes may form [18], but they will stall at shallower depths if they encounter density traps.

If the rheology of the rocks at all points around the periphery of a magma body stalled at a rheological trap can support stresses, an excess pressure may be created in the magma body by density changes consequent on chemical evolution [1]. Such evolution would be the consequence of fractional crystallization which could conceivably lead to supersaturation of any relatively insoluble volatile phase and gas bubble formation, and this could aid dikes in penetrating much further into the overlying rocks, thus overcoming density traps to some extent [1]. A magma body stalled at a density trap may also acquire an excess pressure due to chemical evolution, enabling it to migrate to shallower depths, if the rocks surrounding it are elastic.

The optimum mechanism for allowing mantle melts denser than the crust to penetrate to shallow depths as intrusions or to erupt at the surface is to have a rheological trap a short distance below a density trap [18]. It is then possible for dikes to grow both upward into the crust and downward into the mantle (which behaves elastically on the short timescales of dike propagation [18]) and to use the positive buoyancy of the melt in the mantle to offset the negative buoyancy in the crust [20].

How do these ideas relate to Mercury? If partial melting began in the mantle while a magma ocean produced by a giant impact was still liquid, any melts rising buoyantly through the mantle that were also less dense than the magma ocean would, of course have mingled with the ocean. Any such melts denser than the ocean would have ponded beneath it, with perhaps some small amount of mechanical mixing occurring at the boundary. Only after the ocean had solidified could mantle melts penetrate the resulting crust, and then only under the circumstances described above.

The complete range of possible density structures for Mercury after the solidification of any magma ocean, and of the consequent range of density contrasts between lithosphere and possible mantle melts, is not very different from those that apply to the Moon. As a result the possible outcomes range from no magmas reaching the surface, through magmas reaching the surface only in topographic lows but otherwise stalling as (possibly shallow) intrusions, to circumstances in which large volumes of magma reach the surface. The last option would be favored by the fortuitous proximity of rheological and density traps near the crust-mantle boundary and could be related to the widespread plains-forming units if these are in fact volcanic. Magmas formed by the chemical evolution of mantle melts in

rheological traps would be the best candidates for the pyroclastic deposits associated with the crater Homer. Ultimately these issues will only be clarified by better identification of the composition of surface units, currently rendered difficult both by the spatial and spectral resolution of available data and the complications due to space weathering of Mercury's surface [21]...

References: [1] J. Head and L. Wilson, *G&CA*, 56, 2155, 1992; [2] B. Murray et al., *Science*, 185, 169, 1975; [3] N. Trask and J. Guest, *JGR*, 80, 2462, 1975; [4] R. Strom et al., *JGR*, 80, 2478, 1975; [5] R. Strom, *PEPI*, 156, 1977, [6] D. Wilhelms, *Icarus*, 28, 551, 1976; [7] V. Oberbeck et al., *JGR*, 82, 1681, 1977; [8] P. Spudis and J. Guest, *Mercury*, U of A Press, 118, 1988; [9] M. Robinson et al., *JGR*, 97, 18265, 1992; [10] M. Robinson and P. Lucey, *Science*, 275, 197, 1997; [11] A. Sprague et al. *Icarus*, 109, 156, 1994; [12] R. Jeanloz et al., *Science*, 268, 1455, 1995; [13] W. Benz, W.L. Slattery and A.G.W. Cameron, *Icarus* 74, 516, 1988; [14] A.L. Tyler, R.H.W. Kozłowski and L.A. Lebofsky, *GRL*, 15, 808, 1988; [15] W.B. Tonks and H.J. Melosh, *Icarus* 109, 326, 1992; [16] R. Jeanloz and S. Morris, *Ann. Rev. Earth Plan. Sci.*, 14, 377, 1866; [17] T. Spohn, *Icarus*, 90, 222, 1991; [18] L. Wilson and J.W. Head, *LPS XXXII*, #1297, 2001; [19] J. Weertman, *JGR*, 76, 1171, 1971; [20] S. Solomon, *PLSC*, 6, 1021, 1975; [21] B. Hapke, *JGR*, 106, 10039, 2001.

ESTIMATION OF MERCURY'S OBLIQUITY AND PHYSICAL LIBRATIONS BY EARTH-BASED RADAR SPECKLE DISPLACEMENT INTERFEROMETRY. I.V.Holin, Institute of Radioengineering RAS, Fрязино, Moscow region, Russia, e-mail: holin@mail.cnt.ru

In accordance with "A Procedure for Determining the Nature of Mercury's Core" (S.J.Peale, R.J.Phillips, S. C.Solomon, D.E.Smith, M.T.Zuber, presented at this conference) four parameters should be known to find out internal constitution of Mercury including the size and state of its core. Two of them, the obliquity and the amplitude of physical librations, are not known even roughly. MESSENGER mission includes solving this problem. In addition we consider an approach based on the radar speckle displacement effect.

If we illuminate Mercury by a monochromatic radio wave then due to its rotational-progressive motion the spatial distribution (speckle pattern) of a reflected radar field will run in a "frozen" state on the surface of Earth at a velocity of 200...300 km/s. From measuring this speckle velocity vector it is possible to calculate tangential (with respect to the line of sight) components of the instantaneous spin-vector of Mercury's mantle.

A variety of Earth-based communication and radio facilities are suitable for this goal. For example, near the May 2002 inferior conjunction of Mercury NRAO VLBA antennae at Pie Town and Hancock as the receiving interferometer under Goldstone 3,5 cm illumination may give one-look relative accuracy for the instantaneous tangential spin vector near to one...three parts in 100000 while for the spin-radar Goldstone/Mauna Kea - Hancock it is by nearly another two times higher. This is well enough for obliquity. To measure librations one should repeat the experiment for 10...15 days (a few minutes a day for each baseline) near the same inferior conjunction. Further improvements in accuracy are obtainable through using several inferior conjunctions and additional VLBA and large antennae at Arecibo, Green Bank, Madrid.

NEUTRAL ATOM IMAGING NEAR MERCURY. M. Holmström, S. Barabash, *Swedish Institute of Space Physics (IRF), PO Box 812, SE-98128 Kiruna, Sweden, (matsh@irf.se)*, A. Lukyanov, *School of Mathematics and Information Science, Coventry University, Coventry, CV1 5FB, UK.*

The interaction between energetic ions and a planetary atmosphere produces energetic neutral atoms (ENA) when an ion charge-exchange with a neutral atom, e.g.,



Since momentum is conserved the neutral will have the same velocity as the ion. A property of ENAs is that they, in the absence of gravity, travel in straight lines since they, as neutrals, are unaffected by magnetic and electric fields. Thus, using an ENA imager it is possible to extract global information about the plasma and neutral populations that generated the ENAs. ENA imaging has successfully been applied for Earth's magnetosphere, the most recent example being NASA's IMAGE mission. The next planet to be imaged in ENAs will be Mars. There are two ENA imagers, as parts of the ASPERA-3 instrument, onboard ESA's Mars Express mission (launch 2003). Due to its global nature, ENA imaging is an attractive method of exploring the largely unknown Hermean exospheric and magnetospheric environment on future Mercury missions [1].

Given the phase space distribution of ions and neutrals, and the charge-exchange cross sections, one can compute ENA images. One purpose of such simulated images is to predict typical fluxes that can be expected, and thereby provide design constraints for instruments. Simulated images can also help in interpreting large scale features in observed images. For a more detailed, quantitative, analysis of observed images one can use inversion techniques to extract parameters from a mathematical model. For Mercury, this is a challenging problem for future research.

The key to successfully model the ENA production in the vicinity of Mercury is knowledge of the distribution of neutrals and ions. In this work we consider the problem of computing the ion distribution near Mercury and present simulation results. The magnetic and electric fields are assumed to be external. The magnetic field is a scaled version of the Tsyganenko model of Earth's magnetosphere. The electric field is the convected solar wind field. Then the Vlasov equation

$$\frac{\partial f}{\partial t} + \mathbf{a} \cdot \nabla_v f + \mathbf{v} \cdot \nabla_r f = P - Q,$$

governs the phase space distribution of ions and neutrals. The unknown distribution, or phase space density, function is $f = f(\mathbf{r}, \mathbf{v}, t)$, where \mathbf{r} is position, \mathbf{v} is velocity and t is time. Then $f \Delta \mathbf{r} \Delta \mathbf{v}$ is the number of particles in a small phase space volume element. The acceleration acting on the particles is $\mathbf{a} = \mathbf{a}(\mathbf{r}, \mathbf{v}, t)$. For gravity we have $\mathbf{a} = -GM/|\mathbf{r}|^3 \mathbf{r}$, where G is the gravitational constant and M is the mass of the attracting body. In the presence of electric, \mathbf{E} , and magnetic, \mathbf{B} , fields the Lorentz force gives $\mathbf{a} = q/m(\mathbf{E} + \mathbf{v} \times \mathbf{B})$, where q and m is the charge and mass of each particle, respectively. The gradients, ∇_v and ∇_r , are with respect to the three velocity components and position coordinates, respectively. Sources

and sinks are given by $P = P(\mathbf{r}, \mathbf{v}, t)$ and $Q = Q(\mathbf{r}, \mathbf{v}, t)$, e.g., $P \Delta \mathbf{r} \Delta \mathbf{v}$ is the number of particles produced in a small phase space volume element per time unit.

The Vlasov equation is simply mass conservation in the six-dimensional phase space. When solving the equations we must specify particle sources and sinks, e.g., photoionization and charge-exchange. We also must specify boundary conditions at the outer simulation boundary and at the planet surface. Simulations of the ion distribution, with a photoionization source, have been done for Mars [2], and with a magnetotail proton source for Mercury [3]. The dimensionality of the problem require careful selection of the method to solve the Vlasov equations, otherwise the computational time or memory requirement can be too large. A fast, and highly accurate, characteristic method of solving the Vlasov equations by integrating backwards in time along the phase space trajectories is used. If only point values of the distribution are needed (as when generating simulated ENA images) the memory requirement is minimal. When computing the global distribution, we use an adaptive, hierarchical, grid method to reduce memory requirements. We solve the Vlasov equations near Mercury for the ion distribution, with photoionization of neutrals as the ion source, and present the results of the simulations. Since the neutral and ion distributions are coupled by the source and sink terms and the surface boundary condition, a topic of future research is to solve for the two distributions simultaneously.

An interesting feature of Mercury is the presence of low energy (1-10 eV) neutral atoms (LENA) such as K and Ca, sputtered from the surface by precipitating magnetospheric ions. ENAs are usually considered to travel in straight lines. For LENAs we can not ignore the effect of gravity, due to their low velocity, and must take into account that they travel along ballistic trajectories. This complicates the task of deducing surface emissions from a LENA image. At these low velocities the detector velocity will also affect the images. We show computed trajectories and simulated images of LENAs sputtered from Mercury's surface. The results indicate that it is possible to infer the local emission rates from a LENA image. The fact that LENAs follow ballistic trajectories can even be advantageous, since we can detect atoms emitted from the far side of the planet.

References. [1] Barabash, S., A. Lukyanov, P. C:son Brandt, and R. Lundin, Energetic neutral atom imaging of Mercury's magnetosphere. 3. Simulated images and instrument requirements, *Planet. Space Sci.*, in press. [2] Barabash, S., A. Lukyanov, M. Holmström, and E. Kallio, Energetic neutral atoms at Mars: Imaging of the oxygen escape. Submitted to *J. Geophys. Res.* [3] Lukyanov, A., S. Barabash, R. Lundin, and P. C:son Brandt, Energetic neutral atom imaging of Mercury's magnetosphere. 2. Distribution of energetic charged particles in a compact magnetosphere, *Planet. Space Sci.*, in press.

DIURNAL VARIATION OF Na and K at Mercury. D. M. Hunten¹ and A.L. Sprague¹, ¹Lunar and Planetary Laboratory, The University of Arizona, Tucson, AZ 85721, dhunten@lpl.arizona.edu.

Introduction: We have published data showing a strong morning enhancement in the abundances of both Na and K [1]. Sprague [2, 3] has proposed an explanation, that these elements accumulate on the cold, dark night side and are released in the morning as the surface warms up. Killen and Morgan [4] however present a derivation, showing that such a mechanism cannot produce any enhancement greater than a factor of 3. We show that their derivation contains a subtle error; when this error is corrected, no such limit exists. Their data do not show an obvious morning enhancement. The disagreement in the data is harder to understand; we suggest some possible explanations but do not come to any definite conclusion.

The Derivation: The principal loss mechanism for Na is agreed to be photo-ionization followed by loss to the environment of the solar wind. Presumably some fraction of the ions are caught up in the magnetospheric tail and precipitated back to the surface where they are neutralized and either adsorbed on or implanted in the surface regolith. It is these atoms that Sprague [2] proposed to be released in the morning. In addition, there is a normal source which is assumed to be the same on AM and PM sectors. A simple continuity equation can be derived for this situation. The sunlit surface is divided into morning and evening quadrants, and we write the corresponding mean column abundances as a and p . If the lifetime for atom loss is τ and the fraction of emitted atoms recycled as ions to the night side is f , in steady state the continuity equation reads

$$-a/\tau + p/\tau + f(a + p)/\tau = 0.$$

The three terms represent the loss in the AM sector, the gain in this sector from the normal source process (using the fact that $a/\tau = p/\tau$), and the recycling with efficiency f . The solution is:

$$(a-p)/(a+p) = f,$$

$$\text{or } a/p = ((1+f)/(1-f)).$$

As f approaches unity, a/p approaches infinity, which is reasonable, because all atoms originating in the AM sector re-appear there and it does not matter what is in the PM sector.

Why then do Killen and Morgan [4] find that the upper limit to the ratio is 3? In their formulation of the continuity equation the third term has the average of

the AM and PM sectors $(a + p)/2$ instead of the total $(a + p)$, and their result is:

$$a/p = ((2+f)/(2-f)).$$

Now the value of a/p is 3 when $f = 1$.

That a large diurnal variation by this mechanism is possible does not prove that it is relevant, but there can hardly be any doubt that it must operate at least to some extent.

The Observations: Sprague et al. [1] present the results of a 4-year observing program for Na abundances, and summarize the more limited results for K published by Sprague [2, 3]. For both elements, a strong diurnal variation is found, with maximum in the morning. It is perplexing that the data sets of Potter and Morgan [5], Killen et al. [6] and Potter et al. [7] have not also exhibited this general character of morning side high and late afternoon low Na and K column abundances. One possibility is differences in observing geometry and technique. The Sprague et al. observations were typically near maximum elongation, with the planet in the vicinity of half illumination, so that results for early mornings and late afternoons on Mercury were obtained at different times. Most of the results quoted by Killen and Morgan as showing no diurnal effect were obtained with a solar telescope and may show the AM and PM sectors simultaneously. If a morning enhancement is largely confined to a narrow strip just after dawn, it could be easier to detect when observed from above the terminator than from above the subsolar region, and at times could be completely out of sight.

The speculations summarized above make it clear that no really satisfactory explanation yet exists. Differences in observing style and size of data sets may contribute. For example the K observations discussed in Sprague [3] and the Na observations discussed in Sprague et al [2] were obtained with a long slit which was placed specifically on morning and afternoon locations. When an E/W slit was used the data along the slit were divided into local time bins on Mercury. Potter, Morgan and Killen, who do imaging with an image slicer as well as slit spectroscopy, sometimes do not reduce their images to column abundance based on morning and afternoon, but rather focus attention on Na and K emission brightness which appears patchy and appears in different locations from observing period to observing period [8, 9]. Earlier slit measure-

ments were taken to study the effects of radiation pressure and possible line broadening [10].

Another factor that may be important is correction of data for "seeing smear". The data of Sprague et. al. [1] were all corrected for smear by modeling a trace across the continuum of each individual spectral image. The early published slit spectra of Potter and Morgan [8, 10], and the few images that were published prior to 1997, were not corrected for seeing. However, a set of six Na images obtained in 1997 that were corrected for seeing smear and show the morning side, noon, and early afternoon portions of the planet do not show the maximum column abundance in the morning sector [7]. Thus, there must be more than one physical phenomenon controlling the distribution and maximum Na column. Not enough K data are available to reach a similar conclusion.

Conclusion: The Sprague recycling mechanism can in principle explain a very large morning enhancement of the Na and K abundances. Such enhancements are prominent in the observational data of Sprague and collaborators, but not in those of Potter and collaborators. Although many of the latter data sets may not be suitable for detection of the effect, the discrepancy is still very puzzling.

References: [1] Sprague, A.L. et al. (1997) *Icarus*, 129, 506 – 527. [2] Sprague, A.L. (1992) *JGR*, 97, 18,257 – 18,264. [3] Sprague, A.L. (1992) *JGR*, 98, 1231. [4] Killen, R.M. and Morgan, T.H. (1993) *JGR*, 98, 23,589 – 23,601. [5] Potter, A.E. and Morgan, T.H. (1987) *Icarus*, 71, 472 – 477. [6] Killen, R.M. et al. (1990) *Icarus*, 85, 145 – 167. [7] Potter, A.E., Killen, R.M. and Morgan, T.H. (1999) *Planet. Space Sci.*, 47, 1441 – 1448. [8] [Potter and Morgan (1990), *Science*, 248, 845 – 838. [9] Potter and Morgan, T.H. (1997) *Planet. Space Sci.*, 45, 95 – 100. [10] Potter, A.E. and Morgan, T.H. (1987) *Icarus*, 71, 472 – 477.

ON THE MODELING OF THE MERCURY-SOLAR WIND INTERACTION BY A QUASINEUTRAL HYBRID MODEL. Esa Kallio, and Pekka Janhunen, *Finnish Meteorological Institute, Geophysical Research, FIN-00101 Helsinki, Finland, (Esa.Kallio@fmi.fi, Pekka.Janhunen@fmi.fi).*

The Hermean magnetosphere is anticipated to have certain unique features compared with other planetary magnetospheres. The planet's intrinsic magnetic field is strong enough to form a magnetosphere around the planet. However, it is not clear how the processes in the Hermean magnetosphere resemble the processes that take place in the other magnetospheres. Especially the questions: How effectively the magnetosphere can shield the planet against the solar wind particles, how effectively the magnetosphere can store energy in the magnetotail, and how the interaction between the magnetosphere and the planet's surface, which can take place because of the very tenuous atmosphere, are unknown. Modeling of the solar wind-Mercury interaction is therefore a challenging problem because a physically realistic model should include processes between three highly different components: the solar wind, the magnetosphere, and the planetary surface.

We have developed a 3-D quasi-neutral hybrid model to study the Hermean magnetosphere. The recently developed self-consistent hybrid model, which has been used earlier to study the Mars-solar wind interaction [Kallio and Janhunen, *JGR*, 5617-5634, 2001], includes ions which are moved by the Lorentz force, while electrons are a massless charge neutralizing fluid. The model

includes solar wind protons and planetary ions, say, Na^+ , or K^+ ions. Planetary ions are produced from two sources, by photoionization from a neutral corona, and by ion sputtering from the surface. A fully 3-D neutral corona density model, and fully 2-D (latitude and longitude dependence on the surface) ion emission model from the surface can be used.

The hybrid simulation approach makes it possible to study several plasma physical processes in the vicinity of the planet that are difficult or impossible to model by other self-consistent approaches, such as effects associated with ion finite gyroradius, the velocity difference between different ion species, the large loss cone, or the non-maxwellian velocity distribution function. Especially, the model can be used to study magnetosphere-planetary surface interaction because ions can precipitate to the surface.

Our work has two primary goals. First, the global hybrid model will be used to study basic global plasma physical processes in the vicinity of Mercury. Second, it will provide a tool that will be used to optimize the performance of an ENA instrument planned for Bepi-Colombo mission, and in the future for interpreting the measurements. ENA instrument will measure Energetic Neutral Atoms, ENAs. In the presentation we will show some preliminary results of our hybrid model runs.

IN SEARCH OF LUNAR LIKE RILLES ON MERCURY. A. Kereszturi (Department of Physical Geography, Eötvös Loránd University, H-1083 Budapest, Ludovika tér 2., Hungary (E-mail: irodaweb@irodaweb.hu))

Introduction: Lunar rilles or rimae can be divided into two classes: 1. near straight tectonic structures and 2. sinuous lunar rilles which are traces of ancient lava flows on the Moon's surface [1]. They were carved by thermal erosion of lava flows and/or subsequent collapse of lava tubes on the mare basalt terrains of the Moon [2,3]. Because of the several connection between the surface and planetary evolution of the Moon and Mercury there is reason that on Mercury we can find rilles too. However only some rill like structures are published in the scientific literature [4]. It is interesting to search of rilles on Mercury because if we find some, comparing them with the Moon's we can estimate some characteristics of the lava flows.

Working method: 397 processed images [5] was surveyed with visual method looking for possible rilles. The images were made by the Mariner-10 during its first encounter with 0,2-2 km resolution. The visual searching is somewhat subjective but up to date no better method is known. In the cases of possible rilles the picture code number was the reference code. In this work only their identification was the purpose, morphological comparison and morphometrical measurement – just like the survey of the second encounter's images - will be realized in the future.

We classified one structure as a possible rill if it satisfies the following criterions: 1. Both of the sun illuminated and shadowed side is visible. 2. Based on the illumination it is a negative relief structure. 3. It does not has exact straight alignment. 4. It does not cut across terrains with highly undulating relief. (One can expect lava flows only to lower terrains and not upstream. Of course it is difficult to estimate the exact surface topography.) 5. It does not align with obvious tectonic structures (estimated by the surrounding tectonic pattern.). 6. The structure does not appear to be connected craters.

General tendencies: In spite the upper mentioned there were many problematic cases in the identification. Great problems were the crater chains [6], and chain like structures which are very frequent on Mercury. There were many connected depressions on the images. Based on the appearance we can divide the rill like but possible other kind of features into: 1. crater chains (sometimes consisting only two-three visible craters with linear structures connecting them), 2. pos-

sible tectonic originated nearly straight fault like structures and low relief fold like structures. (The Caloris-basin has many rill like structures. They are not included here, and will be part of a future work.) Because of the disturbing effect of the surrounding terrain, the rill-like structures were more easy to find on nearly plain terrains. During the survey we met with many interesting features, like domes, crater chains some mass movements etc. The great number of connected craters with somewhat sinuous and flow-like structures may suggest a possible process related to the impact melts which may keep its fluid state somewhat after the impact in the hot mercurian surface circumstances. This possible process will be discussed in a future work.

Results: During the survey 70-90 possible rilles and another 50-100 very uncertain cases were found. (Fig. 1.: some examples are in the five row with white arrows at one or both end of the rilles. The two bottom image shows two lunar rilles for comparison (M/1: part of Schröter's Valley, M/2: a rill between the craters Delisle and Diophantus) with same scale.) Most of the rills were around the limit of resolution so width were generally max. 1-2 km. The possible rill's characteristics: 1. Greater part of them were on smooth plains and on smooth crater infill plains. 2. It is difficult to follow them farther than 10-20 times of their width's. 3. Many rills are connected to crater like or elongated pits, some connected to several pits. 4. There are areas where the rill density is 2-3 times higher than the average. In spite of their relative great number many of them can't be taken for certain that it is a sinuous lava channel. Based on these results the rills on Mercury will be good subject to analyze the volcanic activity and behaviour of lavas.

References: [1] Masursky H., Colton G. W. El-Baz F., (1978) Apollo over the Moon, NASA SP-362. [2] Cameron W. S. (1964). JGR 69/2423-2430 [3] Carr M. H. (1974). The role of lava erosion in the formation of lunar rilles and martian channels. Icarus 22/1-23. [4] Martha An Leake The intercrater plains of Mercury and the Moon, Advances in Planetary Geology, NASA TM-84894. [5] Planetary Data System, United States Geological Survey. [6] Schevchenko V. V., Skobeleva T. P. (2001) LPSC32th #1510.

IN SEARCH OF LUNAR LIKE RILLES ON MERCURY. A. Kereszturi

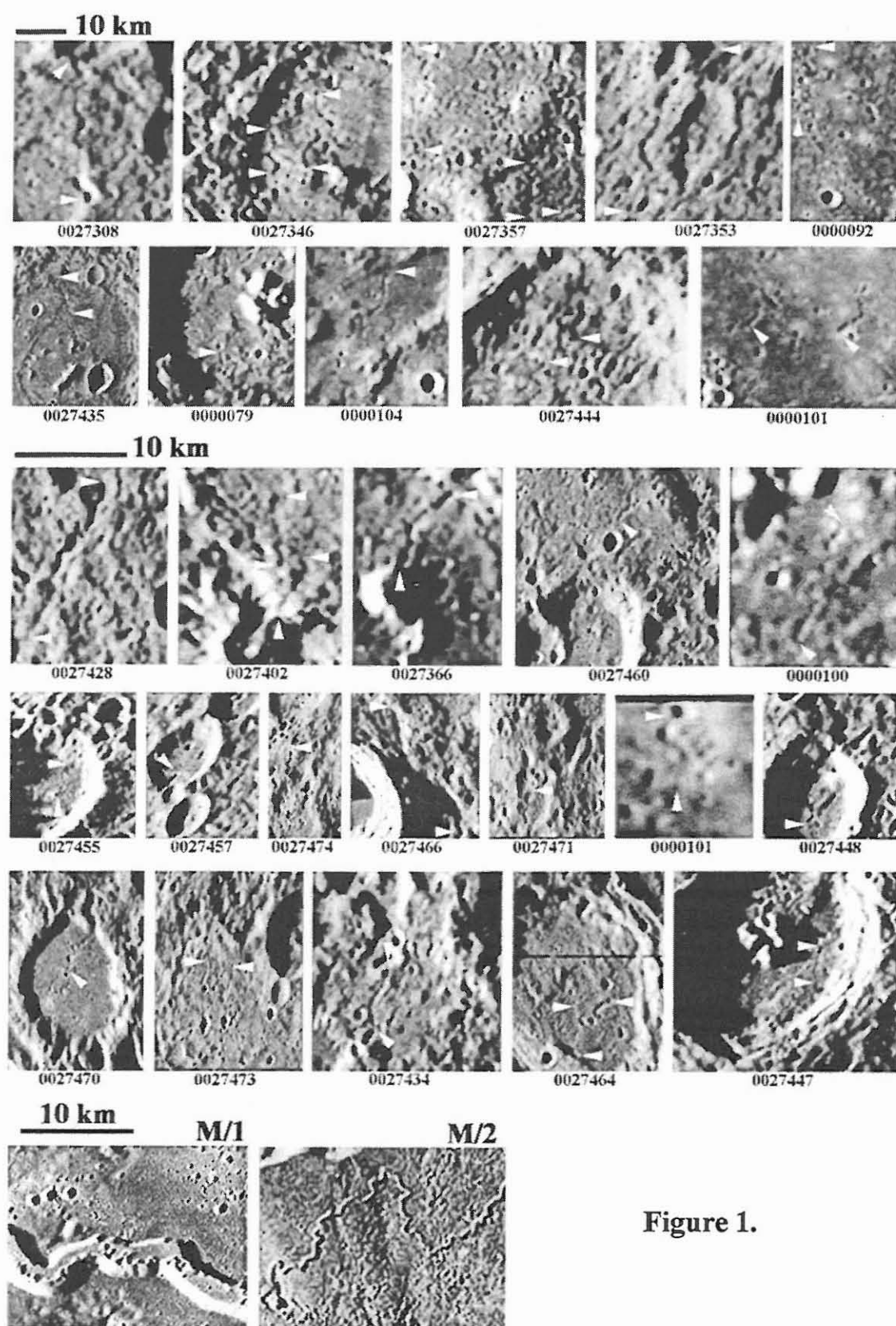


Figure 1.

AR ATMOSPHERE: IMPLICATIONS FOR STRUCTURE AND COMPOSITION OF MERCURY'S CRUST. R. M. Killen¹ and T. H. Morgan², ¹SwRI(6220 Culebra Rd., San Antonio, TX 78228), ²NASA Hq (300 E St. SW, Washington, D. C.)

We examine the possibilities of sustaining an argon atmosphere by diffusion from the upper 10 km of crust, and alternatively by effusion from a molten or previously molten area at great depth. ⁴⁰Ar in the atmospheres of the planets is a measure of potassium abundance in the interiors since ⁴⁰Ar is a product of radiogenic decay of ⁴⁰K by electron capture with the subsequent emission of a 1.46 eV γ -ray. Although the ⁴⁰Ar in the earth's atmosphere is expected to have accumulated since the late bombardment, ⁴⁰Ar in surface-bounded exospheres is eroded quickly by photoionization and electron impact ionization. Thus, the argon content in the exospheres of the Moon, Mercury and probably Europa is representative of current effusion rather than accumulation over the lifetime of the body. Argon content will be a function of K content, temperature, grain size distribution, connected pore volume and possible seismic activity.

Although Mercury and the Moon differ in many details, we can train the solutions to diffusion equations to predict the average lunar atmosphere. Then these parameters can be varied for Hermean conditions. Assuming a lunar crustal potassium abundance of 300 ppm, the observed argon atmosphere requires equilibrium between the argon production in the upper 9 Km of the moon ($1.135 \times 10^{-3} \text{ cm}^{-3} \text{ s}^{-1}$) and its loss. Hodges *et al.* [1], [2] conclude that this loss rate and the observed time variability requires argon release through seismic activity, tapping a deep argon source. An important observation is that the extreme surface of the Moon is enhanced in argon rather than depleted, as one would expect from outgassing of radiogenic argon. Manka and Michel concluded that ion implantation explains the surface enhancement of ⁴⁰Ar. About half of the argon ions produced in the lunar atmosphere would return to the surface, where they would become embedded in the rocks [3], [4]. Similarly, at Mercury we expect the surface rocks to be enhanced in ⁴⁰Ar wherever the magnetosphere has been open over time. Thus the measurement of surface composition will reveal the long-term effects of solar wind-magnetosphere interaction.

We first solve the diffusion equations for radiogenic argon and train the solutions for the lunar atmosphere. Then we use these solutions with the appropriate boundary conditions for Mercury. In order to deter-

mine the porosity required to produce a given atmosphere by diffusion, we used the equations for diffusion of argon through spheres of radius, a , with diffusion coefficient, D , for a time, t . We assumed a fractal distribution of grain sizes, varying the distribution with depth to 10 km, where the connected pore space is assumed to cease. The grain size in lunar rocks has a fractal dimension of about 1.2, where

$$n(l) = A(l/l_0)^{-n}.$$

The mean grain size at the lunar surface varies from about 139 μm to 72 μm , but the median grain size can range from 48 μm to 800 μm depending on the sample (Heiken *et al.*, 1991). The value of A was derived to be 0.25, and n is 1.2 for the cumulative distribution. Partly for computational ease, we assume that the grains are distributed with a fractal dimension 2.5 for the differential number per radius range. This is within the range of measured fractal dimensions for lunar soil samples. The distribution of sizes is assumed to be such that

$$dn/dr = (r/r_0)^{-2.5}.$$

Once the argon has diffused out of the crystalline rock and into a pore space, the effusion to the surface is by Knudsen flow. This process is so much faster than diffusion that it can be considered instantaneous by comparison. We investigate the implications of a range of diffusion coefficients, grain size distributions and connected pore volume with depth.

We assume that loss of argon from the atmosphere is by photoionization and electron impact ionization. That fraction of argon in the atmosphere which is derived from the solar wind can be estimated by measuring ²⁰Ne.

References: [1] Hodges, R.R., J.H. Hoffman, F.S. Johnson and D.E. Evans, (1973) *Lunar Science Conf IV., Geochimica Cosmochimica Acta* 3 Suppl. 4, 2855 - 2864. [2] Hodges, R.R., Jr., and J.H. Hoffman (1974) *Lunar Sci. Conf. V, In Geochim. Cosmochimica Acta* 3, 2955 - 2961. [3] Manka, R.H. and F.C. Michel (1971) *Lunar Science Conf. II, Geochimica Cosmochim Acta Suppl. 2*, 1717 - 1728. [4] Manka, R.H. and F.C. Michel (1973) *In Photon and Particle Interactions with Surfaces in Space* (R. J. L. Gard, Ed.), 429-442, D. Reidel, Dordrecht.

MEASURING THE PLASMA ENVIRONMENT AT MERCURY: THE FAST IMAGING PLASMA SPECTROMETER. P. L. Koehn^{1, 2}, T. H. Zurbuchen², L. A. Fisk², and G. Gloeckler³ ¹koehn@umich.edu, ²University of Michigan, Atmospheric, Oceanic and Space Sciences Department, Ann Arbor, MI 48109-2143, ³University of Maryland, Physics Department, Space Research Group, College Park MD, 20742

Abstract: The plasma environment at Mercury is a rich laboratory for studying the interaction of the solar wind with a planetary magnetosphere. Three primary populations of ions exist at Mercury: solar wind, magnetospheric and pickup ions. An instrument to measure the composition of these ion populations and their three dimensional velocity distribution functions must be lightweight, fast, and have a very large field of view. Composition instruments, however, are traditionally bulky and massive. This provides an opportunity for miniaturization to reduce costs in both mass and power.



Figure 1 - The FIPS entrance system is compact and lightweight, comparable to a soft drink can in size

The Fast Imaging Plasma Spectrometer (FIPS) [1] is an imaging mass spectrometer proposed for, accepted by, and expected to be launched aboard NASA's MESSENGER spacecraft, a Mercury orbiter. This versatile instrument has a very small footprint, requires 2W of power, and has a mass a full order of magnitude less than current, similarly performing systems. It maintains a nearly full-hemisphere field of view,

equally suitable for either spinning or three-axis-stabilized platforms. Its unique cylindrical mirror entrance system and position-sensing time-of-flight telescope allows the rapid imaging of phase-space and identification of particle species. For magnetospheric and planetary missions, where events happen on time-scales of minutes or even seconds, this is especially valuable.

FIPS Performance Summary

Energy Acceptance	0-20 kV/Q
Energy Resolution	3.8%
Angular Acceptance	$\sim 2\pi$ sr
Angular Resolution	10° lat. And long.
M/Q Resolution	4%
Geometric Factor	0.017 cm ² sr
Geometric Factor (pixel)	7.8×10^{-5} cm ² sr/pixel
Voltage Scan Period	~ 1 minute, 2s burst mode
Mass	1.4 kg
Power	2W
Footprint	140 cm ²

This instrument has been extensively simulated with the ray-tracing software package SimIon [2]. A prototype of the entrance system has been constructed at the University of Michigan's Space Physics Research Laboratory, and fully tested at the Goddard Space Flight Center Beam Facility. We will present and compare the results of simulation and testing of the FIPS prototype. It will show that the FIPS instrument is an ideal solution for measuring the plasma environment at Mercury.

References:

- [1] Zurbuchen, T. H., Gloeckler, G., et al., (1998), *SPIE Conference Proceedings, Missions to the Sun II*, International Society for Optical Engineering, 217-224.
- [2] Dahl, D., (2000) Idaho National Engineering Labs.

RESOLVED GROUND BASED OBSERVATION OF MERCURY. L.V.Ksanfomality *Space Research Institute, Moscow.* ksanf@iki.rssi.ru

The results of investigations of astronomical climate in several observatories have shown that the amplitudes of scintillation (flicker) decrease for stars with higher frequency spectra (Ksanfomality and Shakhovskoy, 1967). This means that a short exposure may substantially improve the image resolution of planetary astronomical objects. The use of a high sensitivity CCD detector permits the exposure to be radically diminished. This improves the sharpness of the image, however it does not improve picture distortion. Nevertheless it is possible to find a low distortion picture amid many obtained in observations. 15 short exposure (10 ms) images of the planet Mercury were obtained in December 1999, with a zenith angle of 83-78°, at the Abastumany astrophysical observatory (Republic of Georgia), placed at an altitude 1700 m a.s.l. Only one image (wavelength 533 nm, $\Delta\lambda = 24$ nm) is of low distortion. The telescope was an AZT-11 ($D = 1.25$ m, $F = 16$ m). Mercury was at a geocentric distance of 1.007 a.u., a heliocentric distance of 0.39 a.u. and had a phase of 76°. The coordinates of the subterrestrial point at 03:30 UT, 3.12.1999 were 108°W, 2°26'S. The CCD pixel size was 12 by 14 mcm. The photometric readings were about 1000 counts per pixel.

All images are additionally distorted by refraction in their eastern parts. Despite the fact that the observations were made far from the zenith, about 80°, photometrical sections along the subterrestrial meridian show some details seen in the curve (Fig.1).

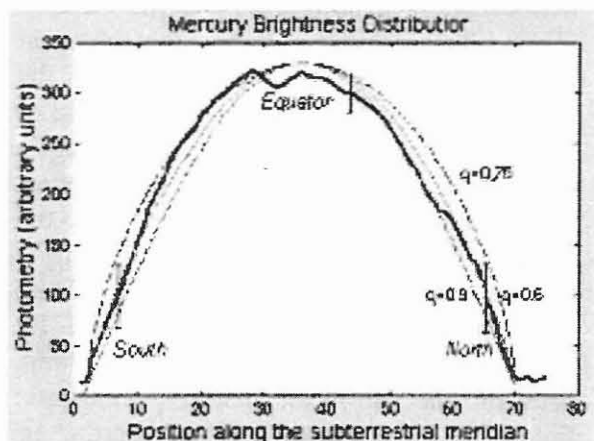


Fig.1. Comparison of the Mercury photometry along the subterrestrial meridian and a $(\cos \phi)^9$ model for the 76° phase.

The suggestion was made that the details seen in the image reveal large blocks of Hermean surface, normally not seen in ground based images of Mercury (Vilas *et al.*, 1988). Occasionally the phase of the planet and the subterrestrial point position were almost the same as when MARINER 10 encountered Mercury in 1974. This

coincidence permits a comparison of the images obtained with the MARINER 10 data, proving the reality of the

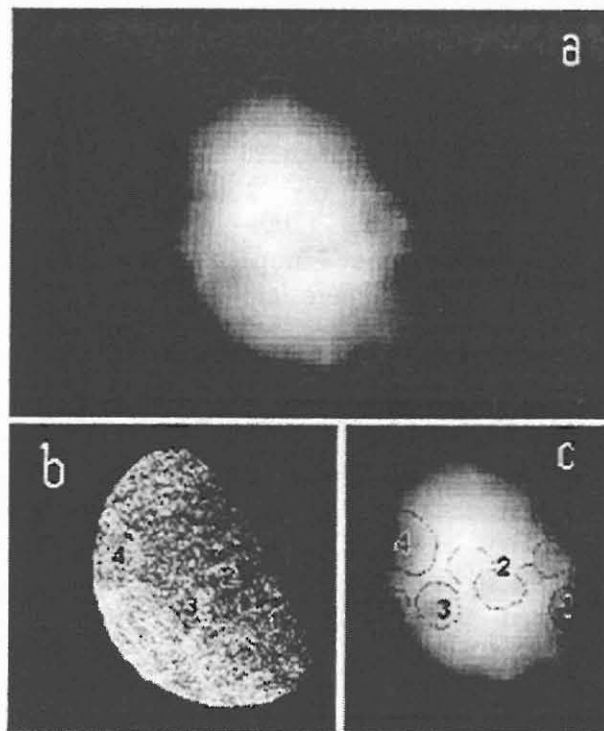


Fig.2. Positions of large details on Mercury's disk (a) in comparison with a MARINER 10 image of the planet (b) and a scheme of large blocks (c).

details. The large dark area 1 was identified with crater Beethoven (20°S, 124°W, center). The three dark spots 2 in the disk center and 120-140°W are also seen in section (b), as is spot 3. Spot 4 was tentatively identified with the Caloris Planitia (30°S, 177°W, center) partly seen in section (b).

Conclusion. Using very short exposures for Mercury ground based observations allows resolved images of the planet to be obtained that are not available using any other ground based techniques. The image resolution is up to 0.4 arc sec instead of 1 to 1.5 arc sec for a moderate sized telescope. The method has much in common with speckle interferometry.

References

- Vilas F., Chapman C.R., Matthews M.S.,
Eds. Mercury. Tucson: Univ.
Arizona Press, 1988. 794 p.
- Ksanfomality L.V., Shakhovskoy A.M. Infralow
Frequency Spectra of Scintillation //
Proceedings of the Crimean Astrophys.
Observ., 1967. V.38. P.264-286.

PROPERTIES OF THE HERMEAN SURFACE. L. Ksanfomality ⁽¹⁾, A. Sprague ⁽²⁾, C. Cremonese ⁽³⁾, L. Jorda ⁽⁴⁾, N. Thomas ⁽⁴⁾, J. Warell ⁽⁵⁾, ⁽¹⁾ Space Research Institute, Moscow, Russia, ksanf@rssi.ru; ⁽²⁾ Lunar and Planetary Laboratory, Arizona State University, USA; ⁽³⁾ Padova Astronomical Observatory, Italy; ⁽⁴⁾ Max Planck Institute fuer Aeronomie, Lindau, Germany; ⁽⁵⁾ Uppsala Astronomical Observatory, Sweden.

There are two Mercury missions projects intended for nearest years, NASA's 'Messenger' (2004) and ESA's 'BepiColombo' (2009). The Mercury Orbiter is the European Space Agency cornerstone. There are many aspects of Mercury which require further study such as the origin and composition of the regolith, processes of surface cratering, the origin of the planet, its internal structure, its magnetosphere, its very rarefied atmosphere (exosphere), its orbital and rotational dynamics, and its thermal history. Despite the signs found for presence of rock-types that widely distributed on the Moon (feldspathoids, anorthosites), the huge differences in the mean density and crust/mantle thickness of the two bodies point to peculiarities of Mercury's surface. There is a good evidence of past volcanic flows. The mid-infrared spectroscopy found indications of heterogeneous crustal composition that is FeO-poor -- <3% and possibly feldspar-rich, with the possibility of low iron pyroxenes and alkali basalts. The only spectral near-infrared feature indicated at some longitudes (Vilas 1988) is a possible pyroxene absorption feature at 0.95 micron, which may be used to investigate the abundance distribution of FeO in the regolith (e.g., Lucey et al. 1995). Mercury reveals as a geologically interesting planet. It has abundant Na and K in a thin atmosphere which appears to have Mercury's surface materials as its source. The physical properties of a regolith, its structure, grain sizes, refraction coefficient and even sizes of boulders may be estimated by methods of spectrozonal photometry (Ksanfomality and Moroz,

1996) and polarimetry (Dollfus and Auriere, 1971). It is possible that there are deposits of buried water ice and/or elemental sulfur. The results of the study of the structure, physical properties and composition of Mercury's regolith, may be used to detect principal features on the origin of Mercury. Thermal infrared spectra have features, too, indicating the possible presence of feldspars, pyroxenes and igneous nepheline-bearing alkali syenite. The wavelength of the thermal emissivity maxima indicate intermediate or slightly mafic rock types as well as considerable heterogeneity in composition (Sprague et al. 1997). The Fe absorption is used as a proxy for FeO, the abundance of which in the Hermean crust and mantle can be used to infer whether or not the planet accreted material from just a narrow feeding zone near its current heliocentric distance (Lewis, 1988; Wasson, 1988). To a lesser extent, the physical properties of crustal layers may be associated with the strange magnetic field of the planet. The existence of Mercury's dipole magnetic field may be the greatest challenge for the basic principles of the theory. There is the hypothesis on Mercury's magnetic field appearing in light of the Mars remnant fields that have been found by MGS. The hypothesis states that the same data on the Hermean resulting magnetic field may be produced, at least partly, by separate magnetized blocks of crust with a random orientation of the field.

ELECTRIC FIELD DOUBLE PROBE ANTENNA FOR THE BEPICOLOMBO/MMO SATELLITE.

H. Laakso, R. Grard, B. Johlander, D. Klinge, and J.-P. Lebreton, ESA Space Science Department, Code SCI-SO, Postbus 299, 2000 AG Noordwijk, The Netherlands (e-mail: Harri.Laakso@esa.int).

Introduction: The Space Science Department of the European Space Agency has been developing double probe antennas for 30 years. The first antennas were successfully operated on the GEOS-1, -2 and ISEE-1 satellites in 1977-1982. The proved concept was also used for the NASA Polar satellite, launched in 1996. However, it was quickly found on Polar that this type of antenna can be unstable in certain occasions. Based upon detailed studies, a new design was approved for the four Cluster satellites, launched in summer 2000. Now after one year of measurements, we know that the new sensor design is providing us with electric field observations of unprecedented quality. Therefore we are proposing to use the same proven technique on the BepiColombo/MMO satellite.

Instrumentation: Electric field measurements are made with a double probe antenna that consists of a pair of electric probes that are placed on the tips of two opposing booms. On a spinning satellite the booms are made of a thin wire and can be quite long, of several tens of meters, in order to have the sensors in a low-noise environment. In addition, the high-quality quasi-static electric field measurements require that the pre-amplifiers are located close to the sensors, outside the main electronics compartment placed inside the satellite. This will be a challenge for a Mercury mission as the environment is very hot. Based upon an initial thermal analysis, however, we have been able to design a pre-amplifier box that can provide a pleasant environment for the instrument electronics.

Scientific Objectives: The main variables monitored with a double probe antenna are the two-dimensional electric fields in the spin plane and the spacecraft potential where the latter is proportional to the electron density. These measurements are of fundamental importance when the structure and dynamics of the Mercury plasma environment is studied. With such observations, one can investigate the problems related to acceleration of charged particles, plasma drifts and flows, plasma waves, and variations of the plasma density. These are important issues as we will attempt to understand the Mercury plasma environment and how it respond to the solar wind variations.

AN ARTIFICIAL SEISMIC IMPACT EXPERIMENT ON BEPI COLOMBO. P. Lognonné¹, D. Giardini², Y. Langevin³, and H. Mizutani⁴, ¹Institut de Physique du Globe de Paris (IPGP), 4 Avenue de Neptune, 94107 Saint Maur des Fosses Cedex, France (lognonne@ipgp.jussieu.fr), ²Eidgenössische Technische Hochschule (ETH), Zurich, Switzerland, ³IAS Orsay, France, ⁴ISAS, Japan.

The Bepi Colombo mission plans to deploy in 2012 a lander on Mercury. A seismometer is considered in the model payload. We propose to use the Solar Electrical Propulsion Module on each of the two spacecrafts to produce active seismic sources, in order to constrain the thickness of the crust and possibly the thickness of the mantle. Assuming the impact position and time to be known by radio-tracking, the two events are needed to achieve a unique determination of both these thickness and mean shear and bulk velocities.

We propose different scenarios, where the lander is able to land up to four days in advance of the impacts, with cost in ΔV of a few tens m/s. Only a light beacon is needed on the SEP module to achieve these scenarios, with no change in the present design of the spacecrafts. We compare the expected signals with those recorded during the Apollo missions by the impacts of the LEM, taking into account the improvements of sensors in terms of sensitivity and bandwidth. We conclude with the expected results and error bars in the determination of the inner structure of the planet, from crust to core. A comparison with other geophysical methods is then done.

SPECIFIC CHARACTER OF THE FORMATION OF MERCURY AS THE DENSEST PLANET. A. A. Marakushev, O. V. Chaplygin and A. V. Bobrov, Institute of Experimental Mineralogy (IEM RAS, 142432 Chernogolovka, Moscow Region, Russia; e-mail: o.chaplygin@lycos.com).

Earth-type planets were initially formed as giant planets, similarly to the planets of the group of Jupiter and simultaneously with the solar mass by the accumulation of aqueous-hydrogen planetesimals, which were similar by physical state to Pluto, Charon, and comets. Gravitational compression was accompanied by melting of the planets whose size increases with the approach to the Sun, with which they also similar in composition.

Development of hydrogen-water-silicate liquid immiscibility in planets was accompanied by their layering to heavy cores and gigantic fluid envelopes. The impulses of high-spin motion of these envelopes resulted in separation of satellites under the action of centrifugal forces. Satellite density varies widely, growing with the approach to dense iron-silicate cores of their parental giant planets. The maximum density of satellites of the peripheral, remote from the Sun planets (Neptune, Uranus, Saturn) does not exceed 1.9 g/cm^3 , but for near-solar giant planets it reaches 3.5 g/cm^3 (Io, the satellite of Jupiter) and 3.3 g/cm^3 (Moon, the satellite of proto-Earth).

In contrast to peripheral near-solar giant planets underwent surface degassing under the action of solar wind. Jupiter in this case lost the part of hydrogen of its fluid envelope, which can be judged from its anomalously high density (1.3 g/cm^3), almost two times higher than that of Saturn (0.7 g/cm^3). The giant planets located nearer to the Sun, completely lost fluid envelopes being transformed into terrestrial planets. They lost satellite systems because of decrease of gravity. Only relicts of their satellites (Moon, Phobos and Deimos) remained. Several dozens of analogues of near-solar giant planets (figure) was revealed in the last years (1995–2001) in the surroundings of the stars, similar to the Sun [1, 2, 3, etc.]. The degree of surface degassing of these planets is traced by the effect of the decrease of their massiveness with the approach to the stars [2].

Terrestrial planets initially were formed as iron-silicate cores of parental giant protoplanets simultaneously with the separation of lighter silicate material into their satellite systems. Cores were formed in the protoplanets in the sequence of the development of chondrite systems, starting with the iron meteorites (I) of the corresponding genetic groups: I (type Netschaev) – HH – H – L – LL. This development was determined by the increase of $\text{H}_2\text{O}/\text{H}_2$ ratio in the fluid envelopes of the protoplanets, which were undergoing degassing under the action of the solar

wind. The development ceased at the different stages upon the complete degassing of planets in the sequence of moving away from the Sun. Proto-Mercury was the first giant planet, which lost its fluid envelope. Therefore Mercury has the most primitive composition, extremely rich in iron (I-HH). Furthermore the content in earth-type planets of nickel-iron phase is found in dependence on the degree of the development of their satellite systems. It increases with the approach to the Sun in the row: Neptune – Uranus – Saturn – Jupiter. The propagation of this regularity to the giant protoplanets of terrestrial group explains well the unique nature of Mercury, whose silicate phase to a considerable extent went away into the satellite system of its parental protoplanet, which the latter then lost.

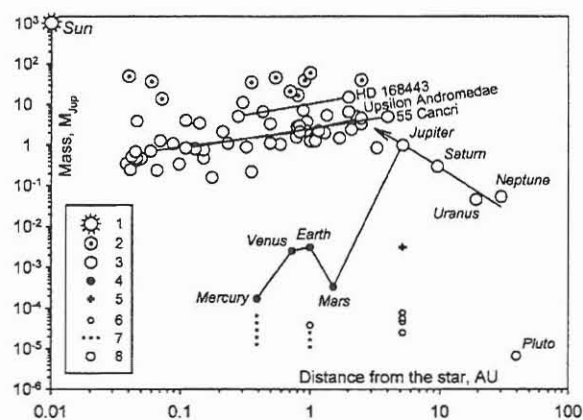


Figure. Planets of the Solar system and their satellites in comparison to the extrasolar planets. 1 – the Sun and analogous stars; 2 – brown dwarfs; 3 – fluid giant planets; 4 – terrestrial planets; 5 – molten iron-silicate core of Jupiter; 6 – the Jovian galilean satellites and the Moon; 7 – supposed lost satellites of proto-Earth and proto-Mercury; 8 – Pluto. M_{Jup} – mass of Jupiter; AU – astronomical unit. Normal growth of the massiveness of planets with the approach to the stars is marked by an arrow, the decrease of their massiveness as a result of the surface degassing under the action of the stars is shown with connodes.

References:

- [1] Mayor, M. and Queloz, D. (1995) *Nature*, 378, N 6555, P. 355. [2] Butler R. P. (1999) *Carnegie Inst. Washington*, 110–112. [3] Marcy G. W. and Butler R. P. (1998) *Ann. Rev. Astronomy and Astrophysics*, 36, 57–98.

RADAR TECHNIQUES FOR THE MEASUREMENT OF MERCURY'S OBLIQUITY AND LIBRATIONS. J. L. Margot, *California Institute of Technology, Pasadena, CA 91125 (margot@gps.caltech.edu)*, S. J. Peale, *Dept. of Physics, U. of Calif. Santa Barbara, CA, 93106*, M. A. Slade, *Jet Propulsion Laboratory/Caltech, 4800 Oak Grove Drive, Pasadena, CA 91109*.

Evidence for a global magnetic field at Mercury [Ness et al., 1974] has raised perplexing questions regarding the existence and nature of the planet's core (see [Schubert et al., 1988] for a review). The problems related to Mercury's core are of great interest because of their implications on how planets evolve thermally and on how they generate magnetic fields. Peale [1988] showed that the measurement of four quantities could place constraints on the size and state of Mercury's core. The required parameters in Peale's experiment are the C_{20} and C_{22} coefficients in the spherical harmonic expansion of the gravity field, the planet's obliquity θ , and the amplitude ϕ of the forced libration in longitude. While the gravitational harmonics are best determined from an orbiting spacecraft, Earth-based radar observations may provide refined estimates of the obliquity and amplitude of the libration. We describe several techniques and attempt to quantify their potential for the proposed measurements.

Tracking identifiable features

A well-known and robust technique for estimating planetary spin states consists in tracking small features in radar maps of the surface [Evans and Hagfors, 1968]. The locations of recognizable features as a function of time obviously depend on the orientation history of the planet. With the completion of the Arecibo upgrade, it should now be possible to obtain 15-30 m resolution images of the front cap of Mercury at inferior conjunction. This may revive interest in the technique, although reliable estimates will require a long time baseline.

Time-delayed interferometry

Radar interferometry techniques rely on observations of the same scene at two nearly identical aspect angles. The success of this method relies on good correlation between the two images, or equivalently that the observed "speckle" patterns are similar [Zebker and Villasenor, 1992]. Single-pass interferometry consists in using two physically separated antennas, while repeat-pass or time-delayed interferometry makes use of the same antenna at two different times. Because the requirements on the viewing geometry are extremely stringent, Slade et al. [1999] have suggested that the detection of interferometric fringes on Mercury would place significant constraints on the obliquity and wobble. This technique is described in detail in [Slade et al., this meeting].

Speckle displacement effect

An independent concept that relies on the same fundamental principles has been proposed by Holin [1988, 1992]. The

idea is to record monochromatic radar echoes at two separate locations and to cross-correlate them in the time domain. Highly correlated echoes will only be obtained when the same "speckle" pattern is observed at both stations, i.e. when the viewing geometry at antenna 1 and time t_1 is the same as the viewing geometry at antenna 2 and time t_2 (figure 1). Measurements of the time delay $t_1 - t_2$ that maximizes the correlation provides information on the spin state of the target.

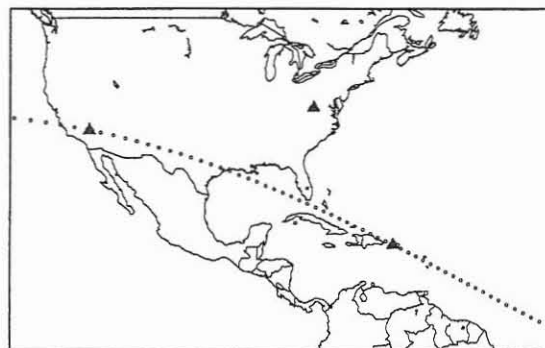


Figure 1: On rare occasions the Arecibo and Goldstone telescopes can observe the same location on Mercury under almost identical viewing geometries, at slightly different receive times. The time delay required to maximize the correlation between the echoes carries information about the spin state of Mercury. In this simulation, radar echoes from Mercury's front cap detected at Arecibo on 2004-09-11 15:54:30 are highly correlated to equivalent Goldstone echoes recorded ~33 seconds later. Circles indicate the path at time increments of one second, triangles show the locations of the telescopes. Calculations include light-travel times and the intervening motions of both planets.

We computed the expected time delays for values of the obliquity and libration amplitudes given by [Peale et al., this meeting] and compared them to the case of Mercury with no librations and zero obliquity. The difference in time delays for Arecibo-Goldstone opportunities are at most ~4 milliseconds for longitude librations of amplitude ~30 arcseconds, with maximum sensitivity when the libration angle is near zero, i.e. when the rate of change in libration angle is maximum. We investigated the changes in time delay due to an obliquity of 2.6 arcminutes with the following baselines: Arecibo-Goldstone, Arecibo-Madrid, and Goldstone-Green Bank Telescope. For the cases considered, the maximum difference in time delay was of order 30 milliseconds, with maximum sensitivity to the obliquity occurring when the baseline has a significant North-South component.

Mercury's obliquity and librations: J. L. Margot et al.

Radar instruments routinely measure ranges to fractions of microseconds, and the measurement of millisecond time delays would ordinarily not present a problem. However, closer inspection of the technique reveals two potential difficulties. First the peak in the correlation function will be broadened due to the fact that speckle patterns correlate over a finite range of aspect angles. The maximum spacing for adequate correlation is given by $B_{\text{crit}} \simeq R\lambda/d$ [Zebker and Villasenor, 1992], where R is the range to Mercury, λ is the wavelength, and d is the extent of the scattering patch on the surface of Mercury. To first order, the width τ of the correlation peak will be given by the time it takes for the speckle pattern to sweep over the distance B_{crit} , i.e. $\tau = B_{\text{crit}}/v$. Representative values for observations at the Arecibo frequency of 2380 MHz near inferior conjunction are $d = 500$ to 1000 km, controlled largely by the roughness of the surface, $v \simeq 100$ km/s, controlled by Earth and Mercury's orbital and rotational motions, and hence $\tau \simeq 100$ milliseconds. Additional broadening of the peak arises because the time delay providing the best correlation varies significantly over the duration of the measurements themselves, because the location on the surface that provides the best correlation changes with time. We computed this broadening to be of order one millisecond per second of integration, hence a difficult tradeoff will have to be reached between measurement accuracy and signal-to-noise ratio.

Measuring time delays to an accuracy of 4-30 milliseconds with a 100 millisecond time resolution seems difficult. However, one cannot exclude that repeated measurement of the *centroid* of the correlation function would provide reasonable estimates of the time delay, and therefore improved values of Mercury's obliquity and librations.

Ephemeris-based estimates

Harmon et al. [2001] report having to correct for range and Doppler offsets to properly align their imagery from run to run and from day to day. These problems are not related to instrumental deficiencies but are related to imperfect predictions for Mercury's range and Doppler time histories. The ephemerides could be inaccurate for a number of reasons: our knowledge of celestial mechanics and/or the equations in our models are imperfect, the orientation model for the Earth is imprecise, the location of the Arecibo Observatory on the surface of the Earth is poorly known, or the orientation model for Mercury is oversimplified. One would hope that the first three explanations can be discarded or at least compensated for, leaving the orientation model for Mercury responsible for residual errors. If ephemerides were re-generated with a non-zero obliquity, and if the corrections showed the extensive collection of images to be a more consistent data set, then a good approximation to the obliquity would be obtained. Harmon et al. [1994] reported that an obliquity of zero resulted in minimum smearing when summing 15 km resolution images. The availability of images at ten times better resolution may warrant a re-examination of this effect.

Focus-based estimates

A closely related technique relies on a focus measure of *individual* images. Since incorrect parameters for the obliquity would result in image defocusing, it may be possible to improve the spin parameters by maximizing the sharpness in the imagery.

Conclusions

Several radar-based techniques have the potential of improving estimates of Mercury's obliquity and amplitude of longitude librations. Because of the significant impact that those measurements may have on important problems in planetary science, the most promising techniques should be pursued vigorously.

References

- John V. Evans and Tor Hagfors, editors. *Radar Astronomy*. McGraw-Hill, New York, 1968.
- J. K. Harmon, P. J. Perillat, and M. A. Slade. High-Resolution Radar Imaging of Mercury's North Pole. *Icarus*, 149:1-15, January 2001.
- J. K. Harmon, M. A. Slade, R. A. Velez, A. Crespo, M. J. Dryer, and J. M. Johnson. Radar mapping of Mercury's polar anomalies. *Nature*, 369:213-215, May 1994.
- I. V. Holin. *Izvestiya Vysshikh Uchebnykh Zavedenii, Radiofizika*, 31(5):515-518, 1988.
- I. V. Holin. *Izvestiya Vysshikh Uchebnykh Zavedenii, Radiofizika*, 35(5):433-439, 1992.
- N. F. Ness, K. W. Behannon, R. P. Lepping, Y. C. Whang, and K. H. Schatten. Magnetic field observations near Mercury: Preliminary results from Mariner 10. *Science*, 185:153-162, 1974.
- S. J. Peale. *The rotational dynamics of Mercury and the state of its core*, pages 461-493. Mercury, University of Arizona Press, 1988.
- G. Schubert, M. N. Ross, D. J. Stevenson, and T. Spohn. *Mercury's thermal history and the generation of its magnetic field*, pages 429-460. Mercury, University of Arizona Press, 1988.
- M. A. Slade, J. K. Harmon, R. M. Goldstein, R. F. Jurgens, and E. M. Standish. A New Technique for High-Accuracy Measurement of Mercury Obliquity and Wobble. In *Lunar and Planetary Science Conference*, volume 30, pages 1143+, March 1999.
- H. A. Zebker and J. Villasenor. Decorrelation in interferometric radar echoes. *IEEE transactions on geoscience and remote sensing*, 30(5):950-959, sept 1992.

**THE MERCURY ATMOSPHERIC AND SURFACE COMPOSITION SPECTROMETER
(MASCS) FOR THE MERCURY: SURFACE, SPACE ENVIRONMENT, GEOCHEMISTRY,
RANGING (MESSENGER) MISSION.**

William E. McClintock
Laboratory for Atmospheric and Space Physics
1234 Innovation Dr.
Boulder Co, 80303-7814
william.mcclintock@colorado.edu

and

Gregory M. Holsclaw
Laboratory for Atmospheric and Space Physics
1234 Innovation Dr.
Boulder Co, 80303-7814
gregory.holsclaw@colorado.edu

MASCS is one of seven science instruments aboard the MESSENGER spacecraft, which will orbit Mercury beginning in 2009. It consists of a small Cassegrain telescope that simultaneously feeds a scanning grating UltraViolet-Visible Spectrometer (UVVS) and a fixed grating Visible-InfraRed Spectrograph (VIRS).

The UVVS will measure the composition and structure Mercury's exosphere, study its neutral and coronal gas, and search for and measure ionized atmospheric species. These measurements will contribute to our understanding of the processes that generate and maintain the atmosphere, the connection between surface and atmospheric composition, the transport of volatile materials on and near mercury, and the nature of the bright radar-reflective materials at its poles.

The VIRS will measure surface reflectance from 0.3 to 1.4 micrometers with a spatial resolution ~ 5 km. This wavelength range contains spectral signatures of Fe⁺⁺, Ca Silicates, TiO₂ and FeO. These measurements will be combined with multispectral images obtained with the Mercury Dual Imaging System and elemental composition measurements from the MESSENGER Gamma Ray and X-Ray Spectrometers to determine composition and study the effects of space weathering on the surface.

In this presentation we describe the capabilities of the MASCS, its measurement and science objectives, and how those objectives help to answer the key science questions that define the MESSENGER Mission.

IDENTIFICATION OF MERCURIAN VOLCANISM: RESOLUTION EFFECTS AND IMPLICATIONS FOR MESSENGER. S. M. Milkovich and J. W. Head, Department of Geological Sciences, Brown University, Providence, RI 02912.

Introduction: Ever since the arrival of Mariner 10 at Mercury in 1974-5 there has been debate over the existence of volcanic features on the surface of the planet. Mercury has two types of plains, smooth and intercrater. Through comparisons with lunar mare, many researchers have concluded that these plains were formed through volcanic processes [1, 2]. Others consider that they are closer to some of the lunar light plains formed by crater ejecta [3]. The identification of landforms typical of extrusive volcanism (e. g. domes, shields, sinuous rilles, calderas, flow fronts) is key to resolving this debate.

Work by Malin [4] indicates that the viewing geometry of Mariner 10 may have been insufficient for the identification of such volcanic features. He addressed this issue by analyzing lunar images under Mariner 10 resolutions (~1-2 km) and various lighting conditions (0-30°) for volcanic features. Since the mercurian images are at about the same resolution as pre-1964 Earth-based telescopic images of the Moon, Malin used such images from the *Consolidated Lunar Atlas* [5] with approximately the same viewing conditions as the Mariner 10 data. Malin was only able to identify lunar volcanic domes and flow fronts under these conditions, and found that volcanic features cannot be identified in images with sun elevation angles above 25°. Due to the limited coverage of mercurian plains at low sun angles (only 15% of the surface was imaged with sun elevation angles < 20° [4] while smooth plains were identified in 40% of the images, or 18% of the surface [6]), Malin was not surprised that volcanic landforms have not been identified on Mercury. He concludes that the only way to identify volcanic landforms in the Mariner 10 data is to look near the terminator. In such images he identifies two possible volcanic domes on Mercury; these are positive topographic features which are reminiscent of lunar domes but are near scarps and other structural features. Recent recalibration of Mariner 10 color data has allowed identification of several features spectrally similar to volcanic flows and pyroclastic fissure eruptions [7].

The question of the mode of formation of the mercurian plains remains unanswered. The upcoming MESSENGER mission to

Mercury will address this question [8]. The MESSENGER mission will meet the resolution and lighting geometry conditions necessary for identification of any lunar-like volcanic features on Mercury.

A Lunar Analog: The Moon makes a useful analog for Mercury. Mare basalt deposits are the primary volcanic feature on the Moon and are often compared to the mercurian plains [1, 2].

Lunar Volcanic Features. A wide variety of landforms are associated with the lunar maria [9]. These include regional *dark mantling deposits* which are interpreted to be caused by pyroclastic eruptions. Glass beads from these eruptions are spread tens to hundreds of km. *Sinuous rilles* are often associated with these deposits as well as the maria; these rilles are meandering channels generally an order of magnitude larger and often much more sinuous than terrestrial lava channels. They are thought to be sites of eruptions and thermal erosion. *Lava flow units* are mapped on the basis of topographic, albedo, and color boundaries but individual flows are usually hard to identify due to impact degradation of individual flow unit boundaries [9]. Flow fronts are more easily identified in near-terminator images [10]. About 50 small *shield volcanoes* (3-20 km basal diameter) are identified but no shields larger than ~20 km are seen [11]. Such volcanoes with diameters over 50 km are common on Earth, Mars, and Venus; this difference is attributed to the lack of lunar shallow neutral buoyancy zones affecting eruption processes [9, 12]. Also conspicuous in their absence are *calderas*; these represent shallow magma reservoirs at shallow neutral buoyancy zones. Finally, several *volcanic complexes* with unusual concentrations of the above features are seen; these are likely sites of multiple high-volume eruptions and the source regions of much of the surrounding lava. The Marius Hills area [35,000 km²] contains 20 sinuous rilles and over 100 domes and cones while the Aristarchus Plateau/Rima Prinz region [40,000 km²] contains 36 sinuous rilles [13]. We assess the detectability of such features under MESSENGER viewing geometry and lighting conditions.

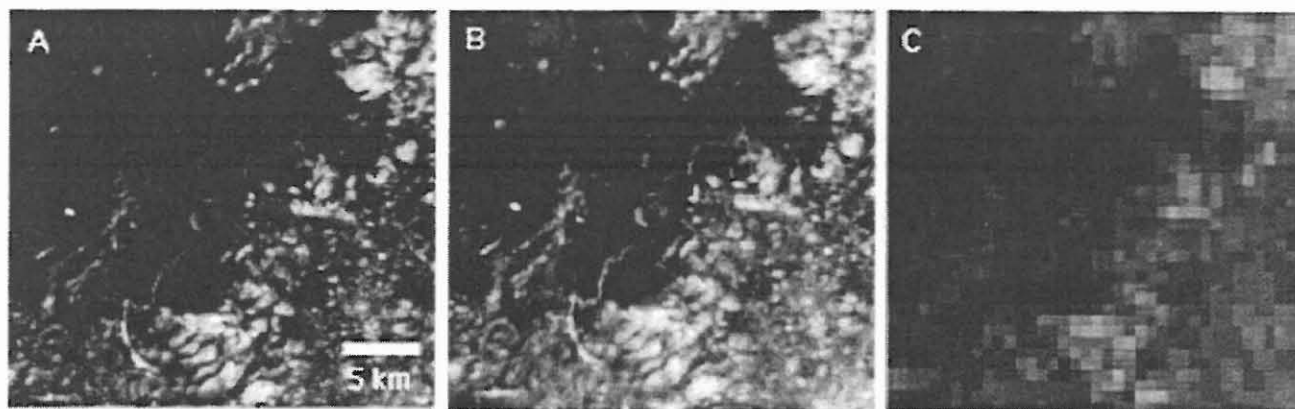


Fig. 1. Hadley Rille (~25 N, 3 E) at Multiple Resolutions. A) 100 m/pxl B) 500 m/pxl C) 2.5 km/pxl. All images from the Clementine Lunar Basemap.

Observations. Three important volcanic sites were selected for this study representing the range of volcanic features described above. The volcanic complexes of Marius Hills (~12 N, 310 E) and Aristarchus Plateau/Rima Prinz (~25 N, 315 E) and the Apollo 15 landing site near Hadley Rille (~25 N, 3 E). Images were taken from the Clementine Lunar Basemaps at 100m/pxl, 500m/pxl, and 2.5km/pxl resolutions. For comparison, the average resolution of Mariner 10 images was 1.5 km/pxl [6] while the anticipated average resolution for MESSENGER is 250 m/pxl [8].

Fig. 1 shows the three images for Hadley Rille, a 120 km long, 1.5 km wide sinuous rille located at the edge of Mare Imbrium. 1a and b show the rille at 100 and 500 m/pxl resolution respectively; it is clearly identifiable in both although its outline is pixelated in the second image. However, at 2.5 km/pxl resolution (Fig. 1c) the rille is not recognizable. Similar results are obtained from the other study sites; at 500 m/pxl the major features are still recognizable while the smaller ones are lost, and at 2.5 km/pxl even the major features are indecipherable. The majority of Mariner 10's images fall into a range of resolutions where some large volcanic features could be identified but others would not.

Fig. 2 shows two ground-based telescopic images of Marius Hills taken at different colongitudes. The image in Fig. 2a has a higher sun elevation angle (26°, [4]) and shows faint topographic features; however, it is difficult to interpret these features. In comparison, Fig. 2b was taken at low sun elevation (6°, [4]) and clearly contains domes and ridges. The only difference between these images is sun elevation. Thus, lighting conditions are an important factor in identifying volcanic features in images. Near-terminator images from Mariner 10 were examined, but no volcanic features were found.

Implications for MESSENGER. One of the major scientific goals of the MESSENGER mission is to determine the formation history of the surface of Mercury [8]. An important aspect of this is the role of volcanism in Mercury's history; MESSENGER needs to be able to search for volcanic landforms under suitable resolutions and viewing geometries to correctly address this issue. This requires adequate coverage of the planet at the resolutions and viewing geometries outlined above.

MESSENGER will build up a full global mosaic in the first 6 months after achieving orbit and cover the planet with stereo images at ~250 m/pxl in the second 6 months. Since the spacecraft will be in an elliptical orbit, the narrow angle imager will be used during high altitude to achieve global monochrome image mosaics

with an average 250 m/pxl resolution [Table 1]. The orbit itself starts in a dawn-dusk configuration and moves through noon-midnight back to dawn-dusk many times during the mission [8].

Will this allow volcanic landforms to be identified? Most of the imaged 45% of the planet is covered with plains that may be volcanic in origin [6]. In the first 6 months the spacecraft will cover ~50 % of the surface from near dawn-dusk orbits. Even if the only plains of possible volcanic origin are the ones already observed, this orbit geometry will allow imaging of a portion of such plains under conditions favorable to the identification of volcanic landforms. In addition, MESSENGER multispectral imaging and spectrometer data will permit further assessment and characterization of candidate volcanic plains [8, 14].

Instrument	No. Polar Zone	Mid Zone	Far Zone
Narrow Angle	—	< 125 m/pxl	< 500 m/pxl
Wide Angle	< 125 m/pxl	< 500 m/pxl	< 1000 m/pxl

Table 1. MESSENGER image resolution. After [8].

Conclusions: Both resolution and viewing geometry play an important role in what sorts of features are visible in an image. To successfully identify volcanic features such as those on the Moon both low sun angle (~10°) and ~500 m/pxl resolution or better are needed. While Mariner 10 did not cover a significant portion of Mercury within these requirements, MESSENGER will be able to do so. The question of the existence of volcanism on Mercury must wait until then to be addressed more confidently.

References: [1] Murray B. C. et al. (1975) *JGR*, 80, 2508-2514. [2] Strom R. G. et al. (1975) *JGR*, 80, 2478-2507. [3] Wilhelms D. E. (1976) *Icarus*, 28, 551-558. [4] Malin M. C. (1978) *Proc. LPSC IX*, 3395-3409. [5] Kuiper G. P. et al. (1967) *Consolidated Lunar Atlas* Tuscon: Univ. of Arizona. [6] Spudis P. D. and Guest J. E. (1988) in *Mercury*, Vilas F. et al., ed. Tucson: Univ. of Arizona Press, 118-164. [7] Robinson M. S. and Lucey P. G. (1997) *Science*, 275, 197-200. [8] Solomon S. C. et al. (2001) *Plan. Space Sci.*, in Press. [9] Head J. W. and Wilson L. (1992) *Geochim. et Cosmochim. Acta*, 56, 2155-2175. [10] Head J. W. and Lloyd D. D. (1973) NASA Spec. Pub 330, Sect. 4, 33-39. [11] Head J. W. and Gifford A. (1980) *Moon and Planets*, 22, 235-258. [12] Head J. W. and Wilson L. (1991) *GRL*, 18, 2121-2124. [13] Whitford-Stark J. L. and Head J. W. (1977) *Proc. 8th Lunar Sci. Conf.*, 2705-2724. [14] Robinson M. S. and Taylor, G. J. (2001) *Met. And Plan. Sci.*, 36, 841-847.

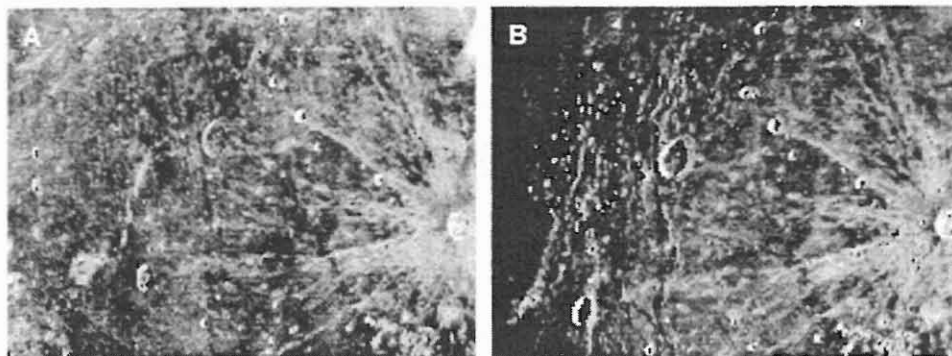


Fig. 2. Two Views of Marius Hills (~12 N, ~310 E) from Groundbased Telescope. The crater Marius (left of center) is 45 km in diameter. A) Sun angle 26°. B) Sun angle 6°. Resolution approximately 2 km/pxl [4].

CRATER PRODUCTION FUNCTION AND CRATERING CHRONOLOGY FOR MERCURY.

G. Neukum¹, B. A. Ivanov² and R. Wagner¹, ¹DLR Institute of Space Sensor Technology and Planetary Exploration, Rutherfordstrasse 2, 12489 Berlin-Adlershof, Germany (Gerhard.Neukum@dlr.de, Roland.Wagner@dlr.de), ²Institute for Dynamics of Geospheres, Russian Acad. Sci., Leninsky Prospect 38/6, Moscow, Russia 117939, (bairvanov@idg.chph.ras.ru).

Introduction: The well investigated size-frequency distributions (SFD) for lunar craters may be used to estimate the SFD for projectiles which formed craters on terrestrial planets and on asteroids [1]. The result shows the relative stability of these distributions during the past 4 Gyr. The derived projectile size-frequency distribution is found to be very close to the size-frequency distribution of Main-Belt asteroids as compared with the recent Spacewatch asteroid data and astronomical observations as well as data from close-up imagery by space missions. It means that asteroids (or, more generally, collisionally evolved bodies) are the main component of the impactor family. A cratering chronology model is established which can be used as a safe basis for modeling the impact chronology of other terrestrial planets, especially Mercury [2, 3].

Impact rate comparison: We compare impact rates on the moon and Mercury using the following procedure: we calculate impact velocities and probabilities for observed Earth crossers and Mercury-crossers with various limiting magnitudes. In this work we used the list of osculating orbits "astorb.dat" as it was presented on <http://asteroid.lowell.edu> In February 2000.

The Opik formulas (refined by Wetherill [4] for the general case of elliptic orbits both for a target and a projectile) are applied for all bodies crossing the orbits of the moon and Mercury. For each target (Mercury or the moon) and projectile (PCA) the impact probability and impact velocity are calculated. The total impact probability and the average impact velocity give numbers necessary to compute the cratering rate. Fig. 1 compares impact velocities on the moon and Mercury.

Production function: Using the lunar impact crater chronology [5] we derive a similar analytical expression for Mercury taking into account the difference in the number of planet-crossers. The Neukum production function (NPF) is approximated as a polynomial function similar to the lunar NPF:

Coefficients are listed in the Table 1; the fit is valid for $15 \text{ m} < D < 362 \text{ km}$.

The coefficient a_0 in the Table 1 is calculated for a crater retention age of 1 Gyr. It corresponds to the cumulative number of craters larger 1 km

$$N(1) = 10^{-3.016675} = 9.62 \cdot 10^{-4} \text{ km}^{-2}$$

Using the same time dependence as for the moon one can propose a similar time dependence for Mercury:

$$N(1) = 6.5 \cdot 10^{-14} (\exp(6.93 T) - 1) + 9.62 \cdot 10^{-4} T$$

Table 1. Coefficients for the Mercurian NPF

n	a_n
0	-3.016675
1	-3.627417
2	$6.038601 \cdot 10^{-01}$
3	1.026714
4	$-3.767761 \cdot 10^{-03}$
5	$-4.204364 \cdot 10^{-01}$
6	$-3.223500 \cdot 10^{-02}$
7	$8.044575 \cdot 10^{-02}$
8	$3.170165 \cdot 10^{-03}$
9	$-6.733922 \cdot 10^{-03}$
10	$1.334403 \cdot 10^{-04}$
11	$1.428627 \cdot 10^{-04}$

Using the polynomial fit one can construct similar equations for $N(10\text{km})$ and $N(30\text{km})$:

$$N(10)/N(1) = 0.00421$$

$$N(30)/N(10) = 0.271$$

Figure 2 presents Mercury/moon cratering rate ratio based on Neukum Production Function (NPF). Fig. 3 compares direct measurements and size-frequency distribution SFD (the "lunar analog") calculated with the polynomial coefficients listed in Table 1.

Conclusion: The general conclusion from several models described above is that the impact cratering rate on Mercury seems to differ more than $\pm 50\%$ from the lunar cratering rate in the same diameter bins. However the shift of crater diameters and diameters of strength/gravity and simple/complex crater transition change the shape of the Mercurian production function in comparison with the lunar PF.

The less frequent asteroid impacts on Mercury do not result in much lower cratering rate: the larger impact velocity increases the crater size in comparison with the impact of the same body on the moon. Finally the cratering rate Mercury-moon ratio varies in the range of 1.0 to 1.3 depending on the steepness $N(D)$ distribution.

References: [1] Neukum G., Ivanov B. and Hartmann, W.K. (2001) 'Cratering Records in the Inner Solar System in Relation to the Lunar Reference System', In: *Chronology and Evolution of Mars, ISSI*, Kluwer (in press). [2] Ivanov B. A. (2001) 'Mars/Moon Cratering Rate Ratio Estimates', *ibid.* [3] Hartmann W.K. and Neukum G. (2001) 'Cratering chronology and the evolution of Mars', *ibid.* [4] Wetherill (1987), *J. Geophys. Res.* 72, 2429–2444. [5] Neukum G. (1983) *Habilitation Dissertation*, Ludwig-Maximilians Univ. München, Germany, 186 pp..

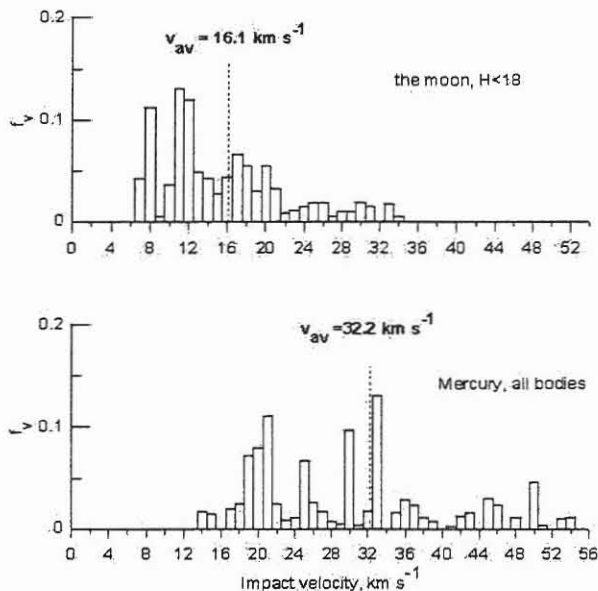


Fig. 1. The impact velocity distribution of the moon and Mercury projectiles (fraction of impacts per interval of 1 km s⁻¹).

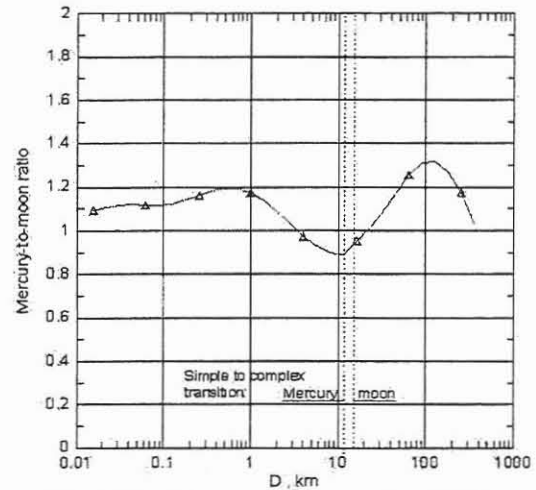


Fig. 2. The Mercury-to-moon ratio of $N>D$

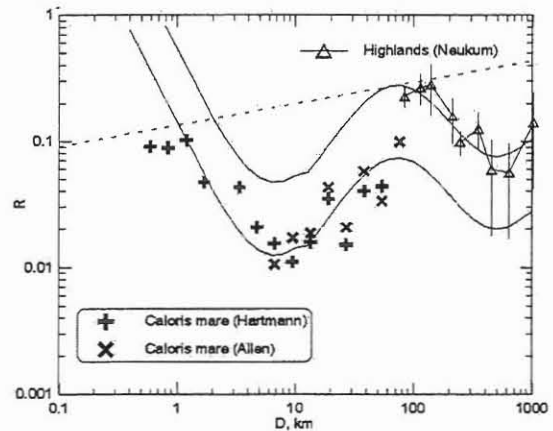


Fig. 3. The mare surface in the Caloris basin is one of few areas suitable for production function measurements of small to intermediate-sized craters on Mercury. The figure compares direct measurements and calculated SFD (the "lunar analog"). The good coincidence of these data shows a definite similarity of projectile SFDs on the Moon and Mercury in the projectile diameter range from 1 to ~100 km with a steep part for smaller craters and the "R-minimum" for craters with $D \approx 8$ km. The age of the Caloris basin is comparable to the age of the Orientale basin.

CONSTRAINING THE MEAN CRUSTAL THICKNESS ON MERCURY. F. Nimmo, NASA Ames Research Centre, Moffett Field, CA 94085, USA (nimmo@gps.caltech.edu).

Introduction

The topography of Mercury is poorly known, with only limited radar and stereo coverage available. However, radar profiles reveal topographic contrasts of several kilometers over wavelengths of ~ 1000 km (Harmon & Campbell 1988). The bulk of Mercury's geologic activity took place within the first 1 Ga of the planet's history (Spudis & Guest 1988), and it is therefore likely that these topographic features derive from this period. On Earth, long wavelength topographic features are supported either convectively, or through some combination of isostasy and flexure. Photographic images show no evidence for plume-like features, nor for plate tectonics; I therefore assume that neither convective support nor Pratt isostasy are operating.

The composition and structure of the crust of Mercury are almost unknown. The reflectance spectrum of the surface of Mercury is similar to that of the lunar highlands (Vilas 1988), which are predominantly plagioclase. Anderson et al. (1996) used the observed centre-of-mass centre-of-figure offset together with an assumption of Airy isostasy to infer a crustal thickness of 100-300 km. Based on tidal despinning arguments, the early elastic thickness (T_e) of the (unfractured) lithosphere was $\leq \sim 100$ km (Melosh 1977).

Thrust faults with lengths of up to 500 km (Watters, submitted) and ages of about 4 Ga B.P. are known to exist on Mercury. Assuming a semicircular slip distribution and a typical thrust fault angle of 10° , the likely vertical depth to the base of these faults is about 45 km. More sophisticated modelling gives similar or slightly smaller answers (Watters, pers. comm., 2001). The depth to the base of faulting and the elastic layer are usually similar on Earth (Maggi et al. 2000), and both are thought to be thermally controlled. Assuming that the characteristic temperature is about 750 K, the observed fault depth implies that the heat flux at 4 Ga B.P. is unlikely to be less than 20 mW m^{-2} for a linear temperature gradient. For an elastic thickness of 45 km, topography at 1000 km wavelength is likely to be about 60 % compensated (Turcotte & Schubert 1982). There are thus likely to be considerable lateral variations in crustal thickness.

Theory

If topography is supported by variations in crustal thickness, pressure gradients exist which may cause the lower crust to flow, thus reducing the topography. An expression for the characteristic relaxation time due to lower crustal flow was obtained by Nimmo & Stevenson (2001). Their approximations, however, break down if heating occurs entirely from within the crust. In this case, the temperature $T(z)$ is given by

$$T(z) = T_s + \frac{Hz^2}{2K} \quad (1)$$

where H is the internal heat generation rate, z is the depth (measured downwards), K is the thermal conductivity and T_s is the surface temperature. The viscosity η of most materi-

g	m.s^{-2}	3.76
radius	km	2440
mantle thickness	km	610
$\Delta\rho$	kgm^{-3}	500
Q	kJmol^{-1}	500
K	$\text{Wm}^{-1}\text{K}^{-1}$	3
T_s	K	400

Table 1: Mercury parameters used in model.

als is strongly temperature-dependent and obeys an Arrhenius relationship which may be written as

$$\eta \sim \eta_b \exp\left(\frac{Q[T_b - T]}{RT_b^2}\right) \sim \eta_b \exp\left(\frac{z}{\delta}\right)^2 \quad (2)$$

with z now measured upwards from the base of the crust. Here T_b is the temperature at the base of the crust, η_b is the viscosity at this depth, Q and R are the activation energy and gas constant, respectively, and δ is the characteristic channel thickness given by

$$\delta = T_b \left(\frac{2KR}{QH}\right)^{1/2} \quad (3)$$

Using the standard Navier-Stokes equation for creeping flow in one dimension and applying continuity, the time constant for lower crustal flow under internal heating τ_H is given by

$$\tau_H = \frac{4}{\sqrt{\pi}} \frac{\eta_b}{k^2 \delta^3 \Delta\rho g} \quad (4)$$

where k is the wavenumber ($=2\pi/\lambda$), $\Delta\rho$ is the density contrast between crust and mantle and g is the acceleration due to gravity. The expression for the time constant under basal heating is identical except for a different numerical constant, but δ then depends on the basal heat flux rather than H (Nimmo & Stevenson 2001).

A dry diabase rheology (Mackwell et al. 1995) is assumed, since this is the strongest of the likely crustal materials. If the crust is indeed mainly composed of plagioclase, maximum crustal thickness estimates will be reduced. The effective viscosity η_b is calculated from the usual stress-strain relationship, assuming a constant stress of 10 MPa (appropriate to a topographic contrast of ~ 1 km). A characteristic wavelength of 1000 km is assumed; other values are given in Table 1.

The nature of the heat flux on Mercury is not well known. The heat generated is thus assumed to be a factor C times the terrestrial heat generation rate at 4 Ga B.P., using the radiogenic abundances of Sun & McDonough (1989). The heat generation is assumed to take place either entirely within the crust, or to be distributed uniformly throughout the crust and mantle. The relaxation timescale is then calculated for different crustal thicknesses.

SPACE WEATHERING IN THE MERCURIAN ENVIRONMENT. S. K. Noble and C. M. Pieters, Brown University, Dept of Geological Sciences, Providence RI 02912. noble@porter.geo.brown.edu

Introduction: Space weathering processes are known to be important on the Moon. These processes both create the lunar regolith and alter its optical properties [1,2,3]. Like the Moon, Mercury has no atmosphere to protect it from the harsh space environment and therefore it is expected that it will also incur the effects of space weathering [3]. However, there are many important differences between the environments of Mercury and the Moon. These environmental differences will almost certainly affect the weathering processes and the products of those processes. It should be possible to observe the effects of these differences in Vis/NIR spectra of the type expected to be returned by MESSENGER. More importantly, understanding these weathering processes and their consequences is essential for evaluating the spectral data returned from MESSENGER and other missions in order to determine the mineralogy and the Fe content of the Mercurian surface.

Mercurian Environment: Because of its proximity to the Sun, Mercury has a flux of impactors 5.5 times that of the Moon [4]. This flux coupled with its greater density makes Mercury more efficient at creating melt and vapor. Per unit area, Mercury will produce 13.5 times the melt and 19.5 times the vapor than is produced on the Moon [4]. Mercury has a magnetic field that will protect its surface from charged particles, reducing the solar wind flux at the planet by a factor of 160 vs. the lunar environment [5]. The combination of these factors then means that melting and vaporization due to micrometeorites will dominate space weathering on Mercury with little or no solar wind sputtering effects [3]. Furthermore, agglutinitic glass-like deposits and vapor deposited coatings should be created much faster and more efficiently on Mercury.

The nanometer-scale metallic Fe particles (npFe⁰) that are ubiquitous in the rims and agglutinates of lunar soil [6] should also be present on Mercury. In the lunar case formation of npFe⁰ is largely derived by vapor fractionation and sputtering of local FeO-bearing material. Neither process requires a H-saturated surface [3]. Even for the endmember case where the surface of Mercury has no native FeO, the iron brought in by meteorites would be sufficient to make the formation of npFe⁰ through vapor fractionation an important process on the planet. Amounts as small as 0.05wt % npFe⁰ is enough to affect the optical properties [2]. The size distribution of metallic Fe particles in a soil strongly controls the effects on the Vis/NIR spectrum. The smallest particles (<5nm) will tend to redden the soil while larger particles (>10nm) will cause darkening [7,8].

The Mercurian environment is also unique in our solar system because of its extreme temperature range. Due to its slow rotation and proximity to the sun, equatorial regions of Mercury can achieve temperatures above 700K during the day, while nighttime temperatures can dip below 100K. These conditions have important effect on diffusion in glass and crystal growth.

Weathering on Mercury: What, if any, effects might Mercury's unique environment have on space weathering products? The possibilities fall into two groups: (1) *Formation processes* - What weathering products are formed on Mercury and how do they compare to those on the Moon? (2)

Evolution processes - Do the products of space weathering change as they are exposed to the Mercurian thermal regime?

Formation Processes: Melt products produced from micrometeorites which impact in the night will look similar to those observed in lunar soil. The only difference should be the rate of formation. Agglutinitic glass and vapor should be forming at a much faster rate. In a mature lunar soil, agglutinates make up as much as 50-60% of the soil. A mature soil on Mercury probably has little, if any, original crystalline material remaining.

On the day side of Mercury, the cooling regime for micrometeorite impacts is going to be somewhat different. Because the base temperature during the day is significantly higher, the cooling rate will be slowed compared to the night side (and the Moon). The slower cooling rate will allow more time for crystallization and make it difficult to form quenched glass. "Agglutinates" as we understand them from lunar soil, may look very different under these conditions if there is sufficient time for the melt to crystallize. Likewise, we might expect rim material (vapor coatings) to be microcrystalline. Perhaps the most important effect that we should expect is that the Fe-particles in both the agglutinate-like material and vapor deposited rims formed during the elevated daytime temperatures will have time to grow to larger sizes.

Evolution processes: Lunar-like agglutinates and vapor deposits formed during the night will eventually be exposed to the heat of the Mercurian day. The thermal regime on Mercury may have significant effects on the npFe⁰. Regardless of whether these products were created in the day or night, they will be exposed repeatedly to extended periods of the 400°C+ temperatures of Mercury's day.

Due to differences in free energy between curved surfaces, npFe⁰ particles in a glass matrix will tend to coarsen via a process well known in material sciences, Ostwald ripening. This process could be acting on the Moon as well, although, in the lunar case the rate of growth is probably much too slow to be perceptible. Because the growth rate is dependent on temperature, the process should be considerably faster on the day side of Mercury than it is on the Moon. During the course of a Mercurian day, the soil at the hottest parts of Mercury will stay above 400°C for about 2 weeks. This increased temperature may be enough to allow the npFe⁰ particles to grow significantly. A vapor deposition experiment of Hapke *et al.* [9] demonstrated that heating npFe⁰-rich vapor coatings to a temperature of 650°C for just one hour is sufficient to remove the ferromagnetic resonance. This presumably occurs because particles of the npFe⁰ have grown to be larger than the range that is measured by FMR techniques (4 - 33 nm in dia. [10]), suggesting that the size of those particles tripled or quadrupled in the course of the experiment.

Determining the rate of Ostwald ripening on Mercury is difficult due to a lack of experimental data. The equation for this process is given below along with estimations of values for each variable. The least constrained, and most important variables are D, the diffusion coefficient, and σ , the surface energy. Considering a wide range of values for these, we

have attempted to bound the possible range of grain growth through time (figure 1).

$$r^3 - r_0^3 = \frac{8}{9} \times \frac{x_{IL}(1 - x_{IL})}{(x_{IS} - x_{IL})^2} \times \frac{D\Omega\sigma}{RTI} \times (t - t_0)$$

r_0 = original size of Fe particles $\approx 3 \text{ nm} = 3 \times 10^{-9} \text{ m}$ [6]
 x_{IL} = fraction of npFe⁰ in rim coating = 0.1 [3] - 0.01
 x_{IS} = fraction of glass = 1
 D = diffusion coef. of Fe in glass = 10^{-17} - $10^{-19} \text{ m}^2/\text{s}$
 Ω = molar volume of Fe = $7.09 \times 10^{-6} \text{ m}^3/\text{mol}$
 σ = surface energy = 0.01-100 mJ/m²
 T = average temperature on Mercury = 400K
 I = thermodynamic factor ≈ 1
 $t-t_0$ = time of exposure

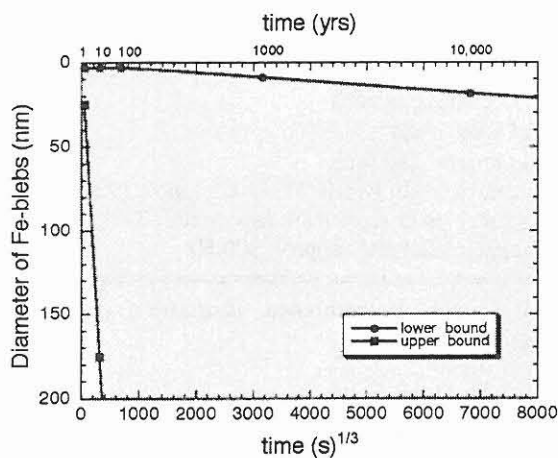


Figure 1. Possible range of effects of Ostwald ripening with time at the equator of Mercury.

Even our most conservative estimates indicate that Ostwald ripening should have a significant effect on some Mercurian soils, doubling the size of the npFe⁰ in a matter of centuries. Of course, with increasing latitude, there is less heat available and the thermal regime becomes much more lunar-like where Ostwald ripening will have little or no effect. Our data is too limited at this point to predict the latitude where that transition will occur. Clearly work needs to be done to constrain the rate of growth and to understand the temperature dependence of this process.

Discussion: Ostwald ripening and the earlier described effects of slower cooling for day side impacts should combine to result in larger Fe particles, on average, near the equator. Since smaller npFe⁰ particles cause reddening and larger ones result in darkening, if Ostwald ripening dominates over npFe⁰ production, we should expect the spectral

continuum to be darkest near the equator and become somewhat redder with increasing latitude.

Our current spectral data set for Mercury is very limited. Most of our spectral data is telescopic [11], largely providing an integrated disk view, masking any possible latitudinal variations, as well as regional differences. Also hidden are maturity differences that we might expect to find at young craters. Recently, though, the surface was mapped over the wavelength range 550-940nm at roughly 200km resolution by the Swedish Vacuum Solar Telescope [12]. Also, two filter data was taken during the Mariner 10 flyby, which confirms that spectral differences exist on a regional scale [13]. These data do not reveal major latitudinal trends, which is not surprising given the limited spatial and spectral resolution of the data.

The shape of the continuum influenced by npFe⁰ can provide information about the Fe-content of a soil. Observational [2], experimental [14], and theoretical [3] data show that the shape of the spectral continuum of lunar soils changes systematically with npFe⁰ content. Thus, for high latitude areas that have not been significantly affected by the processes described above, it should be possible to determine the amount of npFe⁰ present. The amount of npFe⁰ can then be used to constrain the total amount of iron in the soil.

Conclusions: If we can understand the weathering environment on Mercury, then we can predict what the space weathering products will be. By combining these predictions with an understanding of the optical effects of weathering gleaned from laboratory studies of lunar soil, we hope to estimate the total Fe on the surface of Mercury and to provide the necessary tools for evaluation of mineralogy for future missions.

References: [1] Pieters C.M. *et al* (2000) *Meteoritics & Planet. Sci.*, **35**, 1101-1107. [2] Noble S.K. *et al* (2001) *Meteoritics & Planet. Sci.*, **36**, 31-42. [3] Hapke B. (2001) *JGR*, **106**, 10039-10073. [4] Cintala M.J. (1992) *JGR*, **97**, 947-973. [5] Hartle R. *et al* (1975). *JGR*, **80**, 3689-3693. [6] Keller L.P and Clemett S.J. (2001) *LPSCXXXII*, ab# 2097. [7] Keller L.P *et al* (1998) *New Views of the Moon*, 41. [8] Britt D.T. and Pieters C.M. (1994) *GCA*, **58**, 3905-3919. [9] Hapke, B. *et al* (1975) *Science*, **264**, 1779-1780. [10] Housley R.M. *et al* (1976) *PLPSC 7th*, 13-26. [11] Vilas F. (1988) *Mercury*, Univ. of AZ Press, 59-76. [12] Warell J. and Limaye S.S. (2001) *Planet. Space Sci.*, in press. [13] Robinson M.S. and Lucey P.G. (1997) *Science*, **275**, 197-199. [14] Allen C.C. *et al* (1996) *LPSCXXVII*, 13-14.

Acknowledgments: Thanks to Paul Hess for introducing me to the concept of Ostwald ripening and to Yan Liang for patiently explaining the process to me. NASA support (NAG5-4303) is gratefully acknowledged.

A COMBINED STEREO CAMERA/LASER ALTIMETER EXPERIMENT PACKAGE FOR THE BEPICOLOMBO POLAR ORBITER. J. Oberst¹, R. Wagner, H. Hoffmann, R. Jaumann, and G. Neukum, ¹(all authors at: DLR Institute of Space Sensor Technology and Planetary Exploration, Rutherfordstr. 2; D-12489 Berlin, Germany, Juergen.Oberst@dlr.de).

BepiColombo, a mission to Mercury initiated by the European Space Agency (ESA), is scheduled for launch near the beginning of the next decade. Our team proposes to contribute an instrument package to the Mercury Polar Orbiter (MPO) which combines a camera and a laser altimeter. The camera portion of the instrument, inherited from the HRSC (High Resolution Stereo Camera) on Mars Express, is a multiple line scanner, operated in the pushbroom mode. The scanner (Table 1) is proposed to have nine line sensors, 5128 pixels each, oriented perpendicular to the spacecraft's motion. Three of the sensors are pointed forward, nadir, and backward, respectively, to collect stereo data. Other sensors are designed to obtain image data at multiple phase angles, or in color. From a periapsis height of 400 km, the camera, operating at a scan rate of approx. 300 Hz, will obtain a ground pixel size of 10 m. The laser will operate at e.g. 1 Hz, its clock being precisely synchronized with the scanner. The science goals of the instrument are in the general reconnaissance as well as geoscientific studies of the planet (Table 2, see also abstract by Wagner et al., this meeting).

Observations of the libration of Mercury are among the foremost goals of BepiColombo, for which our instrument is uniquely suited. Owing to the slow rotation rate of the planet, image data from adjacent orbits will have good overlap (>50%) near the equator, which is essential for the tracking of Mercury's librations. The typical data analysis will include the automatic extraction of large numbers (estimated > 25,000 per orbit) of triple-tiepoints between the stereo images using digital image matching techniques. These tiepoints, in combination with the range measurements by the laser allow us to accurately model the orbit and attitude of the spacecraft, surface topography, as well as rotation of the planet. For the analysis, the synchronous operation of the laser and the camera is essential, as this will allow us to directly obtain the image line/sample coordinates of all laser surface reflection points (>5000 per orbit) and include them in the analysis.

We simulated data acquisition and analysis for triple stereo image swaths of 30 minutes near pericenter and generated a set of 100 triple-tiepoints (in practice this number will be much larger, see above). The camera parameters described above and the nominal parameters of the spacecraft's polar orbit were adopted. The results of our model suggest that one can determine the orientation of Mercury's rotational axis within less than 1 degree after one orbit. Our current model assumes that unbiased

inertial spacecraft trajectory data are given and suffer from random errors only.

Table 1: Instrument Package Summary

=====	
<i>Laser Altimeter:</i>	
–oper. altitude:	400–1500 km
–typical shot rate:	1 Hz
–vertical (relative) resolution:	< 1 m (expected final absolute accuracy: 40 m)
–pericenter shot spacing:	3000 m (apocenter: 2170 m)
<i>Multiple-Line Scanner:</i>	
–9 CCD lines (3 high-res/stereo; 2 photometric; 4 color) 5128 pixels each	
–pixel size:	7 µm
–focal length:	280 mm
–pericenter swath width:	51.28 km (apo.: 192.1 km)
–pericenter pixel size:	10 m (apocenter: 37.45 m)
–pericenter scan rate:	approx 300 Hz
=====	
Total weight of combined instrument (including digital units):	12.5 kg

Table 2: Key Science Issues

=====	
<i>General Reconnaissance</i>	
–explore "other" hemisphere, not seen by Mariner 10	
–obtain global images at uniform resolution < 200 m/pxl in "full" color	
–carry out high-resolution imaging in selected areas < 10 m/pxl (2–5% of surface).	
<i>Surface Geology</i>	
–update the global inventory of multi-ring structures and young ray craters	
–determine the shape of the mercurian production function in the crater diameter range from basin sizes down to meter-sized craters	
–carry out detailed crater size–frequency measurements on geologic units at smaller crater sizes, e.g. on ejecta blankets of large craters or basins in order to further refine the time–stratigraphic system	
–carry out inter-planet comparisons.	
<i>Surface properties, landforms, and geological processes</i>	
–determine photometric properties of surface materials (albedo, porosity, roughness, etc.) by using images under a wide range of phase angles	
–resolve origin of inter-crater and low-land plains units (volcanic versus ejecta)	

- search for volcanic domes or rilles for undisputed evidence of volcanic activity
- investigate detailed stratigraphy in selected areas by mapping on high resolution imagery.

Geodesy / Precision Cartography

- determine overall shape, such as ellipsoid parameters and COM/COF offsets
- measure the orientation of the spin axis;
- determine precession and librations
- map global topography at absolute spatial and vertical precision better than 200 m and 40 m, respectively
- map high-resolution topography (2–5% of total area) at (relative) spatial and vertical resolution of better than 20 m and 1 m, respectively.

Planetary Interior

- measure moments of inertia to obtain constraints for Mercury's deep interior

- update global inventory of thrust faults to obtain constraints on the planet's thermal history
- measure heights and dip angles of thrust fault to estimate the amount of global contraction
- analyse topography and gravity data to derive thickness and compensation state of the crust.

Mineralogy

- carry out global multispectral mapping at resolutions of 200 to 1000 m/pxl
- map spectral units associated with impact craters and their ejecta in order to define the vertical zoning of material units, making use of craters as "windows" into the mercurian crust
- determine origin inter-crater and low-land plains units (volcanic versus ejecta)
- evaluate effects of space weathering.

=====

SCIENTIFIC MERITS AND TECHNICAL ASPECTS OF A THERMAL/ENERGETIC NEUTRAL PARTICLE DETECTOR ON BOARD THE ESA BEPICOLOMBO MISSION. S. Orsini¹, E. De Angelis¹, A. M. Di Lellis², S. Barabash³, I. A. Daglis⁴, D. Delcourt⁵, E. Kallio⁶, R. Killen⁷, S. Livi⁸, A. Milillo¹, A. Mura¹, P. Wurz⁹, V. Zanza¹⁰, ¹IFSI/CNR, Via Fosso del Cavaliere 100, 00133, Roma Italy (Orsini@ifsi.rm.cnr.it), ²AMDL, Roma, Italy, ³IRF, Kiruna, Swedn, ⁴National Observatory of Athens, Greece, ⁵CNRS, Saint Maur des Fosses, France, ⁶FMI, Helsinki, Finland, ⁷SRI, San Antonio, Texas, USA, ⁸JHU, APL, Laurel, Maryland, USA, ⁹University of Bern, Switzerland, ¹⁰ENEA, Frascati, Italy.

The Neutral Particle/ENA Detectors on board the ESA BepiColombo mission to Mercury has the purpose to investigate the Hermean exospheric composition, the interaction of the solar wind between both the magnetospheric plasma and the planet surface. By applying unfolding techniques, with this instrument we can detect the thermal particles of the exosphere and energetic neutral atoms generated via charge-exchange or sputtering processes. In particular it will be possible:

- (a) to obtain in-situ measurements of the exospheric composition and density;
- (b) to investigate the surface composition of the planet and the global exospheric characteristics, by analyzing the massive sputtered particles;

- (c) to study the exospheric dynamical evolution through ENA remote sensing;
- (d) to image the magnetospheric plasma flow patterns and the variations occurring during disturbed periods by observing the short time fluctuations of the ENA signal; thus providing crucial global information necessary for the interpretation of simultaneous in situ ion measurements;

In the present paper, some details of the scientific merits and technical aspects of this instrument are briefly presented and discussed.

A PROCEDURE FOR DETERMINING THE NATURE OF MERCURY'S CORE. S. J. Peale, *Dept. of Physics, U. of Calif. Santa Barbara, CA, 93106* (peale@io.physics.ucsb.edu), R. J. Phillips, *Dept of Earth and Planet. Sci. Washington U., St. Louis, MO 63130*, S.C. Solomon, *DTM, Carnegie Inst., Washington, DC 20015*, D.E. Smith, *Earth Sci. Dir., NASA/GFSC, Greenbelt, MD 20771*, M.T. Zuber, *Dept. Earth, Atm., Planet. Sci., MIT, Cambridge, MA 02139*.

We review past assertions that the determinations of the four parameters, C_{20} , C_{22} , θ , ϕ , are sufficient to determine the size and state of Mercury's core (Peale, 1976, 1981, 1988). C_{20} and C_{22} are gravitational harmonics, θ is Mercury's obliquity and ϕ is the amplitude of the forced, 88 day period libration in longitude. The upcoming MESSENGER orbiter mission to Mercury (Solomon, *et al.* 2001) with onboard instrumentation capable of measuring these four parameters (Zuber and Smith, 1997), and the possibility of precision measurements of Mercury's spin geometry with radar interferometry techniques (I. Holin, Jean-Luc Margot, M. Slade, separate private communications, 2001) make a re-examination of this proposal particularly relevant.

The two necessary conditions on the core-mantle interaction for the experiment to work are: 1. The core must *not* follow the 88 day physical librations of the mantle. 2. The core must follow the mantle on the time scale of the 250,000 year precession of the spin in Cassini state 1 (See Peale, 1969 for discussion of Cassini states). We shall assume these two conditions are satisfied to develop the method and later establish the constraints on the core viscosity for which they are satisfied. Proposed mechanisms of core mantle coupling other than a viscous coupling do not frustrate the first condition.

The physical libration of the mantle about the mean resonant angular velocity arises from the periodically reversing torque on the permanent deformation as Mercury rotates relative to the Sun. The amplitude of this libration is given by (Peale, 1972),

$$\phi = \frac{3}{2} \left(\frac{B-A}{C_m} \right) \left(1 - 11e^2 + \frac{959}{48}e^4 + \dots \right), \quad (1)$$

where the moment of inertia in the denominator is that of the mantle alone since the core does not follow the librations. The core is assumed axially symmetric so it does not contribute to $B-A$. Dissipative processes will carry Mercury to rotational Cassini state 1 (where spin, orbit precessional and orbital angular velocities remain coplanar) with an obliquity θ close to 0° (Peale, 1988). This leads to a constraint,

$$K_1(\theta) \left(\frac{C-A}{C} \right) + K_2(\theta) \left(\frac{B-A}{C} \right) = K_3(\theta) \quad (2)$$

where the moment of inertia in the denominator is now that of the total planet since the core is assumed to follow the precession. Note that the precession here is not the relatively rapid precession of the spin about the Cassini state in the frame rotating with the orbit, which the core is not likely to follow, but it is the precession of the orbit (with the much longer period) in which frame the spin vector is locked if Mercury occupies the exact Cassini state.

The lowest order gravitational harmonics are expressed in

terms of the moment differences as follows.

$$\begin{aligned} C_{20} &= -\frac{C-A}{M_p a_e^2} + \frac{1}{2} \frac{B-A}{M_p a_e^2} = -(6.0 \pm 2.0) \times 10^{-5}, \\ C_{22} &= \frac{B-A}{4M_p a_e^2} = (1.0 \pm 0.5) \times 10^{-5}, \end{aligned} \quad (3)$$

where the numerical values are estimated for Mercury from Mariner 10 flyby data (Anderson, *et al.* 1986). Eqs. (3) can be solved for $(C-A)/M_p a_e^2$ and $(B-A)/M_p a_e^2$ in terms of C_{20} and C_{22} , determined by tracking the orbiting spacecraft. Substitution of the solutions of Eqs. (3) into Eq. (2) yields a numerical value for $C/M_p a_e^2$ since the K_i are known once the obliquity θ is measured.

Measurement of the amplitude ϕ of the physical libration determines $(B-A)/C_m$ (Eq. (1)) from which three known factors give

$$\left(\frac{C_m}{B-A} \right) \left(\frac{B-A}{M_p a_e^2} \right) \left(\frac{M_p a_e^2}{C} \right) = \frac{C_m}{C} \leq 1. \quad (4)$$

A value of C_m/C of 1 would indicate a core firmly coupled to the mantle and most likely solid. If the entire core or the outer part is fluid, $C_m/C \simeq 0.5$ for the large core size ($r_c \simeq 0.75R$) in current models of the interior (Cassen *et al.*, 1976).

If viscosity of the molten core material is the primary means of coupling the core motion to that of the mantle, two time constants for the relaxation of a relative molten core-solid mantle motion are given by (Peale, 1988).

$$\tau = \frac{r_c}{(\nu\dot{\psi})^{1/2}} \quad \tau = \frac{r_c^2}{\nu}, \quad (5)$$

where the first applies to small viscosities and the latter to large viscosities with $\dot{\psi}$ being Mercury's spin rate and ν the kinematic viscosity. If $\tau \gg 88$ days, the core will not follow the mantle during the latter's 88 day libration, and if $\tau \ll 250,000$ years, the core will follow the precession of the mantle angular momentum as it follows the orbit precession in Cassini state 1. These conditions correspond to

$$4 \times 10^{-4} < \nu < 5 \times 10^8 \text{ to } 4 \times 10^9 \text{ cm}^2/\text{sec}. \quad (6)$$

As this range includes all possible values for the viscosity of likely core material (*e.g.* Gans, 1972), the experiment should work unless some other type of coupling can force the core to follow the 88 day libration of the mantle.

To investigate this possibility, we consider pressure forces on uneven topography at the core-mantle boundary (CMB) (Hide, 1989), the torque exchanged between a non-axisymmetric solid inner core and the asymmetric mantle (Szeto and Xu, 1997) and magnetic coupling (Love and Bloxham, 1994; Buffett, 1992; Buffett *et al.*, 2000). For the first we assume the

MERCURY'S CORE: S. J. Peale et al.

torque exerted on irregular topography at the Earth's CMB accounts for the entire 5×10^{-3} second fluctuation in the length-of-day (LOD) on decadal time scales as proposed by Hide (1989). The maximum of this torque is then scaled to Mercury with the expression $T_M/T_\oplus = \rho_c u_M^2 r_c^3 / (\rho_\oplus u_\oplus^2 r_\oplus^3)$, where the ρ s are the fluid densities, the u s are the relative velocities at the CMB and the r s are the core radii. For an initial relative velocity between the core and mantle being the maximum expected from the mantle libration while the core is rotating uniformly at the mean spin rate, this scaling leads to synchronous rotation of core and mantle after 1.3 years, which is long compared to the 44 days for torque reversal. If the core-mantle torque is added to the equation of relative core-mantle motion, the effect on the forced libration amplitude of the mantle is essentially undetectable. Although the theory of Szeto and Xu (1997) shows in a model-dependent way that a gravitational coupling between a deformed solid inner core can affect the free libration of the mantle, the 88 day forced libration of the mantle is superposed on any larger librations with undiminished amplitude. For magnetic coupling, Love and Bloxham (1994) show that it is unlikely that such coupling could cause the millisecond variations in the LOD for the Earth. Since Mercury's field strength is several orders of magnitude smaller than the Earth's, and since we have already indicated that core-mantle coupling sufficient to cause the variations in the LOD for Earth, when scaled to Mercury, do not affect the 88 day mantle libration amplitude, Mercury's 88 day libration is not affected by the magnetic coupling. Similar conclusions follow when applying Buffett's (1992) model to Mercury.

Measured ranges of values of C_{20} , C_{22} are given in Eqs. (3), and values of the obliquity and of the libration amplitude corresponding to the extreme values of these harmonics are

$$1.7 \lesssim \theta \lesssim 2.6 \text{ arcmin} \quad 20 \lesssim \phi \lesssim 60 \text{ arcsec}, \quad (7)$$

where θ follows from the solution of Eq. (2) and ϕ from Eq. (1) with $\phi = .854(B - A)/C_m$ for $e = 0.206$ and $C_m/C = 0.5$ and $C/M_p a_e^2 = 0.35$ being assumed.

To estimate the required precision of the measurements for meaningful interpretation, we designate the four parameters whose nominal values are given in Eqs. (3) and (7) by η_i and write

$$\Delta \left(\frac{C_m}{C} \right) = \sum_i \frac{\partial}{\partial \eta_i} \left(\frac{C_m}{C} \right) \Delta \eta_i, \quad (8)$$

which gives a maximum uncertainty of

$$\left. \frac{\Delta(C_m/C)}{(C_m/C)^0} \right|_{\max} = \sum_i \left| f_i \frac{\Delta \eta_i}{\eta_i^0} \right| \approx 22\%, \quad (9)$$

where the superscript 0 indicates the nominal values of the parameters, $f_i = -0.83, 0.83, -1, -1$ respectively for the terms in Eq. (9) with $\eta_i = C_{20}, C_{22}, \theta, \phi$, and where the

numerical value corresponds to fractional uncertainties of 0.01, 0.01, 0.1, 0.1 respectively for the four parameters with nominal values $C_{20}^0 = -6 \times 10^{-5}$, $C_{22}^0 = 1 \times 10^{-5}$, $\theta^0 = 3 \text{ arcmin}$, and $\phi^0 = 30 \text{ arcsec}$ being assumed. If instead of the second of Eqs. (3), we assume $C_{22} = -C_{20}/8$ and $C/M_p a_e^2 = 0.35$, then $5.2 \gtrsim \theta \gtrsim 1.0 \text{ arcmin}$ for $2 \times 10^{-5} \lesssim -C_{20} \lesssim 1 \times 10^{-4}$ with the corresponding range of ϕ being shifted only slightly to smaller values. But because the angles are all small, the f_i are not significantly affected in the uncertainty estimate provided C_{22}/C_{20} remains approximately constant.

The maximum error would yield $C_m/C = 0.5 \pm 0.11$ which would distinguish the molten core. Since the numerical coefficients in Eq. (9) are not very sensitive to the nominal values of the parameters, the error estimates remain the same for other reasonable values of the parameters if the fractional uncertainty of each parameter is unchanged. If, on the other hand, we fix each parameter uncertainty to be that value derived from the above assumed fraction of the central value but let the nominal values go to the extremes in Eq. (9), $C_m/C = 0.5 \pm 0.24$ for all minimal nominal values, and $C_m/C = 0.5 \pm 0.065$ for all maximal nominal values. Even the worst case would distinguish a molten core, although the core size would not be well constrained.

Measurement of C_{20} and C_{22} to two significant figures and $\Delta\theta$ and $\Delta\phi$ to a few arcseconds will assure that meaningful bounds on C_m/C are obtained. Simulations of expected laser altimetry and spacecraft tracking data from the MESSENGER orbiter show that even better constraints on these parameters will be obtained (Smith and Zuber, 2001).

References

- Anderson, J.D., et al. (1986) *Icarus* **71**, 337.
 Buffett, B.A. (1992) *J. Geophys. Res.* **97**, 19581.
 Buffett, B.A. et al. (2000) *Science* **290**, 1338.
 Cassen, P.M. et al. (1976) *Icarus* **28**, 501.
 Gans, R.F. (1972) *J. Geophys. Res.* **77**, 360.
 Hide, R. (1989) *Phil. Trans. R. Soc. Lond. A* **bf 328**, 351.
 Love, J.J. and Bloxham, J. (1994) *Geophys. J. Int.* **117** 235.
 Peale, S.J. (1969) *Astron. J.* **74**, 483.
 Peale, S.J. (1972) *Icarus* **17**, 168.
 Peale, S.J. (1976) *Nature* **262**, 765.
 Peale, S.J. (1981) *Icarus* **48**, 143.
 Peale, S.J. (1988) In *Mercury*, (F. Vilas, et al. Eds.), 461, U. Arizona Press.
 Solomon, S.C. et al. (2001) *Planet. Space Sci.* In press.
 Smith, D.E., and Zuber, M.T., (2001) Mercury 2001 Conference.
 Szeto, A.M.K., and Xu, S., (1997) *J. Geophys. Res.* **102**, 27651.
 Zuber, M.T., and Smith, D.E. (1997) *Lun. Planet. Sci.* **XXVIII**.

RATIO OF SODIUM TO POTASSIUM IN THE MERCURIAN EXOSPHERE. A. E. Potter¹, C. M. Anderson², R.M. Killen³, and T.H. Morgan⁴ ¹National Solar Observatory, P.O. Box 26732, 950 N. Cherry Avenue, Tucson, AZ 85726-6732 apotter@noao.edu, ²Department of Astronomy, New Mexico State University, Las Cruces, NM 88003-8001, ³Southwest Research Institute, P.O. Drawer 28510, 6220 Culebra Road, San Antonio, TX 78228-0510, ⁴NASA HQ, 300 E Street SW, Washington, DC 20546-0001.

Introduction: Sodium (Na) and Potassium (K) atoms can be seen in the exosphere of Mercury and the Moon because they are extremely efficient at scattering sunlight. These species must be derived from surface materials, so that we might expect the ratio of sodium to potassium to reflect the ratio of these elements in the surface crust. This expectation is approximately borne out for the Moon, where the ratio of sodium to potassium in the lunar exosphere averages to be about 6 [1], not too far from the ratio in lunar rocks of 2 to 7 [2]. However, the ratio in the Mercury exosphere was found to be in the range 80 to 190 [3], and at least once, as high as 400 [1].

The sodium and potassium atoms seen in the Mercury exosphere represent a balance between production from the surface and loss to space. Only if the production efficiencies and loss rates for Na and K were equal, would the ratio of Na to K in the exosphere reflect the ratio in the surface rocks. Since a value of 100 or more for the ratio of sodium to potassium in the surface rocks seems very unlikely, the high values of the observed ratios suggests that either production efficiencies or loss processes for the two elements are not equivalent.

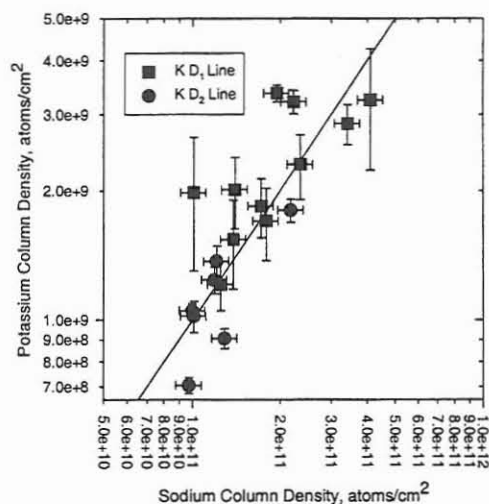
It does not seem likely that source processes should be different on the Moon and Mercury by an order of magnitude. This suggests that loss processes rather than source processes are the cause of the difference between the two. The major loss processes for sodium and potassium on Mercury are radiation pressure and trapping of photoions by the solar wind. Radiation pressure can reach 50-70% of surface gravity, and can sweep sodium and potassium atoms off the planet, provided they are sufficiently hot [4]. Photoionization followed by trapping of the ions in the solar wind is the other major loss process. Photoions are accelerated to keV energies in the magnetosphere, and may either intercept the magnetopause, and be lost from the planet, or impact the planetary surface [5]. Ions that impact the surface are neutralized, and are then available for resupply to the exosphere. The loss efficiency depends on characteristics of the magnetosphere that determine the fraction of the ions that are recycled by neutralization on the surface.

Over the preceding decade, we have collected sodium and potassium data for Mercury at irregular intervals. We analyzed these data to extract values for the Na/K ratio at a variety of conditions on Mercury.

Data Acquisition and Analysis: The instrument used was the stellar spectrograph of the 1.6-meter McMath-Pierce Solar telescope at the National Solar Observatory, Kitt Peak, Arizona. Spectra at resolutions ranging from 100,000 to 150,000 were recorded using an 800 x 800 element Texas Instruments CCD. Observations were made during daylight hours, using image slicers that collected all the light from the planet plus some surrounding skylight. The intensity of the sodium and potassium emissions in the spectra were determined by interpolating the background signal from one side of the emission line to the other and summing the difference from this baseline. The emissions were calibrated using the surface reflection of Mercury as the 'standard candle', using Hapke's model for planetary surface reflectivity and the optical constants derived for Mercury from photometric observations [6,7]. The details of the data processing to extract atom column densities from the spectra have been described in previous publications [9].

Results: The potassium column density is plotted against the corresponding sodium column density in Figure 1.

Figure 1. Sodium and potassium column densities for Mercury at various dates.

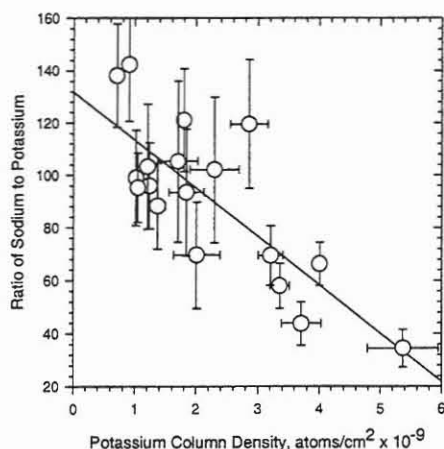


The mean ratio of sodium to potassium densities is 98 ± 20 . The scatter in the ratio suggests that potassium and sodium densities are not closely correlated to one another. We could invoke geographic differences of

Na/K ratio in the surface rocks to explain the scatter, but then we are still left with the original problem of ratio values a magnitude or more larger than seen for the Moon.

If the source and loss processes for sodium and potassium were closely correlated with one another, we expected that the Na/K ratio should be independent of potassium column density. However, this was not the case. Figure 2 shows a plot of the Na/K ratio versus the potassium column density.

Figure 2. Variation of Na/K ratio with potassium column density



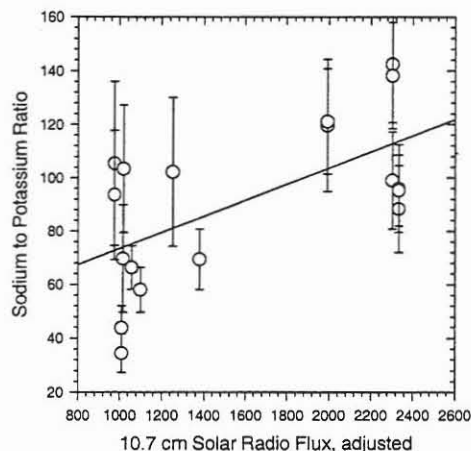
The Na/K ratio decreases with increasing potassium column density. This suggests that the loss rate for potassium varies differently than the sodium loss rate, and this difference is responsible for the range of values observed in the Na/K ratios.

Discussion: The two major loss processes for sodium and potassium on Mercury are radiation pressure and loss of photoions to the solar wind. Radiation pressure for sodium and potassium vary differently with heliocentric velocity of Mercury. However, we found no significant correlation of the Na/K ratio with radiation pressure, leaving differential loss to the solar wind as the probable cause of the Na/K ratio variations. We expect that the loss rate for potassium will be larger than for sodium because the potassium gyro-radius is larger than the sodium gyroradius by a factor of about 2.4. The larger radius makes it more likely that the ion will encounter the magnetopause before impacting the surface. The potassium loss rate must be from 3 to 10 times larger than the sodium loss rate to explain the observed Na/K ratios, assuming the ratio in the surface rocks is of the order of ten, and source efficiencies are similar.

The efficiency of loss of photoions to the solar wind must depend on the configuration of the magnetosphere, which in turn is dependent on the solar wind

and magnetic field parameters in the vicinity of Mercury. Unfortunately, there is no simple way to determine solar conditions at Mercury. However, it is reasonable to think that enhanced solar activity detected at the Earth will often be paralleled by enhanced activity at Mercury. We plotted the Na/K ratio as a function of the 10.7 cm radio flux from the Sun, which is often used as a measure of solar activity, in Figure 3.

Figure 3. Variation of Na/K ratio with 10.7 cm solar radio flux



There is some degree of correlation, with Na/K increasing with increasing radio flux, suggesting that increased solar activity led to a reduced potassium density relative to sodium density.

References: [1] Hunten, D. M. and Sprague, A. L. (1997) *Adv. Space Res.*, 19, 1551-1560. [2] Lodders, K. and Fegley, B. (1998) *The Planetary Scientist's Companion*, Oxford Univ. Press, 177. [3] Potter, A. E., Killen, R. M., and Morgan, T. H. (1997) *Planet. Space Sci.*, 45, 1441-1448. [4] Smyth, W. H. and Marconi, M. L., (1995), *Astrophys. J.* 441, 839-864. [5] Ip, W. -H. (1987) *Icarus* 71 441-447. [6] Hapke, B. (1986), *Icarus* 67, 264-280. [6] Veverka, J., Helfenstein, P., Hapke, B., and Goguen, J. D. (1988) *Mercury*, Univ. Arizona Press, 37-58

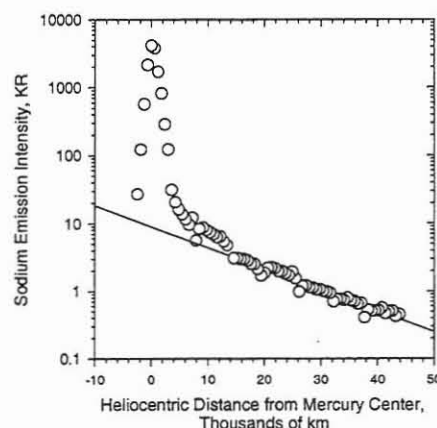
THE DISTANT SODIUM TAIL OF MERCURY. A. E. Potter¹, R.M. Killen², and T.H. Morgan³, ¹National Solar Observatory, P.O. Box 26732, 950 N. Cherry Avenue, Tucson, AZ 85726-6732 apotter@noao.edu, ²Southwest Research Institute, P.O. Drawer 28510, 6220 Culebra Road, San Antonio, TX 78228-0510, ³NASA HQ, 300 E Street SW, Washington, DC 20546-0001.

Introduction: Models of the sodium atmosphere of Mercury predict the possible existence of a comet-like sodium tail [1,2]. Detection and mapping of the predicted sodium tail would provide quantitative data on the energy of the process that produces sodium atoms from the planetary surface. Previous efforts to detect the sodium tail by means of observations done during daylight hours have been only partially successful because scattered sunlight obscured the weak sodium emissions in the tail [3]. However, at greatest eastern elongation around the March equinox in the northern hemisphere, Mercury can be seen as an evening star in astronomical twilight. At this time, the intensity of scattered sunlight is low enough that sodium emissions as low as 500 Rayleighs can be detected.

Observations: We used the 1.6 meter McMath-Pierce Solar telescope at the National Solar Observatory, Kitt Peak, Arizona to observe Mercury after sunset against a dark sky on June 03 and 04, 2000 and again on May 24 and 25, 2001. About eight observations at various positions downstream of Mercury were possible during the 30-40 minutes that Mercury could be observed. Images of the planet or adjacent regions of the sky were placed on a 10 arc sec by 10 arc sec image slicer at the entrance slit of the stellar spectrograph. Spectra of the sodium D lines were recorded on an 800 x 800 element Texas Instruments CCD at a resolution of about 150,000. At this resolution, sodium emission from terrestrial twilight glow is clearly separated from Mercury sodium emission. The resulting spatial-spectral images were analyzed to yield a 10 arc sec by 10 arc sec images of the sodium D emission with 1 arc second pixels. The general procedure for calibration of the data and extraction of the images has been previously described [4].

Results: Sodium D₂ emission was detected along the antisunward direction from Mercury for a distance of about 40,000 km. Observations on May 25, 2001 were directed towards determining the downstream profile of the emission. The intensity of the sodium D₂ in the antisunward direction for May 25, 2001 is plotted in Figure 1.

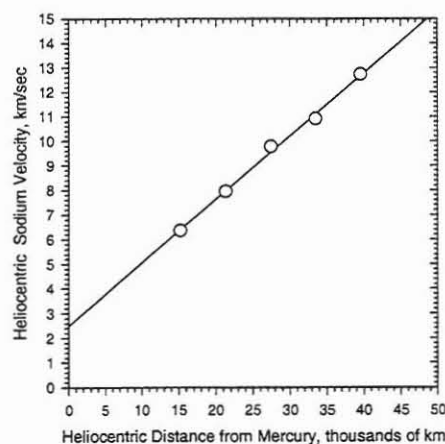
Figure 1. Emission intensity in the Mercury sodium tail, May 25, 2001



The Mercury phase angle on this date was 116.1° , so that the sodium tail was viewed at an angle of 63.9° to the line of sight. The observed apparent distances were divided by the sine of the phase angle to obtain heliocentric distances. The decay of sodium emission with distance results from photoionization of the sodium and lateral spreading of the sodium cloud.

Velocities of sodium atoms in the tail were measured from the Doppler shift of the emission lines. The observed shift is the vector sum of the initial Mercury-Earth shift and the additional shift resulting from solar radiation acceleration on the sodium atoms. Results are shown in Figure 2, where the heliocentric

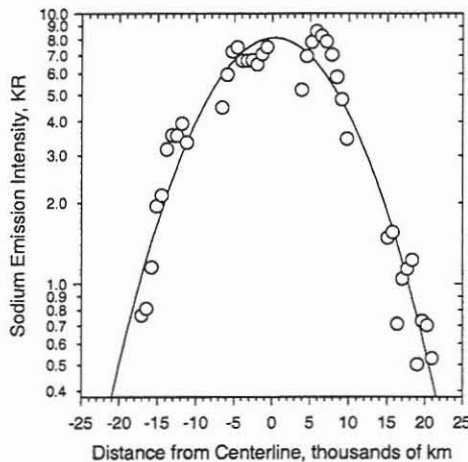
Figure 2. Heliocentric sodium velocity in the Mercury tail



velocity due to radiation acceleration is plotted against heliocentric distance.

Observations of the sodium tail were also accomplished on Jun 04, 2000. The Mercury phase angle on this date was 93.8° so that the tail was viewed at a near-right angle of 86.2° . This angle precluded the accurate measurement of heliocentric Doppler shifts in the sodium emission line caused by solar radiation pressure. However, these observations yielded information on the cross-sectional distribution of sodium in the tail. Results are shown in Figure 3, where the sodium emission intensity is plotted normal to the axis of the tail at a downstream heliocentric distance of about 17,500 km. At this distance, the tail has expanded to a diameter of nearly 40,000 km.

Figure 3. North-south cross-section of sodium tail June 04, 2000, 17,500 km downstream.



Discussion: The fact that an extended sodium tail can be detected is evidence that sodium is produced with sufficient energy to escape the planet. Smyth and Marconi [1] and Ip [2] found that sodium source velocities of 2 km/sec should be sufficient for sodium to escape from the planet under the influence of the maximum solar radiation acceleration. Extrapolation of the heliocentric velocities in the tail down to the location of Mercury suggests that sodium escaped Mercury with a residual velocity of about 2 km/sec in the antisunward direction. The north-south velocity can be estimated from the cross-sectional profile in Figure 3. If we assume that the heliocentric velocity data from Figure 2 apply to the June 04, 2000 observation, we can estimate the time required for the sodium to reach a downstream distance of 17,500 km, at which point, the cloud has expanded north-south to a diameter of about 40,000 km. From this, we estimate that the

initial north-south velocity of the sodium must have been 4-5 km/sec.

Radiation acceleration of sodium atoms on June 04, 2000 was 45% of surface gravity, and on May 25, 2001 was 40% of surface gravity. In both cases, the escape velocity of sodium is reduced from the nominal value of 4.25 km/sec to about 2.5 km/sec. Consequently, the appearance of a sodium tail with sodium velocities in the range 2-5 km/sec implies a source velocity in the range 4-7 km/sec, or 2.5-6.0 eV. Particle sputtering is a likely candidate for production of sodium atoms at these energies. The relatively high sodium velocity at right angles to the Mercury-Sun line suggests that much of the sodium is generated at high latitudes, rather than near the equator.

References: [1] Smyth, W. H. and Marconi, M. L., (1995), *Astrophys. J.*, 441, 839-864. [2] Ip, W. -H., (1986), *Geophys. Res. Lett.*, 13, 423-426. [3] Potter, A. E. and Morgan, T. H., (1997), *Adv. Space Res.*, 19, 1571. [4] Potter, A. E., Killen, R. M., and Morgan, T. H., (1999), *Planet. Space Sci.*, 47, 1441-1448.

RHEOLOGICAL INFERENCES ON THE MERCURIAN CRUST FROM CRATER MORPHOMETRIC ANALYSES OF THE MOON, MARS, AND MERCURY. L. V. Potts¹, R. R. von Frese^{1,2}, and C. K. Shum^{1,3}, Laboratory for Space Geodesy and Remote Sensing Research, The Ohio State University, 470 Hitchcock Hall, 2070 Neil Avenue, Columbus, OH 43210 (potts.3@osu.edu), ²Dept. of Geological Sciences, The Ohio State University, 275 Mendenhall Laboratory, 125 S. Oval Mall, Columbus, OH 43210, ³Dept. of Civil and Environmental Engineering and Geodetic Science, The Ohio State University, 470 Hitchcock Hall, 2070 Neil Avenue, Columbus, OH 43210.

Summary: Analysis of lunar free-air and terrain gravity correlations reveals distinct trends in transient cavity diameter estimates for the multi-ring basins. These trends clearly differentiate the farside crust as having been significantly more rigid than the nearside crust during bombardment time. The lunar crustal dichotomy is also reflected in local estimates of surface roughness developed from the root-mean-squared topography over 64° x 64° patches centered on the basins. For Mercury where gravity observations are lacking, this approach may be useful for developing insight on the rheological properties of the crust. As a test, the roughness values for multi-ring basins on Mercury and the highlands of Mars were evaluated. The trend for Mars is comparable to the trend noted for the less rigid lunar nearside crust. This result is also supported by the analysis of gravity data from the Mars Global Surveyor that suggests superisostatic mantle plugs may underlie the highland basins much like they appear to underlie the prominent basins of the lunar nearside. For Mercury the roughness trend is more comparable to the trend for the more rigid lunar farside crust. While the crust for Mercury was probably much hotter than the lunar crust during bombardment time, its dryness may have promoted strong rigidity.

Introduction: The transient cavity diameters for lunar multi-ring basins inferred from free-air and terrain gravity correlations are consistent with a nearside crust that was thinner, hotter and less rigid than the farside crust during bombardment time [2]. The strength difference between the near and farside lunar crust is clearly evident, for example in Figure 1, from the offset in the linear trends between these diameters and the crustal thickness variations [3].

Hence, in response to lunar impacts, superisostatic mantle plugs developed predominantly in the nearside side crust relative to the farside crust where subisostatic mantle plugs appear to predominate. Furthermore, significantly more basin rings and smoother topography developed in the nearside crust than in the more competent farside crust. These results suggest that local variations in surface topography may also provide insight on the rheological properties of the crust during bombardment time.

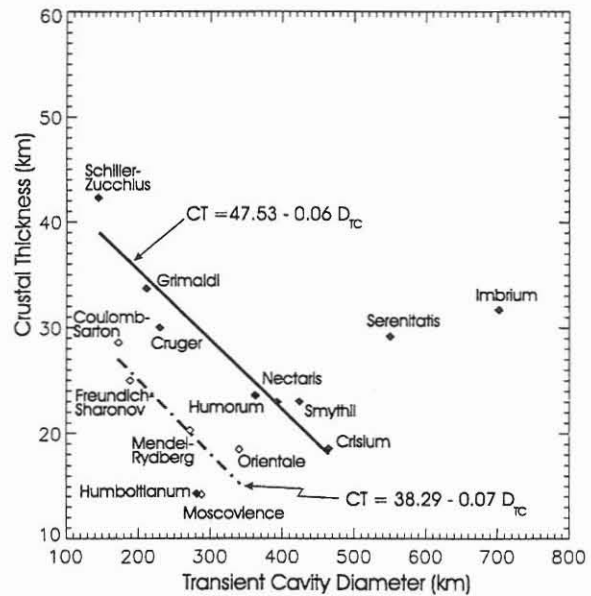


Figure 1. Comparison of transient cavity diameters and crustal thickness for lunar multi-ring basins. Nearside and farside basins are marked by solid and open symbols, respectively.

A similar analysis of the Mars Global Surveyor gravity and topography data suggests that the multi-ring basins of the highlands also may be underlain by superisostatic mantle plugs such as may contribute to the mascon bearing basins of the lunar nearside [5]. Accordingly, the rheological response of the crust of the Martian highlands appears to have been very similar to that of the lunar nearside during bombardment time.

For Mercury where gravity data are lacking, crater morphometric analysis may yield an alternate approach to developing insight on the rheological response of the Mercurian crust to the bombardment. For example, the morphology of Mercurian lobate scarps has provided insights on the planet's thermal evolution [8], the origin of compressional stresses that formed these structures [1], and other mechanical attributes of the crust [9]. In this study, the morphometric properties of multi-ring basins on the Moon, Mars, and Mercury are compared for insight on the rheological response of the Mercurian crust to ancient impacts.

Method: For the purposes of this analysis, crater roughness, (R_q), was evaluated by the root-mean-squared topography over $64^\circ \times 64^\circ$ patches centered on the multi-ring basins of the Moon, Mars, and Mercury. The roughness values were then compared with the transient cavity diameters (D_{TC}) of impact basins that in turn are closely related to the substrate rheology [3]. The transient cavity diameters are commonly inferred from photogeologic interpretation (e.g., [7]), although where gravity data are available (e.g., the Moon and Mars) they may also be interpreted from the terrain-correlated free-air gravity anomalies [4, 5].

Results: Lunar crater roughness values clearly reflect the dichotomized rheological properties of crust at the time of bombardment. In general, roughness values over farside impact basins are twice as large as those of the nearside basins. Moreover, crater roughness for lunar basins increases with increasing D_{TC} . Increased transient cavity diameters also are inversely correlated with age to reflect the growth of the lithosphere and substrate viscosity due to cooling [6]. In particular, the younger Crisium impact developed a larger transient cavity diameter on a more competent lithosphere than did the older Schiller-Zucchi impact, which developed a smaller D_{TC} on a weaker lithosphere with lower crustal viscosity and higher temperatures that facilitated viscous relaxation of crater topography [6, 4].

For Mars, crater roughness and D_{TC} reflect a trend similar to the one found for the nearside lunar basins. In particular, the older Argyre and Sirenum basins of Noachian age have lower roughness values and smaller transient cavities than the younger Hesperian impact basin that developed a larger D_{TC} .

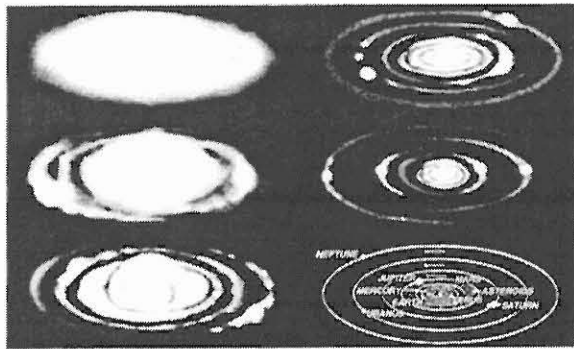
For Mercury, the relationship between roughness and D_{TC} for basins such as Beethoven appears to be similar to that estimated for the lunar farside basins. Hence, the rheological response of the Mercurian crust may have been comparable to that of the lunar farside during bombardment times. The dryness of the relatively hotter Mercurian crust may have facilitated its rigidity during bombardment.

References: [1] Hauck S. A. et al. (2000) *Eos Trans. AGU*, 81, S296. [2] Potts L. V. and von Frese R. R. B. (2001) *Eos Trans. AGU*, 82, S239. [3] Potts L. V. and von Frese R. R. B. (in-review) *JGR-E/2001/001456*. [4] Potts, L. V. and von Frese, R. R. B. (2001) *Eos. Trans. AGU*, 82, S241. [5] Potts, L. V. and von Frese, R. R. B. (2001) *Eos. Trans. AGU*, 82, S248. [6] Solomon, S.C. et al (1982) *JGR*, 87, 3975-4000. [7] Spudis, P. D. (1993). *The Geology of Multi-Ring Impact Basins: The Moon and Other Planets*, Cambridge Univ. Press. [8] Strom R. G. et al. (1975)

JGR, 80, 2478-2507. [9] Watters T.R. et al. (1998) *Geology*, 26, 991-994.

GAS RING CONDENSATION MODEL FOR THE ORIGIN AND BULK CHEMICAL COMPOSITION OF MERCURY. Andrew J.R. Prentice, Department of Mathematics & Statistics, P.O. Box 28M, Monash University, Victoria, 3800, Australia. *E-mail:* AJRP@vaxc.cc.monash.edu.au

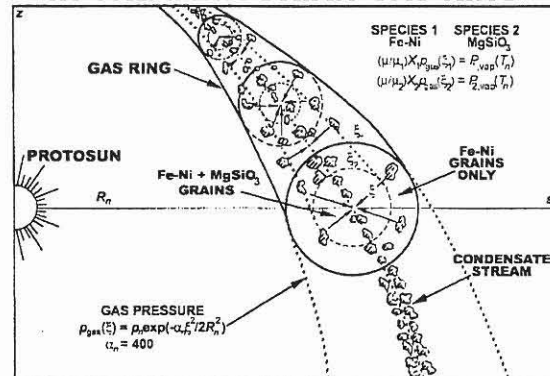
Introduction: Mercury's mean uncompressed density $\sim 5.3 \text{ g/cm}^3$ greatly exceeds that of its neighbour Venus, viz. $\sim 3.9 \text{ g/cm}^3$, suggesting bulk metal to rock mass fractions of 0.67:0.33 instead of 0.33:0.67 [1]. The latter values coincide with the ones expected on the basis of solar elemental abundances [2]. Lewis [3,4] discovered that a natural explanation for Mercury's high metal content existed within his equilibrium chemical condensation model applied to the solar nebula. Reconstruction of the mid-plane temperature T and pressure p_{neb} spatial distributions from all of the planetary density data, including the observation of water ice at Jupiter's orbit, suggested that T and p_{neb} vary with heliocentric distance R (in AU) according as $T(R) = 550 R^{-1.1 \pm 0.2} \text{ K}$ and $p_{\text{neb}}(R) = 10^{-4} R^{-3.85} \text{ bar}$ [5]. At the orbit of Mercury ($R = R_n$, $n=1$), $p_{\text{neb}} = 0.004 \text{ bar}$ and the condensation temperatures of the dominant metal [1: Fe-Ni] and rock [2: MgSiO₃] species are $T_{1,1} = 1520 \text{ K}$ and $T_{1,2} = 1490 \text{ K}$, respectively (see below). Hence if $T(R_1)$ lies just below $T_{1,2}$, only a small quantity of MgSiO₃ can condense and so a relative enrichment of metals occurs. Unfortunately, numerical studies of planetary accretion in a condensate disc show that Mercury drew its mass from a wide range of orbital radii [6]. Any initial chemical inhomogeneity at Mercury's distance would soon be blended out. Also, we need $T_{1,1} - T_{1,2} \geq 60 \text{ K}$ if the density enhancement is to be noticeable, even in the absence of radial mixing.



The Modern Laplacian Theory: According to the modern Laplacian theory of solar system origin, the planetary system condensed from a concentric family of orbiting gas rings [7,8]. Above is a visualization of the original Laplacian hypothesis. The rings were shed from the equator of the rotating proto-solar cloud (PSC) as a means for disposing of excess spin angular

momentum during gravitational contraction, starting at the orbit of Neptune. It is proposed that discrete gas ring shedding is achieved by the action of radial supersonic stress $\langle \rho v_r^2 \rangle = \beta \rho GM(r)/r$ arising from supersonic convective motion. Here $\rho = \rho(r)$ is the local gas density, $M(r)$ is the mass inside radius r , G is the gravitation constant and $\beta \sim 0.1$ is a constant parameter. The total radial stress is $p_{\text{tot}} = \langle \rho v_r^2 \rangle + p_{\text{gas}}$ where $p_{\text{gas}} = \rho \mathcal{R}T/\mu$ is the gas pressure and μ is the mean molecular weight. Now $F_t = \langle \rho v_r^2 \rangle / p_{\text{gas}}$ is greatest at the photosurface (ph). If $F_{t,\text{ph}} \gg 1$, a steep density inversion accompanies the degeneration of turbulence in the radiative outer layers of the PSC. The cloud now stores a dense shell of non-turbulent gas above its photosurface whose base density is a factor $(1+F_{t,\text{ph}})$ times that of the non-turbulent cloud of the same temperature T_{ph} . Choosing $F_{t,\text{ph}} \sim 35$, the orbital radii of successively detached rings match the observed mean geometric spacings of the planets. And as the gas pressure on the mean orbit ($s = R_n$, $z = 0$) of the Mercurian ring is now $p_1 = 36 p_{\text{neb}} \approx 0.14 \text{ bar}$, for which $T_{1,1} - T_{1,2} \approx 85 \text{ K}$, a strong fractionation between iron and silicates takes place.

IRON/SILICATE FRACTIONATION IN THE MERCURIAN GAS RING



The Gas Ring Condensation Model: Above is a schematic view of the gas ring cast off at Mercury's orbit. If the gas has uniform temperature T_n and specific angular momentum $(GM_n R_n)^{0.5}$, where M_n is the PSC mass, the ring has a toroidal structure with gas pressure distribution given by $p_{\text{ring}}(\xi) = p_n \exp(-f)$, where $f \equiv \alpha_n \xi^2 / 2 R_n^2$. Here $\alpha_n = \mu GM_n / \mathcal{R} T_n R_n \approx 400$ is a dimensionless constant and ξ is the local minor radius.

If $X_i (i=1,2)$ and μ_i are the mass fractions and molecular weights of species 1 and 2, the partial pressures

prior to any condensation are $p_{i,n}(\xi) = (\mu/\mu_i)X_i p_{ring}(\xi)$. At any radius ξ , condensation occurs provided that $p_{i,n}(\xi) \geq P_{i,vap}(T_n) \equiv \exp(B_i - A_i/T_n)$, where $P_{i,vap}$ are the thermodynamic vapour pressures and A_i, B_i are empirical constants. Typical values are $X_1/\mu_1 = 2.348 \times 10^{-5}$, $X_2/\mu_2 = 2.523 \times 10^{-5}$, $\mu = 2.379$ and (at 1600 K), $A_1 = 47820$, $B_1 = 16.130$, $A_2 = 63770$, $B_2 = 27.481$. Next, we define $T_{i,n}$ to be the condensation temperatures on the mean orbit where the partial pressures $p_{i,n}(0)$ are a maximum. We have $T_{i,n} = A_i/(B_i - \log_e(p_{i,n}(0)))$. It then follows that condensation is restricted to an inner torus $\xi \leq \xi_i$, where ξ_i is the solution of the equation $p_{i,n}(\xi_i) = P_{i,vap}(T_n)$. It is a simple matter now to show that the condensed mass fraction of species i is given simply by $X_{i,cond} = X_i\{1 - (1 + f_i)\exp(-f_i)\}$, with $f_i = A_i(1/T_n - 1/T_{i,n})$. This equation is also valid for gas rings which have a non-uniform orbital angular momentum distribution $h(s) = h(R_n)(s/R_n)^{2-q}$, where $h(R_n) = (GM_n R_n)^{0.5}$. Here s is the major cylindrical polar radius and $1.5 < q < 2$. Such rings have an elliptic minor crosssection.

After condensation has occurred, the solid grains settle onto the mean orbit R_n to form a concentrated stream. This 'focussing' property of the gas ring is a basic feature of the modern Laplacian theory [9]. Next, as there is no exchange of condensate material between adjacent gas rings, the chemical composition of each planet is uniquely determined by the thermal properties of its own formative ring. Mercury was thus able to enjoy the full benefit of the iron/silicate fractionation process that took place in its ring.

The Predicted Bulk Chemical Compositions:

The table below gives the temperatures T_n and mean orbit pressures p_n which come from a representative simulation of the contraction of the PSC which (1) leads to a sun having the observed mass, (2) accounts for the mean planetary spacings, and (3) leads to a bulk chemical composition for Mercury whose mean density matches the observed uncompressed value. If the PSC is assumed to contract homologously, then $T_n \propto R_n^{-0.9}$ [10,11]. The planet Mercury thus provides a valuable marker for calibrating the run of temperatures. Once this calibration is achieved, the bulk chemical composition of the other planets, including the cores of the gas giant planets, are effectively locked into place.

The last 2 columns of the table are the Fe-Ni-Cr-Co-V alloy mass fraction X_{metal} and the condensate mean density $\langle \rho_s \rangle$, in g/cm^3 . Aside from metal, the main chemical constituents of Mercury are $\text{Ca}_2\text{Al}_2\text{SiO}_7$ (mass fraction: 0.254) and MgAl_2O_4 (0.041). MgSiO_3 – Mg_2SiO_4 makes up only 0.009 of the mass. The main non-metal constituents of Venus are MgSiO_3 – Mg_2SiO_4 (0.499), SiO_2 (0.076), $\text{Ca}_2\text{MgSi}_2\text{O}_7$ (0.041) and MgAl_2O_4 (0.039).

Earth's orbit sees the appearance of (Fe-Ni)S (0.087) and tremolite (0.102). At Mars, nearly all Fe is tied up in (Fe-Ni)S (0.205) and Fe_2SiO_4 (0.180), whilst for the asteroids it is in (Fe-Ni)S (0.200) and Fe_3O_4 (0.193). Lastly, we note that Jupiter's orbit marks the initial condensation of H_2O ice. This makes up 0.341 of the condensate mass, along with 'asteroidal' rock (0.651) and graphite (0.008). Only 33% of the available H_2O vapour can solidify since T_n lies just 5.2 K below the H_2O condensation temperature on the gas ring mean orbit. This feature accounts for the 50%:50% rock:ice mass percents of Ganymede and Callisto [10,11].

Gas ring properties for the sub-Jovian planets

Planet	R_n/AU	T_n/K	p_n/bar	X_{metal}	$\langle \rho_s \rangle$
Mercury	0.387	1632	0.1334	0.670	5.29
Venus	0.723	911	0.0124	0.326	3.89
Earth	1.000	674	3.6×10^{-3}	0.257	3.83
Mars	1.524	459	7.2×10^{-4}	0.054	3.72
Asteroid	2.816	274	5.9×10^{-5}	0.009	3.67
Jupiter	5.203	163	4.9×10^{-6}	0.006	1.83

Conclusions: The original idea of Lewis, coupled with the gas ring model of planetary formation presented here, suggests that iron/silicate fractionation may indeed provide a valid explanation of the anomalously high metal content of Mercury. This model was first put forward one decade ago [12,13].

Acknowledgements: I thank Dr. John D. Anderson [NASA/JPL] for his continued encouragement and Mr David Warren [Tasmania] and the Australia Research Council for financial support.

References: [1] Reynolds R.T. and Summers A.L. (1969) *JGR*, 74, 2494–2511. [2] Anders A. and Grevesse N. (1989) *Geochim. Cosmochim. Acta* 53, 197–214. [3] Lewis J.S. (1972) *Earth & Planet. Sci. Letts.*, 15, 286–290. [4] Lewis J.S. (1974) *Science*, 186, 440–443. [5] Lewis J.S. (1988) in *Mercury* (eds. Vilas F. et al), Univ. Ariz. Press, 651–666. [6] Wetherill G.W. (1980) *Ann. Rev. Astron. Astrophys.*, 18, 77–113. [7] Prentice A.J.R. (1978) *Moon Planets*, 19, 341–398. [8] Prentice A.J.R. (1978) in *The Origin of the Solar System* (ed. Dermott S.F.), Wiley & Sons, 111–161. [9] Prentice A.J.R. (1980) *Aust. J. Phys.*, 33, 623–637. [10] Prentice A.J.R. (1996) *Earth, Moon & Planets*, 73, 237–258. [11] Prentice A.J.R. (2001) *Earth, Moon & Planets*, in press. [12] Prentice A.J.R. (1990) *Meteoritics* 25, 399–400. [13] Prentice A.J.R. (1991) *Proc. Astron. Soc. Aust.*, 9, 321–323.

LOW ALBEDO, BLUE, AND OPAQUE RICH SPECTRAL ANOMALIES IN THE MERCURIAN CRUST.M. S. Robinson¹ and B. R. Hawke², ¹Northwestern University, 1847 Sheridan Road, Evanston, IL, 60208²University of Hawaii, 2525 Correa Road, Honolulu, HI, 96822.

Introduction: Newly calibrated UV (375 nm) and orange (575 nm) Mariner 10 mosaics were interpreted to indicate compositional heterogeneities in the mercurian crust [1,2]. These studies interpreted the calibrated color data according to the view that ferrous iron lowers the albedo and reddens (relative decrease in the UV/visible ratio) a lunar or mercurian soil [3,4,5,6]. Soil maturation has a similar effect with increasing maturity: darkening and reddening a soil with addition of submicroscopic iron metal. In contrast, addition of spectrally neutral opaque minerals (i.e. ilmenite) results in a nearly perpendicular trend to that of iron and maturity: opaque minerals lower the albedo and *increase* the UV/visible ratio. By transforming the Mariner 10 color data (UV and orange mosaics) and thus separating these color trends into two separate parameter images sensitive to *a*) relative abundances of opaque minerals and *b*) combined maturity-and-iron spectral anomalies on the surface can be mapped. Utilizing these parameter maps and the color mosaics, we extend the previous work by identifying occurrences of a relatively low albedo, blue, and opaque rich material (LBO). In addition to the distinct spectral properties of the LBOs we find that this unit typically exhibits diffuse and patchy boundaries. The four best exposures are found stratigraphically below the Rudaki (4°S, 52°W) and Tolstoj (15°S, 165°) plains, and in the areas of Lermontov crater (16°N, 49°W) and Homer basin (1°S, 37°W). With the limited spectral and spatial resolution of the Mariner 10 dataset we cannot uniquely determine the origin of these deposits. However, our observations are most consistent with two theories. 1) The LBOs are a volumetrically significant rock type that composes portions of the crust though compositionally distinct from the average crust or 2) they are relatively thin blankets of pyroclastic material. In the rest of this paper will briefly describe the four best occurrences and discuss the merits of the two possible origins and their significance.

Homer Basin LBO: The Homer Basin LBO exhibits discontinuous, patchy, and diffuse boundaries (Fig. 1) while the central region is continuous. Certainly the color and morphology could represent a complex interfingering 3-D rock unit currently exposed through impact excavation. However, our observations are suggestive of a ballistically emplaced unit (either impact or explosive volcanism). For the Homer LBO there is no centralized impact crater that would

serve as source, though we cannot rule out the possibility that it could be a far flung deposit from a distant basin forming event. We note that the deposit straddles (Fig. 1, white arrow on right) a linear segment of a ring of Homer basin (black arrows) indicating a possible weakness in the crust that might allow ascending magma to reach the surface; morphology consistent

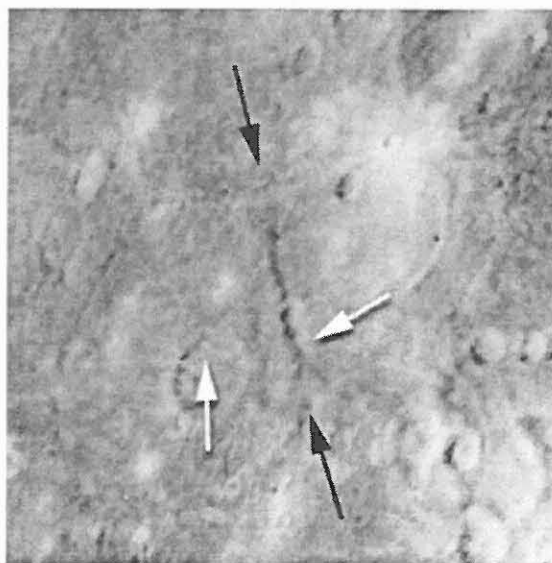


Figure 1. Homer Basin LBO shows up as blue in this spectral parameter image.

with explosive fissure eruptions. However, inside a neighboring crater (left white arrow) the LBO material exhibits a rather uncharacteristically sharp boundary: possibly a slide of loose material from the upper reaches of the crater, burial on the floor by a younger material, or a cross section of a thick component of the crust.

Lermontov Crater LBO: A portion of the LBO material seen northwest of the crater Lermontov (Fig. 2, - 160 km diameter) is somewhat concentric to a small impact crater (black arrow) and may represent material excavated from below during the impact. If this interpretation is correct then there exists a large subsurface rock unit that has been excavated and deposited on the surface. Examination of the albedo, iron-maturity parameter, and opaque index images suggest that the darkest and bluest material (white arrows) in this LBO is found asymmetrically on the southeastern periphery of the deposit. This might indicate that the original buried unit (LBO source) is

thin and near the surface (recall that target material near the surface typically composes the outer reaches of an ejecta blanket and material near the bottom of the crater usually ends up near the rim). Finally it may just be that the crater formed after the LBO and the pattern is simply a mixture of LBO material and average crustal material thrown out by the cratering event.

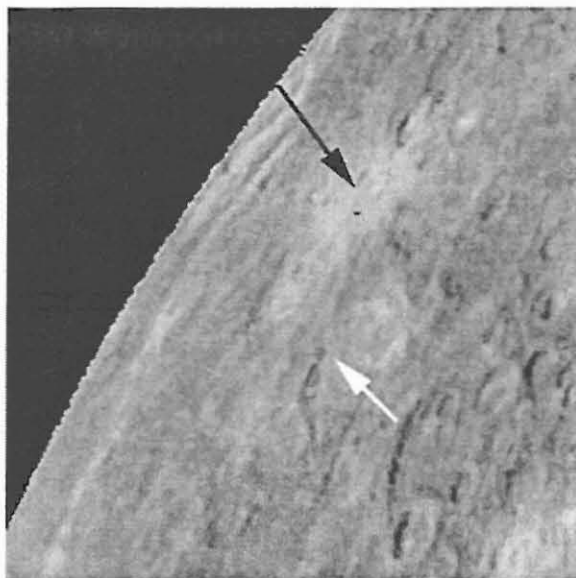


Figure 2. Lermontov crater (orange) and nearby LBO deposit (blue).

Rudaki and Tolstoj LBOs: The Rudaki and Tolstoj LBOs are both overlain by younger smooth plains deposits: their outer margins are similar to the LBOs (discontinuous, patchy and feathered) while their contacts with the younger smooth plains are sharp (see Fig 1 in Robinson and Lucey, 1997). The smooth plains have been interpreted as effusively emplaced lava flows that infilled pre-existing depressions and at these locations flooded and partially buried the older LBO deposits, resulting in the sharp interior contacts. In the Tolstoj basin, the LBO material corresponds to portions of the asymmetrical NE-SW trending Goya formation (interpreted as ejecta pattern of the basin) and the older intercrater plains [7,8]. This relation suggests that the LBO overlies two distinct morphologic units with significant age differences, most easily explained by as a relatively thin ballistically emplaced layer (either pyroclastic or impact ejecta). Alternatively, it may be the case that the Goya Formation is actually larger than mapped by Spudis and Guest (1988) and the unit boundaries need to be revised to correspond to the spectrally defined LBO boundary.

Significance: The Mariner 10 spectral information is extremely limited, however using the simple rela-

tionships explained above one can infer some relative compositional information from the data. The LBOs are consistent with a material that is relatively (to the average crust) enriched in opaque content (i.e. ilmenite) and might also have a slight enrichment in FeO (speculating on patterns seen in the maturity-plus-iron parameter). From known silicate mineralogy, telescopic spectra [9], and lunar analogy one can speculate that these materials are more mafic than the average mercurian crust. The easiest way of creating compositional heterogeneities in a planetary crust is through volcanic activity (intrusions, effusions, or pyroclastic) [10]. With current data we cannot make definitive identification of the emplacement mechanisms of the LBOs. However, the diffuse, patchy, and discontinuous morphology of the deposits argue for a ballistic emplacement, either from impact or explosive volcanism. Positive identification of pyroclastic deposits on Mercury would have dramatic implications for understanding the mercurian volatile inventory. Since Mercury formed so close to the Sun, presumably a very hot location, it should have been relatively depleted in volatiles. However, pyroclastic eruptions are driven by the release of gases such as CO, CO₂, SO₂, and H₂O. If the LBOs identified here are pyroclastic materials they represent key information regarding the environment in which Mercury formed.

No matter how the LBOs were formed, their spectral properties and morphology are most easily explained as compositional heterogeneities in the mercurian crust an important result on its own merit.

References: [1] Robinson, M.S. and P.G. Lucey, *Science*, 275, 197-200, 1997. [2] Robinson, M.S. and G.J. Taylor, *Meteoritics and Planet. Sci.*, 36, 841-848, 2001. [3] Hapke B, C. Christman, B. B. Rava, J. Mosher, *Proc. Lun. and Planet. Sci. Conf.*, 11, 817-821, 1980. [4] Rava, B., and B. Hapke, *Icarus*, 71, 397-429, 1987. [5] Cintala M.J., *Jour. Geophys. Res.*, 97, 947-973, 1992. [6] Lucey, P.G., D.T. Blewett, B. Ray Hawke, *Jour. Geophys. Res.*, 103, 3679-3699, 1998. [7] Schaber G.G. and J.F. McCauley, *Geological map of the Tolstoj quadrangle of Mercury (H-8)*, U.S. Geol. Surv. Map I-1199, 1980. [8] Spudis, P.D. and J.E. Guest, In *Mercury* (F. Vilas, C. R. Chapman, and M. S. Matthews, eds), University of Arizona Press, 118-164, 1988. [9] Vilas, F., C.R. Chapman, and M.S. Matthews, *Mercury*, University of Arizona Press, Tucson, AZ, 794 pp., 1988. [10] Basaltic Volcanism Study Project, *Basaltic Volcanism on the Terrestrial Planets*, Pergamon Press, New York, 1286 pp., 1981.

COMPLEXITY OF THE MERCURIAN CRUST. M.S. Robinson¹, G.J. Taylor², P.G. Lucey¹, and B.R. Hawke², Northwestern University, 1847 Sheridan Road, Evanston, IL, 60208, ²University of Hawaii, 2525 Correa Road, Honolulu, HI, 96822.

Introduction: Mercury has been visited by only one reconnaissance spacecraft, Mariner 10, over 25 years ago. This mission executed three flybys, but only imaged one hemisphere of the planet and carried no instruments capable of making direct compositional measurements of Mercury. Thus, our current state of knowledge concerning Mercury is in many ways similar to what we knew about the Earth's moon at the dawn of the space age [1]. From the Mariner 10 dataset [2] it is known that Mercury underwent a complex and rich geologic history. The planet is heavily cratered, tectonically deformed, volcanically resurfaced, and has an anomalously high bulk density (5.4 g/cm^3) suggesting an iron rich core that occupies a greater percent of its volume than that of the other terrestrial planets [cf. 3]. One of the outstanding problems remaining from the Mariner 10 mission is a first order cataloging of the compositional diversity of the mercurian crust.

Results. With the limited spectral and spatial resolution of the Mariner 10 images detailed compositional mapping is not possible. However, utilizing well known color properties of silicate materials [4,5,6] color differences can be mapped and reasonable 1st order compositional inferences can be made. In general, the addition of ferrous iron to a silicate mineral or glass darkens the material and reddens the visible spectral slope (decrease the UV/orange color ratio). This correlation of albedo and color ratio due to variations in ferrous iron is mimicked by variation of maturity of lunar, and likely mercurian, soils. In the course of the space-weathering maturation process, vacuum reduction of ferrous iron causes relatively blue immature soils to darken and spectrally redden [7]. Thus, since the Mariner 10 data examined here consist of only two wavelengths, it is problematic to decouple the spectral effects of ferrous iron content and maturity due to space weathering. However, increases in the abundance of spectrally neutral opaque minerals, such as ilmenite, tend to darken but decrease the spectral redness of silicate soils [4]. Rotation of two key parameters (UV/orange ratio versus orange albedo), so that the two trends are perpendicular to the axes, should result in decoupling the effects of ferrous iron plus maturity and opaque mineral abundance variations. This coordinate rotation results in images of two parameters, one sensitive to ferrous iron plus maturity and the other to opaque mineral content [8]. It is apparent that spatially coherent structures in the parameter one image (iron plus maturity) are mostly associated with crater rays and ejecta suggesting that this parameter is dominated by maturity variations and that major variations in ferrous iron are not present. The spatial patterns in the parameter two image are not

related to ejecta or crater rays and so are most likely compositional units formed by other geologic processes.

From newly calibrated Mariner 10 color mosaics and parameter images, units were mapped that correspond with previously mapped smooth plains deposits [8,9]. The smooth plains associated with Rudaki crater [$2^\circ\text{S}, 55^\circ\text{W}$] and Tolstoj basin [$16^\circ\text{S}, 163^\circ\text{W}$] can each be distinguished by their relatively smooth texture, embaying margins, and color properties. In both cases the smooth plains overlie material that is spectrally distinct (low albedo, relatively blue, opaque rich - LBO, see Robinson and Hawke, this volume). The Rudaki plains exhibit a relatively large (-30%) deficiency in the opaque parameter relative to the hemispheric median, while Tolstoj plains are only 5% below the hemispheric median. At both sites the maturity-plus-iron parameter of the smooth plains is equivalent to the hemispheric median.

The exact composition of the units seen in these data can only be inferred from lunar analogy as no samples or other relevant compositional data exist for Mercury. Regarding the smooth plains, the observation that they do show high contrast boundaries in the parameter and color ratio images implies they are compositionally distinct from the basement material (Table 1), supporting the previous morphological interpretation that some mercurian plains units are indeed volcanic in origin [reviewed in ref. 1]. These same plains (volcanic) units show relatively low contrast boundaries ($\pm 2\%$) in the maturity-plus-iron image relative to the hemispheric median, indicating that they have very similar FeO contents to the rest of the mercurian crust imaged by Mariner 10, for comparison, Mare Crisium on the Moon shows a -23% difference in a maturity-plus-iron image derived from Mariner 10 flyby images (Table 1). Earth-based remote sensing data indicate that the mercurian average FeO crustal abundance is $< 6 \text{ wt percent}$ [cf. 10] and more recently constrained to $\sim 3 \text{ wt\%}$ [11]. Since the plains are indistinguishable from the global median in the maturity-plus-iron parameter we infer that the observed lava plains have FeO abundances of $\sim 3 \text{ wt\%}$.

One of the most striking features imaged by Mariner 10 is the Kuiper-Muraski crater complex. Kuiper, superposed on the crater Muraski, is one of the youngest large impact craters on Mercury [1]. Kuiper has an opaque index equivalent to Muraski; but the iron-maturity parameter indicates that Kuiper is relatively immature, consistent with its fresher morphology, thus explaining the color difference (relatively blue). The opaque index for both materials is very low, possibly similar to a lunar soil formed from an anorthositic crust [8]. For the portions of Mercury

imaged in color the regions with the lowest opaque index are associated with craters, consistent with a layer at depth that is deficient in opaque minerals resurfaced by later processes. This layer may be analogous to an ancient lunar anorthosite crust. Consistent with this hypothesis Earth-based remote sensing has tentatively identified anorthosite on Mercury [12].

	<u>Opaque</u>	<u>Iron-maturity</u>
Crisium / Median ¹	1.45	0.77
Crisium / Basement	1.26	0.64
Basement / Median ¹	1.16	1.20
Rudaki / Median ²	0.70	1.02
Rudaki / Basement	0.55	1.08
Basement / Median ²	1.27	0.95
Tolstoj / Median ³	0.95	0.99
Tolstoj / Basement	0.70	1.14
Basement / Median ³	1.37	0.87

Table 1. ¹Median value for lunar eastern hemisphere imaged by Mariner 10 [13] ²Median value for mercurian incoming hemisphere, ³Median value for mercurian outgoing hemisphere [Table reproduced from 9].

Significance. The color anomalies found around the Kuiper-Muraski complex are consistent with a lunar like anorthositic crust that undergoes space weathering alteration [14]. This same spectral unit (the mature portion) makes up the majority of the mercurian crust imaged by Mariner 10. The observation that the smooth plains exhibit distinct color supports the interpretation that at least some of the smooth plains were volcanic in origin and have a composition different than that of "average Mercury". Finally the LBO spectral unit indicates a third compositional unit may exist.

These spectral and morphologic findings are significant not only in identifying color units and identifying smooth plains as lava flows, but that there are

compositional heterogeneities within the mercurian crust. The Mariner 10 data give a hint of the possible complexity of the mercurian crust. Advanced remote sensing instruments carried onboard future Mercury orbiters (MESSENGER, Bepi-Columbo) will be mapping in detail these and many other anomalies at a level of detail both spectrally and spatially such that their nature and origins may be understood.

References. [1] Spudis, P.D. and J.E. Guest, In *Mercury* (F. Vilas, C. R. Chapman, and M. S. Mathews, eds), University of Arizona Press, 118-164, 1988. [2] Vilas, F., C.R. Chapman, and M.S. Mathews, *Mercury*, University of Arizona Press, Tucson, AZ, 794 pp., 1988. [3] Basaltic Volcanism Study Project, *Basaltic Volcanism on the Terrestrial Planets*, Pergamon Press, New York, 1286 pp., 1981. [4] Rava, B., and B. Hapke, *Icarus*, 71, 397-429, 1987. [5] Hapke B., C. Christman, B. B. Rava, J. Mosher, *Proc. Lun. and Planet. Sci. Conf.*, 11, 817-821, 1980. [6] Lucey, P.G., D.T. Blewett, B. Ray Hawke, *Jour. Geophys. Res.*, 103, 3679-3699, 1998. [7] B. Hapke, W. Cassidy, E. Wells, *Moon* 13, 339, 1975. [8] Robinson, M.S. and P.G. Lucey, *Science*, 275, 197-200, 1997. [9] Robinson, M.S. and G.J. Taylor, *Meteoritics and Planet. Sci.*, 36, 841-848, 2001. [10] Vilas, F., C.R. Chapman, and M.S. Mathews, *Mercury*, University of Arizona Press, Tucson, AZ, 794 pp., 1988. [11] Blewett, D. T., Lucey, P. G., Hawke, B. R., Ling, G. G., and Robinson, M. S., *Icarus*, 129, 217-231, 1997. [12] A.L. Sprague, R.W.H. Kozlowski, F.C. Witteborn, D.P. Cruikshank, and D.H. Wooden, *Icarus* 109, 156 (1994). [13] Robinson, M.S., Hawke, B.R., Lucey, P.G. and Smith, G.A., *Jour. of Geophys. Res.*, 97, p. 18,265-18,274, 1992. [14] Cintala M.J., *Jour. Geophys. Res.*, 97, 947-973, 1992.



Figure 1. Mariner 10 color parameter image showing the incoming hemisphere and major features discussed in text. Red is formed as inverse of the opaque index (increasing redness indicates decreasing opaque mineralogy), green component is the iron-maturity parameter and blue shows the relative color (UV/orange ratio). North is to the right, Lermontov crater is ~160 km in diameter. The relatively blue material (LBO) is discussed in Robinson and Hawke (this volume).

The Magnetic Field and Magnetosphere of Mercury

C. T. Russell

Institute of Geophysics and Planetary Physics
and
Department of Earth and Space Sciences
University of California, Los Angeles

The most naive picture of planetary magnetism is that a planet is hottest at initial accretion, the iron sinks to the center, if there is sufficient energy a magnetic field is generated, and when the planet cools the dynamo stops. In this picture, the large rocky planets, such as the Earth, should have active dynamos and the small rocky planets such as Mercury should not. In fact Mercury does appear to have an active dynamo while larger bodies such as Mars and Venus do not. The dynamos in the cores of these two planets either ceased or in the case of Venus perhaps never began. Thus the story of the generation of a planetary magnetic field is more complicated than the naive picture and includes the effect of the crust and mantle in allowing the core to cool so that a solid inner core can condense and provide the energy for the dynamo.

We can learn about the interior of Mercury from its gravitational and magnetic fields but from the Mariner 10 flybys these have been but poorly constrained. In the case of the magnetic field the solution for the quadrupole moment is almost totally unconstrained. Orbiter measurements such as planned on the Messenger and Bepi Colombo missions are essential to determine the high order magnetic field.

The solar wind plasma confines Mercury's magnetic field to a teardrop-shaped region with a long tail in the antisolar direction. The solar wind is so strong at Mercury's orbit and the planetary magnetic moment so weak that the standoff distance of the solar wind flow at the subsolar point is very close to the planet's surface. Thus relative to the size of Mercury, already the smallest of the terrestrial planets, its magnetosphere is small. There is not much room for a radiation belt as we have on Earth. Nevertheless, the magnetosphere of Mercury is of great interest to magnetospheric physicists because of something else Mercury lacks, a significant atmosphere. In the terrestrial magnetosphere the magnetic field is rooted in a highly electrically conducting ionosphere caused by the ionization of the Earth's ionosphere. This ionosphere enables the coupling of the solar wind momentum with the atmosphere through the generation of current systems that close in the ionosphere. Since this coupling is not expected at Mercury, the nature of the solar wind magnetosphere interaction might be quite different at Mercury than at Earth. These differences in turn can provide insights into how the various magnetospheric processes work. Thus, one of the overall objectives of the Messenger and Bepi Colombo missions is to examine these magnetospheric processes. The sparse data obtained from the Mariner 10 missions in 1974 and 1975 indicates that analogues of terrestrial processes do occur at Mercury but that there are important differences in the ways in which these processes work.

REPEAT-ORBIT INTERFEROMETRIC PRECISION MEASUREMENT OF MERCURY OBLIQUITY. M. A. Slade¹, R. F. Jurgens¹, J.-L. Margot², and E. M. Standish¹, ¹JPL/Caltech, Mail Stop 238-420, Pasadena, CA 91109-8099 (marty@shannon.jpl.nasa.gov); ²Div. Geol. & Planet. Sciences, California Institute of Technology, Pasadena, CA 91125.

Introduction: Repeat-orbit or time-delayed interferometry has been widely used for SAR-based observations of such terrestrial phenomena as flow of glaciers and post-seismic displacements from radar on Earth-orbiting satellites and spacecraft. Repeat-orbit interferometry has also obtained fringes while investigating the measurement of topography of the Moon from Arecibo radar observations (Stacy, 1993). Because of the unique spin-orbit resonance of Mercury, the locus of the subradar point on Mercury crosses over itself many times per year. Moreover, the locus of the subradar track repeats these crossings from year to year over many years. Given the proper geometry, these subradar point crossings offer the opportunity for interplanetary repeat-orbit interferometry via Earth-based radar observations. The ephemerides of Mercury and Earth, and the orientation of the Earth, are all known to sufficiently high-precision with respect to "inertial space" to enable this kind of interferometry. This capability would merely be a curiosity, since Earth-based radar lacks the signal-to-noise to measure planetary-scale topography, except that the technique can be used to measure Mercury's obliquity (and possibly the forced libration in longitude). Combining very accurate measurements of the obliquity and the forced libration in longitude with Mercury-orbiter-based measurements of the low-order and degree Mercury gravity field can place constraints on the size and state of Mercury's fluid core (Peale, 1988; Peale *et al.*, this meeting).

Implications of a Fluid Core: Repeat-orbit interferometry thus holds out the hope that, in combination with improved values of c_{20} and c_{22} for Mercury (from, e.g., MESSENGER), the size and state of a putative fluid core can be determined. Why is it believed that Mercury still has a fluid core today? The idea of the existence of a fluid core is based on the magnetic field observed by Mariner 10 (Ness *et al.*, 1974), which is explained most simply by a dynamo in a currently molten core. If Mercury has such a core, then Peale (1988) has shown that dissipation will carry Mercury to rotational Cassini state 1 (in which the spin vector, the orbit precession angular velocity vector, and the orbit normal vector are all coplanar). The obliquity θ will be close to, but not exactly zero. Under plausible conditions, a libration ϕ in longitude will be forced with an 88 day period. The dynamics of Mercury's orbit, along with the Mariner 10 gravity field and associated uncertainties, imply the following ranges according to Peale (1997):

$$\begin{aligned} 1.7 \text{ arcmin} < \theta < 2.6 \text{ arcmin} \\ 20 \text{ arcsec} < \phi < 60 \text{ arcsec} \end{aligned}$$

The size and state of Mercury's core can be deduced from measurement of θ and ϕ along with determination of c_{20} and c_{22} of the gravity field to modest accuracy (Peale, 1997). Radar observations of radar-bright features at the poles of Mercury have improved the limits on the obliquity (Harmon *et al.*, 1994). Further improvements in the knowledge of the obliquity, and measurement of ϕ present a challenging problem in astrometry. Radar imaging of the equatorial regions of Mercury using sub-microsecond bauds may offer a method to measure ϕ that does not require interferometry. Following small radar features over many years may well be the best method for determining ϕ . Such imaging would be done each time the repeat-orbit interferometry was attempted. Additional imaging observations aimed just at measuring ϕ may prove to be necessary.

High Accuracy Interferometry: The repeat-orbit technique uses interferometry between observations of same subradar point on Mercury viewed in precisely the same geometry at greatly different times. The "baseline" is constructed from the two (very slightly different) positions of the observing point on Earth as viewed from Mercury. Figure 1 gives a cartoon of the geometry of the repeat-orbit interferometry. Detailed predictions will be shown for future observations through the year 2009. This technique uses some of the same mathematical formulations as Goldstein *et al.* (1988), and Zebker and Goldstein (1986). For example, the "fringes" for 0.2 microsecond baud voltage samples will appear in the first few Fresnel zones surrounding the subradar point on the two dates, and will begin about an hour before maximum intensity and fade completely over the hour following, if voltage data are obtained at the appropriate times (Goldstein, personal communication, 2000).

In summary, exploration of this technique seems warranted, given the high science value of contributing to constraints on the size and state of Mercury's (assumed) fluid region of its core.

References:

- Stacy, N. J. S., Ph.D. dissertation, Cornell Univ., Ithaca, NY, 1993.
- Ness *et al.*, *Science*, **185**, 151-154, 1974.
- Peale, S. J., in *Mercury*, 461-493, Univ. of Arizona Press, 1988.

REPEAT-ORBIT INTERFEROMETRY: M. A. Slade et al.

Peale, S. J., *Lun. Planet. Sci.* XXVII, 1081-1082, 1997.

Harmon *et al.*, *Nature*, **369**, 213-215, 1994.

Goldstein *et al.*, *Radio Science* **23**(4), 713-720, 1988.

Zebker and Goldstein, *JGR* **91**(B5), 4993-4999, 1986.

"INTERFEROMETRY" FOR OBLIQUITY, WOBBLE

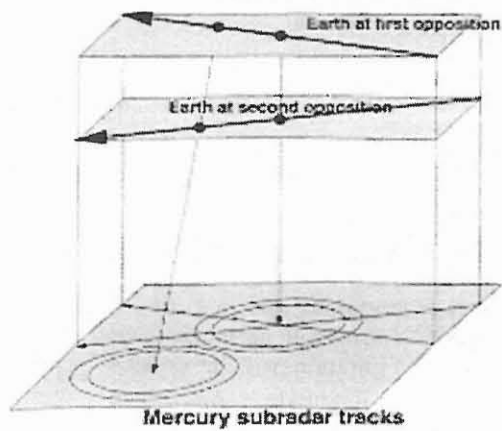


FIGURE 1. Mercury Repeat-Orbit Interferometry

ESTIMATING THE LIBRATION OF MERCURY BY REMOTE SENSING OF GRAVITY AND ALTIMETRY. D.E. Smith, NASA GSFC, Greenbelt, MD 20771 (dsmith@tharsis.gsfc.nasa.gov); M.T. Zuber, Massachusetts Institute of Technology, Cambridge, MA 02139; S.J. Peale, Dept. of Physics, U. of Calif., Santa Barbara, CA 93106; R.J. Phillips, Dept. of Earth and Planet. Sci., Washington U., St. Louis, MO 63130; and S.C. Solomon, DTM, Carnegie Inst. Of Washington, Washington, DC 20015.

One of the most intriguing scientific questions about Mercury is whether the planet possesses a liquid core [1,2]. One way that this can be ascertained [3-6] is through the measurement of the longitudinal libration of Mercury about its rotation axis. The MESSENGER mission to Mercury [7] will attempt this measurement by deriving the rotation of the planet from remotely sensed observations of the Mercury gravity field and the planet's shape. For a fully fluid core the libration is expected to be a ~350-m-amplitude oscillation (at the equator) about the mean rotation of the planet. Thus, the shape of the planet undergoes a librational oscillation in the same way that features on the surface participate in the motion. In this sense altimetric topography can be considered analogous to imaging, with the important exception that for altimetry, the long wavelengths corresponding to low degrees and orders in a spherical harmonic expansion, can be precisely determined from orbital measurements. The rotation of the planet thus introduces a time dependence of the topographic image in an inertial (*i.e.* fixed) reference frame and the libration is a variation in the planetary rotation rate, manifest as an oscillation of the topographic image. Similarly, gravity measures the distribution of mass within a planet and as such can be viewed as providing a vertically integrated "image" of the internal density structure. For a librating planet the gravitational field will also reveal a variation in the rotation rate, manifest as an oscillation of the field with respect to an inertial reference frame. While the long-wavelength gravity field contains contributions from the radial distribution of mass with depth, the long wavelength terms are most sensitive to the mass distribution of the deep interior. Thus, both the topography and the gravity independently can be used to determine the (irregular) rotation of a planet, although the topographical method measures the rotation of the crust while the gravity measures the rotation of the distributed mass, and these are not necessarily identical. For example, for a planet that contains a fluid outer core that is effectively decoupled from the mantle the gravity field will not librate in the manner of a solid body. The libration obtained from the variable rotation of the gravity field will represent a combination of contributions due to a librating mantle and a differentially rotating fluid core. Differential rotation of the Earth's inner core had been theoretically predicted from three-

dimensional geodynamical models [8] and subsequently reported from seismic observations [9]. A difference between the libration of the lithosphere as determined from altimetry and the deep interior as determined from gravity, if it could be detected, might provide further insight into the nature of core-mantle coupling.

Our approach for libration recovery differs from those proposed previously through imaging and landers in several ways, one of which is that it utilizes long rather than short-wavelength observations of the planet. To illustrate our reasoning we may consider a topographic signal of the form

$$H_m = A_m \sin(m\lambda), \quad (1)$$

where A is amplitude and m is the wave number, equivalent to spherical harmonic degree or order. The physical libration will be defined by a small rotation in longitude, $\Delta\lambda$, which will be characterized by a corresponding change in topography of ΔH_m , where

$$\Delta H_m = m A_m \cos(m\lambda) \Delta\lambda, \quad (2)$$

Planetary topography is known to exhibit fractal properties [10], in which the power of topography $\propto m^{-\alpha}$, where $\alpha \approx 2$. Thus

$$\frac{\Delta H_m}{\Delta H_{m+1}} \propto \frac{m}{m+1} \frac{(m+1)^2}{m^2} \times \text{hot} \propto \frac{m+1}{m} > 1, \quad (3)$$

where *hot* refers to higher order terms. Thus, in general,

$$\Delta H_m > \Delta H_{m+1}. \quad (4)$$

Expressions (3) and (4) demonstrate that, for a given $\Delta\lambda$, and a single surface feature, long wavelength topography should exhibit greater variance than short wavelength topography. Thus, if measured with sufficient accuracy, long wavelength topography provides a stronger signal for estimating librational motion than does short wavelength topography. A similar reasoning can be invoked for the gravity.

In order to determine the accuracy with which the libration can be derived from MESSENGER we conducted a simulation of the mission. Our initial simulation [11] was based on the mission design in place at the time of initial selection.

In the simulation the tracking data, sampled at 10-s intervals, were assumed to be unbiased, characterized by 1-mm/s noise (10x worse than typical X-band), and obtained by a single Deep Space Network (DSN) tracking station located at Goldstone, CA with a 5° lower elevation limit. No data were acquired within 1° of the sun, a time gap of nearly 2 days every 58 days. Except for the $C_{2,0}$ and $C_{2,2}$ terms the “truth” or *a priori* gravity model was generated from the model of normalized coefficients: $C_{l,m} S_{l,m} = 8.0 \times 10^{-5} / l^2$. The $C_{2,0}$ ($= -2.7 \times 10^{-5}$) and $C_{2,2}$ ($= 1.6 \times 10^{-5}$) terms are the only coefficients for which there are estimated values [12,13].

The simulated altimetry data, with 1-Hz sampling and ± 1 -m range precision, were unbiased, and acquired only when the spacecraft was over the northern hemisphere. The “truth” topography model was a modified 16x16 degree and order spherical harmonic model of the lunar topography with degree 1 terms set to zero (no center of figure/center of mass offset). Because the Moon is smaller than Mercury the model may have slightly greater spectral power than might be expected for a planet the size of Mercury by an amount equal to the ratio of the accelerations of gravity at the surface (~ 2.6). This does not affect the fundamental outcomes of the study as the method depends only on the longest wavelengths, where there is the greatest topographic power.

The initial spacecraft orbit was determined from the simulated tracking data in 10-day segments without any *a priori* knowledge of the gravity field. From a combination of nine of these arcs (1 Mercury year) we estimated values of an 8x8 gravity model. This model was adopted as the *a priori* model for subsequent analysis of all the tracking and altimetry data. Using this *a priori* gravity field the orbit of the spacecraft was determined for the full 4 Mercury years and normal equations developed from which a 16x16 gravity model was estimated. We then analyzed the altimetry data using orbits generated with the updated gravity field, formed normal equations for the topography, and solved for a 16x16 topography model that was adopted as the *a priori* topography model. Finally, all the tracking data and the altimetry data were reprocessed utilizing the new models and simultaneously analyzed to provide “final” gravity and topography models, and estimates for the libration amplitude and phase as detected in both the gravity and topography signals.

The ability to estimate the librations as measured in terms of returning to the initial value after starting from zero was:

- Amplitude of the physical libration in longitude:
 ± 0.000010 radians
- Phase of the physical libration:
 ± 0.000012 radians

This solution represents an 8% estimated accuracy of recovery of the expected amplitude and is adequate for discrimination of a liquid vs. solid core [3-6]. Although that early mission design was not significantly different from the present mission we are now in a position to include more details about the orbit, the spacecraft, and operational constraints and so are re-simulating the libration experiment.

Our simulation results provide confidence that librations as well as topography, gravity, rotation rate and pole position can be derived at levels adequate to ascertain core state from MESSENGER. Moreover, we note that separate analysis of gravity and topography observations has the potential to distinguish differences, should they exist, in the physical librations of the planetary surface and interior and may thus have implication for the existence of a solid component to the core. If such a situation existed and was detectable it would constrain models of core-mantle coupling, and have significant implications for internal dynamics and thermal state [6]. Updated simulation results will allow understanding of the libration sensitivity to the present orbit design, spacecraft parameters and operational constraints, and enable the approach to determining the core state to be refined.

References. [1] Solomon S.C. (1976) *Icarus*, 28, 509. [2] Schubert G. et al. (1988) in *Mercury*, p. 429, ed. F. Vilas, C.R. Chapman, and M.S. Matthews, Univ. Ariz. Press, Tucson. [3] Peale S.J. (1976) *Nature*, 262, 765. [4] Peale S.J. (1981) *Icarus*, 48, 143. [5] Peale S.J. (1988) in *Mercury*, p. 461, ed. F. Vilas, C.R. Chapman, and M.S. Matthews, Univ. Ariz. Press, Tucson. [6] Peale S.J. et al. (2001) this issue. [7] Solomon S.C. et al. (2001) *Planet. Space Sci.*, in press. [8] Glatzmaier G.A. and Roberts P.H. (1995) *Nature*, 377, 203. [9] Song X. and Richards P.G. (1996) *Nature*, 382, 221. [10] Turcotte, D.L. (1987) *JGR*, 92, 597-601, [11] Zuber M.T. and Smith D.E. (1997) *LPSC XXVIII*. [12] Anderson J.D. et al. (1987) *Icarus*, 71, 337. [13] Anderson J.D. et al. (1997) *Icarus*, in press.

MANTLE CONVECTION AND THERMAL EVOLUTION OF MERCURY REVISITED. V. S. Solomatov, C. C. Reese,
Department of Physics, New Mexico State University, Las Cruces NM 88003, USA.

Introduction. The question of whether mantle heat transport in Mercury occurs by conduction or convection [1-4] was eventually settled in favor of convection [5-7]. Indeed, quantitative estimates of convective instability and convective heat transport showed that convection must occur although not as vigorously as on Earth. Some observational support for convection was argued to be the presence of a magnetic field on Mercury which is easier to explain with mantle convection than without it. Rapid solidification of the iron core predicted by convective models and the cessation of generation of the magnetic field can be avoided if a sufficiently large amount of antifreeze is present (it can be anything but sulfur is the most likely candidate). Although convection seems to be a reasonable theory, results based mainly on studies of constant viscosity convection can substantially overestimate the vigor of convection [8]. Since previous models predicted a marginally unstable mantle with weak convection one might wonder if convection occurs at all for realistic rheologies. The goal of this study is to investigate models of mantle convection and thermal evolution of Mercury, which take into account realistic temperature- and pressure-dependent viscosity, partial melting and differentiation.

Viscosity. Viscosities of planetary mantles are poorly constrained, however, the range of viscosity laws suggested by laboratory experiments [9] provides a reasonable parameter space to explore provided the rheology is controlled by olivine. If pyroxene is the dominant component then the mantle is likely to be even stiffer. Also the choice between the two major mechanisms, diffusion creep and dislocation creep, depends on the grain size. The grain size in the Earth's upper mantle seems to be at the boundary between the two creep mechanisms. The transitional grain size seems to be close to the grain size observed in mantle xenoliths [9,10]. Since the pressure at the bottom of Mercury's mantle is less than 10 GPa, no phase transformations and thus no phase induced recrystallization is expected. Therefore, grain growth in olivine is controlled by coupled Ostwald ripening of all phases present in the mantle [11]. With all the uncertainties in the diffusion coefficients of major diffusing species (Si, Mg and O) the grain size is likely to be controlled by volume diffusion (meaning that the grain size varies as $\sim t^{1/3}$) and is about 1 cm during most of planetary evolution provided Ostwald ripening occurs at subsolidus temperatures. If temperatures exceeded solidus during some period of evolution the grain size would be bigger. In either case, this seems to be big enough to warrant the transition to dislocation creep [10]. Therefore, the argument that the mantle of Mercury might have a very small grain size and, as a result, an arbitrarily small viscosity (in the diffusion creep regime the viscosity depends on the grain size as $\eta \propto d^m$ where m is typically 2 or 3) is very difficult to support. The models presented below assume dislocation creep in which viscosity does not depend on the grain size.

Convection and thermal evolution. In the absence of

plate tectonics, mantle convection, if it occurs at all, must occur in the stagnant lid convection regime [10,12]. It is driven by small temperature differences, on the order of 200 K, controlled by rheology rather than by the total temperature difference across the convective layer (which would be the case for constant viscosity convection). Application of scaling relationships for temperature- and pressure- dependent viscosity convection [10] with realistic rheologies to Mercury suggests two conclusions. Firstly, convection occurs only at sufficiently high temperatures, higher than 1800 K for "dry" mantle and higher than 1500-1600 K for "wet" mantle. Secondly, the range of temperature (and the heat flux) in which convection occurs without melting (assuming dry solidus of peridotite) is very small: about 10 K (between 9 and 13 mW m⁻²) for "dry" mantle and 100 K (between 6 and 22 mW m⁻²) for "wet" mantle. Further insight into this problem can be obtained with the help of parameterized convection calculations of thermal evolution [13]. These calculations show (Figs. 1 and 2) that melting occurs during very early stages of evolution causing differentiation of nearly all (~90%) radioactive isotopes into the crust. The rest of thermal evolution occurs in the conductive regime.

Conclusion. Constraints on mantle rheology and convection with variable viscosity suggest that Mercury could be convective only during the very early stages of evolution accompanied by extensive melting and differentiation. Subsequently convection and melting have been absent and the planet has been cooling down in a conductive regime. In this model generation of the magnetic field on Mercury is due to mechanisms other than convection in the core including remnant magnetization caused by magnetic field generation during the early period of intensive cooling (similar to the model suggested in [14] for Mars) or by thermoelectric emf [6]. These calculations further support the conclusion that not only plate tectonics but any type of convection is difficult to sustain on the terrestrial planets [13,15].

References. [1] S. V. Majeve, *Astrophys. Lett.*, 4, 11-16, 1969; [2] G. Schubert et al., *Geophys. J. R. Astron. Soc.*, 18, 441-460, 1969; [3] R. W. Siegfried and S. C. Solomon, *Icarus*, 23, 192-205, 1974; [4] D. C. Tozer, *Philos. Trans. R. Soc. London Ser A*, 301, 381-399, 1979; [5] D. J. Stevenson et al., *Icarus*, 54, 466-489, 1983; [6] G. Schubert et al., in *Mercury*, Univ. Arizona, pp. 429-460, 1988. [7] T. Spohn, *Icarus*, 90, 222-236, 1991; [8] V. S. Solomatov, *Phys. Fluids*, 7, 266-274, 1995; [9] S.-I. Karato and P. Wu, *Science*, 260, 458-461, 1993. [10] V. S. Solomatov and L.-N. Moresi, *J. Geophys. Res.*, 105, 21795-21818, 2000; [11] V. S. Solomatov et al., *Phys. Earth Planet. Inter.*, in press. [12] V. S. Solomatov and L.-N. Moresi, *J. Geophys. Res.*, 101, 4737-4753, 1996; [13] C. C. Reese et al., *Icarus*, 139, 67-80, 1999; [14] F. Nimmo and D. J. Stevenson, *J. Geophys. Res.*, 105, 11969-11979, 2000. [15] C. C. Reese et al., *J. Geophys. Res.*, submitted.

MANTLE CONVECTION: SOLOMATOV AND REESE

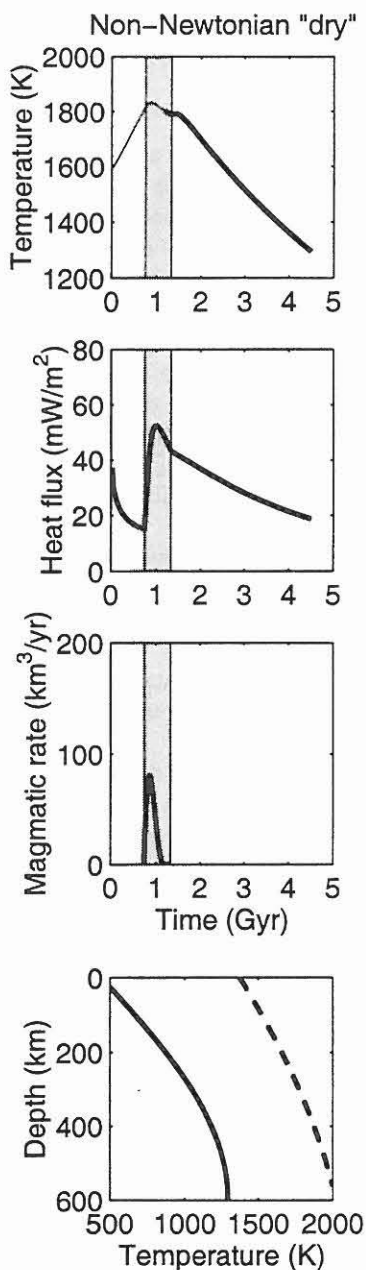


Figure 1: Thermal evolution models for Mercury. The viscosity is controlled by dislocation creep in "dry" olivine. The shaded region indicate the time interval when convection took place. Convective recycling of mantle material through supersolidus regions results in an extensive magmatism and fast depletion of the mantle in the abundances of radioactive elements. Thin line in top figure indicates supersolidus mantle. The bottom figure shows the present-day temperature distribution (solid line) and solidus (dashed line).

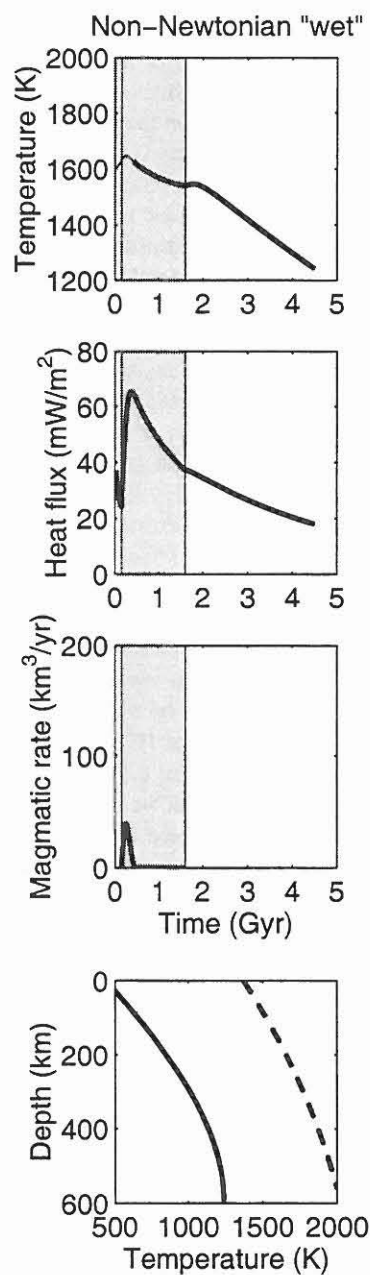


Figure 2: Same as Fig. 1 except that mantle is assumed to be "wet".

THE MESSENGER MISSION TO MERCURY. Sean C. Solomon¹, Ralph L. McNutt, Jr.², Robert E. Gold², Andrew G. Santo², and the MESSENGER Team, ¹Dept. of Terrestrial Magnetism, Carnegie Institution of Washington, 5241 Broad Branch Road, N.W., Washington, DC 20015 (scs@dtm.ciw.edu), ²The Johns Hopkins University Applied Physics Laboratory, Laurel, MD 20723.

Introduction. Mercury is an extraordinary planet. The closest planet to the Sun, Mercury has the largest diurnal range in surface temperature yet has polar deposits that may consist of water ice [1]. Mercury is the only planet locked in a spin-orbit resonance, an important though poorly understood constraint on dynamical and internal evolution [2]. It has the largest uncompressed density and, by inference, the greatest mass fraction of iron-nickel of any planet or satellite [3], a compositional anomaly that is a critical clue, not yet deciphered, to the processes by which the inner planets formed [4-7]. Mercury has a strong internal magnetic field and presumably a hydromagnetic dynamo in a fluid outer core [8], yet the known portion of the surface has a density of impact craters indicating that geological activity largely ceased early in planetary history [9]. Mercury's magnetic field gives rise to a small magnetosphere with many similarities to that of the Earth [10], yet the presence of only a tenuous atmosphere and ionosphere [11] and the greater proximity to the Sun affect the nature of solar wind interaction with the planet in ways still poorly discerned.

Mercury is also the least explored planet save Pluto. Most of what is known comes from the three flybys of Mercury by Mariner 10 in 1974 and 1975. With the recognition that gravity-assisted trajectories, using available launch and propulsion systems, now permit the insertion of a spacecraft into Mercury orbit [12], the need for the intensive exploration of the innermost planet has recently been recognized by both NASA and the European Space Agency.

MESSENGER, a *MERCURY* Surface, Space *ENVIRONMENT*, *GEOCHEMISTRY*, and *RANGING* mission to orbit Mercury for one Earth year after completing two flybys of that planet and two flybys of Venus, was selected for flight under NASA's Discovery Program in July 1999. The lead institutions for MESSENGER are the Carnegie Institution of Washington and the Applied Physics Laboratory of The Johns Hopkins University. Additional members of the MESSENGER consortium include Composite Optics, Inc., a leader in lightweight spacecraft structures, GenCorp Aerojet, a leader in spacecraft propulsion systems, Goddard Space Flight Center, the University of Colorado, and the University of Michigan. Co-engineered with planetary scientists from twelve institutions, MESSENGER has been designed to accommodate the severe near-Sun thermal environment and supply the required large spacecraft velocity change while enabling all scientific observations.

Scientific Objectives. A substantially improved knowledge of Mercury will add critical new insight into how terrestrial planets formed and evolved [13]. Determining the composition of Mercury, with its anomalously high ratio of

metal to silicate, will provide a unique window on the processes by which planetesimals in the primitive solar nebula accreted to form planets. Documenting the global geological history will elucidate the role of planet size as a governor of magmatic and tectonic history for a terrestrial planet. Characterizing the nature of the magnetic field of Mercury and the size and state of Mercury's core will allow us to generalize our understanding of the energetics and lifetimes of magnetic dynamos in solid planets and satellites. Determining the nature of volatile species in Mercury's polar deposits, exosphere, and magnetosphere will provide critical insight into volatile inventories, sources, and sinks in the inner solar system.

Key questions to be addressed by MESSENGER include:

What planetary formational processes led to the high metal/silicate ratio in Mercury?

What is the geological history of Mercury?

What is the nature and origin of Mercury's magnetic field?

What is the structure and state of Mercury's core?

What are the radar-reflective materials at Mercury's poles?

What are the important volatile species and their sources and sinks on and near Mercury?

These questions define the scientific objectives for the MESSENGER mission. In order of priority, these objectives are to determine (1) the chemical composition of Mercury's surface, (2) the planet's geological history, (3) the nature of Mercury's magnetic field, (4) the size and state of the core, (5) the volatile inventory at Mercury's poles, and (6) the nature of Mercury's exosphere and magnetosphere.

Measurement Requirements. The above scientific objectives in turn lead to the mission measurement requirements. Scientific objective (1) leads to a requirement for global maps of elemental composition at a resolution sufficient to discern major units and to distinguish material excavated and ejected by young impact craters from a possible veneer of cometary and meteoritic material. Information on surface mineralogy is also important. Objective (2) leads to the requirement for global monochrome imaging at a resolution of hundreds of meters or better, topographic profiles across key geological features from altimetry or stereo, and spectral measurements of major geologic units at spatial resolutions of several kilometers or better. Objective (3) leads to a requirement for magnetometry, both near the planet and throughout the magnetosphere, as well as for energetic particle and plasma measurements so as to isolate external from internal fields. Objective (4) can be met by

THE MESSENGER MISSION TO MERCURY: S. C. Solomon et al.

altimetric measurement of the amplitude of Mercury's physical libration and determination of the planet's obliquity and low-degree gravitational field. Objective (5) can be met by remote and in situ identification of neutral and charged species in the polar atmosphere, remote assessment of surface composition, particularly hydrogen content, and imaging and altimetry of polar-region craters. Objective (6) leads to measurement requirements for the identification of all major neutral species in the exosphere and all charged species in the magnetosphere.

Payload. The MESSENGER measurement requirements are met by a suite of seven scientific instruments plus the spacecraft communication system [14]. There is a dual imaging system for wide and narrow fields-of-view, monochrome and color imaging, and stereo; X-ray and combined gamma-ray and neutron spectrometers for surface chemical mapping; a magnetometer; a laser altimeter; a combined UV-visible and visible-near-infrared spectrometer to survey both exospheric species and surface mineralogy; and an energetic particle and plasma spectrometer to sample charged species in the magnetosphere. The payload instrumentation provides functional redundancy across scientific objectives and yields important consistency checks of results obtained with more than one instrument.

Mission Design. The baseline MESSENGER mission employs state-of-the-art chemical propulsion and multiple gravitational flybys to reach Mercury orbit [15]. Both the flybys and the orbit have been optimized to satisfy all scientific measurement requirements while meeting the constraints of the Discovery Program. The mission profile has also been carefully tailored to include prudent schedule and mass margins and reserves. Fuel reserves and maneuver schedule margins are included to provide resiliency and to minimize risk in mission implementation.

Launched in March 2004 by a Delta 2925H-9.5 during a 20-day launch window, MESSENGER executes two gravity assists at Venus and two at Mercury. Orbit insertion is accomplished at the third Mercury encounter in April 2009. The periapsis altitude and orbit phasing for MESSENGER are optimized to balance thermal constraints against science requirements. The inclination (80°) and initial latitude of periapsis (60°N) result from a complex set of trade-space optimizations driven by imaging, altimetry, and radio science coverage requirements as well as thermal input and spacecraft mass. A 12-hour orbit period simplifies thermal design and mission operations. The orbital phase of the mission lasts four Mercury years, needed to measure the amplitude of the planet's physical libration, and two Mercury solar days, which will permit repeat imaging coverage of all terrain for stereo measurements and high-resolution observations of targets of interest.

Spacecraft Description. MESSENGER is a 3-axis, zero-biased, momentum-controlled spacecraft [15]. The design approach makes use of commonly available materials,

minimal moving parts, and maximum heritage. Key design concepts include a ceramic-cloth sunshade, an integrated lightweight structure and high-performance propulsion system, dual phased-array antennas, a fully redundant integrated electronics module for avionics functions, a solar array incorporating optical solar reflectors, and a high level of spacecraft autonomy. The sunshade maintains the spacecraft at room temperature. The integrated structure and propulsion system provides ample mass margin. The solar array provides thermal margin even if the panels are inadvertently pointed directly at the Sun at Mercury perihelion.

Expected Data. During each of the flybys of Mercury, regions unexplored by Mariner 10 will be seen for the first time. New data will be gathered on Mercury's exosphere and magnetosphere as will the first information on surface composition. Approach and departure movies as well as high-resolution imagery will bring the mission alive to both the scientific community and the public at large. During the orbital phase of the mission, MESSENGER's science strategy shifts to detailed global mapping; characterization of the exosphere, magnetosphere, and polar deposits; acquisition of gravity field and topographic data for elucidation of internal structure; and focused investigation of high-priority targets identified during the flybys. All mission data will be provided to the Planetary Data System and the scientific community as soon as processing and validation are complete.

MESSENGER will be the first spacecraft to visit Mercury in more than 30 years and the first spacecraft to be placed in orbit about that planet. Observations to be made during the MESSENGER mission can be expected to advance substantially our knowledge of the formation and evolution of Mercury and of the terrestrial planets in general. Comparative studies of planetary geology, planetary composition and structure, magnetic field generation, and planetary exospheres and magnetospheres will all benefit from the new information that MESSENGER will reveal.

References. [1] J. K. Harmon, *Adv. Space Res.*, 19, 1487, 1997; [2] S. J. Peale, in *Mercury*, Univ. Arizona, p. 461, 1988; [3] R. W. Siegfried II and S. C. Solomon, *Icarus*, 23, 192, 1974; [4] S. J. Weidenschilling, *Icarus*, 35, 99, 1978; [5] A. G. W. Cameron, *Icarus*, 64, 285, 1985; [6] J. S. Lewis, in *Mercury*, Univ. Arizona, p. 651, 1988; [7] G. W. Wetherill, in *Mercury*, Univ. Arizona, p. 670, 1988; [8] J. E. P. Connerney and N. F. Ness, in *Mercury*, Univ. Arizona, p. 494, 1988; [9] R. G. Strom, *Adv. Space Res.*, 19, 1471, 1997; [10] C. T. Russell, D. N. Baker, and J. A. Slavin, in *Mercury*, Univ. Arizona, p. 514, 1988; [11] D. M. Hunten, T. H. Morgan, and D. E. Shemansky, in *Mercury*, Univ. Arizona, p. 562, 1988; [12] C.-W. Yen, *J. Astron. Sci.*, 37, 417, 1989; [13] S. C. Solomon et al., *Planet. Space Sci.*, in press, 2001; [14] R. E. Gold et al., *Planet. Space Sci.*, in press, 2001; [15] A. G. Santo et al., *Planet. Space Sci.*, in press, 2001.

MERCURY'S ATMOSPHERIC SPECIES. A. L. Sprague, Lunar and Planetary Laboratory, University of Arizona, Tucson, AZ 85721. sprague@lpl.arizona.edu

Introduction: Several attempts with ground-based spectrographs were made to find CO₂ in Mercury's atmosphere during the 1960's [1], [2], [3], [4], [5], and 1970's [6]. But no atmosphere was discovered until Mariner 10 identified H, He, and possibly O with the Broadfoot et al. airglow polychromator [7], [8] and made several upper limit measurements with the solar occultation instrument. In these experiments, limited wavelength bands were pre-determined based upon optical requirements and expectations of what might exist in an entirely unknown atmosphere. In 1985, Potter and Morgan were studying a phenomenon called the Ring effect observed as infilling of Fraunhofer lines in the reflected continuum from the lunar surface. For comparison, they shifted their view to Mercury and beheld significant emission lines, high above the continuum at 5890 and 5896 Å, the wavelengths of the Na resonance lines [9]. This discovery renewed ground-based spectroscopic search efforts that have resulted in discoveries of K [10], Ca [11] and set an upper limit on Li [12].

The pressure of the known atmosphere is $\sim 10^{-12}$ b. Mercury's atmospheric atoms do not collide appreciably with one another, only with the surface. For this reason it is called a surface-bounded-atmosphere. If the atmosphere were homogeneously distributed and its atoms assumed a Maxwellian speed distribution it would be called a surface-bounded-exosphere [13]. But Mercury's atmosphere has multiple speed distributions with some and perhaps all species having multiple speed components that result from differing source, release, and recycling mechanisms. All of the known species were discovered by measuring emission of some, but not all, strong resonance lines in the ultraviolet and visible wavelengths. It is likely that MESSENGER [14] will make new discoveries with its atmospheric and surface composition spectrograph (MASCS) [15] because it covers the region from 1150 to 6000 Å with no breaks and a resolving power sufficient to observe very faint resonant emissions above Mercury's limb.

Multiple Speed Components: For H and He at least two populations, a high temperature, and a low temperature, were discovered as a result of modeling density and height profiles above the planet's limb. For H, Shemansky and Broadfoot suggest that the cold component results from atoms hopping from the night side and the smaller warmer component is coupled to

the surface temperatures of the day side [16]. Smith et al. [17] modeled the Mariner 10 He data iteratively until nearly matching the line-of-sight abundances that were measured as the slit was moved across the disk of Mercury. The He extends to 3000 - 4000 km above the surface and thus was seen against the night side of the planet and well off the sub-solar limb. Departures from the model, which attempted to rigorously reproduce the gas-surface interactions of He adsorption and desorption across the day and night side, were significant pointing toward the conclusion that the physics of adsorption and desorption processes were not well understood.

For Na, detection of multiple speed components was possible because the width and shape of the resonant emission line could be observed and modeled. Potter and Morgan [18] partially resolved the hyperfine splitting of the strongest (D2) emission line—subsequent modeling revealed a large fraction of the atoms must be near a most probable speed of 600 m s⁻¹ with an equivalent temperature of ~ 500 K. The wings of the line could be fitted with a significant fraction of much hotter Na, perhaps up to ~ 1000 K. Later observations by Killen et al. [19], with latitudinal discrimination made at the Anglo Australian telescope in Australia, measured lines with no evidence of the hyper-fine structure, indicating much warmer temperatures and higher speed atoms with multiple speeds being observed at the equator and polar regions (~ 600 - 1500 K). Imaging searches have been made for an extended Na corona like that seen at the Moon by Mendillo et al. [20] but to date no evidence for such has been found at Mercury in images that have been properly corrected for "seeing smear".

For K, there are no measurements to date which can be used to discriminate multiple speed components.

For Ca, Bida et al. [11] observed off-planet emission above and beyond the southern hemisphere of Mercury using the sensitive KECK faint object spectrograph. Bida et al. interpret line widths to indicate high speed and hot ($\sim 12,000$ K) atoms. The equivalent most probable speed for Ca is ~ 2.2 km s⁻¹, still considerably less than Mercury's escape velocity of 4.2 km s⁻¹.

Atmospheric Sources, Release and Recycling Processes: The multiple speeds indicate that there are multiple physical processes at work to either provide new atoms to the atmosphere from meteoritic, surface

ATMOSPHERIC SPECIES: A. L. Sprague

and sub-surface materials or to provide atoms that have adsorbed on to the surface and are being released into the atmosphere for the second time or more. The processes that appear to be at work are meteoritic volatilization (including the steady flux of interplanetary dust particles), outgassing and thermal desorption (evaporation), photo-stimulated desorption (photodesorption), and some type of high energy sputtering. In addition, a small component of Na and other atomic species, especially H and He come from the Sun and are delivered to the surface as ions in the solar wind. Of course, Mercury's intrinsic magnetic field must, and does play a role because neutrals are quickly ionized and interact in unknown ways with the fields near and above the surface.

Differentiating One Source from Another:

There is a 3 decade history of theoretical models attempting to decipher the data in terms of the sources, release mechanisms and recycling processes [7], [8], [9], [10], [11], [12], [16], [17], [19], [21], [22], [23], [24], [25], [26] and others. Visual models of Na and K coronae by Smyth and Marconi [27] of different speed distributions have been helpful aids for exploration of the effects of solar radiation pressure and escape. Studies of ions and their interaction with the magnetosphere and Mercury's surface are very important [28], [29], [30].

Atmosphere and Surface Link: Obviously the atmosphere and surface are linked by the gas-surface interface--the place where collisions, storage, and release occur. But, does the atmospheric composition reflect, in any way, the surface composition? This has been a question devotedly studied by many, most of them referenced above, especially since the discovery of Na and K. The cosmochemical importance of knowing if Mercury is enriched in Na and K over amounts predicted by standard solar system formation theories is great. The issue of volatiles at Mercury is one of intense interest. Discoveries to be made by instrumentation on MESSENGER may permit us to finally answer the question driving ground-based telescopic observations of both surface and atmosphere.

References: [1] Spinrad, H. et al. (1965) *Astrophys. J.* 141, 1155 - 1160. [2] Moroz, V.I. (1965) *Soviet Astron. A.J.* 8, 882 - 889. [3] Binder, A.B. and Cruikshank, D.P. (1967) *Science* 155, 1135. [4] Bergstralh, J.T. et al. (1967) *Astrophys. J.* 149, L137 - L 139. [5] Belton, J.J.S. et al. (1967) *Astrophys. J.* 150, 1111 - 1124. [6] Fink, U. et al. (1974) *Astrophys. J.* 287, 407 - 415. [7] Broadfoot et al. (1974) *Science* 185, 166 - 169. [8] Broadfoot et al. (1976) *Geophys.*

Res. Lett. 3, 577 - 580. [9] Potter and Morgan (1985) *Science*, 229, 651 - 653. [10] Potter and Morgan (1986) *Icarus*, 67, 336 - 340. [11] Bida et al. (2000) *Nature*, 404, 159 [12] Sprague et al. (1996) *Icarus*, 123, 345 - 349. [13] Chamberlain and Hunten (1987) *Academic Press* Orlando, 481. [14] Solomon, S. et al. (2001) *In Press* [15] Gold, R.E. et al. (2001) *In Press*. [16] Shemansky and Broadfoot (1977) *Rev. Geophys. and Space Phys.* 15, 491 - 499. [17] Smith et al. (1978) *J. Geophys. Res.* 83, 3783 - 3790. [18] Potter and Morgan (1987) *Icarus*, 71, 472 - 477. [19] Killen et al. (1999) *Planet. and Space Sci.* 47, 1449 - 1458. [20] Mendillo et al. (1991) *Geophys. Res. Lett.* 18, 2097 - 2100. [21] Sprague et al. (1990) *Icarus*, 84, 903 - 105. [22] Sprague (1992a) *J. Geophys. Res.* 97, 18257 - 18264 [23] Sprague (1992b) *J. Geophys. Res.* 98, 1231. [24] Killen and Morgan (1993) *J. Geophys. Res.* 98, 23589 - 23601. [25] Killen et al. (2001) *J. Geophys. Res.* *In Press*. [26] McGrath et al. (1986) *Nature*, 323, 696 - 697. [27] Smyth, W.H. and M.L. Marconi (1995) *Ap. J.* 441, 839 - 864. [28] Christon et al. (1987) *Magnetotail Physics*, Johns Hopkins University Press. [29] Cheng et al. (1987) *Icarus* 71, 430 - 440. [30] Ip, W.H. (1993) *Astrophys. J.* 356, 675 - 681.

Acknowledgments: I would like to acknowledge all the people whose work on Mercury's atmosphere, or related to Mercury's atmosphere I did not reference in this brief abstract.

MID-INFRARED SPECTROSCOPY OF MERCURY'S SURFACE WITH BASS. A. L. Sprague¹, R. W. Russell², D. K. Lynch², A. L. Mazuk², K. L. Donaldson¹. ¹Lunar and Planetary Laboratory, University of Arizona, Tucson, AZ 85745, sprague@lpl.arizona.edu, ²Aerospace Corporation, El Segundo, CA, 90245-4691.

Introduction: Measurements of Mercury's thermal emission spectrum were made at the 3 m NASA Infrared Telescope Facility (IRTF) in Mauna Kea, Hawaii on March 21 and 22, 1998, and on May 11 and 12, 1998. The physical parameters of the observations are given below in Table I.

Table I

	21 Mar 1998	12 May 1998
	22 ^h UT	20 ^h UT
Elongation	E18°	W25°
Right Asc.	1 ^h 7 ^m 4.75 ^s	1 ^h 44 ^m 12.6 ^s
Dec.	9° 56' 15.4"	7° 32' 13.4"
Helio. Dis. AU	0.3260874	0.4325478
Geo. Dis. AU	0.8564186	0.9648811
Diam.	7.85"	6.97"
Frac. Ill.	0.363	0.558
Phase Angle	105.9°	83.3°
sub-E Lat.	-5.99°	0.44°
sub-E Long.	106.3°	58.0°
sub-Sol Lat.	0.0°	-0.0°
sub-Sol Long.	0.3°	141.3°

The major purpose of the observations was to obtain information regarding the physical and chemical properties of Mercury's surface materials. In theory telescopic mid-infrared observations of planetary surfaces should yield spectral features that can be assigned to know Reststrahlen and other mineralogically caused features [1,2]. When taken as a whole, however, differences between the 14 published spectra obtained with different instruments exhibit differences which cannot be explained easily by differences in the chemical make up of Mercury's soils, rocks and minerals observed. Thus, another purpose of these observations was to compare thermal emission spectra from the BroadBand Array Spectrograph (BASS) on the IRTF to those obtained by four other telescope, circular variable filter (CVF), and spectrograph configurations: 1) the AT1 CVF on the IRTF [1] 2) the High Resolution Grating Spectrometer (HIFOGS) from the IRTF [2] that exhibited spectral features resembling silicate Reststrahlen bands, transparency features, and from the 1m, Kuiper Airborne Observatory (KAO), in one case from 5 - 7 μ m, a significantly high emission feature [3]. The BASS spectra are also compared to those obtained with the McMath Pierce 1.5m Solar Tele-

scope on Kitt Peak with the Fourier transform spectrometer (FTS) [4], and to a spectral composite from mid-infrared (8 - 13 μ m) images obtained with the Mid-Infrared Array Camera (MIRAC) and the Steward Observatory 2.4m telescope on Kitt Peak [5]. All comparisons are inexact because of different viewing geometry on Mercury (sub-solar longitude and sub-Earth longitude), spectrograph aperture size (which can either isolate a portion of the illuminated surface or include the entire Earth-facing disk of Mercury), diffraction limit of the telescope used which is a function of telescope mirror diameter (limits the spatial resolution on the surface), and spectrograph resolving power ($\lambda/\Delta\lambda$). A comparison of telescope and spectrograph parameters is given in Table II.

Table II

Reference	[1]	[2]	[3]	[4]	[5]	[6]
Telescope diameter (m)	3	3	1	15	24	3
Diffraction limit at 10 μ m (arcseconds)	0.73	0.73	22	15	09	0.73
Spectrograph resolving power at 10 μ m	~40 CVF	~250 grat-ing	~250 grat-ing	~10 ⁴ FTS	~40 CVF	~50 prism
Spectrograph aperture size	slit 0.5 x 3	1, 0.5	3	>10	0.5	3
Mercury diameter (arcseconds)	7.7	7.9	6.5	7.7, 7.6	8.8	8.7
Fraction illuminated	0.6, 0.6	0.5, 0.3	0.5, 0.5	0.6, 0.6, 0.7	0.4, 0.4	0.4, 0.6

Instrumentation: The Aerospace Corporation's broadband array spectrograph (BASS) was used for these measurements. The BASS instrument is a low resolution spectrograph that covers the 2.9 to 13.5 μ m spectral region. The instrument consists of two 58 - element Blocked Impurity Band (BIB) detector arrays, two uniquely curved prisms, two mirrors, a beam splitter and the field optics. The BIB arrays have high

quantum efficiency, high responsivity, and are sensitive to less than $28\text{ }\mu\text{m}$. This along with the rest of the uniquely designed instrument, gives a background-limited instrument that can simultaneously scan the entire spectral region at once with a resolving power of ~ 50 .

Results: Spectra for the two dates and unique surface regions sampled exhibit different features. They are both much smoother than the spectra obtained with HIFOGS from the IRTF [2] and from the KAO [5], yet show more structure than the FTS spectra [4]. One difference between the BASS [6] and FTS [4] measurements is the short wavelength end of the spectrum. Measurements by Cooper et al. [4] do not cover the region of the Christiansen emission maximum if it is present short of $8\text{ }\mu\text{m}$. The BASS data begin at $5\text{ }\mu\text{m}$ and show a Christiansen emission maximum near $8\text{ }\mu\text{m}$ consistent with [1] and [2]. The composite spectrum of Sprague et al. [5] did not cover the spectral region short of $8.13\text{ }\mu\text{m}$.

References: [1] Tyler, A.L. et al. (1988) *GRL*, 15, 8, 808-811. [2] Sprague et al. (1992) *Icarus*, 109, 156 - 167. [3] Emery et al. (1998) *Icarus* 136, 104 - 123. [4] Cooper, B. et al. (2001) *JGR*, *In Press*. [5] Sprague et al. (2000) *Icarus* 147, 421 - 432. [6] Sprague et al. (1996) *Bull. Amer. Ast. Soc.*, 30, 3, 50P.06 (1998).

Acknowledgments: We thank the IRTF observing technicians for their extra day-time observations required to obtain these Mercury spectra and Mike Sitko for his help at the telescope.

THE GEOLOGICAL HISTORY OF MERCURY Paul D. Spudis, Lunar and Planetary Institute, 3600 Bay Area Blvd., Houston TX 77058; spudis@lpi.usra.edu

The Mariner 10 mission in 1974 mapped about half the surface of Mercury. On the basis of these data, we have a first-order understanding of the geology and history of the planet [1,2]. Mercury's surface shows intercrater plains, basins, smooth plains, craters, and tectonic features (Figure 1).

Intercrater plains Mercury's oldest surface is its intercrater plains [1,3], which are present (but much less extensive) on the Moon. The intercrater plains are level to gently rolling terrain that occur between and around large craters. The plains predate the heavily cratered terrain, and have obliterated many of the early craters and basins of Mercury [1,4]; they probably formed by widespread volcanism early in mercurian history.

Craters Mercurian craters have the morphological elements of lunar craters: the smaller craters are bowl-shaped, and with increasing size, they develop scalloped rims, central peaks, and terraces on the inner walls [3]. The ejecta sheets have a hilly, lineated texture and swarms of secondary impact craters. Fresh craters of all sizes have dark or bright halos and well developed ray systems. Although mercurian and lunar craters are superficially similar, they show subtle differences, especially in deposit extent. The continuous ejecta and fields of secondary craters on Mercury are far less extensive (by a factor of about 0.65) for a given rim diameter than those of comparable lunar craters. This difference results from the 2.5 times higher gravitational field on Mercury compared with the Moon [3]. As on the Moon, impact craters on Mercury are progressively degraded by subsequent impacts [1,4]. The freshest craters have ray systems and a crisp morphology. With further degradation, the craters lose their crisp morphology and rays and features on the continuous ejecta become more blurred until only the raised rim near the crater remains recognizable. Because craters become progressively degraded with time, the degree of degradation gives a rough indication of the crater's relative age [4]. On the assumption that craters of similar size and morphology are roughly the same age, it is possible to place constraints on the ages of other underlying or overlying units and thus to globally map the relative age of craters (Fig. 1).

Basins At least 15 ancient basins have been identified on Mercury [4]. Tolstoj is a true multi-ring basin, displaying at least two, and possibly as many as four, concentric rings [4,5]. It has a well-preserved ejecta blanket extending outward as much as 500 km from its rim. The basin interior is flooded with plains that clearly postdate the ejecta deposits. Beethoven has only one, subdued massif-like rim 625 km in diameter, but displays an impressive, well-lineated ejecta blanket that extends as far as 500 km. As at Tolstoj, Beethoven ejecta is asymmetric. The Caloris basin is defined by a ring of mountains 1300 km in diameter [4,6,7]. Individual massifs are typically 30 to 50 km long; the inner edge of the unit is marked by basin-facing scarps [7]. Lineated terrain extends for about 1,000 km out from the foot of a weak discontinuous scarp on the outer edge of the Caloris mountains; this terrain is similar to the "sculpture" surrounding the Imbrium basin on the Moon [4,7]. Hummocky material forms a broad annulus about 800 km from the Caloris mountains. It consists of low, closely spaced to scattered hills about 0.3 to 1 km across and from tens of meters to a few hundred meters high. The outer boundary of this unit is gradational with the (younger) smooth plains that occur in the same region. A hilly and furrowed terrain is found antipodal to the Caloris basin, probably created by antipodal convergence of intense seismic waves generated by the Caloris impact [8].

Smooth plains The floor of the Caloris basin is deformed by sinuous ridges and fractures, giving the basin fill a grossly polygonal pattern. These plains may be volcanic, formed by the release of magma as part of the impact event, or a thick sheet of impact melt. Widespread areas of Mercury are covered by relatively flat, sparsely cratered plains materials [4, 9]. They fill depressions that range in size from regional troughs to crater floors. The smooth plains are similar to the maria of the Moon, an obvious difference being that the smooth plains have the same albedo as the intercrater plains. Smooth plains are most strikingly exposed in a broad annulus around the Caloris basin (Fig 1). No unequivocal volcanic features, such as flow lobes, leveed channels, domes, or cones are visible. Crater densities indicate that the smooth plains are significantly younger than ejecta from the Caloris basin [4]. In addition, distinct color units, some of lobate shape, are observed in newly processed color data [10]. Such relations strongly support a volcanic origin for the mercurian smooth plains, even in the absence of diagnostic landforms [4,9,10].

Tectonic features Lobate scarps are widely distributed over Mercury [4,9,11] and consist of sinuous to arcuate scarps that transect preexisting plains and craters. They are most convincingly interpreted as thrust faults, indicating a period of global compression [11]. The lobate scarps typically transect smooth plains materials (early Calorian age) on the floors of craters, but post-Caloris craters are superposed on them. These observations suggest that lobate-scarp formation was confined to a relatively narrow interval of time, beginning in the late pre-Tolstojan period and ending in the middle to late Calorian Period. In addition to scarps, wrinkle ridges occur in the smooth plains materials. These ridges probably were formed by local to regional surface compression caused by lithospheric loading by dense stacks of volcanic lavas, as suggested for those of the lunar maria [4,11].

Geological history The earliest decipherable event in Mercury's history was the formation of its crust. By analogy with the Moon, Mercury may have experienced early global melting, similar to the lunar "magma ocean", whereby large-scale melting of at least the outer few hundred kilometers of the planet would concentrate low-density plagioclase into the uppermost part of the crust. If this process operated during early mercurian history, then its crust is probably composed largely of anorthositic rocks. Such a composition is consistent with full-disc spectra [12] and Mariner 10 color data for Mercury [13], which suggest that Mercury's surface is similar to the Apollo 16 site in the highlands of the Moon [10,12,13]. The early cratering record of Mercury has been largely destroyed by the deposition of the intercrater plains, but the largest multi-ring basins have been partly preserved. Sometime during the heavy bombardment, intercrater plains materials largely obliterated the older crater population (Fig. 1). The global distribution of the intercrater plains suggests that they may be at least partly volcanic in origin, although subsequent cratering has converted the original surface to breccia. The Tolstoj basin impact marked the beginning of the Tolstojan Period, still a time of high impact rates. The Caloris impact formed the largest well-preserved basin on Mercury's surface (Fig. 1) and provided an extensive stratigraphic datum on the planet. Catastrophic seismic vibrations from the Caloris impact probably formed the hilly and furrowed terrain on the opposite side of the planet. Shortly after the Caloris impact, massive extrusions of flood lavas formed the smooth plains. A rapidly declining cratering rate has produced minimal changes to Mercury's surface since the final emplacement of the smooth plains (Fig. 1). This low rate of cratering presently continues to produce regolith on all surface units.

References [1] Mariner 10 Special Issue (1975) *JGR* **80**. [2] Vilas F. et al., eds. (1988) *Mercury*. Univ. Arizona Press, 794 pp. [3] Gault D. E. et al. (1975) *JGR* **80**, 2444. [4] Spudis P.D. and Guest J.E. (1988) in *Mercury*, 118-164. [5] Schaber G.G. et al. (1977) *PEPI* **15**, 189. [6] McCauley J.F. (1977) *PEPI* **15**, 220. [7] McCauley J.F. et al. (1981) *Icarus* **47**, 184 [8] Schultz, P.H. and Gault, D.E. (1975) *The Moon* **12**, 159-177. [9] Strom, R.G. et al. (1975) *JGR* **80**, 2478. [10] Robinson M.R. and Lucey P.G. (1997) *Science* **275**, 197-200. [11] Melosh H.J. and McKinnon W.B. (1988) In *Mercury*, 374-400. [12] Vilas F. (1988) in *Mercury*, 59-77. [13] Robinson M.R. and Taylor G.J. (2001) *Meteoritics Planet. Sci.* **36**, in press.

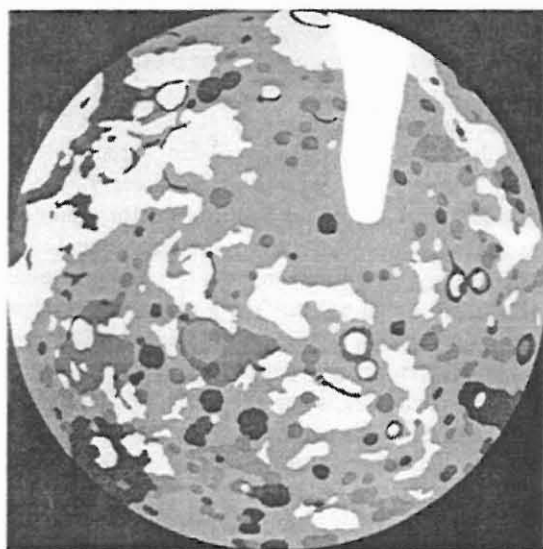


Figure 1 Geological map of the planet Mercury. Dark browns and tans – pre-Tolstojan craters, basins, and intercrater plains. Lighter browns and orange – Tolstojan craters and plains, respectively. Blues – units of the Caloris basin and craters of Calorian age. Pink – Calorian smooth plains. Greens and Yellows – Mansurian and Kuiperian age impact craters. After [4].

THE X-RAY SPECTROMETER FOR MERCURY MESSENGER. R. D. Starr¹, G. C. Ho², C. Schlemm², R. E. Gold², J. O. Goldsten², W. V. Boynton³, and J. I. Trombka⁴, ¹Department of Physics, The Catholic University of America, Washington, DC 20064 (richard.starr@gsfc.nasa.gov), ²Johns Hopkins University, Applied Physics Laboratory, Laurel, MD 20723 (george.ho@jhuapl.edu, chuck.schlemm@jhuapl.edu, robert.gold@jhuapl.edu, john.goldsten@jhuapl.edu), ³Department of Planetary Science, Space Sciences Building, University of Arizona, Tucson, AZ 85721 (wboynton@gammal.lpl.arizona.edu), ⁴Goddard Space Flight Center, Code 691, Greenbelt, MD 20771 (uljit@lepvax.gsfc.nasa.gov).

Introduction: Mercury is the closest planet to the Sun and because it is so close, it is difficult to study from Earth-based observatories. Its proximity to the Sun has also limited the number of spacecraft to visit this tiny planet to just one, Mariner 10, which flew by Mercury twice in 1974 and once in 1975. Mariner 10 provided a wealth of new information about Mercury, yet much still remains unknown about Mercury's geologic history and the processes that led to its formation. The origin of Mercury's metal-rich composition is just one area of investigation awaiting more and improved data to sort between competing hypotheses. Mercury plays an important role in comparative planetology, and many of the processes that were important during its formation are relevant to the Earth's early history.

MESSENGER (MErcury Surface, Space ENvironment, GEochemistry, and Ranging) is a Discovery mission that has been designed to fly by and orbit Mercury [1], [2], [3]. It will launch in March 2004, fly-by Mercury in 2007 and 2008 and enter an elliptical orbit in April 2009. During the one-year orbital phase, a suite of instruments on board the MESSENGER spacecraft will study the exosphere, magnetosphere, surface, and interior of Mercury. One of these instruments will be an X-Ray Spectrometer (XRS) that will measure surface elemental abundances. Remote X-ray spectroscopy has been accomplished before on the Apollo 15 and 16 missions, and more recently on NEAR Shoemaker [4].

The MESSENGER XRS will measure characteristic X-ray emissions induced in the surface of Mercury by the incident solar flux. The K α lines for the elements Mg, Al, Si, S, Ca, Ti, and Fe will be detected with spatial resolution on the order of 40 km when counting statistics are not a limiting factor. These measurements can be used to obtain quantitative information on elemental composition.

X-ray remote sensing: The X-ray spectrum of a planetary surface measured from orbit is dominated by a combination of the fluorescence excited by incident solar X-rays and coherently and incoherently scattered solar X-rays. The sampling depth is dependent on energy, but is always less than 100 μ m. The most prominent fluorescent lines are the K α lines (1–10 keV) from the major elements Mg (1.254 keV), Al (1.487

keV), Si (1.740 keV), S (2.308 keV), Ca (3.691 keV), Ti (4.508 keV), and Fe (6.403 keV). The strength of these emissions from planetary surfaces is strongly dependent on the chemical composition of the surface as well as on the incident solar spectrum, but is of sufficient intensity to allow orbital measurement by detectors like those on the MESSENGER spacecraft.

The coherently and incoherently scattered solar X-rays are one source of background signal. Astronomical X-ray sky sources, which could also be sources of background, are eliminated at Mercury, because the XRS is collimated to a 12° field of view, and the planet completely fills the field of view even when the spacecraft is at apoapsis.

Because incident solar X-rays are the excitation source for X-rays generated from a planetary surface, knowledge of the solar spectrum is necessary for quantitative analyses. The solar flux from 1 to 10 keV is composed of a continuum and discrete lines, both of which vary with solar activity. This process is well understood and theoretical models accurately predict the solar spectrum. The solar intensity decreases by three to four orders of magnitude from 1 to 10 keV. Fluorescent lines as well as the scatter-induced background, therefore, have greater intensity at lower energies. As the level of solar activity increases, relatively more output occurs at higher energies, the slope of the spectrum becomes less steep, and the overall magnitude of the X-ray flux increases. This process is called hardening.

Instrument Design: The XRS is an improved version of the NEAR Shoemaker X-Ray Spectrometer design [5]. Three gas proportional counters view the planet, and a state-of-the-art Si-PIN detector mounted on the spacecraft sunshade views the Sun. (See Table 1.) The energy resolution of the gas proportional counters (~850 eV at 5.9 keV) is sufficient to resolve the X-ray lines above 2 keV, but Al and Mg filters on two of the planet-facing detectors are required to differentially separate the lower energy X-ray lines from Al, Mg, and Si. This balanced filter technique has worked well on NEAR Shoemaker [4]. A Be-Cu honeycomb collimator provides a 12° FOV, which is smaller than the planet at apoapsis and eliminates the X-ray sky background.

Table 1. XRS Characteristics

Measured Elements	Mg, Al, Si, S, Ca, Ti, Fe
Solar Monitor	Si-PIN, 300 μm thick, 0.12 mm^2
Detectors	3 gas proportional counters, 10 cm^2 each
Field-of-view	12°, Be-Cu honeycomb collimator
Window	Beryllium 25 μm
Balanced Filters	8.5 μm Mg; 8.5 μm Al
Energy Range	0.7 to 10 keV
Energy Resolution	850 eV fwhm @ 5.9 keV
Maximum input rate	20 kHz
Integration period	50 s @ perihelion; 2000 s @ aphelion

Improvement of the signal to background ratio compared to the NEAR XRS was of primary importance in the design for MESSENGER. Background reduction in the planet-facing gas tubes is enhanced by a set of anti-coincidence wires, located near the periphery of the tubes, which detect penetrating cosmic-ray and gamma-ray events. An internal Be liner blocks X-rays produced by cosmic-ray interactions in the detector Ti tube walls.

It is also important to note that the XRS observing geometry on MESSENGER will be significantly improved over that on NEAR. Measurements where the solar incidence angle and detector-viewing angle are less than 60° and the instrument field of view is filled by the planet are best. On MESSENGER these conditions will occur about 50% of the time. On NEAR this number was only about 5%.

The solar monitor that tracks the solar X-ray input to the planet, is a small ($\sim 0.1 \text{ mm}^2$) Si-PIN detector with a thin Be window that provides thermal protection. The NEAR Shoemaker mission was the first to fly the high-resolution ($\sim 600 \text{ eV}$ at 5.9 keV) Si-PIN X-ray detector technology (as a solar flux monitor). An

improved version was subsequently flown on the Mars Pathfinder rover. The XRS solar flux monitor is a third-generation design that uses discrete resets rather than resistive feedback to compensate for diode leakage currents. This design gives it better energy resolution ($\sim 300 \text{ eV}$ at 5.9 keV) and greater radiation immunity.

XRS Sensitivities: The MESSENGER X-Ray Spectrometer will detect several elements of geologic significance on the surface of Mercury. The spatial resolution will depend upon proximity to the planet and the intensity and shape of the exciting solar spectrum. Table 2 lists the required integration times for identifying the listed elements at the 10% uncertainty level for different solar conditions for MESSENGER. Integration times vary due to elemental abundance, solar spectrum and background rejection efficiency. Because of the very steep slope of the incident solar spectrum, the fluorescence from the heavier elements (Fe, Ti, and Ca) will only be detected during solar flares. Fluorescence from Mg, Al, and Si will be detected even during quiescent solar conditions.

The XRS will attain its finest spatial resolution ($\sim 40 \text{ km}$) at perihelion, which occurs over Mercury's Northern Hemisphere. However, due to the extreme elliptical orbit of the MESSENGER spacecraft, this will amount to only 15 minutes out of every 12-hour orbit or 180 hours during the one-year orbital phase of the mission. In the Southern Hemisphere spatial resolution will be $\sim 3000 \text{ km}$.

References: [1] Solomon, S. C. *et al.* (2001) Planet. Space Sci. accepted for publication. [2] Gold R. E. *et al.* (2001) Planet. Space Sci. accepted for publication. [3] Santo A. G. *et al.* (2001) Planet. Space Sci. accepted for publication. [4] Trombka, J. I. *et al.* (2000) Science **289**, 2101-2104. [5] Trombka, J. I. *et al.* (1997) JGR **102**, 23,729-23,750. [6] Brückner J. and Masarik J. (1997) Planet. Space Sci. **45**, 39-48.

Table 2. XRS Observation Times

Element	Assumed abundances	Proportional counter with 95% background rejection		Proportional counter with 75% background rejection	
		Normal	Flare	Normal	Flare
Fe	2.3%	—	80 s	—	2 min
Ti	1.0%	—	3 min	—	4 min
Ca	4.0%	—	10 s	—	30 s
Si	21.5%	7 min	2 min	18 min	3 min
Al	3.0%	2 hr	22 min	8 hr	50 min
Mg	22.5%	5 min	2 min	11 min	3 min

Counting times are those required to reproduce the assumed composition at the 10% uncertainty level. Assumed abundances are from Brückner and Masarik [6]. Count rates are scaled from those made by NEAR in July 2000 (1.78 AU) to the assumed composition at Mercury (at 0.387 AU).

MERCURY: AN END-MEMBER PLANET OR A COSMIC ACCIDENT? G. J. Taylor and E. R. D. Scott, Hawai'i Institute of Geophysics and Planetology, School of Ocean and Earth Science and Technology, University of Hawai'i at Manoa, Honolulu, HI 96822, USA; gjtaylor@higp.hawaii.edu

Introduction: Mercury is unique. It is the densest planet, undoubtedly because it has a large metallic core. Spectral observations indicate that its surface is low in FeO (the best guess is around 3 wt% [1], but it might have none). Unambiguous lava plains have low FeO, indicating that their source regions in the mercurian mantle also contain little FeO, 2-3 wt% [2]; we infer that the entire mercurian mantle is low in FeO. In contrast, the bulk silicate Earth [3] and Venus [2] contain more FeO (about 8 wt%), and Mars contains about 18 wt% [4]. Do these compositional features of Mercury reflect its location near the Sun? Lewis [5] suggested that temperature gradients in the solar nebula led to variations in chemical composition of the planets. The FeO variation from Mercury to Earth and Venus to Mars is consistent with this idea. Alternatively, could Mercury simply be the product of stochastic events [6]? In this view, the terrestrial planets accreted from material from the whole inner solar system [7], and Mercury's high density is due to a large impact that removed much of its original mantle [8] or other processes that fractionated metal from silicate [9]. So, is Mercury an end-member planet that contains a record of its formation near the Sun? Or is it an accident of accretion and giant impacts?

Width of planetary accretion zones: Wetherill [7] modeled the accretion of the terrestrial planets from a disk of lunar to Mars-sized embryos. He found widespread gravitational mixing of the embryos and their fragments, which ensured that each terrestrial planet formed from material originally located throughout the inner solar system (0.5 to 2.5 AU). Thus any initial radial chemical variations in the compositions of the planetesimals would be largely erased as the planets accreted. Wetherill [7] found no obvious tendency for Mercury-like planets to be derived from material initially located at the inner edge of the disk of embryos. However, these models appear incompatible with the inferred mantle FeO concentrations of the planets, which increase with heliocentric distance from 2-3 wt% at Mercury to 18 wt% at Mars.

Subsequent modeling by Chambers and Wetherill [10] confirmed that Earth- and Venus-like planets accrete from broad zones. However, their models suggest that Mars may be a single embryo, i.e., a body that formed during earlier runaway growth when orbits were nearly circular and coplanar. Thus, Mars may be derived from a restricted part of the nebula that was poorly sampled by the other planets. Accretion models

for Mercury are critically dependent on the assumed initial conditions and the reason for its small size. We suggest that Mercury may be small and chemically distinctive because it also formed from a single embryo.

Clues from chondrites: The notion that chondrites were the building blocks of the planets has a long history, but enthusiasm for the idea has waned. S. R. Taylor [6] argued instead that stochastic events were largely responsible for chemical differences between terrestrial planets and that chondrite groups and planets are unrelated because they formed in separate locations. We have suggested [11] that certain chondrites and terrestrial planets are related because chondritic ingredients were transported across the nebula.

Ca-Al-rich inclusions. CAIs and refractory grains with exceptionally ^{16}O -rich compositions are found in all chondrite groups including CI, CM, E, and O chondrites, and micrometeorites. Their chemical and oxygen isotopic compositions indicate formation in a dust-enriched location, most probably near the protosun [12]. Efficient distribution to cooler regions favors transportation by bipolar outflows [13].

Forsterite grains. Comets contain forsterite grains, which are absent in the interstellar medium [14]. They probably formed close to the protosun either by annealing of interstellar grains [15] or by condensation. Outward transport was provided by mixing in the nebula [16,17] or by bipolar outflows.

Chondrules. The inferred depletion of refractory elements in chondrules from O and E chondrites and the ^{16}O -rich nature of Al-rich chondrules and forsteritic condensates suggest that chondrules and their associated Fe,Ni grains partly formed from condensates by a CAI-related process [18]. Since chondrules and metal grains in metal-rich chondrites were hurled outwards after they condensed [19], chondrules, CAIs and forsterite grains may have been transported by one process [13]. If chondrules had formed by melting of dust-balls at the accretion location, we should find vesicular chondrules in CM chondrites [20], but none is present.

This evidence for outward transport of thermally processed materials from near the protosun suggests that terrestrial planets could have formed from similar materials. One class of chondrites may be particularly suitable as examples of Mercury building blocks. The discovery of three new chondrite groups (CR, CH and Bencubbin-like) among Antarctic meteorites has greatly expanded the compositional range of chondrites

[21-25]. The new chondrites have normal levels of refractory elements but are richer in metallic Fe (some were classed as iron meteorites) and poorer in volatile elements like Na, K, and S than other chondrites. Bencubbin-like chondrites have more metal (~80 wt%) than Mercury (~70 wt%) and comparable FeO concentrations.

Did Mercury's formation involve a giant impact? Most authors have embraced the idea that Mercury's high concentration of metal is a result of a giant impact that preferentially removed most of the silicate mantle [8]. However, the existence of metal-rich chondrites and the evidence for formation of their constituents near the protosun diminishes the need for such an event. In addition, successful impact models required extreme conditions: a) targets containing 32 wt% metallic iron; b) head on collisions at 20 km/s or oblique impacts at implausibly high collision speeds of 35 km/s [26]; c) removal of all silicate ejecta as sub-centimeter-sized particles by the Poynting-Robertson effect to prevent silicates from reaccreting on to Mercury [8]. Most important, the impact model does not account for the unusually low bulk FeO concentration of Mercury.

Compositional diversity among the terrestrial planets: Chondrites are quite diverse in composition. We propose that primary chemical differences among planetesimals were more important than giant impacts in establishing planetary compositions. However, the nebular processes responsible for diverse chondritic compositions are not clear. The low volatile abundances of metal-rich chondrites are consistent with Lewis' equilibrium nebula condensation theory [5] and some metal grains have compositions consistent with condensation above 1200 K [27]. However, these chondrites could not have accreted above 1200 K, as Lewis inferred for Mercury, because their metal grains cooled in days or weeks to below 600 K [28]. Rapid condensation of metal and silicate in localized nebular processes may have triggered accretion of planetesimals. Thus Mercury may be small and metal-rich because only a small fraction of the metal and an even smaller fraction of the silicate condensed and accreted. The remainder of the metal and silicate probably accompanied the volatiles into the Sun. The feeding zone for Mercury might have included planetesimals from further out in the nebula, as argued by Wetherill [7], but it seems to have been dominated by planetesimals formed near its current location. Venus and Earth are also quite distinct from Mars, shown strikingly by their low FeO (about 8 wt%, versus 18 wt% for Mars). This suggests they might also have formed mostly from metal-rich chondrites (including enstatite chondrites), and possibly from planetesimals formed well within the orbit of Mars.

Conclusions: Mercury does not appear to be the accidental product of stochastic processes. While we cannot rule out its formation from planetesimals throughout the inner solar system or that it was modified by a giant impact, a strong case can be made that it is a surviving planetary embryo that formed from materials near its current location. Metal-rich chondrites are reasonable analogs for the material that accreted to form Mercury. In fact, they might dominate the population of planetesimals that formed Mercury, Venus, and Earth, the metal-rich, FeO-poor planets.

This idea can be tested by the MESSENGER mission. If similar to metal-rich chondrites, the bulk composition of Mercury should be low in FeO (as it appears to be), have chondritic relative abundances of refractory elements (Th/U, Al/Th), no enrichment in refractory elements over chondrites, and be low in volatile elements (K).

References: [1] Blewett, D. T. et al. (1997) *Icarus* **129**, 217-231. [2] Robinson, M. S. and Taylor, G. J. (2001) *MAPS* **36**, 841-847. [3] Jagoutz, E. et al. (1979) *PLPSC 10th*, 2031-2050. [4] Longhi, J. et al. (1992) *Mars*, 184-208. [5] Lewis J. S. (1972) *EPSL* **15**, 286-290. [6] Taylor S. R. (1991) *Meteoritics* **26**, 267-277. [7] Wetherill G.W. (1994) *GCA* **58**, 4513-4520. [8] Benz W. et al. (1988) *Icarus* **74**, 516-528. [9] Weidenschilling, S. J. (1978) *Icarus* **35**, 172-189. [10] Chambers J. E. and Wetherill G. W. (1998) *Icarus* **136**, 304-327. [11] Scott, E. R. D., et al. (2001) *MAPS*. (abstract), in press. [12] Scott E. R. D. and Krot A. N. (2001) *MAPS* submitted. [13] Shu F. H. et al. (2001) *Astrophys. J.* **548**, 1029-1050. [14] Hanner M. S. (1999) *Space Sci. Rev.* **90**, 99-108. [15] Nuth J. A. et al. (2000) *Nature* **406**, 275-276. [16] Stevenson D. J. (1990) *Astrophys. J.* **348**, 730-737. [17] Meibom A. et al. (2000) *Science* **288**, 839-841. [18] Scott E. R. D. and Krot A. N. (2001) *MAP*, submitted. [19] Krot A. N. et al. (2001) *Science* **291**, 1776-1779. [20] Maharaj S. V. and Hewins R. H. (1998) *MAPS* **33**, 881-887. [21] Weisberg M. K. (1999) *LPS* **30**, #1416. [22] Scott E. R. D. (1988) *EPSL* **91**, 1-18. [23] Grossman J. N. et al. (1988) *EPSL* **91**, 33-54. [24] Weisberg M. K. et al. (1993) *GCA* **57**, 1567-1586. [25] Weisberg M. K. et al. (1995) *Proc. NIPR Symp.* **8**, 11-32. [26] Wasson J. T. (1988) In *Mercury* ed. F. Vilas et al., pp.622-650. [27] Meibom A. et al. (1999) *JGR* **104**, 22,053-22,059. [28] Meibom, A. et al. (2000) *Science*, **288**, 839-841.

APPLICATION OF AN UPDATED IMPACT CRATERING CHRONOLOGY MODEL TO MERCURY'S TIME-STRATIGRAPHIC SYSTEM. R. J. Wagner¹, U. Wolf¹, B. A. Ivanov², and G. Neukum¹, ¹DLR Institute of Space Sensor Technology and Planetary Exploration, Rutherfordstrasse 2, D-12489 Berlin, Germany, ²Institute for Dynamics of Geospheres, Russian Acad. Sci., Leninsky Prospekt 38/6, Moscow, Russia 117939 (e-mail of corresponding author: Roland.Wagner@dlr.de)

Introduction: During three close encounters with Mercury in 1974-1975, the camera onboard the Mariner-10 spacecraft has acquired images of 40-45 % of the total surface at spatial resolutions between 1 and 4 km/pxl, with highest resolutions obtained in selected areas down to about 100 m/pxl. In this work we present results from crater size-frequency measurements carried out on various geologic units, using a recently updated crater production function polynomial and impact cratering chronology model derived for Mercury [1, and references therein] in order to reassess the time-stratigraphic system established for Mercury [2, 3, 4]. These investigations are prerequisite for further studies during two upcoming orbiting missions to Mercury, ESA's *Bepi-Colombo* and NASA's *Messenger*.

Geologic overview: Mercury exhibits a lunar-like surface, dominated by numerous *impact craters* and *multi-ring basins* in various states of preservation [5, 6].

Geologic units: Three major geologic units were identified [7]: (a) *densely cratered terrain* (highlands), with (b) interspersed smooth areas, the so-called *inter-crater plains*, and (c) lightly cratered *low-land plains* (or *smooth plains*). Inter-crater plains generally embay densely cratered highlands and old degraded multi-ring structures, hence are younger [7]. Emplacement of inter-crater plains very likely caused crater obliteration in highland areas at crater diameters smaller than about 30 km, thus changing the shape of an otherwise ideal highland-type crater size-frequency distribution similar to the one found in lunar highland areas [8]. Low-land plains occur preferentially in association with impact structures, and in patches in highland areas [8]. They resemble lunar maria (except in brightness) and, as these, also feature wrinkle ridges [4]. Modes of emplacement for inter-crater plains and low-land plains are controversially discussed: some investigators favor an impact origin [7, 9], others conjecture a volcanic origin, despite the lack of unequivocal volcanic features [4, 5, 6].

Craters and multi-ring basins: Numerous basins with diameters larger than about 200 km and with at least two rings were found on Mercury [4]. Many of them are highly degraded and hence rather old features [10]. The *Caloris* basin is the youngest and largest one (about 1300 km in diameter) known so far. Craters, similar in morphology to lunar craters, and, as these,

with increasingly complex forms with increasing diameters, were subdivided into 5 erosional classes, ranging from fresh, bright ray craters (class C5) to heavily degraded crater ruins (C1) [3]. Some of the basins and craters provide important stratigraphic markers and were used to subdivide Mercury's geologic history into time-stratigraphic systems and chronologic periods [1, 2, 3, 4, 8].

Tectonic features: Mercury was tectonically active in the past. Lineaments with trends of NE-SW and NW-SE in the equatorial regions, and E-W in the polar regions, predate the younger multi-ring basins and are believed to have been created by tidal despinning [11]. Thrusting events, caused by rapid cooling and contraction of Mercury, created a large number of scarps and scarp systems, such as *Discovery Rupes*, which extend over several hundred kilometers [11].

Crater size-frequency measurements and cratering chronology: It has been discussed by several investigators that the shapes of crater size-frequency distributions measured on bodies in the inner solar system closely resemble each other, and also resemble the size distribution observed for Main Belt asteroids, which hence provide the major impactor source [1, 12, and references therein]. The lunar production function (polynomial of 11th degree), was refined recently and applied to Mercury, taking into account differences in crater scaling between the two bodies [1, 12] (polynomial coefficients in [1]). This polynomial is used to fit measured crater size-frequency distributions. Relative ages of geologic units are given as cumulative frequencies equal to, or greater than, a reference diameter of 10 km (Tab. 1). Estimates for Mercury/moon cratering rate ratios were used to derive a cratering chronology model function for Mercury [1, and references therein] (Fig. 1). It is characterized (a) by a rapid change in cumulative frequency with time for model ages older than about 3.3 Gyr (1 Gyr = 1 billion years), due to an exponential decay in cratering rate during the Late Heavy Bombardment (LHB) period, and (b) by only a small decrease in cumulative frequency with time for ages younger than about 3.3 Gyr, due to a more or less constant cratering rate ever since [1, 12]. Both cumulative frequencies for geologic units, based on the refined lunar production function, and their corresponding updated cratering model ages differ from values published earlier [8].

Time-stratigraphy of Mercury: Mercury's geologic history was subdivided into five time-stratigraphic systems or chronologic periods [2, 3, 4]: (1) *pre-Tolstojan*, (2) *Tolstojan*, (3) *Calorian*, (4) *Mansurian*, and (5) *Kuiperian* (see Fig. 1).

Pre-Tolstojan: This period ranges from the formation of a crust until the formation of the Tolstoj multi-ring basin. Impacts created most of the highlands and a great number of now degraded multi-ring basins. Inter-crater plains were emplaced also in this period. Older highlands show a tectonic imprint of tidal despinning (lineaments). Toward the end of this period, planetary cooling and contraction started, creating scarps and scarp systems [4].

Tolstojan: The Tolstoj basin was created 3.97 Gyr ago, an age comparable to the 3.9 - 4 Gyr given by [4]. Smooth plains were emplaced, either by volcanism or impact. Tidal despinning and planetary contraction continued, causing lineaments and scarp systems to form [4].

Calorian: The impact of a large asteroid created the Caloris basin about 3.77 Gyr ago. This age derived in our model is much less than the one given by [4] and is closer to the model age of the lunar Orientale basin. The Late Heavy Bombardment ends within this period.

Mansurian, Kuiperian: After the heavy bombardment, the cratering rate has been more or less constant until today. Younger craters formed, superposing older units such as multi-ring basins and scarp systems [4]. Youngest formations on the mercurian surface are bright ray craters such as Kuiper (60 km diameter). This time-stratigraphic scheme is far from complete since only 40-45 % of Mercury's surface are known today, and since the spatial resolution of most parts of the surface imaged is not sufficient.

References: [1] Ivanov B. A. et al. (2001) *this volume*. [2] Holt H. E. (1978) in: *Repts. Planet. Geol. Prog.*, NASA TM-79729 (abstract), 327. [3] McCauley J. F. et al. (1981) *Icarus* 47, 184-202. [4] Spudis P. D. and Guest J. E. (1988) in: *Mercury* (F. Vilas, C. R. Chapman, and M. S. Matthews, eds.), Univ. of Arizona Press, Tucson, 336-373. [5] Murray B. C. et al. (1974) *Science* 185, 169-179. [6] Murray B. C. et al. (1975) *JGR* 80, 2508-2514. [7] Trask N. J. and Guest J. E. (1975) *JGR* 80, 2462-2477. [8] Strom R. G. and Neukum G. (1988) in: *Mercury* (F. Vilas, C. R. Chapman, and M. S. Matthews, eds.), Univ. of Arizona Press, Tucson, 336-373. [9] Wilhelms D. E. (1976) *Icarus* 28, 551-558. [10] Pike R. J. and Spudis P. D. (1987) *Earth, Moon, and Planets* 39, 129-194. [11] Melosh H. J. and McKinnon W. B. (1988) in: *Mercury* (F. Vilas, C. R. Chapman, and M. S. Matthews, eds.), Univ. of Arizona Press, Tucson, 374-400. [12] Neukum G. et

al. (2001) in: *Chronology and Evolution of Mars*, ISSI, Kluwer (in press).

Geologic Unit	Cum. frequency (D>10 km)		Crat. model age (Gyr)	
	[8]	this work	[8]	this work
Kuiper	-	(4.04e-6)	-	(1.0)
Mansur	-	(2.31e-5)	-	(3.5)
Caloris	6.85e-5	7.51e-5	3.85	3.77±0.06
Beethoven	1.53e-4	1.22e-4	3.98	3.86±0.05
Tolstoj	2.65e-4	2.51e-4	4.06	3.97±0.05
Pushkin	3.45e-4	2.72e-4	4.10	3.98±0.06
Haydn	3.65e-4	2.76e-4	4.11	3.99±0.06
Dostojewskij	5.49e-4	2.75e-4	4.17	3.99±0.06
Chekhov	4.04e-4	4.15e-4	4.12	4.05±0.08
Highlands	5.99e-4	4.81e-4	4.18	4.07±0.03

Table 1: Cumulative frequencies (for D>10 km) and associated cratering model ages for major geologic units, craters and basins. Older values from [8] compared to updated values (this work). Uncertainties for cumulative frequencies (both [8] and this work) are on the order of 20 - 30%, translating into model age uncertainties of 0.03 - 0.06 Gyr ([8], and this work).

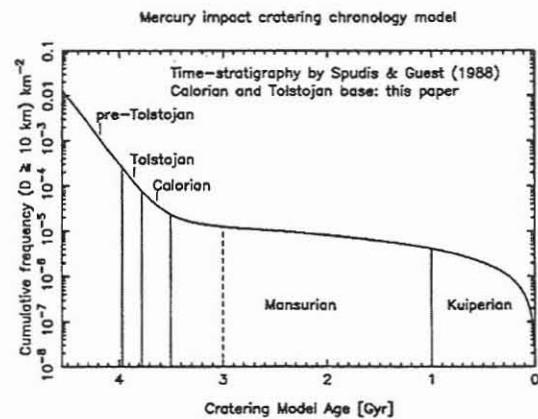


Figure 1: Mercury's impact cratering chronology model [1], applied to the time-stratigraphic system by [4]. Age boundaries for the Mansurian and Kuiperian periods based on age estimations [4] (see also Tab. 1). Lower boundaries for Tolstojan and Calorian periods determined from crater size-frequency measurements by [8], with application of the refined production function and the corresponding cratering model ages from the model function discussed in [1].

DISK-RESOLVED MULTICOLOR PHOTOMETRY AND SPECTROSCOPY OF MERCURY. J. Warell, *Institutionen för Astronomi och Rymdfysik, Uppsala Universitet, Box 515, SE-751 20 Uppsala, Sweden, (johan.warell@astro.uu.se).*

Multicolor photometric observations of the poorly known (in terms of Mariner 10 coverage) hemisphere of Mercury have been performed with the Swedish Vacuum Solar Telescope (SVST) on La Palma at maximal elongations from the Sun in 1997 and 1998. The photometry was obtained in twilight and calibrated with standard star observations made shortly following the Mercury observations. The work is based on a subset, in the longitude range 160–310 degrees, of high-resolution CCD image data covering the global surface of Mercury obtained by Warell and Limaye [1].

The disk-integrated spectrum of Mercury displays a linear slope from 650 to 940 nm with the same reddening ($\sim 17\%$ / 1000 Å) as the CCD spectrum by Vilas [2]. The slopes of these two spectra are larger than previously published spectrophotometry, and indicate that the average Hermean regolith is considerably more mature than lunar anorthosite regions. The spectrophotometry presented here provides negative evidence for the presence of the putative absorption feature at 930 nm due to presence of Fe^{2+} in pyroxenes, though a band depth of 4% is possible within the photometric error budget. No effect of phase reddening is observed between phase angles of 63° and 84° .

Multicolor photometry of resolved bright and dark albedo features on the Hermean disk shows a variation in spectral slopes for these features which is smaller than that from laboratory bidirectional reflectance spectra of lunar maria and highland soils for the same geometries. This indicates that the scattering properties are more homogeneous for Mercury and that there is no clear relation between reflectivity and chemical properties at spatial scales of ~ 300 km on the poorly known hemisphere.

There is an inverse relation of spectral slope with emission angle for Hermean albedo features; i.e. the spectral slope increases as the terminator is approached. The relation is the

same for the brightest and darkest features. This property of the Hermean regolith is most similar to that of Apollo 14 mature highland bulk surface soil. The inclination of the spectral slope–emission angle relation is larger for Mercury than for the Moon, indicating that the average Hermean regolith is more back-scattering and that this effect increases for longer wavelengths.

Filter ratio images of the Hermean disk show that color variations are less than 2% with respect to the surroundings at a spatial scale of ~ 300 km. All slight color variations visible in the data are attributable to seeing effects and the spatial location of sampling CCD pixels with respect to the regolith albedo pattern.

Low resolution spectroscopic observations in the 5000–11 000 Å range were carried out with the 2.6-m Nordic Optical Telescope (NOT) in June 1999. The seeing ranged from 0.8 to 1.3 arcseconds, allowing spectra from rather well-defined surface regions in the longitude range 200–300 degrees to be obtained. Very good correction for telluric absorptions has been possible thanks to extensive calibration observations.

The increase in spectral slope with emission angle found by the disk-resolved spectrophotometry with the SVST is verified with the NOT spectroscopy. The spectra are practically featureless and no obvious absorption bands are visible; there are however possible very broad and shallow absorption features shortward of 6000 Å and longward of 8500 Å. The disk integrated spectral slope is somewhat smaller than that determined from the SVST spectrophotometry. Further results of the current analysis of the NOT spectra will be presented.

References: [1] Warell, J. and Limaye, S.S. (2001), "Properties of the Hermean regolith: I. Global regolith albedo variation at 200 km scale from multicolor CCD imaging", *Planetary and Space Science Special Mercury Issue* (in press). [2] Vilas, F. (1985), "Mercury: Absence of Crystalline Fe^{2+} in the Regolith", *Icarus* 64, 133–138.

A STUDY OF MERCURY-LIKE ORBITS. J. Warell, O. Karlsson, E. Skoglöv, *Institutionen för Astronomi och Rymdfysik, Uppsala Universitet, Box 515, SE-751 20 Uppsala, Sweden, (johan.warell@astro.uu.se).*

We have performed a series of n -body numerical integrations of particles in heliocentric orbits which are closely similar to that of Mercury (in a , e and i). The calculations have been performed with the 15th order integrator RADAU [1] with a variable step size, including the perturbations of the eight major planets. The purpose of the study was to determine the dynamics of objects near Mercury's heliocentric distance, the possibility of temporary captures by Mercury, routes of transfer of Near Earth Objects (NEO:s) within the inner solar system, and the effect of resonances in this region.

After an initial integration to determine what types of orbital elements are susceptible to close encounters with Mercury, a total of 10 000 objects were integrated for 15 000 years. From this sample, 675 objects were selected which spent a minimum of 10 days within the Hill radius of Mercury (at a Hermeocentric radius of about 200 500 km) during at least one approach, and an integration of 100 000 years was performed. A subset of 17 objects whose approaches were extraordinarily long or numerous was then selected and integrated for 1200 years, to study the dynamics of the encounters in detail. Two follow-up integrations lasting 10^8 years were finally made to study objects whose secular evolution in a and e caused long-term excursions from the Mercury zone, and those objects whose orbits were found to be Hermeocentric for extended periods of time.

We find that (1) there exists retrograde Hermeocentric orbits which are stable for at least 100 000 years (Hermeocentric elements around $a_H = 111\,000$ km, $e_H = 0.38$ with anomalistic periods $P_H = 16$ days), thus numerically verifying the analytical work of Rawal [2]; (2) objects originally in closely

Hermean heliocentric orbits may secularly increase the semi-major axis due to numerous encounters with Mercury, followed by passages through the secular ν_2 resonances with Venus [3, 4] which increase the eccentricity to attain Venus crossing orbits (Fig. 3); this evolution forms a possible way of producing NEO:s from orbits inferior to Earth's; (3) objects may be repeatedly intermittently locked in the 1:1 mean motion resonance with Mercury and follow Trojan-like horse-shoe orbits for up to at least 23 000 years with periods of around 80 years in the Hermeocentric frame of motion (Fig. 2); (4) objects may be subject to temporary satellite captures by Mercury with orbits within the Hill sphere for durations of at least 90 days (Fig. 1).

Based on the estimated number of kilometer size Amor asteroids, as well as on Weidenschilling's [5] model of the solar nebula and the retainment of objects larger than 10 km within Mercury's perihelion distance, we also estimate that the number of objects in Mercury-like orbits existing today is less than 10^{-3} .

References: [1] Everhart, E. (1985) in *Dynamics of Comets: Their Origin and Evolution* (eds. Carusi and Valsecchi), pp. 185–202. [2] Rawal, J.J. (1986) *Earth, Moon, and Planets* 36, 135–138. [3] Michel, P. and Froeschlé, C. (1997), *Icarus* 128, 230–240. [4] Michel, P. (1997), *Icarus* 129, 348–366. [5] Weidenschilling, S.J. (1978), *Icarus* 35, 99–111.

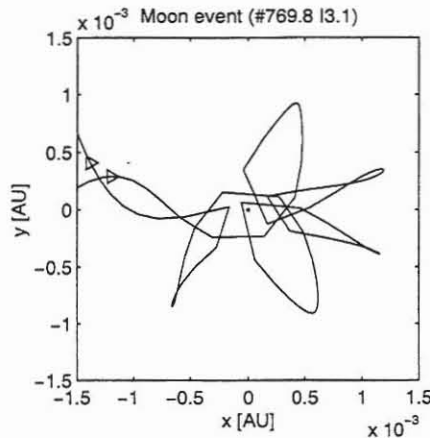


Figure 1: Example of an temporary satellite capture by Mercury. Arrows indicate direction of motion of particle. The Sun is on the negative x-axis, Mercury is at the origin.

MERCURY-LIKE ORBITS: Warell, Karlsson and Skoglöv

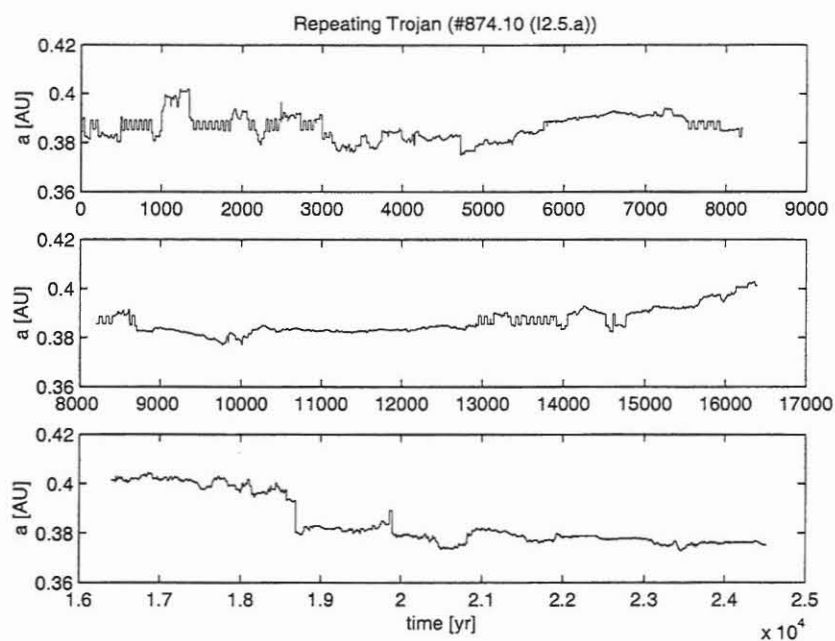


Figure 2: Example of an object repeatedly entering and exiting a Trojan horse-shoe orbit (at $t=500\text{--}900$, $1400\text{--}1900$ years, etc.).

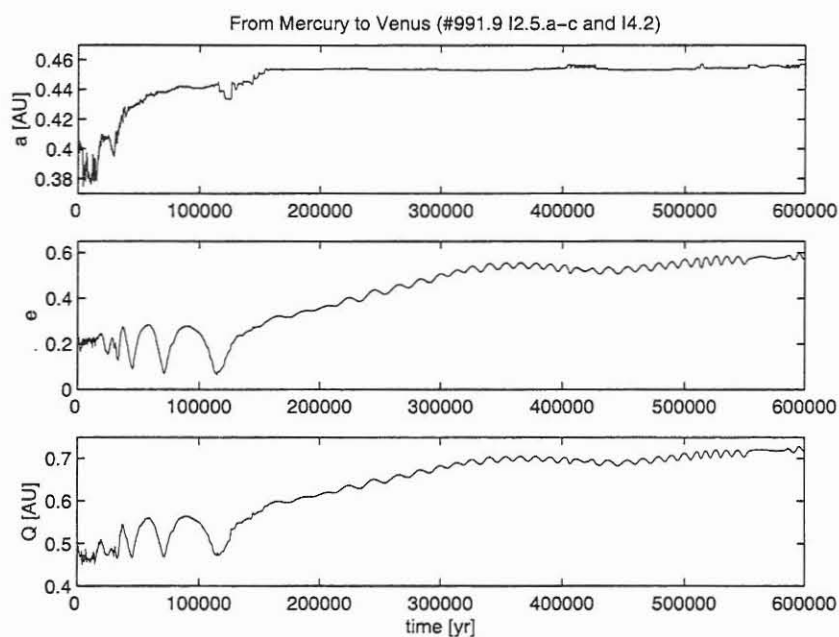


Figure 3: Object in transit from the Mercury to the Venus dominated regime via the secular ν_2 resonance (the value of a for Venus is 0.723 AU).

MECHANICAL MODELING OF THE DISCOVERY RUPES THRUST FAULT: IMPLICATIONS FOR THE THICKNESS OF THE ELASTIC LITHOSPHERE OF MERCURY.

T. R. Watters¹, R.A. Schultz², M. S. Robinson³, and A. C. Cook¹, ¹Center for Earth and Planetary Studies, National Air and Space Museum, Smithsonian Institution, Washington, D.C. 20560 (twatters@nasm.si.edu); ²Geomechanics-Rock Fracture Group, Department of Geological Sciences, Mackay School of Mines, University of Nevada, Reno; ³Department of Geological Sciences, Northwestern University, Evanston, Illinois 60208.

Introduction: One of the most remarkable discoveries of the Mariner 10 mission to Mercury was the existence of hundreds of landforms described as lobate scarps [1, 2, 3]. Based on morphology and offsets in crater wall and floor materials, lobate scarps are interpreted to be the surface expression of thrust faulting [1, 2, 3, 4, 5]. The largest lobate scarp on the hemisphere imaged by Mariner 10 is Discovery Rupes. Located in the southern hemisphere, Discovery Rupes is over 500 km in length [1, 2]. New topographic data for Mercury, derived from digital stereoanalysis, using updated Mariner 10 camera orientations [6, 7], indicates that Discovery Rupes is up to ~1.5 km high [4, 5]. These data are also providing the first quantitative measurements about the morphometry of Discovery Rupes. Using the new topographic data, it is possible to test the validity of kinematic models proposed for lobate scarps by mechanically modeling the long and short wavelength topography across Discovery Rupes.

Topography and Analysis: Topography of Discovery Rupes was obtained using an automated stereo matching process that finds corresponding points in stereo images using a correlation patch [cf. 8]. A stereo intersection camera model is then used to find the closest point of intersection of matched points which specifies their location and elevation. The derived digital elevation model (DEM) has a grid spacing of 2 km/pixel (Figure 1) [also see 9, 10].

The greatest relief on Discovery Rupes occurs roughly midway along the length of the scarp (south of the 60-km-diameter Rameau crater, Figure 1). The average relief of the scarp in this area is about 1.3 km (Figure 2) [4]. The new topographic data reveal a shallow trough roughly 100 km west of the base of the scarp (Figure 1). This trough is interpreted to be evidence of a trailing syncline and the distance between it and the surface break defines the cross-strike dimension of the upper plate of the Discovery Rupes thrust fault.

Mechanical Model: The 3-D boundary element dislocation program Coulomb 2.0 was used to predict the surface displacements associated with the Discovery Rupes thrust fault. The dislocation method has been successfully applied to terrestrial faults [11, 12] where the magnitude of offset along the fault is known and when the remote stress state or

frictional/constitutive properties of the fault are unknown [13, 14]. The magnitude and sense of offset are specified along the fault, then the stresses and material displacements are completely determined using the stress functions for an elastic halfspace [15]. An acceptable match between the model and the topography constrains admissible values. We then calculate the displacement vectors to predict changes in topography due to the surface-breaking thrust fault beneath Discovery Rupes.

Results and Implications: Iteratively adjusting the displacement D , fault dip θ , and depth of faulting T , good fits to the topography are obtained for a relatively narrow range of the fault parameters (Figure 2, 3). Depths of faulting $T < 30$ km and $T > 40$ km (Figure 2) produce unacceptable fits to the topography. The best fits to the topography across Discovery Rupes are for a depth of faulting $T = 35$ to 40 km, fault dip angle $\theta = 30^\circ$ to 35° , and $D = 2.2$ km (Figure 4). A tapered displacement distribution with minima at the fault tips is assumed based on examining the offset where the fault breaks the surface. Where the Discovery Rupes thrust fault cuts the floor of Rameau crater (Figure 1), there is no significant offset suggesting that the cumulative structural relief developed while the fault was blind and propagating up toward the surface.

Our results suggest that the Discovery Rupes thrust fault cuts the mercurian crust to a depth of up to 40 km. There are examples of terrestrial thrust faults that cut to comparable depths. The Wind River thrust in the Rocky Mountain foreland in Wyoming extends to a depth of 36 km (with a uniform dip of 30° to 35°) [16], cutting the entire elastic lithosphere T_e . On Earth's continents, T_e typically coincides with the thickness of the seismogenic crust T_s (ranging from ~10-40 km), with T_e often less than T_s [17, 18]. On Mars, the Amenthes Rupes thrust fault extends to a depth comparable to estimates of T_e for the highlands [19] (~20-30 km) [20, 21]. If the Discovery Rupes thrust fault extends to a depth of ~40 km, it may cut the entire mercurian elastic and seismogenic lithosphere. An estimate of T_e from depth of faulting provides insight into the thermal structure of the mercurian crust at the time the faults formed. The effective elastic thickness is thought to be controlled by the depth of the 450° to 600°C isotherm below which the lithosphere is too weak to support long-

term stresses [17, 22]. Our results suggest a thermal gradient of $\sim 8^\circ\text{K km}^{-1}$ and a heat flux of $\sim 24 \text{ mW m}^{-2}$ at the time Discovery Rupes formed. These estimates will be testable when MESSENGER [23] and Bepi Colombo returns new gravity and topographic data.

References: [1] Strom R.G., Trask N.J. and Guest J.E. (1975) *J. Geophys. Res.*, 80, 2,478-2,507. [2] Cordell, B.M. and Strom R.G. (1977) *Phys. Earth Planet. Inter.*, 15, 146-155. [3] Melosh H.J. and McKinnon W.B. (1988) *in Mercury*, 374-400. [4] Watters T.R., Robinson M.S. and Cook A.C. (1998) *Geology*, 26, 991-994. [5] Watters T.R., Robinson M.S. and Cook A.C. (2001) *Planet. Space Sci.*, in press. [6] Robinson, M.S., Davies, M.E., Colvin, T.R. and Edwards, K.E. (1999) *J. Geophys. Res.*, 104, 30847-30852. [7] Robinson, M.S. and Lucey, P.G. (1997) *Science*, 275, 197-200. [8] Day, T., Cook, A.C. and Muller, J.P. (1992) *Intern. Arch. Photo. Rem. Sensing* 29, 801-808. [9] Wilkison, S.L., Robinson, M.S., Watters, T.R.

and Cook, A.C. (2001) this volume. [10] Cook, A.C., Watters, T.R. and Robinson, M.S. (2001) this volume. [11] King, G.C.P., Stein, R.S. and Rundle, J.B. (1988) *J. Geophys. Res.*, 93, 13307-13318. [12] Taboada, A., Bousquet, J.C. and Philip, H. (1993) *Tectonophysics*, 220, 223-241. [13] Rudnicki, J.W., (1980) *Annu. Rev. Earth Planet. Sci.*, 8, 489-525. [14] Bilham, R. and King, G. (1989) *J. Geophys. Res.*, 94, 10204-10216. [15] Okada, Y., (1992) *Bull. Seismol. Soc. Am.*, 82, 1018-1040. [16] Brewer, J.A., Smithson, S.B., Oliver, J.E., Kaufman, S., and Brown, L.D. (1980) *Tectonophysics*, 62, 165-189. [17] McKenzie, D. and Fairhead, D. (1997) *J. Geophys. Res.*, 102, 27523-27552. [18] Maggi, A., Jackson J.A., McKenzie, D. and Priestley, K. (2000) *Geology*, 28, 495-498. [19] Schultz, R.A. and Watters, T.R. (2001) Submitted to *Geophys. Res. Lett.* [20] Zuber, M.T., et al., (2000) *Science*, 287, 1788-1793. [21] Nimmo, F., (2001) *Lunar Planet. Sci.*, XXXII, abs. 1370. [22] Watts, A.B. (1994) *Geophys. J. Int.*, 119, 648-666. [23] Solomon et al., (2001) *Planet. Space Sci.*, in press.

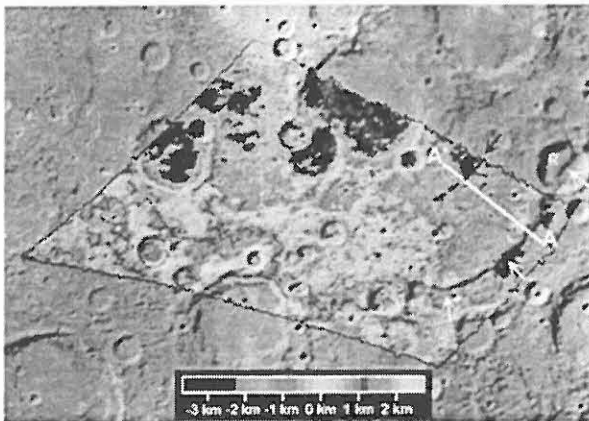


Figure 1. Color-coded DEM generated using Mariner 10 stereo pair 27399 and 166613, overlaid on an image mosaic. The white line indicates the location of the topographic profile across Discovery Rupes (white arrows) shown in Figure 2 and 3. The black arrow and dashed line shows the location of a shallow depression. Rameau crater is indicated by an R on the image. Elevations relative to 2439.0 km reference sphere.

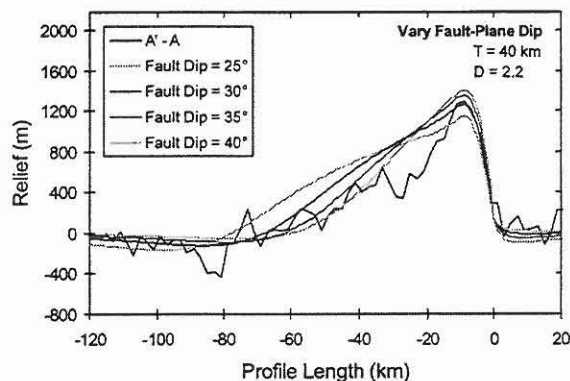


Figure 3. Comparison between predicted structural relief and a topographic profile across Discovery Rupes. Fault-plane dip θ is varied while the depth of faulting and displacement are constant. Profile location is shown in Figure 1. Vertical exaggeration is 30X.

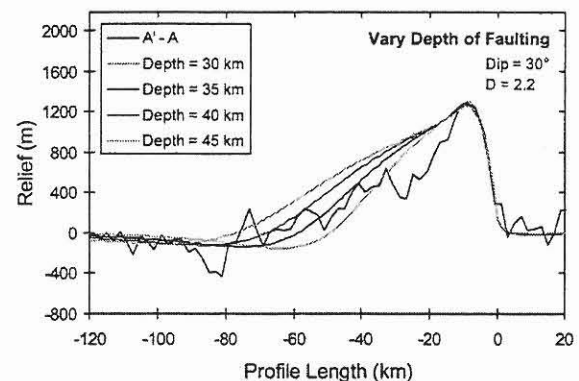


Figure 2. Comparison between predicted structural relief and a topographic profile across Discovery Rupes. Depth of faulting T is varied while the fault-plane dip and displacement are constant. Profile location is shown in Figure 1. Vertical exaggeration is 30X.

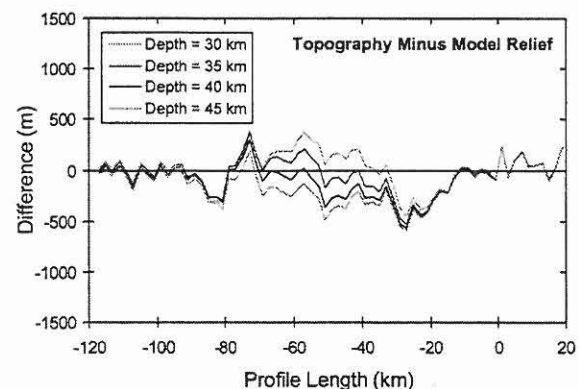


Figure 4. Difference between topography and predicted structural relief for model runs shown in Figure 2. Plots indicate that the best fit is obtained for depth of faulting $T = 35-40 \text{ km}$. Vertical exaggeration is 30X.

QUALITY ASSESSMENT OF MARINER 10 DIGITAL ELEVATION MODELS. S. L. Wilkison¹, M. S. Robinson¹, T. R. Watters², and A. C. Cook², ¹Department of Geological Sciences, Northwestern University, Evanston, Illinois 60208, ²Center for Earth and Planetary Studies, National Air and Space Museum, Washington D. C. 20560.

Introduction: New camera positions and orientation data [1] were used to create a new map of Mariner 10 stereo coverage [2]. The automated digital stereo analysis provides continuous topographic data with 1-2 km spatial resolution and 0.5 to 2 km vertical resolution [2]. Wilkison et al. [3] reported an analysis of crater topography using this stereo data, examining the depth to diameter ratio (d/D) for immature and mature complex craters within a DEM (digital elevation model) of the Discovery Quadrangle. The d/D results [3] agree with those of Pike [4] for mature complex craters. However, the d/D results [3] for immature complex craters diverged from that of Pike [4]. Crater depth shallows as the immature complex craters approached the pixel size of the stereo matching box, or "patch", which was typically 5 to 12 pixels (in radius), with image resolution of 1-2 km. We hypothesized that the patch size used in matching the stereo images created a smoothing effect of the topography within the DEM. To determine how the patch size was affecting the topography of the DEM, we performed a series of simple tests. These tests allow us to realistically place bounds on the accuracy and precision of the Mariner 10 DEMs.

Background and Method: As part of the process of stereo image analysis, automated digital stereo matching finds corresponding points in image pairs. Patterns of pixels from a reference image are searched for within the accompanying stereo image. This automated stereo matching process is performed by comparing pixel patterns between the images within correlation windows, or patches. Typical correlation patch sizes range from 5 by 5 pixels [5,6,7] to 9 by 9 and 21 by 21 pixels [8,9]. The matching program used with our study, the UCL "Gotcha" program, uses patch radius sizes of 5-12 (11 by 11 to 25 by 25 pixels) [10,11].

Precision within the DEMs. To better understand the quality of the Mariner 10 DEMs and to determine if the DEMs provide repeatability of the low frequency topography (relative to the patch size), we produced DEMs resulting from varying the correlation patch sizes (patch sizes 5-12). Profiles across topography are plotted to show the variation within a given elevation with different correlation patch sizes. Figure 1 shows the DEM with the location of the topography profile. Figure 2 shows the topography across this region from the 27399/166613 stereo pair. Patch sizes 5 through 12

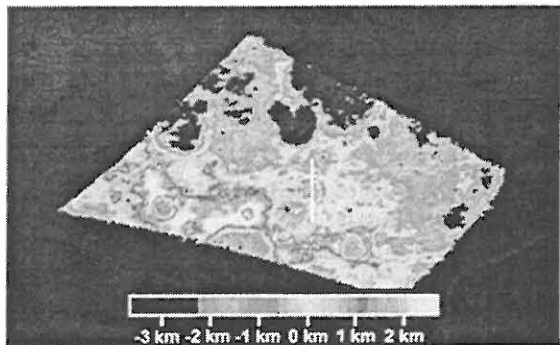
are shown. Figure 2 indicates that the larger the patch size, the more smoothed the topography becomes; as the patch size increases, the area over which the average is determined also increases. This observation explains the trend that we observed with the d/D measurements [3]; the patch size created an artificial shallowing of crater depth. Table 1 shows d/D measurements from the profiles in Figure 2; the topography is smoothed and the d/D decrease with increased patch size. The increased noise with the smaller patch sizes is probably due to an artifact of the matching algorithm.

Accuracy within the DEMs. The smoothing trend observed from varying the correlation patch size is an effect somewhat equivalent to performing a low-pass filter on DEM data with different sized boxfilters. We tested this comparison by applying a low-pass boxfilter (with varying box sizes of 5 by 5, 7 by 7, 9 by 9, 11 by 11, 15 by 15, 21 by 21, and 35 by 35 pixels) to two DEMs. The Kilauea DEM from the Kilauea Compiled Volcanology Dataset, produced by JPL in 1992, has a resolution of 9.146 m/pixel. The Apollo 17 DEM was created from topographic data from the USGS 1:50,000 scale map of the Taurus-Littrow Valley [12], with a resolution of 10 m/pixel. Topographic profiles were measured from each of the low-pass filtered DEMs (as shown in Figure 3 and 4). Both sets of topographic profiles indicate the same trend; as the boxfilter size increases, smoothing of the topography increases (a larger boxfilter averages over a larger area). Measurements of d/D from both sets of profiles also show smoothing as box size increases. The smoothing of topography trend observed with the Mariner 10 data is also observed with these high quality "known" DEMs, indicating that the smoothing of topography is a real effect and not due to inaccuracy within the Mariner 10 DEMs.

Conclusions: We observed smoothing of topography with larger correlation patch sizes and "noise" with smaller correlation patch sizes. The low-pass boxfilter test on "known" DEMs indicate that the smoothing effect is real and not an artifact of the Mariner 10 stereo images. Future studies will include implementing different matching programs with different correlation patch sizes in the hope of decreasing the "noise" observed within the lower patch sizes, and examining specific craters on many DEMs with different patch sizes.

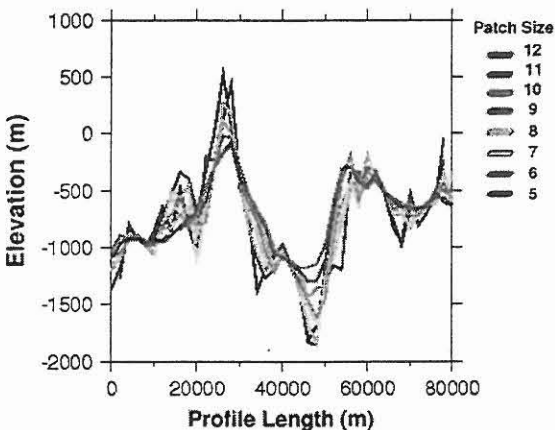
References: [1] Robinson M. S. et al. (1999) *JGR*, 104, 30847-30852. [2] Cook A. C. and Robinson M. S. (2000) *JGR*, 105, 9429-9443. [3] Wilkison S. L. et al. (2000) *LPSC XXXII*, #2118. [4] Pike R. (1988) in *Mercury*, pp165-273. [5] Schenk P. M. and Moore J. M. (1995) *JGR*, 100, 19009-19022. [6] Schenk P. M. et al. (1997) *GRL*, 24, 2467-2470. [7] Schenk P. M. and Moore J. M. (2000) *JGR*, 105, 24529-24546. [8] Oberst et al. (1996a) *LPSC XXVII*, p. 973. [9] Oberst et al. (1996b) *Planet. Space Sci*, 44, 1123-1133. [10] Day et al. *International Archives of Photogrammetry and Remote Sensing*, XXIX, B4, 801-808. [11] Thornhill et al. (1993) *JGR*, 98, 23581-23587. [12] Preliminary Topographic Map of Part of the Littrow Region of the Moon, March 1972, USGS Flagstaff, [13] Watters T. et al. (this volume).

Figure 1. Color-coded digital elevation model generated using Mariner 10 stereo pair 27399 and 166613



[13]. The white line indicates the location of the topographic profile shown in Figure 2. The elevations are relative to the 2439 km radius reference sphere.

Figure 2. Comparison between topographic profiles taken from DEMs generated with different correlation



patch sizes. The profile location is shown in Figure 1.

Table 1. d/D ratios determined from the topographic profiles shown in Figure 2. The location of the crater is shown in Figure 1.

Patch Size	
5	0.0803
6	0.0800
7	0.0756
8	0.0636
9	0.0570
10	0.0481
11	0.0437
12	0.0382

Figure 3. Comparison between topographic profiles taken from a DEM filtered with varyingly sized low-pass boxfilters. Shown is a profile of topography measured from a DEM from the Kilauea Volcanology Compiled Dataset by JPL, 1992. Spatial resolution of the DEM is 9.146 m/pixel.

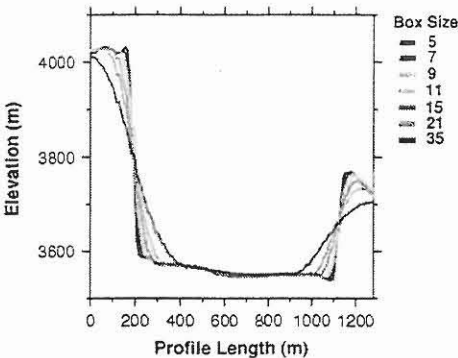
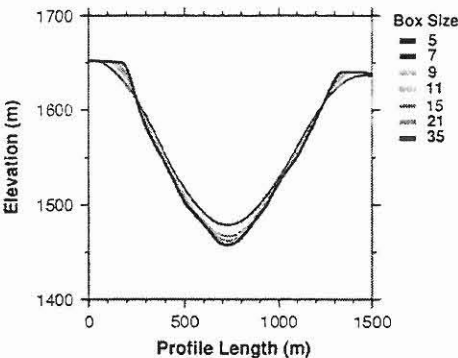


Figure 4. Comparison between topographic profiles taken from a DEM filtered with varyingly sized low-pass boxfilters. Shown is a profile of topography measured from a lunar crater (Mocr) from a DEM derived from the USGS 1:50,000 scale map of the Taurus-Littrow Valley [12]. Spatial resolution of the DEM is 10 m/pixel.



HIGH DEFINITION IMAGING OF MERCURY'S SURFACE AND ATMOSPHERE. J. K. Wilson, M. Mendillo, and J. Baumgardner.

High Definition Imaging (HDI) is a means of obtaining nearly diffraction-limited images of telescopic targets through a turbulent atmosphere without adaptive optics. The method involves taking thousands of high-speed (1/60th second) video images of an object, and then selecting the small fraction of those images which occurred during instances of "perfect seeing" to construct a final, high-resolution image.

In 1998 we obtained nearly diffraction-limited images of Mercury's surface using a digital imaging video system on the Mt. Wilson 1.5m telescope. These images reveal dark "mare-like" areas punctuated by brighter spots. In November of 2000 we tested our complete HDI system on Mercury, including an image slicer/spectrograph, using the 2.1m telescope at McDonald Observatory. Our ultimate goal is to obtain high-resolution, monochromatic images of Mercury's sodium atmosphere to better understand the surface distribution and variability of the atmospheric source mechanisms.

Photon- and electron-stimulated desorption of alkalis from model mineral surfaces:
relation to Planetary atmospheres.

B. V. Yakshinskiy and T. E. Madey

Department of Physics and Astronomy, and Laboratory for Surface Modification
Rutgers, The State University of New Jersey

To investigate source mechanisms for the origin of Na and K in the tenuous atmospheres of the planet Mercury and the Moon, we are studying the photon - and electron - stimulated desorption (PSD and ESD) of alkali atoms from amorphous silicon dioxide films grown on a metal substrate . The ultrahigh vacuum measurement scheme for ESD and PSD of alkalis includes an efficient pulsed low-energy electron source, as well as mechanically-chopped UV light from a mercury arc source, a highly sensitive detector based on surface ionization, and the use of a time-of-flight technique. We find that bombardment of Na (K) covered silica surface by ultraviolet photons or by low energy electrons ($E > 4$ eV) causes desorption of supra-thermal Na and K atoms with velocity distribution peaks at 1000 m/s and 650 m/s, respectively. These values are consistent with the “hot” components of the lunar and Mercurian atmospheres. The ESD yield demonstrates a resonance-like feature at ~ 11 eV and a shoulder at 25eV excitation energy (O_2s excitation). The mechanism of desorption is identified as an electronically excited charge-transfer from the silica substrate to neutralize the surface alkali ion, followed by desorption of the alkali atom [1]. These data strongly suggest that PSD by UV solar photons ($E > 4$ eV) is a dominant source process for Na and K in the tenuous lunar atmosphere. Although there are insufficient electrons in the solar wind to produce the observed lunar sodium atmosphere, there appear to be sufficient UV solar photons to maintain the atmosphere by desorbing Na from the surface. In the case of Mercury, where long-wavelength solar photons cause significant heating of the surface (~ 700 K) at the sub solar point, thermal desorption of Na and K is believed to contribute to the tenuous atmosphere, but PSD is likely to play a major role in that case also.

[1] B.V.Y. & T.E.M., *Nature*, vol. **400**, p. 642 (1999)

THE MERCURY PLASMA ENVIRONMENT: MHD PREDICTIONS AND MERCURY PICKUP IONS.

T. H. Zurbuchen^{1,2}, P. L. Koehn², L. A. Fisk², G. Gloeckler³, and K. Kabin⁴, ¹thomasz@umich.edu, ²University of Michigan, Atmospheric, Oceanic and Space Sciences Department, Ann Arbor, MI 48109-2143, ³University of Maryland, Physics Department, Space Research Group, College Park MD, 20742, ⁴University of Alberta, Department of Physics, Edmonton, AL T6G 2J1, Canada.

Abstract: The Mercury environment is dominated by two particle populations: the solar wind and ions originating from Mercury. The absence of any significant ionosphere and atmosphere creates a magnetosphere that differs from the Earth's and may affect the transfer of energy from the solar wind to magnetospheric plasma. We use three-dimensional MHD simulations from Kabin et al. [1] to model fundamental magnetospheric processes in the planet's vicinity.

Due to its close vicinity to the Sun, the solar wind momentum flux is ~ 10 times larger than the momentum flux at Earth [see, e.g., Russell et al. (1988) [2]. At the same time, Mercury's intrinsic magnetic field is relatively weak. Under normal solar wind conditions, this magnetic field is able to hold off the solar wind, preventing it from striking the planet's surface. This is not always the case, however. For example, during fast coronal mass ejections the solar wind ram pressure can be sufficient to compress the magnetopause to the surface. This direct interaction gives rise to sputtered particles that provide a direct probe of the surface composition. Most of these particles are released in a neutral state and are eventually ionized. The resulting pickup ions move through Mercury's magnetosphere.

We apply the results of recently modeled three-dimensional MHD interactions of the solar wind and Mercury's magnetosphere to predict the plasma and composition measurements on MESSENGER, a Mercury orbiter scheduled for launch in 2004. We then use this simulated MHD structure of the magnetosphere to record the trajectories of newly created magnetospheric and near-surface pickup ions. During certain parts of the MESSENGER orbit, these ions are observed during their first gyration. The observed particles therefore provide a good measure for the neutral particle environment near Mercury. During other, more distant parts of the MESSENGER orbit, the spatial distribution of particles depends on the large-scale structure of the Mercury magnetosphere. Detailed pickup ion measurements therefore provide direct information about the Mercury surface composition, and the structure of the Mercury magnetosphere.

We will present the simulated trajectories and spatial distributions of these pickup ions, as well as predictions of particle fluxes measured by the Fast Imaging Plasma Spectrometer (FIPS), one of the mass spectrometers on board the MESSENGER spacecraft.

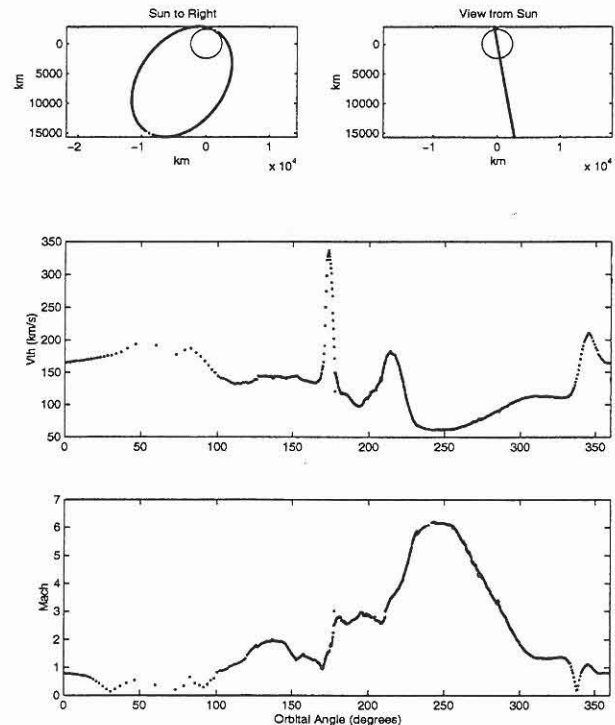


Figure 1: Simulated plasma measurements during one particular orbit of the MESSENGER spacecraft in the Mercury Environment.

References:

- [1] Kabin, K., et al. (2000), *Icarus*, 143, 397-406.
- [2] Russell, C.T., Baker, D.N., and Slavin, S.A., (1988), University of Arizona Press, Eds. F. Vilas, C. R. Chapman, and M. S. Mattheus, 514-561.

